MODELING OF
EXTERIOR ROTOR PERMANENT MAGNET MACHINES
WITH CONCENTRATED WINDINGS

VŨ XUÂN HÙNG

MODELING OF
EXTERIOR ROTOR PERMANENT MAGNET MACHINES WITH CONCENTRATED WINDINGS

Proefschrift

ter verkrijging van de graad van doctor
aan de Technische Universiteit Delft,
op gezag van de Rector Magnificus prof. ir. K.C.A.M. Luyben,
voorzitter van het College voor Promoties,
in het openbaar te verdedigen op dinsdag 25 september 2012 om 12.30 uur

door Hùng VŨ XUÂN
Master of Electrical Engineering, Hanoi University of Science and Technology
geboren te Hagiang, Vietnam.

Dit proefschrift is goedgekeurd door de promotor:
Prof. dr. J.A. Ferreira

Copromotor:
Dr. ir. D.J.P. Lahaye

Samenstelling promotiecommissie:

Rector Magnificus, voorzitter
Prof. dr. J.A. Ferreira, Technische Universiteit Delft, promotor
Dr. ir. D.J.P. Lahaye, Technische Universiteit Delft, copromotor
Prof. dr. ir. A.W. Heemink, Technische Universiteit Delft
Prof. ir. Mart van der Meijden, Technische Universiteit Delft
Prof. dr. ir. Johan Gyselinck, Université libre de Bruxelles
Prof. dr. ir. Herbert de Gersem, Katholieke Leuven Universiteit
Dr. ir. H. Polinder, Technische Universiteit Delft

Cover design by HA VU

Printed by Proefschriftmaken.nl || Uitgeverij BOXPress
The Netherlands

ISBN: 9789088914690

Dedicated to my father
To my family
Tặng con trai yêu, Vũ Quang Minh

ACKNOWLEDGMENTS

The research presented in this thesis was carried out at the Delft University of Technology in The Netherlands, in the research group Electrical Power Processing (EPP) headed by Professor Braham Ferreira, an *IEEE Fellow*. During my Ph.D, I worked with many wonderful people. They contributed to the work presented in this thesis either directly or indirectly. I would like to take this opportunity to thank those people for their contribution.

Firstly, I would like to express my gratitude to my promoter, Professor Braham Ferreira for the leadership and patience he showed and the guidance and support he gave me during my studies and the writing of this thesis. If without our monthly meetings and his brilliant feedback, I would never have been able to find my way in engineering research.

I would like to thank to my daily supervisor, Dr. Domenico Lahaye for his many fruitful discussions about finite element computation, his guidance, and useful comments for improving the writing this thesis. I am deeply grateful to you.

I am grateful to my daily supervisor in EPP group, Dr. Henk Polinder for many invaluable discussions involving this thesis as well as my papers. His expert knowledge of electrical machines helped me to understand many complicated physical phenomena in electric machines in more depth.

I would like to say thanks to Dr. Martin Hoeijmakers, who was my daily supervisor in the second year of my Ph.D research. He gave me a “kick start” in finite element computation. Many fruitful discussions in the electromagnetic field modelling helped me to save time. I feel indebted to you.

I would like to express my gratitude to my doctoral examination committee, Prof. Herbert de Gersem, Prof. Johan Gyselinck, Prof. Mart van der Meijden and Prof. Arnold W. Heemink for spending a large amount of time on reading on my draft thesis and giving valuable comments and suggestions.

I highly appreciate the help of Rob Schoevaars. His experience and assistance helped me overcome all practical problems.

I am sincerely grateful to Ms. Veronique van der Varst, who works at the International Cooperation Office, CICAT of the TU Delft. She helped me to solve many problems for example with my work-permit and visa and with financial procedures.

A sincere thank you to Ms. Melanie Bailey who did the English editing of the manuscript.

I am grateful to the secretary of the department and EPP group, Suzy Sirks-Bong and Laura Bruns. They indirectly contributed to my achievement.

My thanks to Ha Vu who did the cover design.

My thanks to Martin van der Geest who translated the summary of this thesis to Dutch.

I would like to thank to my officemate Ani Sam for his friendship and help. He is my true friend. We discussed many things from electric machines to life. He believes that we did not become officemates by chance, but that God arranged this. I thank his God for giving us this opportunity.

I would like to thank to Aleksandar Borisavljević and his wife, Veronica Pišorn for their kindness when I met with difficulty.

I would like to thank to my PhD friends in EPP group for their friendship. Special thanks to my friends in the project "Mastervolt project", Marcelo and Yi Wang for many fruitful discussions and good cooperation.

I would like to thank to all of my Vietnamese friends, too many to mention by name, in The Netherlands for their friendship and brotherhood. They made the years of my Ph.D research in The Netherlands enjoyable.

Vietnamese do not have tradition of thanking to those who are very close relative. It is considered as not necessary. Untraditionally, I would like to thank to my wife and my lovely son, V.Q. Minh, and all of my family members for their love, understanding, and sacrifice.

Last but not least, I would like to thank the Vietnamese people for funding my studies through so-called "Vietnamese government scholarship for overseas study or Project 322". This research is funded in part by the international cooperation office of the TU Delft, CICAT and EPP group. I highly appreciate the support of these organisations.

Delft, August 2012

Vũ Xuân Hùng

TABLE OF CONTENTS

LIST OF ABBREVIATIONS AND SYMBOLS

Abbreviations

2D	Two Dimensions
3D	Three Dimensions
A rms	Ampere root mean square
AC	Alternative Current
AC/DC	Alternative Current/Direct Current
AFPMs	Axial Flux Permanent Magnet Machines
ALE	Arbitrary Lagrangian-Eulerian
CFD	Computational Fluid Dynamics
CPMR	Number of cogging torque cycles per mechanical revolution
DC	Direct Current
DC/DC	Direct Current/Direct Current
EMF	Electromotive Force
FEA	Finite Element Analysis
FEM	Finite Element Method
GCD	The Greatest Common Divisor
GPIB	General Purpose Interface Bus
LCM	The Least Common Multiple
MMF	Magnetomotive force of a phase
MMFs	Magnetomotive Force of three phases
NdFeB	Neodymium Ferrite Boron
PM	Permanent Magnet
RFPMs	Radial Flux Permanent Magnet Machines
RMS, rms	The Root Mean Square
TFPMs	Transverse Flux Permanent Magnet Machines
vs.	Versus

Main Symbols

$\widehat{B}$	Amplitude of flux density, [T]
$\widehat{B}_{g1}$	Amplitude of the fundamental flux density in air gap due to magnets, [T]
$\widehat{B}_{t1}$	Amplitude of the fundamental flux density of a tooth, [T]

$\widehat{B}_{sak}$	Flux density amplitude of the k^{th} space harmonic due to stator current-carrying windings of phase *a* alone, [T]
$\widehat{B}_{sk}$	Flux density amplitude of the k^{th} space harmonic due to three-phase current-carrying windings, [T]
$\hat{i}_s$	Amplitude of stator current, [A]
$\widehat{K}_1$	Amplitude of the fundamental component of electric loading, [A/m]
$< n_a(\theta_s) >$	Average value of the turn function of phase *a*
A_{Cu}	Cross section of Copper wiring, [m^2]
A_{slot}	Cross section of slot, [m^2]
A_z	The magnetic vector potential in the z-direction, [Wb/m]
$B_{g\ mean\_sat}$	Mean flux density in air gap during saturated magnetic circuit, [T]
$B_{g\ mean\_unsat}$	Mean flux density in air gap during unsaturated magnetic circuit, [T]
$B_{g,0}$	Mean air gap flux density due to magnet at positions opposite the magnet, [T]
$B_{g,max}$	Max air gap flux density due to magnet at positions opposite the magnet, [T]
B_n	Normal (radial) component of flux density, [T]
B_r	Remanent flux density of magnet, [T]
B_{ry}	Mean flux density of rotor yoke, [T]
B_{sy}	Mean flux density of stator yoke, [T]
B_t	The tangential component of the flux density, [T]
b_s	Slot opening width, [m]
c	Specific heat, [J/kg/K]
C	Thermal capacitance, [J/K]
d_{cu}	Diameter of Copper wiring, [m]
d_i	The thickness of plastic electric insulation, [m]
D_{ir}	Interior diameter of rotor, [m]
D_{os}	Outer stator diameter, [m]
D_s	Outer stator diameter, [m]
e_a	Instantaneous electromotive force of phase *a*, [V]
e_{a1}	Fundamental instantaneous EMF of phase *a*, [V]
f	Fundamental frequency of rotating field, [Hz]
F	Factor concerning thermal conduction of slot windings and end windings
$F_a()$	MMF function of phase *a* due to current of phase *a* alone, [A.turn]
g	Physical air gap length, [m]
g_{eff}	Effective air gap length, [m]

G_r	The Grashof number, dimensionless number
h	Heat transfer convection coefficient, [W/K/m^2]
h_0	Slot opening depth, [m]
H	Magnet field strength, [A/m]
h_s	Slot height, [m]
h_{sy}	Height of stator yoke, [m]
h_t	Tooth height, [m]
I_1	The rms of fundamental stator current, [A]
J_s	Current density of source, [A/m^2]
k	Thermal conductivity, [W/m/K]
k_C	Carter factor/coefficient
k_{Cu}	Copper thermal conductivity, [W/m/K]
k_e	Eddy current coefficient
k_i	The thermal conductivity of electric insulation material, [W/m/K]
k_{exc}	Excess loss factor
k_{fill}	Filling factor
k_h	Hysteresis coefficient
k_s	Factor accounting for increasing amplitude of short current during transient of three-phase short circuit
k_{safe}	Safe factor
k_{sat}	Saturation correction factor
k_{sh}	Shape factor, which is ratio of interior diameter of rotor and rotor length
k_v	Thermal conductivity of varnish, [W/K/m]
k_{pt}	Thermal conductivity of plastic, [W/K/m]
K_{w1}	Fundamental winding factor
L_{aa}	Self-inductance of phase *a*, [H]
L_{ab}	Mutual inductance between phase *a* and *b*, [H]
l_{cu}	Average length of a turn, [m]
l_e	The average length of the end winding, [m]
L_{end}	End leakage inductance, [H]
L_l	Leakage inductance, [H]
l_l	Thickness of iron lamination, [m]
L_m	Main synchronous inductance, [H]
l_m	Radial length of magnet, [m]
l_r	Rotor length, [m]
l_s	Stator length, [m]

L_s	The synchronous inductance, [H]
L_s	Stator length, [m]
L_{slot}	Slot leakage inductance, [H]
m	Number of phases
m_{ew}	The mass of an end winding, [kg]
m_{sw}	The mass of a slot winding, [kg]
n	Rotation of rotor per minute, [rpm]
n	The number of iron laminations
$N_{\lambda l}$	Number of winding cycles
$n_a()$	Turn function of phase a
$N_a()$	Winding function of phase a
N_c	The number of turns per tooth
N_{coil}	The number of coils of a PM machine
N_{layer}	The number of layers of winding
N_p	The number of cogging torque cycles per pole pair
N_s	The number of cogging torque cycles per slot
N_{slot}	Slot number
N_t	The number of teeth
$\mathrm{N_{uD}}$	The Nusselt number, dimensionless number
N_w	The number of turns of windings of a phase
N_c	The number of turns per coil
p	The number of pole pairs
P_e	Mean electromagnetic power, [W]
P_{exp}	Experimental stator iron loss, [W]
P_r	The Prandtl number, dimensionless number
P_s	Specific slot permeance functions, [H/m]
P_{Cu_sw}	Copper power loss in slot windings, [W]
P_{Cu_ew}	Copper power loss in end windings, [W]
P_{fe_st}	Iron loss in stator teeth, [W]
P_{fe_sy}	Iron loss in stator yoke, [W]
P_{edd_ry}	Eddy current loss in rotor yoke, [W]
G_r	Grashof number, dimensionless number
Q	The number of slots
q	The number of slots per pole per phase
R	Thermal resistance, [K/W]
R_a	The Rayleigh number, dimensionless number

Re	The Reynolds number, dimensionless number
rpm	Rotations per minute
r_s	Stator radius, [m]
R_s	Stator winding resistance of a phase, [Ω]
S	Integral surface
t_m	Thickness of magnet or length of magnet in the direction of magnetization
T	Temperature, [K, ^{o}C]
T_e	Electromagnetic torque, [Nm]
U_{a1}	The rms of fundamental voltage of phase a, [V]
v^{th}	The v^{th} harmonic order
W_a	Winding vector of phase a
w_m	Pole width, [m]
w_s	Equivalent slot width, [m]
W_t	Tooth width, [m]
w_t	Tooth width, [m]
z	The number of slots or the number of teeth

Greek Symbols

$\hat{}$	Amplitude
ψ	Flux linkage, [Wb]
∇	Gradient operator
$\widehat{\Phi}_{s1}$	Amplitude of fundamental flux per pole pitch due to the MMFs, [Vs, Wb]
$\nabla\times$	Curl operator
$\nabla\cdot$	Divergent operator
ϕ_{s1}	Fundamental flux per pole pitch due to the three-phase MMFs, [Vs , Wb]
$\nabla\varphi$	Gradient of the scalar electric potential, [V/m]
$\widehat{\Phi}_{t1}$	Amplitude of the fundamental flux passing through a tooth, [Vs , Wb]
$\widehat{\psi}_{a1,s\_ideal}$	Amplitude of the fundamental flux linkage of phase a due to MMFs of stator windings in the ideal case, [Wb]
ω	Angular rotation velocity, [rad/sec]
ω	Electric angular frequency, [rad/sec]
υ	Kinematic viscosity, [m^2/s]
δ	Mechanical angle corresponding to a slot pitch, [rad]

β	Angular displacement between the field produced by the magnet and the stator current, [rad]
φ	The scalar electric potential, [V]
ρ	The weight (mass) density, [kg/m^3]
ϕ	Flux, [Wb]
σ	The Stefan-Boltzmann constant, σ=5.67*10^{-8} [W.m^{-2}.K^{-4}]
θ_0	Rotor initial angle, [rad]
λ_1	Wave length angle, [rad]
γ_{Fe}	Weight density of iron, [kg/m^3]
ω_m	Angle speed of rotor, [rad/sec]
θ_m	Displacement angle of rotor, [rad]
θ_r	Mechanical angle in the rotor coordinate, [rad]
α_{rad}	Equivalent radiation coefficient, [W/K/m^2]
θ_s	Mechanical angle in the stator coordinate, [rad]
μ	Permeability, [H/m]
μ	Dynamic viscosity, [Pa.s, kg/m/s]
2α	Pole arc, [rad]
β	The Steinmetz constant
μ_o	Permeability of air, μ_o =4π10^{-7} [H/m]
μ_{rm}	Relative permeability of magnet
σ	Air gap shear stress, [N/m^2]
σ	Electric conductivity, [S/m]
τ_p	Pole pitch, [m]
τ_s	Slot pitch, [m]

Subscripts

1	The first harmonic
a1	The fundamental component of phase *a*,
c	Coil
c	Convection
c1,s	Conductor, first harmonic, due to the current-carrying conductor in stator slot
cog	Cogging
Cu	Copper
dst	Destination
e	Eddy current

ew	End winding
exc	Excess
exp	Experiment
ext	External
fe or Fe	Iron
g1	Air gap and the first harmonic
h	Hysteresis
i	Induced
i	Insulation
ir	Interior, rotor
k	The k^{th} harmonic
m	Magnet
m	Mechanical
mech	Mechanical
n	Normal component
or	Outer, rotor
os	Outer, stator
pt	Plastic
r	Rotor side
r	Radiation
rad	Radiation
ry	Rotor yoke
s	Source
s	Stator side
sa	Stator and phase *a*
sak	Stator, phase *a* and the k^{th} harmonic order
sat	Saturation
sk	Spoke
src	Source
st	Stator tooth (teeth)
sw	Slot windings
sy	Stator yoke
t	Tangential component
t	Tooth
t1	Tooth and the first harmonic
t1,m	Tooth and the first harmonic due to magnet

t1,s	Tooth and the first harmonic order due to stator current-carrying windings,
tol	Total
v	Varnish
w	Windings

CHAPTER 1

INTRODUCTION

1.1. Background

Generator systems play an important role in maritime vessels. Such systems usually have a multi-component architecture as shown in Figure 1.1. In this figure, the generator is driven by the rotation of a prime mover. This rotation is usually provided by an internal combustion engine. Other components are the power electronic converters, batteries, and control and supervision systems that process and regulate the electrical energy [Bol 2005], [Gut 2009].

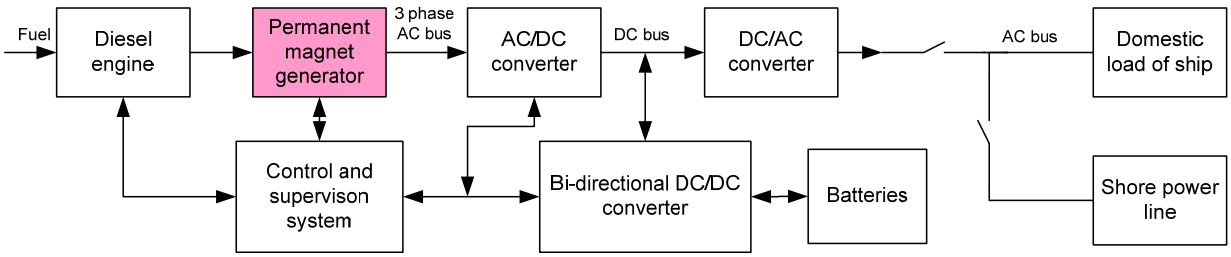

Figure 1.1. Generator system schematic in vessel applications.

In marine applications, diesel engines are preferred to gasoline engines. Diesel engines are indeed cheaper and safer to operate as diesel vapors are not explosive. The safety is specially required in the marine application, since the engine works in saline environments causing corrosion, strong vibration, and high environmental temperatures. The diesel engine needs a starter such as direct current (DC) starter motor in conventional diesel engine systems, which can generate high torque during engine starting. For a higher integration level and power density, an electric machine can be designed to work with dual operation modes, namely, a motor mode during starting of the diesel engine and a generator mode at normal operation. Electronic converters for starting diesel engines are specially designed with higher power so that the generator system becomes more complicated and expensive.

To increase fuel efficiency and reduce acoustic noise, the system produces energy-on-demand, which means that the speed of the diesel engine is increased when more energy is needed by the

load. All components therefore need to be adapted to perform efficiently within a wide range of output power levels. Therefore, a variable speed permanent magnet generator is used as a solution as it fulfills most of the requirements of the power generation stage. In addition, the battery pack provides energy when the system is in standby and during transients that exceed the generator's response time or the permanent magnet (PM) generator's maximum output power. It compensates for the slow dynamic response of the diesel engine with large moments of inertia. The diesel engine is automatically started when a big enough load is detected, i.e., a load that exceeds the continuous rated battery power. For very small loads, the energy is taken from the batteries [Gut 2009], [Hol 2003].

The permanent magnet machine is mounted on the same shaft as the diesel engine. There are no gearboxes, so that the system reduces noise and maintenance and increases lifespan and reliability. The PM machine is integrated on the flywheel of a diesel engine in such a way that it requires short end windings and an outer rotor. Therefore, an exterior rotor surface-mounted PM machine with concentrated windings is the most suitable in this application. This is because the PM machine has a simple and rugged structure, short end-windings, and good conductive heat transfers between windings and teeth, and is easy to manufacture. Moreover, it is known to have high power and high electromagnetic torque density. A disadvantage of the PM machine is high rotor eddy current losses which can however be limited by design optimization of slot/pole combination, pole number, magnet width and slot opening, etc [Ref 2010], [Zhu 2011a], [Fei 2010].

For thermal management, the diesel engine is cooled by seawater. This water supply can be diverted to cool down the generator prior to cooling the diesel engine [Gut 2010].

To convert the alternative current (AC) voltage of the generator to DC voltage, a bridge rectifier is used [Nog 2006], [Nog 1998], [Mal 2003], [Mal 2001], [Wan 2008]. The converter can work in dual model, namely as a rectifier and as an inverter. Output of the rectifier is connected to a DC capacitor bank. The DC capacitor is used as an energy-storing device to limit the ripple of the DC voltage. The DC capacitor along with conductor (integrated in the generator) keeps the DC-link voltage higher than the magnitude of the line-line voltage of the generator. This is needed to block the freewheeling diodes of rectifier, so that the rectifier operates properly. The converter can also operate as an inverter to start diesel engine [Yan 2010], [Sat 2011].

The DC/DC-12/360 V converter is a bidirectional converter [Yi 2010], [Ras 2001]. During the transient and overload operation, it transfers energy from batteries to the DC bus. During normal operation mode, the DC/DC converter gets energy from the DC bus to charge batteries.

DC/AC converter converts DC voltage (360V) into one phase alternate current (AC) voltage (220V/50Hz) supplying for domestic loads in the vessel application [Ras 2001], [Yi 2011], [Sat 2011].

As mentioned earlier, the generator system described in this thesis is intended for use in vessel applications. However, the concept and results might also be used for generator systems in other applications such as in vehicles, mobile ground power station, etc.

1.2. Problem Statement

This thesis originates from a research project into the design of a generator system in a vessel application. This project framework is divided into four parts:

- Design optimization of generator,
- Thermal management and design integration,
- Design of converters, and
- Design of control system.

This thesis is limited to design optimization, the electromagnetic aspects, and the thermal model of generator. The mechanical aspects of the generator, the diesel engine and design converters are beyond the scope of this research.

Each application has individual characteristics so that the choice of generator structure needs to be studied with care. Different applications will lead to different choices of structure of the PM machine. The criteria to select generators for ship application are ease of mounting on a diesel engine, possibility of integration in a flywheel of a diesel engine, high torque density, high efficiency, and cost-effectiveness. Therefore, the exterior rotor PM machine with concentrated windings is preferred for this application. This thesis will focus on the analysis and design the PM machine.

For slotted PM machines, combination of slot and pole number, magnetic saturation, slotting effect, and fringing effect strongly influence on voltage ripple, cogging torque, torque ripple, mean torque, stator iron loss, and rotor iron loss. Because of magnetic saturation, fringing effect and slotting effect, an analytical model is not accurate enough to be selected for estimating performances of the PM machines. However, it can be used to determine a feasible range for design parameters. To select the most suitable structure of PM machine for the application, an accurate model including magnetic saturation, fringing effect and slotting effect should be developed. Therefore, nonlinear transient finite element analysis (FEA) including rotor motion is

the best choice for comparing the performances of PM machines. Both the analytical model and the finite element method (FEM) model will be developed in this thesis.

It was found during analysis that the conventional literature of the slotting effect using the Carter factor is limited with regard to the small slot opening. In traditional analytical models, while the slot opening decreases, the Carter factor decreases so that air gap flux density increases. Therefore, the voltage (also mean torque) increases. However, it was found in this study in the range of small slot opening that when the slot opening decreases, the leakage flux through the tooth tips in fact increases. This leads to a decrease in the voltage and torque. Therefore, the trend of the voltage and torque calculated by the transient FEM is different from the trend of internal voltage and torque calculated by conventional analytical models at small slot opening; this never has been mentioned in literature. Therefore, the influence of slot openings on flux linkage, voltage, electromagnetic torque, rotor eddy current loss, and stator loss is addressed in this thesis.

A nonlinear transient 2D-FEM model is not suitable for design optimization, because it is too time-consuming. The design optimization requires many iterations to find an optimal solution. Therefore, a hybrid model will be developed for design optimization in order to compromise between calculation time and calculation accuracy.

Hybrid models are discussed in literature [Lee 1991], [Bi 1996], [Chu 2003], [Ilh 2010]. The hybrid models in [Lee 1991] and [Bi 1996] are an improvement on the analytical model in the calculation of the air gap flux density. However, they do not take into account the influence of the magnetic saturation and tooth tips on voltage and torque at the small slot opening. For the kind of the model in [Chu 2003], the correction factors calculated by the FEM model for certain dimension sets of the PM machines are presented in the tables or curves. Clearly, the data presented in tables or curves cannot include all situations, so that the model is only suitable for the analysis of PM machines with a certain range of dimensions rather than for design optimization. Recently, Ilhan *et al* [Ilh 2010] tried to improve the design model for the flux switching PM machines by combining the magnetic equivalent circuit (considering magnetic saturation) and the Fourier analysis or the time harmonic FEM analysis (without considering magnetic saturation). It is obvious that the method limits the general applicability because of the use of a complicated magnetic equivalent circuit; if a simple magnetic circuit is used, the model would lack the accuracy for the magnetic saturation effect. However, the proposed hybrid model in this study can apply for the different configurations of the PM machines, because we use the analytical equations combining the automated nonlinear static FEM with the single rotor position. The hybrid model is an improvement on the analytical model in term of accuracy and on the transient FEM model in term of fast calculation. The proposed hybrid model in this thesis takes

slotting, fringing and magnetic saturation effects into account and overcomes the limitation of the traditional analytical design model at small slot opening. It can be used for the design optimization of the PM machines.

To take into account the thermal aspect in the design of the PM machine, a circuit thermal model coupled to the transient FEM model including rotor motion should be developed. Thermal model is updated at each iteration of design process. Therefore, the influence of temperature on the change of material properties along with the constraint of temperature of windings and magnets can be taken into account. The model for analysis and design of the PM machine is therefore improved.

To validate the developed models experimentally, a number of external rotor PM machines with concentrated windings should be designed, manufactured and tested.

1.3. Objectives of Thesis

With the foregoing problem description, the main objectives of the thesis are:

- To find the most suitable structure of the PM machine in a flywheel for small-scale ship application,
- To develop electromagnetic models such as an analytical model, a static FEM model, an automated nonlinear dynamic FEM model including rotor motion and a hybrid model for better compromise between computation time and accuracy for the design of the PM machine,
- To develop the circuit thermal model coupled with the automated transient FEM model including rotor motion for the design of PM machines taking into account thermal constraint,
- To validate the developed models,
- To study the influence of design parameters on the performances of the PM machine; with special attention to slotting effect, and
- To design PM machines for the application.

A number of scientific contributions were generated from the implementation of the above objectives. They are as follows:

- New insights into the influence of the slotting effect on the performance of the PM machines at the small slot opening for such things as flux linkage, internal voltage, electromagnetic torque, and iron losses (see Chapter 5, 6, and 7);
- Methods for separating the slotting effect and the fringing effect in FEM computation to evaluate the Carter factor expressions in literature ;

- A design process based on the hybrid model (see Chapter 5) and the automated transient FEM including rotor motion (see Chapter 4) considering thermal constraints (see Chapter 8); and
- Results of analysis and comparison to find the most suitable configuration of the PM machine in a flywheel in small-scale ship application (see Chapter 2, 3, 6 and 9).

1.4. Research Approach and Thesis Layout

In order to reach the objectives outlined above, the research method had to be approached as follows:

- First of all, the potential configurations of PM machines are reviewed and compared to select the most suitable one for the application,
- Then the analytical model is developed for the initial design of the PM machine,
- The nonlinear transient FEM model including rotor motion is developed for adjustment of the design and analyses of performances,
- Circuit thermal model is developed and coupled to the electromagnetic model. This forms a multi-physic model which is used for the design of the PM machines considering the temperature constraint,
- Next, models are validated by experiments,
- Afterward, typical PM machines are further compared to find out the best one, and
- Finally, two additional PM machines with fully open slot and semi-open slot are manufactured for further validating the slotting effect.

To achieve the objectives mentioned above, this PhD thesis is organized as shown in the flowchart in Figure 1.2.

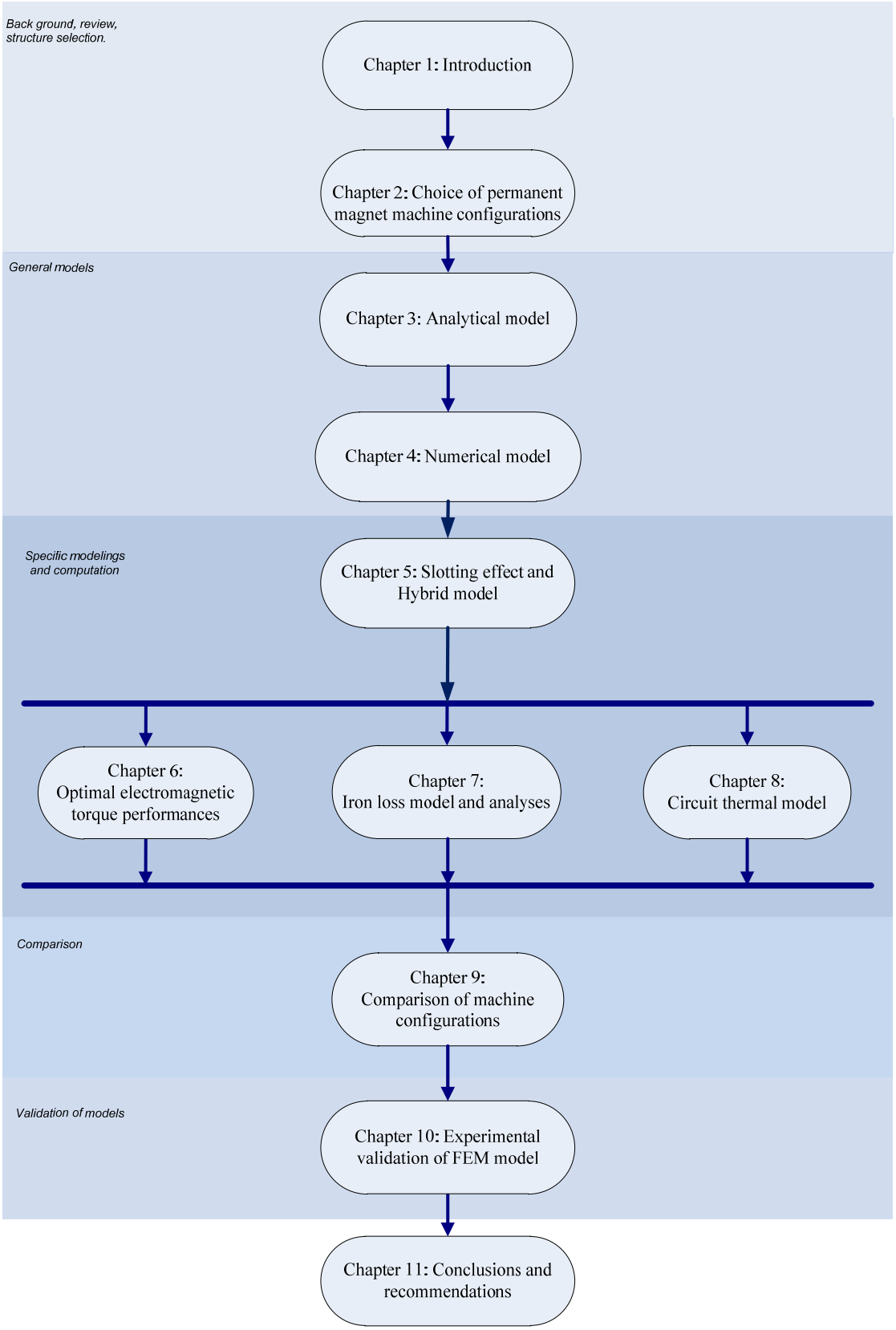

Figure 1.2. Outline of this thesis.

The following is a summary of the contents of each chapter.

In Chapter 2 a choice is given of PM machines from different configurations such as radial flux machines, axial flux machines, synchronous reluctance machine, surface-mounted permanent magnet machines, interior and exterior rotor PM machines, and single layer winding and double-layer winding PM machines. The goal of this chapter is to give an understanding of the advantages and disadvantages of different structures of electric machines and to find the most suitable PM machine for small-scale ship application. As a result, the radial flux exterior rotor PM machine with double-layer concentrated windings is selected for the application. This is because it is easy to mount on diesel engines, well integrated in a flywheel, has a high efficiency and high power density, and is cost effective.

In Chapter 3, the analytical model for fast analysis and the initial design of the PM machine is given. The equations of air gap flux density produced by magnets, flux per pole, and flux passing through a tooth are presented. The armature field and other armature quantities such as the turn function, the winding function, the winding factor, MMFs and inductances are investigated. The equations of self-inductance, mutual inductance, and leakage inductance for the PM machines with different combinations of slot and pole are formulated. General equations for calculating electromotive force, voltage, mean electromagnetic power, mean electromagnetic torque and losses are given. The design constraints for design of the fractional-slot concentrated winding PM machine with the magnets protected from the demagnetization are investigated. The sizing equations for initial design of the PM machine are derived. The MMF-harmonic is used to choose configuration of concentrated windings for minimum rotor eddy current loss.

In Chapter 4, the automated FEM model for the design of the PM machine is developed. The FEM model includes magnetic saturation and rotor motion. Equations for calculating flux linkage and internal voltage are given. The FEM model coupled to the circuit model is developed. The demagnetization model is developed to estimate the demagnetization of magnets. This is to ensure that the designed PM machine is safe after the worst operation. These form an efficient tool for the analysis and design of the PM machine.

In Chapter 5, the slotting effect on the magnetic field, flux linkage, and internal voltage of the PM machines with concentrated windings is investigated. This shows that the conventional literature regarding slotting effects using the Carter factor is limited in the range of the small slot opening. A new view about the influence of the slotting effect on flux linkage and internal voltage at small slot opening is presented, which has never been described in literature before. The correction factors including the slotting effect, fringing effect, and magnetic saturation are proposed to improve the analytical model. The analytical model incorporating the static FEM

forms the hybrid model. This model overcomes the limitations of traditional calculation using the Carter factor. The hybrid model utilizes the advantages of the fast calculation of the analytical model and the accurate calculation of the FEM model. It can be used for design optimization.

In Chapter 6, the influence of design parameters such as slot and pole combination, slot opening, magnet width, and magnetic saturation on cogging torque, torque ripple and mean torque is discussed. The analysis of the PM machines with different combinations of slot and pole leads to a proposed process for evaluating the peak-peak cogging torque. The relation between mean electromagnetic torque and slot opening is evaluated and can be used to estimate slot opening for maximizing mean electromagnetic torque. The relation has not been described in literature before. It is found from analysis results that selecting the correct combination of slot and pole number and optimizing the major design parameters such as pole width and slot opening are an efficient way to minimize the peak-peak cogging torque or torque ripple. The analysis therefore gives insight into the effect of design parameters on electromagnetic torque performances.

In Chapter 7, models of iron losses are developed. The relation between stator iron loss and slot opening are evaluated. The influence of slot opening, operation models, segmented magnets, etc on rotor eddy current loss is discussed. The distribution of eddy currents and eddy current losses in the rotor of concentrated winding exterior rotor PM machines in flywheels is studied. The proposed method makes it possible to monitor the eddy current losses in rotors as a function of time, rotor speed, operating mode and stator slot opening. It can be used to select the slot opening that minimizes rotor eddy current losses while it maximizes the internal voltage. It therefore constitutes an indispensable tool in the design of PM machines by taking the eddy current losses in the rotor into account.

In Chapter 8, a circuit thermal model for design of PM machines considering thermal constrain is presented. A solution for improving heat transfer from the PM machine to the environment is proposed. The thermal model is experimentally verified. Simulation and experimental results show good agreement.

In Chapter 9, the typical PM machines with different combinations of slot and pole numbers are compared in order to find the most suitable combination for the application in this thesis. Ferrite and neodymium PM machines as well as surface-mounted and inset PM machines are also compared.

In Chapter 10, simulation and experimental results of the PM machines are compared in order to validate the dynamic FEM model. The nonlinear transient FEM model for calculating

flux linkage, internal voltage, load voltage, load current, mean electromagnetic torque, iron loss and reactance is validated. The transient FEM model during three-phase short circuit is also validated. Two additional PM machines with fully open slot and semi-open slot are manufactured for the further validation of the slotting effect. Simulation and experimental results show good agreement.

In Chapter 11, the most important contributions reached in the thesis are summarized and recommendations for further research on the subject are made.

CHAPTER 2

CHOICE OF PERMANENT MAGNET MACHINE CONFIGURATIONS

2.1. Introduction

There are many different configurations of the permanent magnet (PM) machine. In addition, each application has individual characteristics. The different applications can lead to different choices. Therefore, the choice of PM machine configuration should be made with care. In this chapter, there is a review of PM machines with different configurations such as radial, axial and transverse flux PM machines, interior and exterior rotor PM machines, concentrated and distributed winding PM machines, etc. The aim is to compare the advantages and the disadvantages of PM machines in order to select the prototype of PM machine that is most suitable for vessel applications. A configuration of a PM machine, which meets the criteria for the vessel application, will be selected for further study in the next chapters.

Many criteria can be used to assess a PM machine such as torque per mass, torque per volume (or torque density), torque per cost, power per mass, power density, power per mass, efficiency, etc. The choice of a criterion or multi-criteria for the assessment is mainly dependent on the application. Assessments based on multi-criteria often lead to a better choice because the results are the compromise between criteria which are in conflict with each other. A multi-criteria are used to select generators for vessel application. These are:

- the ease of mounting on a diesel engine,
- the possibility of integration in the flywheel of a diesel engine,
- cost-effectiveness,
- high torque density, and
- high efficiency.

After comparing machine configurations, the exterior rotor PM machine with concentrated windings is selected. This is because it well satisfies the above criteria. Once the configuration

has been chosen, the cooling methods, concentrated winding configuration and materials used in PM machines are discussed.

In this thesis, the term "concentrated windings" refers to the non-overlapping windings that have the number of slot per pole per phase q smaller than 1, viz., the fractional number, while the term "distributed windings" refers to the overlapping windings with q greater than 1. In the special case is where the number of slots per pole per phase is equal to 1, the winding might be non-overlap, but might also be overlap [Pol 2007]. It should be noted that in a PM machine with concentrated windings q is always a fraction. However, a PM machine with a fractional slot has non-overlap (if q<1) or overlap windings (q>1).

2.2. Electric Machines and Their Application

2.2.1. Electric Machine Types

In this section, an overview is given of electric machine types in generator system of the vessel application. This is done in order to gain an understanding of their advantages and disadvantages.

Possible choices of electric generator include DC brushed, electrically excited synchronous (including claw-pole machines [Bol 2005], [Owe 2011]), induction, switched reluctance, permanent magnet assisted synchronous reluctance (switched flux), and permanent magnet machines. The PM machine as shown in Figure 2.1 is preferred for this application because of its high torque density, high power density, high efficiency, high power factor, and ease of manufacturing [Zhu 2009b], [Ref 2010], [Bol 2005], [Jah 2011]. According to research results in [Dor 2010], [Bol 2005], [Mor 2007b], other machines have the following main advantages and disadvantages compared to the PM machine:

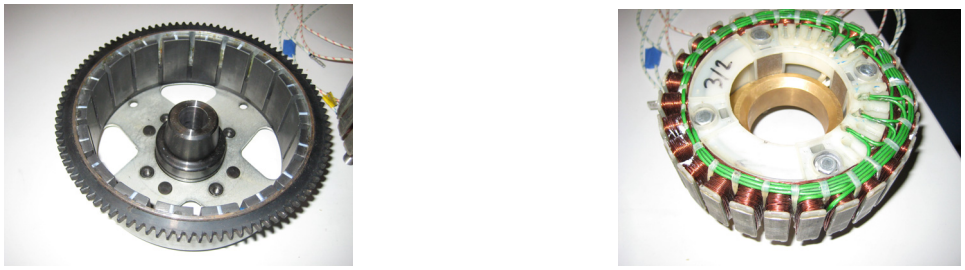

a) b)

Figure 2.1. A PM machine for vessel application: a) rotor, b) stator.

- The DC brushed generator has carbon brushes and a mechanical commutator so that its reliability and efficiency are low. It causes electromagnetic interference that can influence other

electric devices. It needs regular maintenance and has short life span. Therefore, this machine is not used in most of applications in industry.

- The electrically excited synchronous generator, shown in Figure 2.2, has simple and rugged structure. The price of this machine is very low. However, it needs a DC power source as well as carbon brushes and conduction rings to provide electric power to excitation windings. This machine has Copper losses in the rotor, lower efficiency, lower power density, and less reliability than a PM machine. Therefore, the machine is not preferred for use in the application in this thesis.

- The induction generator has been used in many applications. This is because of the low cost and rugged structure as well as good performance. However, the induction generator cannot work independently. It has to use lagging reactive power from other sources, e.g., an electric grid and/or capacitors in order to convert mechanical energy into electrical energy. Induction generators also have lower efficiency, a lower power factor, and lower power density than the PM machines [Dor 2008], [Dor 2010], [Buc 2008]. Therefore, a PM generator is preferred to an induction generator in the application in this thesis.

a) b)

Figure 2.2. Electrically excited synchronous machine in a more conventional generator system for vessel application: a) rotor with windings, b) stator with water-cooling.

- There are many types of reluctance generator but the most popular is the switched reluctance generator. The reluctance machine as shown in Figure 2.3 is a double-saliency electric machine with non-overlap stator windings and with a passive rotor. The machine has some advantages such as low cost and lack of a permanent magnet, ease of manufacture and the possibility of operation at high speeds and in high temperature environments. It however has a high torque ripple, high mechanical vibration, and significant acoustic noise [Bol 2005]. It needs a starter to start it. Other than is the case with the reluctance machine, the switched reluctance generator requires a converter to drive it in order to minimize torque ripple. In comparison with the PM machines, according to [Jac 1996], [Jac 1999] and [Bol 2005], the main advantage of the reluctance machine as well as the switched reluctance machine is low cost as a result of the lack

of PM or rotor windings. However, the machines have higher current ripple, higher torque ripple, higher noise, higher iron loss, lower efficiency, a lower power factor, and lower power density than the PM machine. Therefore, the reluctance machine as well as the switched reluctance machine is not selected for the vessel application considered in this study.

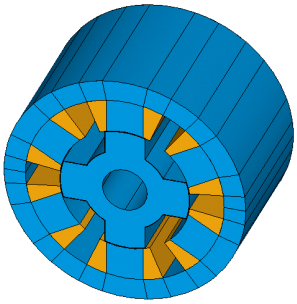

Figure 2.3. Reluctance generator [Rol 2002].

- The switched flux or flux switching PM machines as shown in Figure 2.4 combine the advantages of the reluctance machine and the PM machine. Permanent magnets are put in the stator side. Compared to the reluctance machines, they have higher power density but higher cost because of magnet cost. Compared to the PM machines, according to [Zhu 2011b] and [Bol 2005], they have lower cost. This is the main advantage of switched flux PM machines. However, they have lower power density, lower efficiency (because of high eddy current loss due to slotting effect), a lower power factor, higher torque ripple, and noise. Because of the disadvantages, the switched flux PM machine is not selected for the vessel application considered in this study.

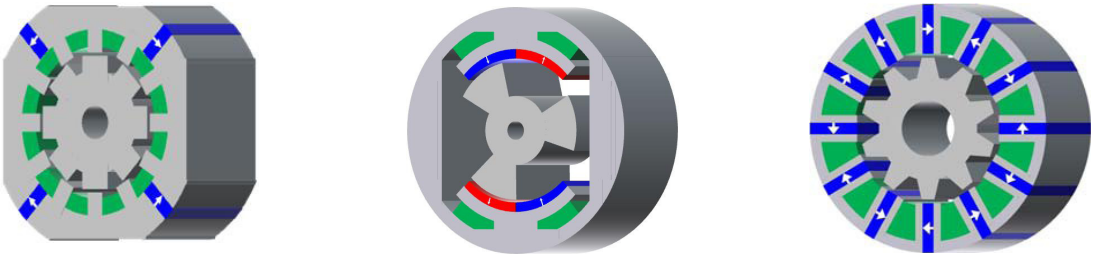

a) b) c)

Figure 2.4. a) double-salient, b) flux-reserval, and c) switched-flux PM machine [Zhu 2011b].

2.2.2. Distributed versus Concentrated Winding PM Machines

A distributed winding PM machine generally has a more sinusoidal magnetomotive force (MMF) distribution and electromotive force (EMF) waveform than a concentrated winding PM machine. The distributed winding (Figure 2.5a) however has longer end winding than the concentrated

winding so that a PM machine with concentrated winding (Figure 2.5b) has a lower Copper losses and a higher power density [Ref 2010], [Dor 2011]. Furthermore, a concentrated-winding PM machine is easier to manufacture and cheaper; especially with a segmented stator structure as shown in Figure 2.6. It has higher fault tolerance capability [Bol 2005], [Ref 2010]. Besides, a selected PM machine will be integrated in a flywheel and mounted on the shaft of a diesel engine, so short end windings are important. Therefore, a PM machine with concentrated windings is preferred in the ship application considered in this thesis.

a) b)

Figure 2.5. a) Stator with distributed winding of a PM machine of hybrid Toyota Prius (Toyota©); b) a concentrated-winding PM machine of hybrid Honda Civic (Honda©).

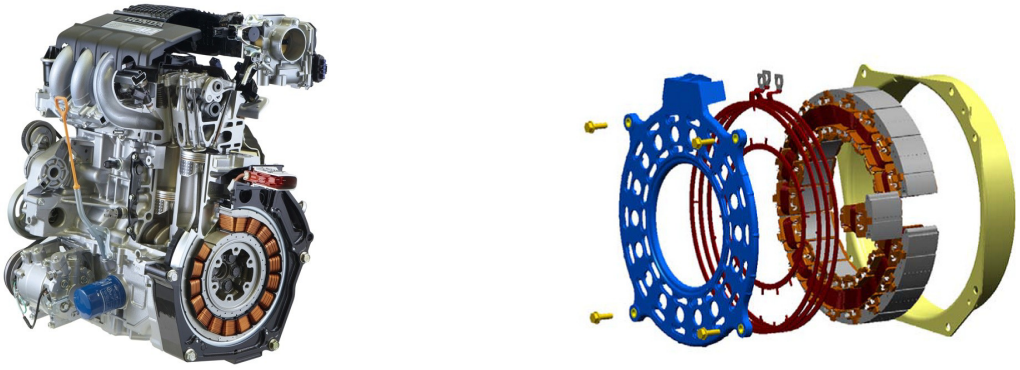

Figure. 2.6. Integrated PM machine with concentrated windings and segmented stator structure in CR-Z hybrid-electric powertrain, Honda, [Jah 2011], [Ref 2010].

2.2.3. Exterior versus Interior Rotor PM Machines

The exterior rotor PM machine is normally the surface-mounted PM machine (as shown in Figure. 2.7 a, b) or the inset PM machine (as shown in Figure. 2.7 c). The surface-mounted PM machine as shown in Figure 2.7a has a simple structure, so it is widely used in many applications. To reduce the ripple of air gap flux density, voltage and torque, the varying air gap length is

made by curving the surface of magnets as shown in Figure 2.7b [Mas 2004], [Cha 2011]. The inset PM machine can be used to improve the reluctance torque in some cases. The comparison of the surface-mounted and inset PM machines will be presented in Chapter 9, so they are not discussed here. The exterior rotor PM machine with buried magnets (as shown in Figure. 2.7 d) is rare, because its rotor yoke should be made from iron laminations, it would be weaker in mechanical structure and higher in cost than the solid rotor yoke. An external rotor surface-mounted PM machine with concentrated windings integrated in a flywheel for vessel application is presented in Figure 2.8. Figure 2.9 depicts an external rotor PM machine with a continuous power of 64 kW, a peak power of 81 kW, a continuous torque of 500 Nm, and a peak power per total mass about 2.6 kW/kg, which is used in an electric truck developed by Protean Electric®.

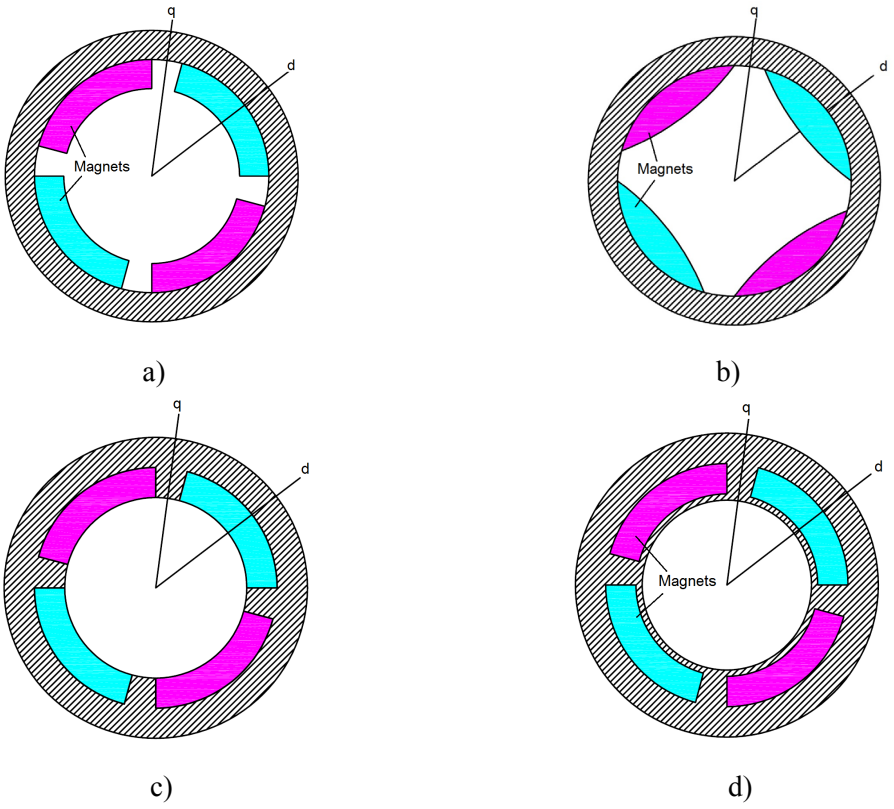

Figure 2.7. Different exterior rotor structures: a) surface-mounted magnets; b) surface-mounted magnets with curved surface; c) inset magnets; d) buried magnets.

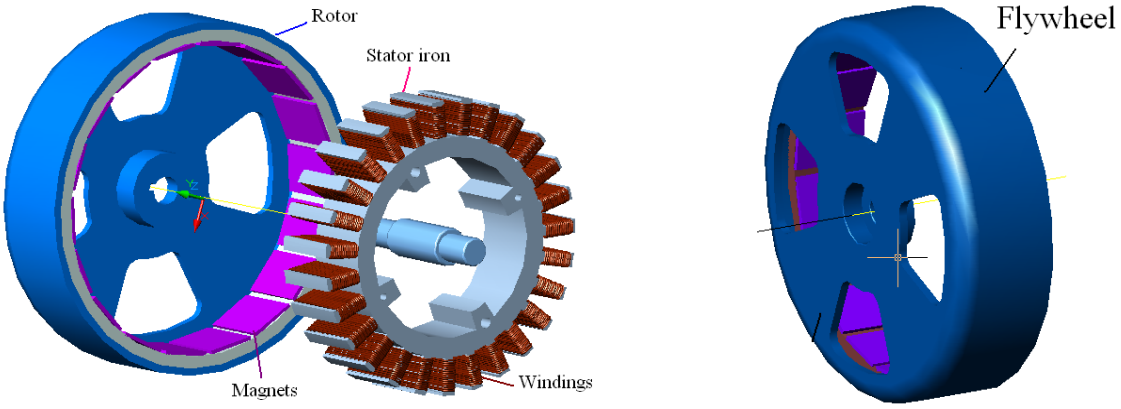

Figure 2.8. Exterior rotor surface-mounted PM machine with concentrated windings for ship application.

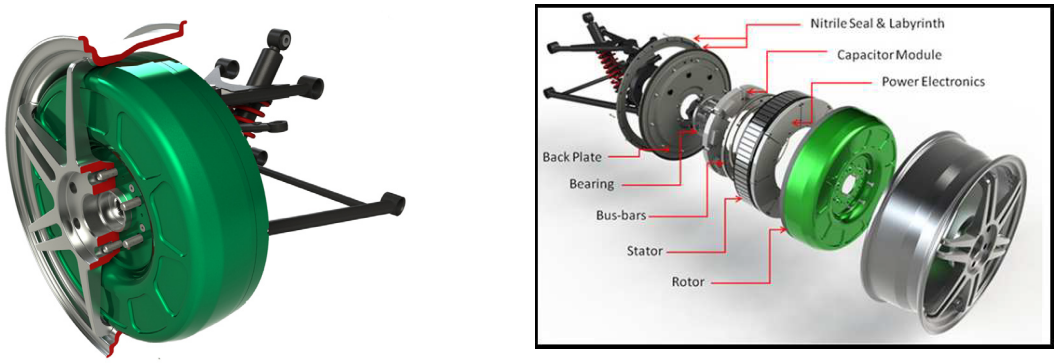

Figure 2.9. External rotor surface-mounted PM machine with concentrated windings in a flywheel of electric Protean Ford truck, Protean Electric® [Pro 2012].

In contrast, there are many types of configurations of the interior rotor PM machine, such as those shown in Figure 2.10 including surface-mounted magnets, inset magnets, buried magnets, V-shaped magnets, and the permanent magnet assisted synchronous reluctance machine [Par 2005], [Mor 2007b], [Yam 2011], [Nia 2005]. The buried PM machine as well as the PM assisted synchronous reluctance machine is often used in applications that require a wide constant-power speed range [Nia 2005], [Bar 2012]; its magnet is safe from the viewpoint of demagnetization. The interior rotor PM machine is used in many applications; static part is put externally so it is safe for users. However, for applications, which require integrating the electric machine in a flywheel, the outer rotor PM machine has the following main advantages in comparison with interior rotor PM machines:

- It is better to integrate the machine in a flywheel, making system more compact.

- The air gap diameter is larger than that of interior rotor PM machines with the same rated power and volume, so it might allow for a higher torque density.
- Moment of inertia is higher than that of inner rotor PM machines, because of the higher rotor diameter. This is a requirement for applications in which the PM machine is mounted on the shaft of a diesel engine.

Because of the above-mentioned advantages, an external rotor PM machine is preferred in the ship application considered in this thesis

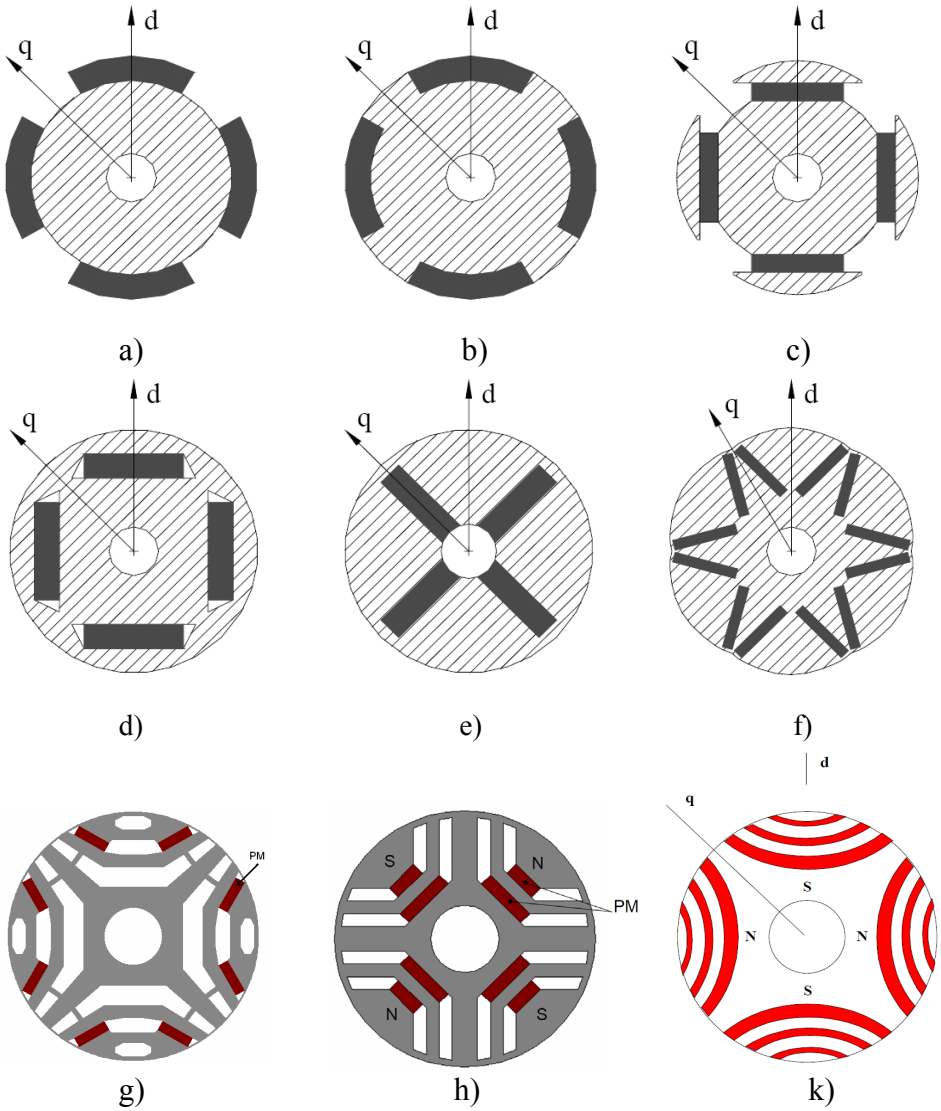

Figure 2.10. Different interior rotor structures: a) surface-mounted magnets; b) inset magnets; c), d), e) buried magnets; f) V-shaped buried magnets [Par 2005]; g), h), k) permanent magnet assisted synchronous reluctance machines, [Nia 2005], [Pia 2004].

2.2.4. Radial Flux versus Axial Flux PM Machines

Compared to axial flux PM machines (AFPMs), radial flux outer rotor PM machines (RFPMs) are more suitable to integrate in the flywheel of a diesel engine and more robust. AFPMs and RFPMs have the same performance in terms of torque density, torque per mass, and efficiency [Ayd 2004]. However, AFPMs normally have two sides (two rotors or two stators) to obtain an attractive force balance. The air gap is therefore twice higher than in RFPMs. More magnet mass and/or ball bearings are needed for the AFPMs as well as more windage loss [Sah 2001]. Therefore, the cost of AFPMs is higher than that of RFPMs. The cost of manufacturing of a RFPM is also lower than that of an AFPM, because the technology for making RFPM is mature. Therefore, for the application considered, it is more advantageous to use a RFPM than an AFPM. It should be noted that the AFPMs are more suitable to application requiring a short axial length than RFPMs are. Figure 2.11 illustrates a slotted axial-flux surface-mounted PM machine with double rotor, while Figure 2.12 presents a double-rotor-single-stator axial flux Torus type non-slotted surface mounted PM machine.

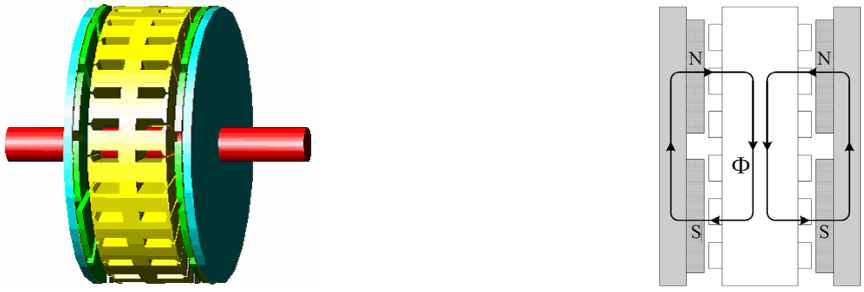

a) b)

Figure 2.11. a) Slotted axial-flux surface-mounted PM machine with double rotor [Che 2005], b) Illustration of the flux direction.

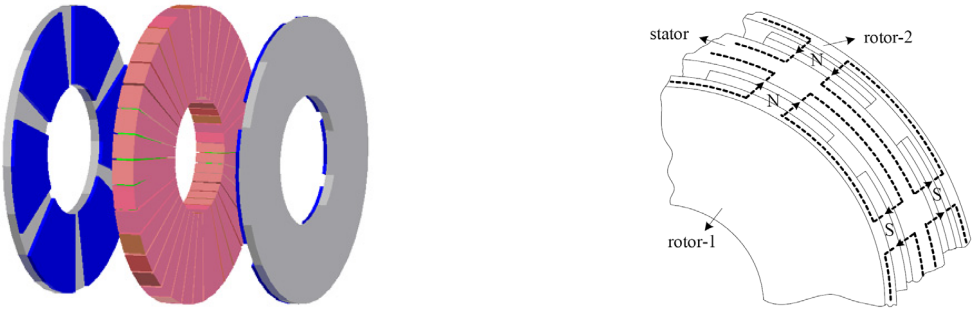

a) b)

Figure 2.12. a) Double-rotor-single-stator axial flux Torus type non-slotted surface mounted PM machine configuration, b) 3D Flux directions of the TORUS machine, [Ayd 2004].

2.2.5. Transverse Flux versus Other Types of PM Machines

For a transverse flux PM machine (TFPM) as shown Figure 2.13, the number of windings is always the same as the number of phases and is independent of the number of poles [Deo 2010], [Man 2011], [Yan 2009], [Che 2011b]. In this way, it is possible to produce TFPMs with a high number of poles that can efficiently convert energy at low rotation speed without gearboxes. For other PM machines, the number of slots increases with the pole number, so that the number of poles is limited by mechanical issue. A transverse flux PM machine seems to be suitable for application with high power and low rotor speed such as wind turbines. Recently, a TFPM was also developed for electric vehicles (Figure 2.14) in [Man 2011], [Bol 2005], because of torque density of the transverse flux PM machine is higher than that of other electric machines. However, according to [Deo 2010] and [Man 2011], a transverse flux PM machine has a low power factor and very high cost. Because of the cost, a transverse flux PM machine is not selected for small-scale ship applications.

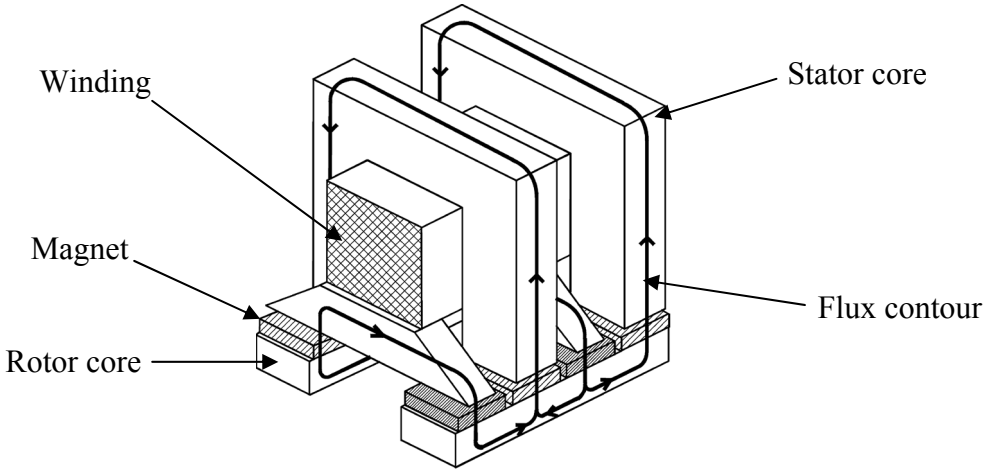

Figure 2.13. Transverse flux PM machine with one phase [Rol 2003].

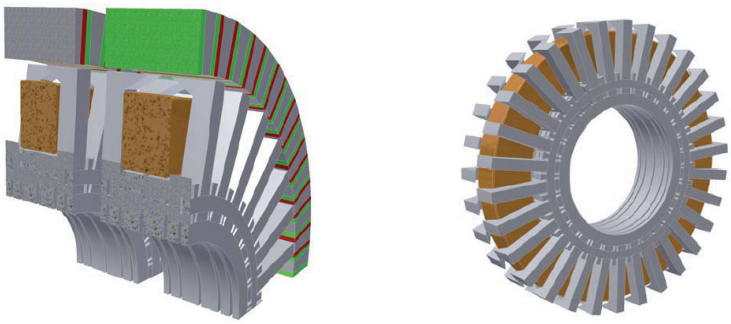

a) b)

Figure 2.14. a) Transverse flux PM machine with two phases, an external rotor and buried magnets; b) one phase stator of transverse flux PM machine for an electric vehicle [Man 2011].

2.2.6. Double Rotor versus Single Rotor of Radial Flux PM Machine

For the double rotor radial PM machine shown in Figure 2.15a, the diameter of the external rotor is significantly larger than that of the internal rotor. Moreover, mean electromagnetic torque is proportional to the square of the rotor diameter. Therefore, the outer rotor produces most of electromagnetic torque. Besides, the cost of magnets and active materials is significantly increased in comparison with the single rotor PM machine (Figure 2.15b). The heat transfer ability of the double rotor is poorer than that of the single rotor, especially for inner windings and inner magnets. Therefore, the double rotor is generally not used in industry application.

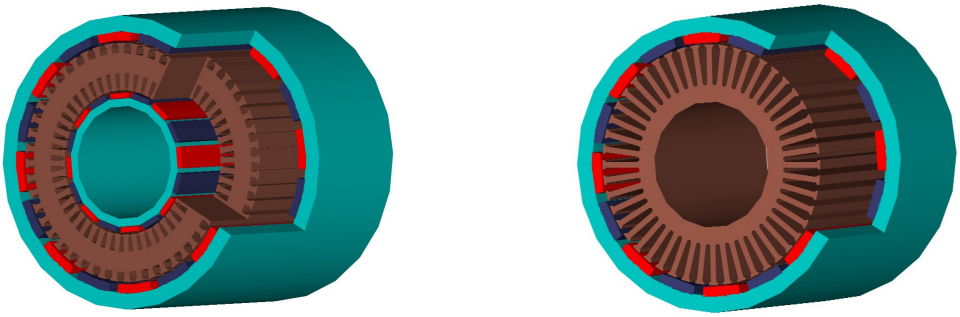

a) b)

Figure 2.15. 3D configurations of PM machines; a) single outer rotor surface-mounted PM machine; d) double rotor surface-mounted PM machine [Par 2005].

2.2.7. Single Layer versus Double-Layer Concentrated Windings

The double–layer means that there are two coil sides within each slot; while the single–layer means that there is one coil side within each slot. The single layer winding has a higher fundamental winding factor and good abilities for field-weakening mode (i.e., constant power, rotor speed range higher than the rated speed) and it is fault tolerant. However, the double-layer winding has some advantages, in comparison with single layer windings, such as shorter end windings, smaller space harmonic components of MMF and EMF, smaller torque ripple and less rotor eddy current loss [Ref 2008b], [Bia 2006]. For the vessel application, field-weakening mode and fault tolerant mode are not required. Therefore, double layer windings are chosen for the application considered in this study.

2.2.8. Conclusions of this Section

From the above comparisons, it can be seen that a radial flux exterior rotor PM machine with concentrated windings shown in Figure 2.16 is the most suitable for small-scale vessel

application. This is because it can be well integrated in a flywheel of a diesel engine so that the generator system becomes more compact. Moreover, it has high torque density and high efficiency and is cheap.

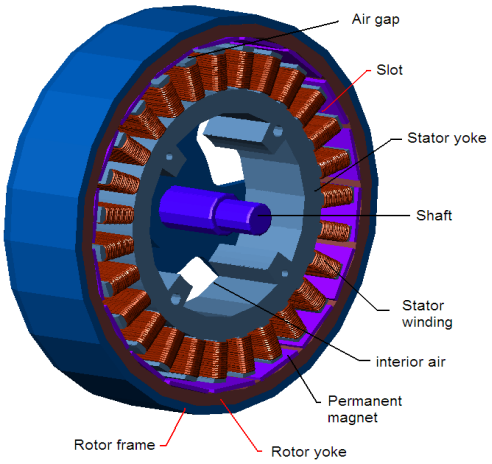

Figure 2.16. Prototype of studied radial flux, exterior rotor, surface-mounted PM machine with concentrated windings in a flywheel.

2.3. Thermal Management Concept for Selected Machine

The diesel engine is cooled by seawater. This water can be diverted to cool down the generator prior to cooling the diesel engine. The use of seawater for cooling leads to biological fouling, and corrosion. Thus, the materials used for the cooling plate and water duct should be of a top quality alloy, e.g. Copper-Nickel-iron $CuNi_{10}Fe$ or Titanium. For ship applications, Copper-Nickel alloys are preferred because of their intrinsic bacteriostatic and fungicidal properties. Copper-Nickel alloys triple the thermal conductivity of Titanium alloys. The dimension of cooling plate and tube should also be big enough to prevent fouling. These increase the price of the system. Figure. 2.17 presents the concept of water-cooling. To compromise between power density and price, the PM machine required is designed with two options; it is capable of working with water-cooling or with natural cooling. It was learned from the thermal measurements of generators in ship applications that the maximum power of a generator with natural air-cooling should be reduced to 40%-50% of that of water-cooled generator power. It is noteworthy that the working temperature of windings and the iron of PM machines is around 120^{o}C, which is higher than the surface temperature of the diesel engine (around 80^{o}C). Therefore, the heat flux from the diesel engine cannot go into the generator. The measured mean temperature of the air inside the housing in steady state is about 50 ^{o}C.

Heat transfer between winding layers is poor, because the thermal conductivity of the electrical insulating varnish layer is small, about 0.15-0.18 W/m/K. Heat transfer of iron in the radial direction is about 30 W/m/K. The thermal management is more efficient, if the number of winding layers is minimal. This should be taken into account during the design process of the PM machine.

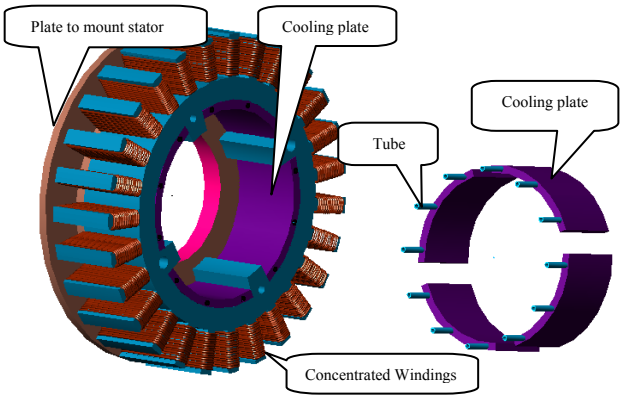

Figure 2.17. Illustration of a water-cooled concept for a generator.

2.4. Layout of Fractional Slot Concentrated Windings

As mentioned above, the double-layer concentrated winding is preferred to the single-layer concentrated winding for the ship application considered in this thesis. Some authors [Cro 2002], [For 2010], [Lib 2004], [Mag 2003], [Mag 2007] investigated the method used to find the layout of the fractional-slot concentrated-windings for achieving the maximum fundamental winding factor. A review is presented here. Afterwards, the winding factors and the MMF of five typical PM machines, namely 24-slot/16-pole, 27-slot/18-pole, 24-slot/20-pole, 27-slot/24-pole and 24-slot/28-pole PM machines, corresponding to slot/pole combination of 3/2, 3/2, 6/5, 9/8 and 6/7 are calculated.

2.4.1. Winding Feasibility

There are various combinations of slots and poles, but the combinations are only feasible if slot number per phase as well as slot number per number of winding cycle is an integer number. It therefore should satisfy the following equation [For 2010], [Bia 2006]:

$$\frac{Q}{m.GCD(Q,p)} = k \tag{2.1}$$

where, Q is slot number, m is the number of phases, p is the number of pole pairs and k is an integer number and GCD stands for the greatest common divisor.

2.4.2. Determination of Winding Layout

The method for finding the concentrated winding layout is demonstrated below for a PM machine with slot number Q=24 and pole number $2p$=20.

The fraction of the number of slot per pole per phase q must be reduced to a fraction, which cannot be irreducible as

$$q = \frac{Q}{2pm} = \frac{c}{d} \tag{2.2}$$

where, c and d are integer numbers.

When substituting Q=24, $2p$=20 and m=3 into (2.2), we obtain q= 2/5.

The five steps to determinate winding layout (known as Cros's method) are presented as [Cro 2002], [Lib 2004]:

(1). Find a sequence S_r: The sequence S_r includes the numbers "1" and "0" only. The number of "1" in the sequence is equal to c and the number of "0" is equal to $(d\text{-}c)$. The sequence S_r can be presented as [Cro 2002], [Lib 2004], [Mag 2003],

$$S_r = \overbrace{\underbrace{111\ldots111}_{c}\,\underbrace{000\ldots000}_{d\text{-}c}}^{d}$$

For example, if Q=24, $2p$=20, c=2 and d=5, we have S_r=11000.

(2). Find a sequence S_f: The sequence S_f is found by redistributing the sequence S_r such that as regularly as possible. For example, if we have S_r=11000, then we obtain S_f =10010.

(3). Find a sequence S_w: The sequence S_w is found by repeating the sequence S_f Q/c times [Cro 2002], [Mag 2007]. For the example of Q=24, $2p$=20, we obtain Q/c=24/2=12 times and the sequence S_w as shown in Figure 2.18. The sequence S_w is associated to the usual phase sequence (AC'BA'CB'…) as shown in Figure. 2.18; where A' presents the return conductor corresponding to conductor A.

(4). Make the first layer of winding: The conductors corresponding to the numbers "1" of the sequence S_w in the step 3 are selected to make the first layer of winding of the double layer concentrated winding as shown in Figure 2.18, [Cro 2002].

(5). Make the second layer of winding: The second layer of the winding obtains by filling the corresponding conductors on the other sides of the slots as shown in Figure 2.19.

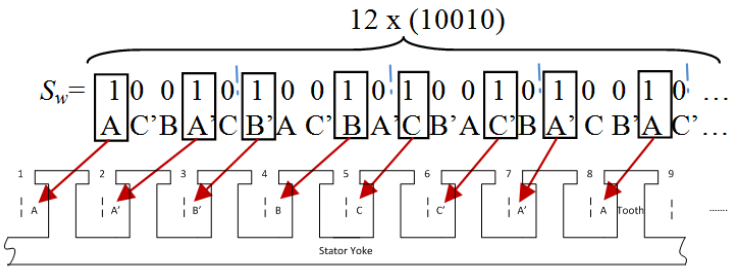

Figure 2.18. Making the first layer of concentrated windings of a 24-slot and 20-pole PM machine in the steps 3 and step 4.

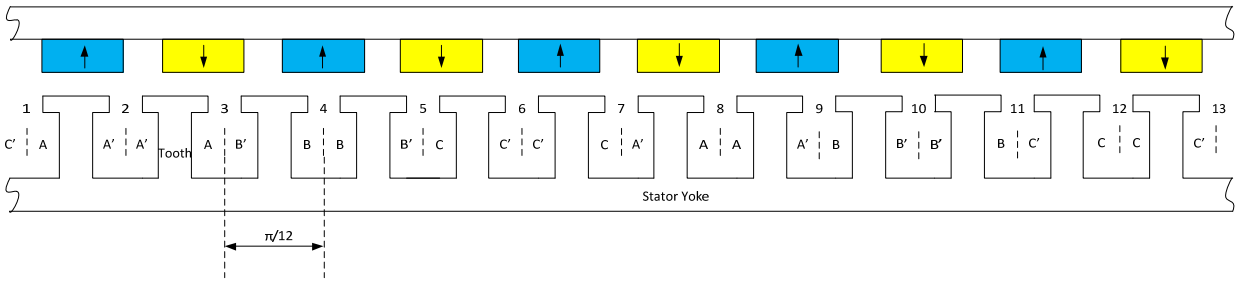

Figure. 2.19. Double-layer winding layout of a 24-slot and 20-pole PM machine.

2.4.3. Winding Factor

To calculate the fundamental winding factor, we can use the winding vector method in [Mag 2003], [Lib 2004] or the star vector of slot [Pyr 2008]. Indeed, the results when using the two methods are the same, but they are presented in different ways.

Using the Winding Vector

To calculate the fundamental winding factor, a vector W_a will be defined to describe winding layout of phase A [Cro 2002], [Mag 2003], [Lib 2004]. The slot is numbered from 1 to Q as in Figure. 2.19. The vector W_a includes the numbers with the absolute value of the i^{th} element, $|W_a(i)|$ equal to the slot number index and its sign depending on the direction of the conductor in the slot, i.e., getting plus (+) for the conductors A and getting minus (-) for the return conductors A'. If both layers of one slot contain conductors of the same phase, the number of the slot is written twice in the vector W_a. For the double-layer-winding, the vector W_a has $2Q/3$ elements. Therefore, the winding vector W_a of phase a of a three-phase PM machine with 24 slots and 20 poles is

W_a=[1 -2 -2 3 -7 8 8 -9 13 -14 -14 15 -19 20 20 -21].

The vector electromotive force (EMF) of the conductor corresponding to the i^{th} element of the winding vector W_a is written in per unit as [Mag 2003], [Lib 2004]

$$\overrightarrow{E_i} = sign(W_a(i))e^{j\gamma_i}, \quad \forall i = 1,2,...,2Q/3 \tag{2.3}$$

where γ_i is the angle of vector E_i. The angle is calculated as,

$$\gamma_i = \frac{2\pi p}{Q} i = \frac{2\pi p}{Q} |W_a(i)| \tag{2.4}$$

Fundamental winding factor for double layer winding is defined as equation (2.5), [Mag 2003], [Lib 2004]

$$K_{w1} = \frac{\left| \sum_{i=1}^{2Q/3} \overrightarrow{E_i} \right|}{2Q/3} \tag{2.5}$$

Using the Star Vector of Slots

Figure 2.20 presents a star of slot of a PM machine with 24 slots and 20 poles, which can be used to calculate the EMF and the fundamental winding factor. Specifications of the star of slots are, [Bia 2006]:

- The number of spokes is equal to number of slots of 24.
- The number of the periodicities t of the machine (or number of winding cycles) is $t=GCD(Q, p)=2$.
- The number of spokes per cycle is equal to $Q/t=12$.
- The angle between two spokes α_s is $\alpha_s=2\pi t/Q=\pi/6$.
- The electric angle between adjacent slots is $\alpha=2\pi p/Q=5\pi/6$.

From start vector of slot, the fundamental winding factor can be formulated for each slot/pole combination as presented in [Ish 2006], [Bia 2006], [Pyr 2008].

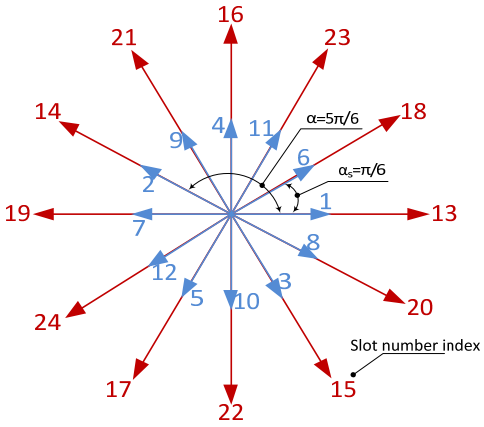

Figure 2.20. The star of slots of a PM machine with 24 slots and 20 poles.

Result of Calculations of Studied PM Machines

The winding layout of a typical PM machine is presented in Table 2.1, while the winding vector and fundamental winding factor are shown in Table 2.2.

Table 2.1. Winding layout.

Combination of slots/poles	Slot/pole number	*q*	Winding layout	Periodic number of winding	Type of periodicity
3/2	24/16	1/2	AA'BB'CC'…	8	Identity
3/2	27/18	1/2	AA'BB'CC'…	9	Identity
6/5	24/20	2/5	AA'A'AB'BBB'CC'C'C…	4	Anti-identity
9/8	27/24	3/8	AA'A'AAA'BB'B'BBB'CC'C'CCC'…	3	Identity
6/7	24/28	2/7	AA'A'AB'BBB'CC'C'C…	4	Anti-identity

** q is the number of slots per pole per phase, which is calculated by equation (2.2), i.e., q=c/d. If d is an even number, the winding distribution or winding layout is periodic. Otherwise, the winding distribution is antiperiodic* [Cro 2002].

Table 2.2. Winding vector W_a and Fundamental winding factor K_{w1}.

Combination of slots/poles	Slot/pole number	*q*	Winding layout	Winding factor K_{w1}
3/2	24/16	1/2	[1 -2 4 -5 7 -8 10 -11 13 -14 16 -17 19 -20 22 -23]	0.866
3/2	27/18	1/2	[1 -2 4 -5 7 -8 10 -11 13 -14 16 -17 19 -20 22 -23 25 -26]	0.866
6/5	24/20	2/5	[1 -2 -2 3 -7 8 8 -9 13 -14 -14 15 -19 20 20 -21]	0.933
9/8	27/24	3/8	[1 -2 -2 3 3 -4 10 -11 -11 12 12 -13 19 -20 -20 21 21 -22]	0.945
6/7	24/28	2/7	[1 -2 -2 3 -7 8 8 -9 13 -14 -14 15 -19 20 20 -21]	0.933

Table 2.2 compares the fundamental winding factor of the studied PM machines. As can be seen, the fundamental winding factor of the PM machine with 27slots/24 poles (machine 5) is the greatest, while the fundamental winding factors of the ones with 24slots/20poles (machine 3) and 24slots/28poles (machine 4) are the same. The fundamental winding factor of conventional PM machines (machine 1 and machine 2) with a slot/pole combination of 3/2 is the smallest. The higher the fundamental winding factor, the higher the EMF and mean electromagnetic torque, if the PM machines have the same number of turns of windings per phase and current loading. However if the number of turns per phase and the current loading are different, there is no guarantee that the mean electromagnetic torque will be bigger when the winding factor is greater. Apart from the criterion of choosing the combination of slot and pole for maximizing the winding factor, there are some other criteria such as choices of the combination of slot and pole for minimizing rotor eddy current loss (this will be presented in Section 3.13, Chapter 3) and minimizing cogging torque (this will be presented in Subsection 6.4.1, Chapter 6).

2.5. Materials Used in PM Machines

In this section, the major materials used in permanent magnet machines such as permanent magnet material, lamination steel, and stainless steel are reviewed.

2.5.1. Permanent Magnet Material

The most popular magnet materials for PM machine are the ferrites, bonded neodymium-iron-boron (NdFeB), sintered Neodymium-iron-boron, bonded or sintered Samarium and Cobalt.

Ferrite, Neodymium and Samarium magnets are classified as hard magnets [Hen 1994]. The best grades of hard permanent magnets have straight demagnetization characteristic throughout the second quadrant at room temperature. This characteristic in the second quadrant is called the demagnetization characteristic, as shown in Figure 2.21. The magnet's operating point generally moves reversibly up and down the straight part of the characteristic. The slope of the characteristic B(H) is approximated by the permeability of the magnet. The other form of the demagnetization characteristic presenting the relation of the intrinsic polarization J and magnet field strength $H_{m,}$ is also shown in Figure 2.21. However, in this research, the demagnetization characteristic refers to the B(H) curve. Magnet flux density B_m relates to other parameters at room temperature as follows [Hen 1994], [Pyr 2008], [Mce 2011], [Mar 2005], [Sta 2001]

$$B_m=\mu_o H_m+J \qquad or \qquad B_m=\mu_o\mu_{rm}H_m+B_r \tag{2.6}$$

where, μ_o of $4\pi.10^{-7}$ A/m, is permeability of air, μ_{rm} is relative permeability of magnet and B_r is remanent flux density of the magnet.

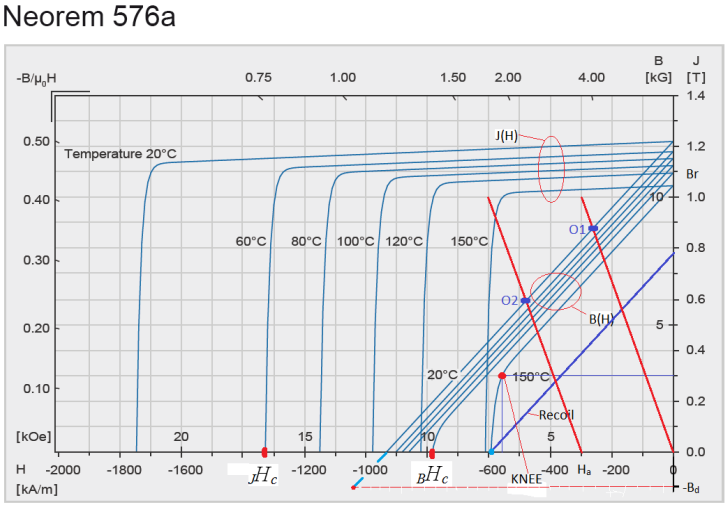

Figure 2.21. Typical demagnetization curves of a sintered NdFeB magnet: flux density versus magnetic field strength, B(H) and polarization versus magnetic field strength, J(H) at different temperatures. Main parameters at 20°C: remanent flux density B_r=1.22 T, coercive force ${}_BH_c$=930 kA/m, ${}_JH_c$= 1750 kA/m. Illustration of no-load point O1 and load point O2. (Neorem Magnet, 2011).

The relative recoil permeability of the hard magnets is in the range of 1.0-1.1, i.e. close to that of air. This is an important property because it helps to limit the demagnetizing effect of armature reaction. Magnet materials come into both isotropic and anisotropic forms. An isotropic material has the same properties in all directions. Anisotropic materials have a preferred direction of magnetization with increased remanence and coercivity [Hen 1994], [Mar 2005].

The hard magnets (at room temperature) can withstand a demagnetizing field that is actually sufficient to reverse the flux in the magnet (but the value should be greater than the demagnetizing value of $-B_d$, shown in Figure 2.21), and still recover with no permanent loss of magnetism [Hen 1994]. For soft magnets, they have a knee in the second quadrant at room temperature. However, a hard magnet material, which has a straight demagnetization characteristic at room temperature, may develop a knee in the second quadrant at higher temperatures for rare earth magnets, or at lower temperatures for Ferrite magnets. For example, in Figure 2.21, a knee emerges when the working temperature of the Neodymium magnet is higher than 100 °C. If the operating point is forced below the knee, then when the demagnetizing field is removed the magnet recovers along a lower recoil line. Figure 2.21 shows an example in which the demagnetizing field is just sufficient to reduce magnet flux to zero. The magnet "recoils" along the depressed recoil line (here assuming straight line, but in fact the recoil line

bending toward B-axis [Ruo 2010]), but it has lost some of its remanent flux. This loss is irreversible [Mar 2005], [Hen 1994], [Ruo 2010].

Generally, the remanent flux density B_r decreases with temperature. This effect is usually specified in terms of the reversible temperature coefficient of B_r. The remanent flux density at temperature T^{o}C can be written as [Hen 1994], [Mar 2005],

$$B_{r(T)} = B_{r(20)}[1+\alpha_{Br}(T-20)/100] \tag{2.7}$$

where $B_{r(20)}$ is the value of B_r at 20^{o}C. α_{Br} is the reversible temperature coefficient of B_r in percentage per Celsius degree; α_{Br} in range of -0.03 to -0.18 (%/^{o}C), [Mce 2011], [Mag 2012].

The Ferrite magnets have a low remanent flux density (around 0.4 Tesla), low power energy, low coercive force, negligibly small electric conductivity and maximum operating temperature (around 300 ^{o}C, [Mar 2005]). Although the power density of a Ferrite magnet as well as the coercive force is only about 1/3 that of a rare-earth sintered magnet; the maximum energy product $(BH)_{max}$ of Ferrite is about 1/9 that of a rare-earth sintered magnet, its price is very low about 1/10 that of a rare-earth sintered magnet, and there is no magnet eddy current loss [Mar 2005]. Hence, the Ferrite PM machine is still widely used.

A bonded plastic Neodymium magnet has a remanant flux density around 0.7 Tesla, higher remanent flux density than Ferrite magnets but lower than that of a sintered rare-earth magnet. It has very low electric conductivity of about 1/100-1/200 that of a sintered rare-earth magnet, so magnet eddy current loss is very small. This magnet is compressed or injected in a plastic material so that it can be of complex shape and it can also be magnetized in any directions. This material is very suitable with complex pole configurations like a Halbach magnet [Hen 1994].

Sintered rare-earth permanent magnets made of Neodymium-Iron-Boron or Samarium–Cobalt have high energy density, high coercive force, and maximum operating temperature (up to 180 ^{o}C for NdFeB and 350 ^{o}C for SmCo). They however have high electric conductivity. This leads to significant magnet eddy current loss. Their remanence flux density is in the range of 1-1.35 Tesla.

Samarium–Cobalt magnet permanent materials Sm_xCo_y (e.g: $SmCo_5$, Sm_2Co_{17}; Sm_2Co_{17} are better than $SmCo_5$ in all aspects [Mar 2005]) and are known as having excellent thermal stability and distinguished resistance to corrosion. Because of the high cost, Samarium Cobalt magnets are only used in special applications where temperature changes across a broad range or environment and is corrosive, such as a chemical environment. Demagnetized temperature is up to 350^{o}C.

A bonded Samarium magnet is analogous to a bonded Neodymium magnet, but the former has a higher working temperature and higher cost.

Another magnet, Alnico magnet (an alloy of aluminum-nickel-cobalt, Al-Ni-Co), has a remanent flux of about 0.65 T, high resistance to corrosion, very high working temperature (up to 538 ^{o}C), [Mce 2011], but very low coercive force and low resistance to demagnetization. Therefore, Alnico magnets are being superseded by rare earth magnets.

2.5.2. Lamination Steel

Lamination steel is used to make the stator core. It is a kind of soft magnetic alloy with 95%-97% Iron and 1%-3% Silicon, which has narrow hysteresis loops, low coercivity and high permeability. These properties are quite different to those of hard magnetic alloys such as Ferrite or rare-earth magnet. The higher the percentage of Silicon, the higher the electric resistance, so there is smaller eddy current loss, but lower permeability. The thinner the lamination, the smaller the iron loss, but the higher the cost [Mar 2005], [Hen 1994], [Mce 2011]. Figure 2.22 presents typical BH curves of lamination steel. The material with higher saturated flux density can be used to make the electric machine with higher power density.

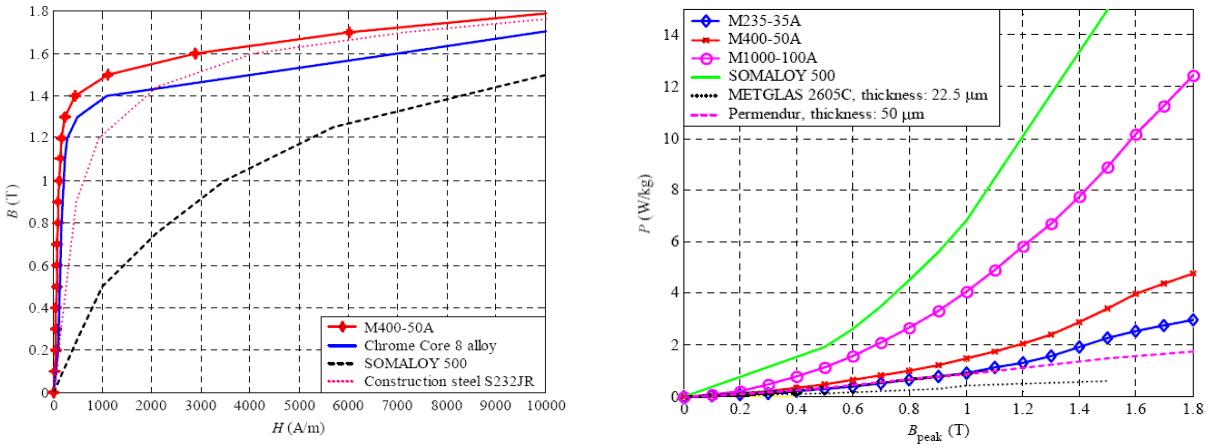

a) b)

Figure 2.22. BH curve and iron loss per kilogram of some lamination steels: a) BH curve of typical lamination steels, b) core loss of materials at frequency of 50 Hz, [Par 2005].

2.5.3. Ferrite Stainless Steel

Ferrite stainless steels are ferromagnetic and used for rotor yokes and flywheels . Generally, their magnetic properties are not as good as those of soft magnetic alloys, but they are cost-effective, especially for applications, which must withstand corrosive environments. Additionally, the relatively high electrical resistivity of Ferrite stainless steels results in small eddy current loss in rotor yokes. These stainless steels have soft magnetic properties such as high magnetic permeability, low coercive force, and low residual flux density. Note that if the material works in a cold environment, its coercivity will increase while permeability will reduce. When exposed to magnetic fields, it will retain some magnetic effects, hence acting as a weak permanent magnet [Mce 2011].

2.5.4. Copper Wire

Copper wire used in electrical machines is usually categorized according to the electric insulation material used. Table 2.3 gives a list of the insulation classification codes together with maximum allowed working temperatures.

Table 2.3. Copper wire electric insulation classifications.

Insulation class	Y	A	E	B	F	H	C
Maximum allowed temperature (^{o}C)	90	105	120	130	155	180	>180

2.6. Specifications of Studied PM Machines

In this thesis, four real PM machines are considered. They are referred to as machines A, B, C, and D. All these machines have the same BH curve of stator iron lamination as shown in Figure 2.23. A discussion of core loss characteristics is done in Chapter 7. For the purpose of reference, main specifications of these machines are listed in Table 2.4 while Figure 2.24 shows a cross section of the PM machine with necessary notes.

A part from the real four PM machines above, a virtual Neodymium PM machine is designed to compare with Ferrite PM machine A presented in Chapter 9. Another six virtual machines generate from PM machine B. They have the same stator and rotor diameters, ratio of slot opening to slot pitch, ratio of pole width to pole pitch, and magnet thickness, but different pole number or slot number. These PM machines are used for studying the influence of slot and pole combinations in Chapter 9.

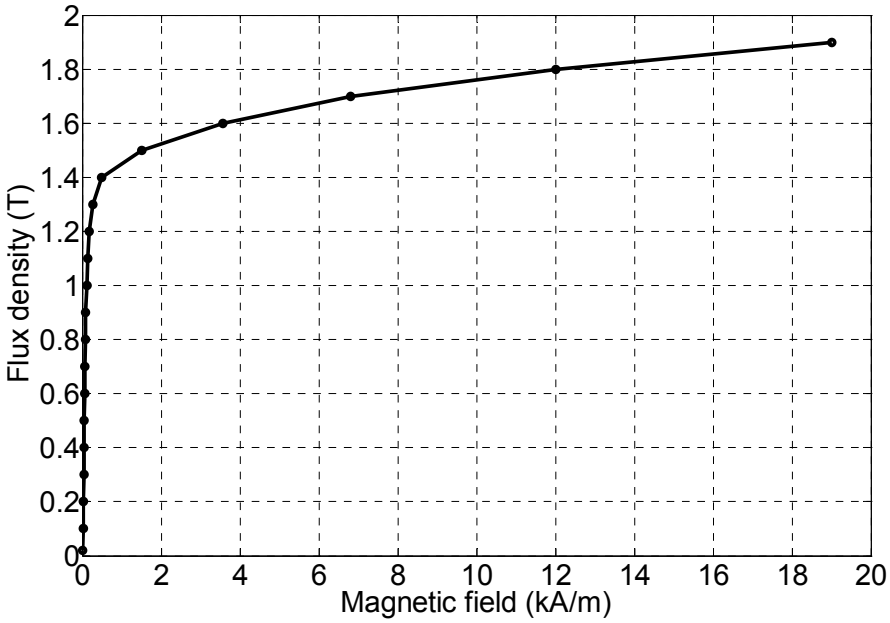

Figure 2.23. BH curve of iron lamination material.

Table 2.4. Main specifications of real PM machines.

Specifications	Machine A	Machine B	Machine C	Machine D
Rated power (W)	3000	3000	9000	9000
Rated RMS line-line voltage (V)	220	200	200	200
Maximum speed (rpm)	3600	3600	3600	3600
Thickness of rotor yoke (mm)	3	3	7	7
Magnet dimensions $L_m x W_m x T_m$ (mm)	45x27x8	45x20x2	50x22.5x5	50x22.5x5
Material of magnets	$FeSr_{12}O_{19}$	Neodymium	Neodymium	Neodymium
Recoil permeability of magnet (T)	1.05	1.05	1.05	1.05
Remanent flux density	0.405	1.2	1.2	1.2
Coercive force H_c,(A/m) at room temperature	3.09×10^5	9.30×10^5	9.30×10^5	9.30×10^5
Tooth number N_t	24	27	27	27
Tooth thickness w_t (mm)	5	5	8.05	8.05
Stator tooth height h_t (mm)	15	15	26.4	26.4
Number of poles $2p$	16	18	18	18
Outer stator diameter D_{os} (mm)	156	156	180	180
Interior stator diameter D_{is} (mm)	100	100	95	95
Stator length l_s (mm)	35	35	45	45
Stator lamination thickness d (mm)	0.35	0.35	0.35	0.35
Stator yoke height h_{sy} (mm)	10	10	12.5	12.5
Number of laminations	98	98	128	128
Coil winding number N_{coil}	24	27	27	27
Number of turns per coil N_c	56	57	18	20
Winding parallel branches	1	3	2	2
Winding diameter (mm)	0.8	0.7	1.5	1.5
Slot opening b_s (mm)	6.9	6	3.9	12.9
Air gap length g (mm)	2	2	2	2
Electric conductivity of rotor yoke (S/m)	1.67×10^6	1.67×10^6	1.67×10^6	1.67×10^6
Electric conductivity of magnets (S/m)	0	6.67×10^5	6.67×10^5	6.67×10^5
Conductivity of steel lamination (S/m)	1.92×10^6	1.92×10^6	1.92×10^6	1.92×10^6

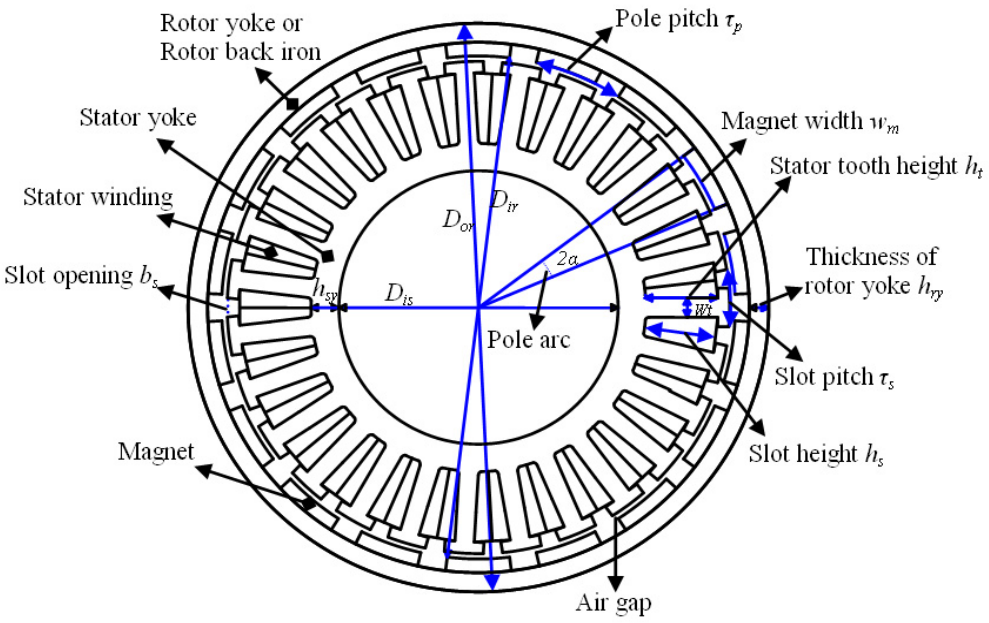

Figure 2.24. A cross section of an external rotor PM machine with concentrated windings.

2.7. Conclusions

In this chapter a review and comparison of PM machines with different configurations, such as PM machines, electrically excited synchronous machines and reluctance machines; radial, axial and transverse flux PM machines; exterior and interior rotor PM machines; concentrated and distributed PM machines; and single and multiple rotor PM machines are presented. The advantages and disadvantages of the machines are discussed. The exterior rotor PM machine configuration with double-layer concentrated windings is selected for the small-scale ship application. This is because it can be well integrated in a flywheel of diesel engine, has a high efficiency and a high power density, and is cost effective. Additionally, the concept-establishing layout of concentrated windings for maximizing the fundamental winding factor is presented. This is indispensable foundation knowledge for the study of PM machines with concentrated windings. In addition, some of the main materials used in PM machines, such as permanent magnets, Ferrite stainless, lamination iron, and Copper are discussed.

CHAPTER 3

ANALYTICAL MODEL

3.1. Introduction

In Chapter 2, we motivated the choice of an exterior rotor surface-mounted PM machine with double-layer concentrated windings. In this chapter, the focus is on the development of an analytical model of the PM machine with concentrated windings for initial design. The analytical model is the cornerstone to develop the hybrid model intended in Chapter 5. The model will be used for the design of the PM machines in the small-scale ship application in the study. Further refinement of the design required can be done by using an automated nonlinear transient FEM including rotor motion, which will be investigated in the next Chapters.

The purpose of the analytical model is for initial design so that the study focuses on the fundamental component of the magnetic field neglecting higher harmonic components. The analytical model is generally developed for the fractional slot PM machines with different combinations of slot and pole. The principle of superposition is used. The air gap magnetic field produced by the magnets and the air gap magnetic field due to the current-carrying windings are first calculated separately. Afterwards, the total air gap magnetic field is equal to the sum of the magnetic field produced by the magnets and the current-carrying windings. Other quantities such as flux linkage, flux passing through tooth, internal voltage, electromagnetic torque, etc can be derived from the magnetic field in the air gap.

This chapter will start with the assumptions for establishing the analytical model. Next, analytical equations of the magnetic field produced by the magnets are presented. Subsequently, the winding function, the magnetic field due to the current-carrying windings and other armature quantities such as the fundamental winding factor, inductances, etc are investigated in Section 3.4. In section 3.5, the total magnetic field in the air gap and magnets can be obtained by summation of the no-load magnetic field and the armature field. Once the air gap magnetic field has been obtained, the electromotive force (EMF), voltage, electromagnetic power, electromagnetic torque, and losses are derived in Section 3.6 to Section 3.10. Afterwards, the design constraint concerning magnet protection from demagnetization corresponding to different

operating modes is discussed in Section 3.11. Sizing equations for initial design of the PM machine are given in Section 3.12. In Section 3.13, the distribution of magnetomotive force and its harmonic components are investigated to estimate the influence of combinations of slot and pole (or winding layout) on rotor eddy current loss; the results obtained will be used to explain FEM calculation results in Chapter 9. Finally, some conclusions are drawn.

3.2. Assumptions

Several assumptions are made when establishing the analytical model as follows:

- the flux density between adjacent magnets is assumed equal to zero, i.e., the leakage flux between adjacent magnets is neglected,
- the magnetic flux crosses the air gap perpendicularly, i.e., there are only radial flux density components,
- the edge effects of magnets, the fringing effect, the end effect and the stator slotting effect are neglected,
- the permanent magnet machine is symmetrical regarding mechanics, magnetic circuit and electric circuit, and
- the magnetic circuit is not saturated and the permeability of iron is infinite.

3.3. Magnetic Field due to Permanent Magnets

In this Section, the modeling of the flux density in the air gap is investigated first. Next, typical Carter factor expressions found in literature, accounting for the slotting effect, are given (these expressions will be evaluated by FEM computation in Chapter 5). Finally, the fundamental flux linkage per pole and the fundamental flux passing through a tooth are given. The magnetic field produced by magnets will be used to derive other quantities such as EMF, electromagnetic power and electromagnetic torque presented in other sections.

Modeling of Flux Density in Air-gap Produced by the Magnets

The stator slotting effect causes a non-homogeneous flux density in the air gap. The air gap flux density decreases at positions opposite the slot opening. This is illustrated as curve (1) of Figure 3.1. The air gap flux density at positions opposite the magnet is approximately modelled by the rectangular waveform as curve (2) in Figure 3.1, with the horizontal axis denoting mechanical angle in rotor coordinate and the vertical axis denoting the flux density.

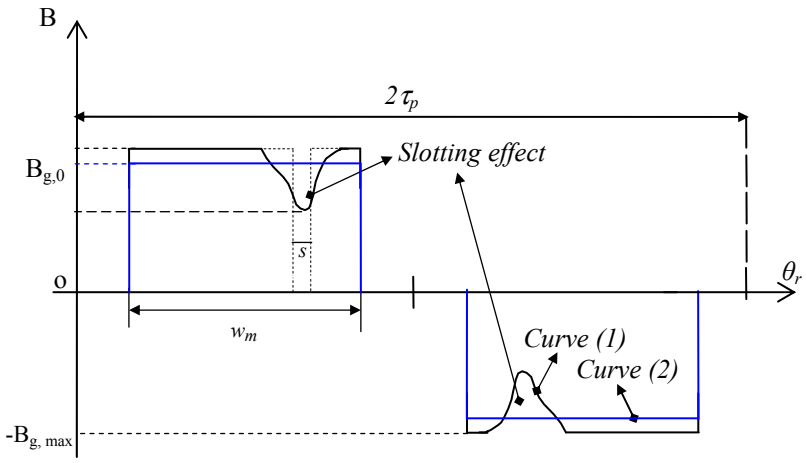

Figure 3.1. a) Geometry of an exterior rotor surface-mounted PM machine with concentrated windings; b) Illustration of the flux density in the air gap during no-load, where pole pitch τ_p, pole width w_m, mean air gap flux density $B_{g,0}$ at positions opposite magnet, maximum air gap flux density $B_{g,max}$.

The rotor coordinate and stator coordinate as shown in Figure 3.2 are chosen in such a way that the relation between stator angle and rotor angle can be expressed as,

$$\theta_s = \theta_r + \theta_m \tag{3.1}$$

where, θ_s is the mechanical angle along the stator periphery, θ_r is the mechanical angle in the rotor coordinate, and $\theta_m = \omega_m t + \theta_0$ where ω_m is the angular speed of the rotor and θ_0 is the rotor initial position which is chosen to be equal to zero.

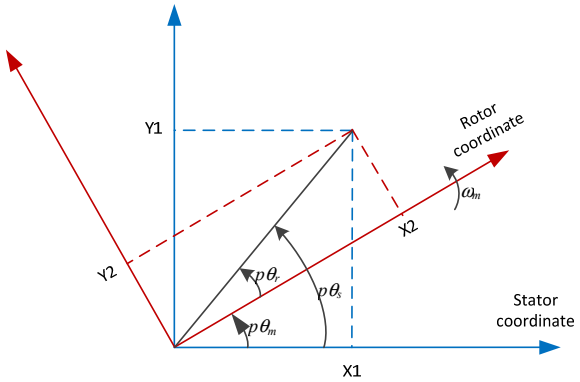

Figure 3.2. Relation between coordinates.

The flux density in the air gap can therefore be expressed in the rotor coordinate as,

$$B_g(\theta_r)=\begin{cases} B_{g,0} & if\ (\pi/2-\alpha)/p \le \theta_r \le (\pi/2+\alpha)/p \\ -B_{g,0} & if\ (3\pi/2-\alpha)/p \le \theta_r \le (3\pi/2+\alpha)/p \\ 0 & otherwise \end{cases} \tag{3.2}$$

where, the electric angle 2α is the pole arc, $\alpha=\frac{\pi}{2}\frac{w_m}{\tau_p}$, τ_p is the pole pitch, and w_m is the pole width.

The relation of the mean air gap flux density produced by magnets and remanent flux density of the magnets can be expressed as [Sle 1990], [Sle 1992], [Han 1994], [Hen 1994]

$$B_{g,0}=\frac{l_m}{l_m+\mu_{rm}g_{eff}}B_r \tag{3.3}$$

where, l_m is the length of magnet in the radial direction, μ_{rm} is the relative permeability of the magnet, and g_{eff} is the effective air gap.

The air gap radial flux density produced by the magnets, which is represented as a function of stator angle and rotor angle, can be presented into the form of the Fourier series as follows [Sle 1990], [Sle 1992]

$$B_g(\theta_s,\theta_m)=\frac{4}{\pi}B_{g,0}\sum_{\nu=1,3,5,\ldots}\frac{\sin(\nu\alpha)}{\nu}\sin(\nu p(\theta_s-\theta_m))=\sum_{\nu=1,3,5,\ldots}\hat{B}_{g\nu}sin(\nu p\theta_r) \tag{3.4}$$

where, $\theta_m \equiv \omega_m t$ is the rotation angle of the rotor, ω_m is rotor angular speed, $\hat{B}_{g\nu}$ is the amplitude of the ν^{th} harmonic of the flux density in the air gap. The amplitude of the ν^{th} harmonic of flux density in the air gap can be expressed as,

$$\hat{B}_{g\nu}=\frac{4}{\nu\pi}B_{g,0}\sin(\nu\alpha) \tag{3.5}$$

For the purpose of the initial design, it is only necessary to present the fundamental space component hereafter. The calculation can however be adapted for calculation with high harmonic space components.

The fundamental flux density in the air gap due to the magnets can be written as

$$B_{g1}(\theta_s,\theta_m)=\hat{B}_{g1}sin(p(\theta_s-\theta_m))=\hat{B}_{g1}sin(p\theta_s-p\omega_m t) \tag{3.6}$$

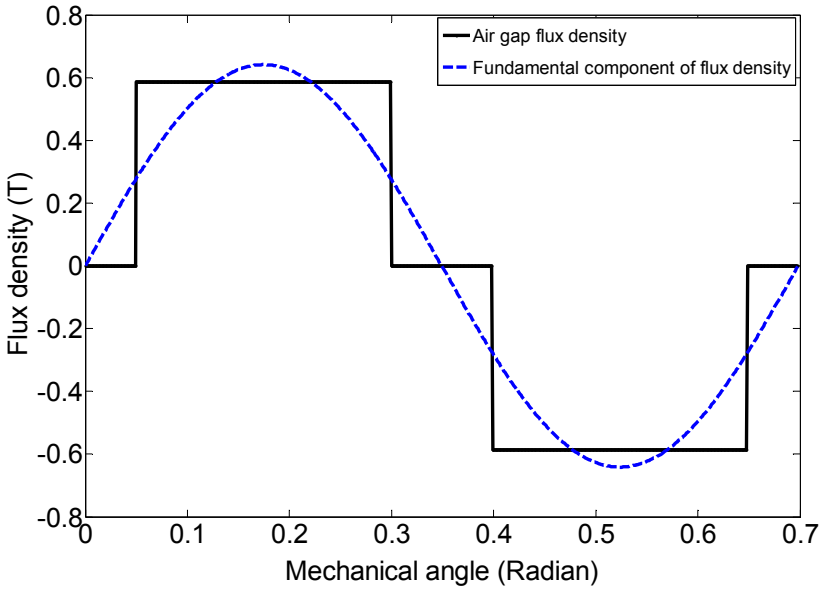

Figure 3.3. Illustration of flux density in the air gap produced by magnets, for the PM machine *B*.

Carter Factor

To include slotting effect for analysis and design of electric machines, F.W. Carter was the first to propose a solution for the problem of slotting effect, around the 1920s, [Car 1906], [Car 1926]. According to Carter's principle, the effective air-gap length g_{eff} is used, instead of the physical air gap length g. The effective air gap presents the effective value including the influence of slotting. The effective air gap length g_{eff} is determined by using Carter's factor k_C, given as,

$$g_{eff}=k_C g \tag{3.7}$$

The Carter factor k_C is defined as the ratio of the maximum flux density (flux density with zero slot opening width) to the mean flux density in the air gap at positions that opposite the surface of the magnet [Car 1926], [Pyr 2008]. It can be expressed as,

$$k_C=\frac{B_{g,\max}}{B_{g,0}}=\frac{g_{eff}}{g}=\frac{\tau_s}{\tau_s-s}=\frac{\tau_s}{\tau_s-\gamma g} \tag{3.8}$$

where, τ_s is slot pitch, b_s is stator slot opening width, g is physical air gap length, and s is defined as shown in Figure 3.1.

The following expressions of the factor γ have been proposed to calculate the Carter factor,

$$\gamma=\frac{(b_s/g)^2}{5+(b_s/g)} \tag{3.9}$$

$$\gamma = \frac{(b_s / g)^2}{4.4 + 0.75(b_s / g)} \tag{3.10}$$

$$\gamma = \frac{4}{\pi}\left[\frac{b_s}{2g}\arctan\left(\frac{b_s}{2g}\right) - \ln\sqrt{1+\left(\frac{b_s}{2g}\right)^2}\right] \tag{3.11}$$

$$\gamma = \frac{2b_s}{\pi g}\left[\arctan\left(\frac{b_s}{2(l_m+g)}\right) - \frac{(l_m+g)}{b_s}\ln\sqrt{1+\left(\frac{b_s}{2(l_m+g)}\right)^2}\right] \tag{3.12}$$

$$\gamma = \frac{\tau_s}{g}\left\{\frac{b_s}{\tau_s} - \frac{4g}{\pi\tau_s}\ln(1+\frac{\pi b_s}{4g})\right\}. \tag{3.13}$$

Equations (3.9)-(3.11) were given for the wound field machines, but they were used for PM machines in the current literature of analytical design [Han 1994]. Equations (3.9) and (3.10) can be found in [Nas 1964] and [Han 1994] while equation (3.11) was given by Carter in [Car 1926], and equation (3.12) is given by [Qis 1985] for PM machines. The equation (3.13) can be found in [Han 1994], [Lip 1996]. Most the equations were given from the conformal transformation, except for the equation (3.13) which was formulated by using analytical calculation. As can be seen from the above equations, the Carter factor increases when g/τ_s decreases and/or b_s/τ_s increases. There are many equations for calculating Carter factor in literature. These can lead to confusion for the designers. The evaluation of the Carter factor expressions will be done by comparing finite element computations in Chapter 5.

It should be noted that when the rotor position changes, the waveform of the flux density in the air gap changes. However, the Carter factor is assumed to remain constant, so that the factor can be calculated at a certain rotor position.

Derivation of Flux Equations

The maximum value of the fundamental flux per pole passing through the windings can be obtained as,

$$\phi_{g1} = \iint_S \vec{B}\cdot\vec{n}dA = \int_0^{\pi/p} \hat{B}_{g1} sin(p(\theta_s - \theta_m)) l_s r_s d\theta_s \tag{3.14}$$

where, $\vec{n}$ is the positive (outer) normal unit vector of the infinitesimal area dA, l_s is stator length, and r_s is the radius at middle air gap, approximately equal to the radius of stator.

By developing the equation (3.14), we obtain

$$\phi_{g1} = \frac{2}{p}\hat{B}_{g1} l_s r_s \cos(p\theta_m) = \frac{2}{p}\hat{B}_{g1} l_s r_1 \cos(p\omega_m t) = \hat{\Phi}_{g1}\cos(p\omega_m t) \tag{3.15}$$

where,

$$\hat{\Phi}_{g1} = \frac{2}{p}\hat{B}_{g1} l_s r_s \tag{3.16}$$

The fundamental space component of flux passing through a tooth due to the magnets has a maximum value as [Mil 1989],

$$\phi_{t1,m} = \int_{\pi/(2p)-\delta/2}^{\pi/(2p)+\delta/2} \hat{B}_{g1} sin(p(\theta_s - \theta_m)) l_s r_s d\theta_s = \int_{-\delta/2}^{\delta/2} \hat{B}_{g1}\cos(p(\theta_s - \theta_m)) l_s r_s d\theta_s \tag{3.17}$$

where, δ is the mechanical angle corresponding to the slot pitch, $\delta=2\pi/N_t$ and N_t is the tooth number. From the equation (3.17), we obtain

$$\phi_{t1,m} = \frac{2}{p}\hat{B}_{g1} l_s r_s \sin(p\frac{\delta}{2})\cos(p\theta_m) = \hat{\Phi}_{t1,m}\cos(p\omega_m t) \tag{3.18}$$

where,

$$\hat{\Phi}_{t1,m} = \frac{2}{p}\hat{B}_{g1} l_s r_s \sin(p\frac{\delta}{2}) = \hat{\Phi}_{g1}\sin(p\frac{\delta}{2}) = \hat{\Phi}_{g1}\sin(p\frac{\pi}{N_t}) \tag{3.19}$$

With the above equations for the tooth flux, the flux density in the tooth during no-load can be easily calculated.

3.4. The Armature Field and Other Armature Quantities

In this section, the turn function, the winding function, and magnetomotive force (MMF) are investigated first. Next, the magnetic field due to the stator current-carrying windings alone is given. Then, the flux linkage, the fundamental winding factor, and inductances are addressed. Afterwards, three examples illustrating the calculation of the magnetic field and inductances of PM machines with different combinations of slot and pole are presented. Finally, a summary of calculation results of the magnetic field and inductances is given.

3.4.1. The Turn Function, Winding Function and MMF

In this subsection, the equations of the turn function, the winding function, and the MMF are given. Those functions will be used to calculate flux linkage, inductances and three-phase MMFs in the next subsections.

The turn function $n(\theta_s)$ of a phase expresses the number of wire turns wound around a tooth and the direction of wound wires [Nua 1998], [Kyu 2010], [Mac 1995]. If the flux due to the turns wound around a tooth and carrying one unit of current goes out the stator surface, the sign of this function is plus. Vice versa, if the flux goes into the stator surface, the sign is minus[1].

The winding function of a phase (illustration for phase *a*) $N_a(\theta_s)$ is defined as the difference between the turn function and the average value of the turn function $< n_a(\theta_s) >$ [Mac 1995], [Nua 1998], [FY 2006], [Lip 1996] i.e.,

$$N_a(\theta_s) = n_a(\theta_s) - < n_a(\theta_s) > \tag{3.20}$$

The winding function indicates the regions in which flux would be produced by one unit of current in the turns. In the equation (3.20), the average of the turn function is simply calculated as,

$$< n(\theta_s) >= \frac{1}{2\pi} \int_0^{2\pi} n(\theta_s) d\theta_s \tag{3.21}$$

$$< N(\theta_s) >= \frac{1}{2\pi} \int_0^{2\pi} N(\theta_s) d\theta_s = 0 \tag{3.22}$$

According to [FY 2006] and [Mac 1995], the MMF of a phase (for example, phase *a*), due to current of the phase alone, at any point in the air gap is related to the winding function of the phase as

$$F_a(\theta_s) = N_a(\theta_s).i_a \tag{3.23}$$

It can be seen from equation (3.23) that the winding function can be considered as the MMF due to a unit current. Similar to the calculation of the flux density in the air gap, the total MMF in the air gap is the sum of the MMF distributions of all phases. Some examples for establishing the functions will be presented in Subsection 3.4.6. From the equation (3.23), we can derive the expression for calculating the air gap flux density of phase *a* due to the current of the phase alone, based on the winding function, as

$$B_{sa}(\theta_s) = \frac{\mu_0}{g'_{eff}} F_a(\theta_s) = \frac{\mu_0}{g'_{eff}} N_a(\theta_s) i_a \tag{3.24}$$

[1] Examples in Section 3.46 demonstrate the turn and winding functions.

Again note that the reference point θ_s=0 is chosen such that the winding function is an even function, i.e., $N_a(\theta_s)=N_a(-\theta_s)$. If so, the Fourier series of the winding function, the flux density, and the MMF of a phase have only co-sinusoidal space components.

The MMFs of the three-phase current-carrying windings can be obtained by applying the superposition theorem as follows,

$$F_s(\theta_s) = F_a(\theta_s) + F_b(\theta_s) + F_c(\theta_s) = N_a(\theta_s)i_a + N_b(\theta_s)i_b + N_c(\theta_s)i_c \tag{3.25}$$

Substituting the equation (3.20) into equation (3.25) and considering the fact that the average value of the turn function of each phase in the symmetrical three-phase winding system is identical and the sum of three-phase currents is zero, we obtain

$$F_s(\theta_s) = n_a(\theta_s)i_a + n_b(\theta_s)i_b + n_c(\theta_s)i_c \tag{3.26}$$

The equation (3.26) will be used to plot the MMFs distribution in Section 3.13.

3.4.2. Magnetic Field of Stator Current-Carrying Windings

For simplicity, it is assumed in the analysis that the current is sinusoidal and the initial angle of the current of phase *a* is zero. The three phase currents are given by

$$i_a = \hat{i}_s \cos(\omega t) \tag{3.27}$$

$$i_b = \hat{i}_s \cos(\omega t - \frac{2}{3}\pi) \tag{3.28}$$

$$i_c = \hat{i}_s \cos(\omega t - \frac{4}{3}\pi) \tag{3.29}$$

The space harmonics of the magnetic flux density are calculated in the following order. First, the flux density in the air gap is determined for the case where only phase *a* conducts a current that is equal to the amplitude. Next, the flux density of this phase is written as a Fourier series. Afterwards, the flux density of phases *b* and *c* can be derived from that of phase *a* by means of shifting $2\pi/3$ radians for both the spatial angle and the electric angle. Finally, the total flux density in the air gap is calculated by adding three flux density distributions.

For transparence in interpretation, some important assumptions are repeated here, namely that the stator teeth and slot can be replaced by a smooth surface, the magnetic flux crosses the air gap perpendicularly, iron permeability is infinite, and the flux density is constant over a tooth pitch.

The stator coordinate is chosen in such a way that only co-sinusoidal space components are presented. Flux density in air gap produced by MMF of phase *a* can be expressed in form of a Fourier series as follows [Pol 2007]:

$$B_{sa}(\theta_s) = \sum_{k=1}^{\infty} \hat{B}_{sak} \cos(k \frac{2\pi}{\lambda_1} \theta_s) \tag{3.30}$$

where, θ_s is the stator angle of a point in the air gap, and λ_1 is the wave length (in radian angle) of the fundamental space harmonic; $\lambda_1 = 2\pi/N_{\lambda 1} = 2\pi/\mathrm{GCD}(N_t, p)$ where $N_{\lambda 1}$ is the number of winding cycles which depend on a combination of slot and pole (i.e., the winding configuration shown in Chapter 2). For example, with a slot/pole number of 24/16, 27/18, 24/20, 24/28, 27/24, $N_{\lambda 1}$ is respectively equal to 8, 9, 2, 2 and 3.

The amplitudes of the space harmonics of the flux density in equation (3.30) are calculated by using the Fourier transform:

$$\hat{B}_{sak} = \frac{2}{\lambda_1} \int_0^{\lambda_1} B_{sa}(\theta_s) \cos(k \frac{2\pi}{\lambda_1} \theta_s) d\theta_s \tag{3.31}$$

where $B_{sa}(\theta_s)$ is calculated according to equation (3.24) or by using an equivalent magnetic circuit of the machine.

The flux density distribution of the other phases are equal to the flux density distribution of phase *a* except for a shift in the angle position [Pol 2007]

$$B_{sa}(\theta_s) = \sum_{k=1}^{\infty} \hat{B}_{sak} \cos(k \frac{2\pi}{\lambda_1} \theta_s) \cos(\omega t) \tag{3.32}$$

$$B_{sb}(\theta_s) = \sum_{k=1}^{\infty} \hat{B}_{sbk} \cos(k(\frac{2\pi}{\lambda_1} \theta_s - \frac{2\pi}{3})) \cos(\omega t - \frac{2\pi}{3}) \tag{3.33}$$

$$B_{sc}(\theta_s) = \sum_{k=1}^{\infty} \hat{B}_{sck} \cos(k(\frac{2\pi}{\lambda_1} \theta_s - \frac{4\pi}{3})) \cos(\omega t - \frac{4\pi}{3}) \tag{3.34}$$

The total flux density in the air gap is the sum of the three flux density distributions as [Pol 2007],

$$B_s(\theta_s) = B_{sa}(\theta_s) + B_{sb}(\theta_s) + B_{sc}(\theta_s) = \sum_{k=1}^{\infty} B_{sk} \tag{3.35}$$

where,

$$\left.\begin{aligned} B_{sk} &= \hat{B}_{sk}\cos(k\frac{2\pi}{\lambda_1}\theta_s - \omega t) \quad for\ k = 3n+1, \forall n = 0,1,2,3... \\ B_{sk} &= \hat{B}_{sk}\cos(k\frac{2\pi}{\lambda_1}\theta_s + \omega t) \quad for\ k = 3n-1, \forall n = 1,2,3... \\ B_{sk} &= 0 \quad for\ k = 3n, \forall n = 1,2,3... \end{aligned}\right\} \tag{3.36}$$

It is shown from equation (3.24) and results of the examples in Section 3.46 that the amplitude of flux density can be expressed as

$$\hat{B}_{sak} = \hat{B}_{sbk} = \hat{B}_{sck} = k_{Bk}\frac{\mu_0}{g'_{eff}}N_c\hat{i}_s; \quad g'_{eff} = (l_m/\mu_{rm} + g_{eff}) \tag{3.37}$$

$$\hat{B}_{sk} = \frac{3}{2}\hat{B}_{sak} = \frac{3}{2}k_{Bk}\frac{\mu_0}{g'_{eff}}N_c\hat{i}_s \tag{3.38}$$

In equation (3.37), N_c is the number of turns of a coil. k_{Bk} is a constant corresponding to the k^{th} harmonic, depending on winding configuration i.e., depending on the combination of slot and pole. This factor will be explained further in Subsection 3.4.6.

3.4.3. Flux Linkage due to Current-Carrying Windings

In this subsection, the flux linkage and mutual flux are derived, which will be used to establish expressions of the winding factor and inductances in the next Subsections.

The flux linkage of phase *a* due to the three-phase winding MMFs can be calculated as follows [Ref 2006], [Lip 1996], [Mac 1995],

$$\psi_{a,s} = \iint_S n_a(\theta_s)B_s(\theta_s)dA = l_s r_s\int_0^{2\pi} n_a(\theta_s)B_s(\theta_s)d\theta_s \tag{3.39}$$

where, $n_a(\theta_s)$ is the turn function of phase *a* and *S* is the integral surface which is an enclosed surface in the air gap covering the stator surface.

To derive equation of the flux linkage with respect to the winding function, we substitute the equation (3.20) into the equation (3.39) and consider the Gauss's law i.e.,

$$\oint_S \vec{B}_s(\theta_s).d\vec{A} = 0 \quad \Rightarrow \quad \int_0^{2\pi} B_s(\theta_s)l_s r_s d\theta_s = 0 \tag{3.40}$$

Therefore, the equation (3.39) can be rewritten as

$$\psi_{a,s} = \iint_S N_a(\theta_s)B_s(\theta_s)dA = l_s r_s\int_0^{2\pi} N_a(\theta_s)B_s(\theta_s)d\theta_s = \frac{\mu_0 l_s r_s}{g'_{eff}}\int_0^{2\pi} N_a(\theta_s)F_s(\theta_s)d\theta_s \tag{3.41}$$

The flux linkage of phase *a* due to the MMF of phase *a* alone can be written as,

$$\psi_{aa} = \iint_S n_a(\theta_s) B_{sa}(\theta_s) dA = l_s r_s \int_0^{2\pi} N_a(\theta_s) B_{sa}(\theta_s) d\theta_s = \frac{\mu_0 l_s r_s}{g'_{eff}} \int_0^{2\pi} N_a(\theta_s) F_{sa}(\theta_s) d\theta_s \qquad (3.42)$$

The flux linkage of winding phase *b* due to a current winding phase *a* is [Mac 1995]

$$\psi_{ba} = \iint_S n_b(\theta_s) B_{sa}(\theta_s) dA = l_s r_s \int_0^{2\pi} N_b(\theta_s) B_{sa}(\theta_s) d\theta_s = \frac{\mu_0 l_s r_s}{g'_{eff}} \int_0^{2\pi} N_b(\theta_s) F_{sa}(\theta_s) d\theta \qquad (3.43)$$

3.4.4. The Fundamental Winding Factor

In Chapter 2, the fundamental winding factor was defined and calculated based on the electromotive force. Here, an alternative definition of the winding factor will be given, but it gets the same result. The goal of this subsection is to give insight into the relation between the fundamental quantities such as air gap flux density, flux linkage, etc by calculating the fundamental winding factor. It is assumed that the fundamental component is the torque-producing component. Otherwise, the calculation of the winding factor can easily be adapted from the following things.

The fundamental winding factor is the ratio of the actual fundamental flux linkage of a phase to the ideal flux linkage of the phase due to current-carrying windings. The fundamental winding factor can be written as,

$$K_{w1} \equiv \frac{\psi_{a1,s}}{\psi_{a1,s\_ideal}} = \frac{\hat{\psi}_{a1,s}}{\hat{\psi}_{a1,s\_ideal}} \qquad (3.44)$$

The actual fundamental flux linkage of a phase can be calculated according to the equation (3.41), by replacing $B_s(\theta_s)$ with $B_{s1}(\theta_s)$. While the ideal flux linkage of a phase is the multiplication of the number of conductors per phase and the flux linkage due to a current-carrying conductor. The actual fundamental flux linkage of a phase and the ideal flux linkage are calculated as follows.

The actual fundamental flux linkage

Assuming that the fundamental flux density in the air gap is

$$B_{s1}(\theta_s) = \hat{B}_{s1} \cos(p\theta_s) \qquad (3.45)$$

From (3.24), the winding function, at time t=0, i.e., $i_a = \hat{i}_s$ can be expressed as

$$N_a(\theta_s) = \frac{g'_{eff}}{\mu_0 \hat{i}_s} B_{sa}(\theta_s) \tag{3.46}$$

Substituting (3.32) into (3.46), at time t=0, i.e., i_a=$\hat{i}_s$, we obtain

$$N_a(\theta_s) = \frac{g'_{eff}}{\mu_0 \hat{i}_s} \sum_{k=1}^{\infty} \hat{B}_{sak} \cos(k \frac{2\pi}{\lambda_1} \theta_s) = \sum_{k=1}^{\infty} \hat{N}_{ak} \cos(k \frac{2\pi}{\lambda_1} \theta_s) \tag{3.47}$$

where,

$$\hat{N}_{ak} = \frac{g'_{eff}}{\mu_0 \hat{i}_s} \hat{B}_{sak} \tag{3.48}$$

Substituting (3.37) into (3.48), we obtain

$$\hat{N}_{ak} = k_{Bk} N_c \tag{3.49}$$

The actual fundamental flux linkage of a phase can be deducted from (3.41) as

$$\begin{aligned} \psi_{a1,s} &= l_s r_s \int_0^{2\pi} N_a(\theta_s) B_{s1}(\theta_s) d\theta_s = l_s r_s \int_0^{2\pi} \left(\sum_{k=1}^{\infty} \hat{N}_{ak} \cos(k \frac{2\pi}{\lambda_1} \theta_s) \right) \hat{B}_{s1} \cos(p\theta_s) d\theta_s = \ldots \\ &= l_s r_s \int_0^{2\pi} \hat{N}_{a1} \cos(p\theta_s) \hat{B}_{s1} \cos(p\theta_s) d\theta_s = l_s r_s \hat{N}_{a1} \hat{B}_{s1} \pi \end{aligned} \tag{3.50}$$

The ideal flux linkage

The maximum fundamental flux per pole pitch due to the three-phase stator windings can be obtained by integrating the flux density around the air gap surface in a pole pitch [Mil 1989]. This means that

$$\phi_{s1} = \int_{-\frac{\pi}{2p}}^{\frac{\pi}{2p}} \hat{B}_{s1} \cos(p\theta_s - \omega t) l_s r_s d\theta_s = \frac{2}{p} l_s r_s \hat{B}_{s1} \cos(\omega t) = \hat{\Phi}_{s1} \cos(\omega t) \tag{3.51}$$

where,

$$\hat{\Phi}_{s1} = \frac{2}{p} \hat{B}_{s1} l_s r_s \tag{3.52}$$

The maximum fundamental space component of the flux passing through a tooth due to the three-phase stator MMFs can be calculated as,

$$\phi_{t1,s} = \int_{-\delta/2}^{\delta/2} \hat{B}_{s1} \cos(p\theta_s - \omega t) l_s r_s d\theta_s \tag{3.53}$$

By developing the equation (3.53), we obtain

$$\phi_{t1,s} = \frac{2}{p} \hat{B}_{s1} l_s r_s \sin(p\frac{\delta}{2}) \cos(\omega t) = \hat{\Phi}_{t1,s} \cos(\omega t) \tag{3.54}$$

where,

$$\hat{\Phi}_{t1,s} = \frac{2}{p} \hat{B}_{s1} l_s r_s \sin(p\frac{\delta}{2}) = \hat{\Phi}_{s1} \sin(p\frac{\delta}{2}) = \hat{\Phi}_{s1} \sin(p\frac{\pi}{N_t}) \tag{3.55}$$

The amplitude of the fundamental space component of the flux links due to a coil side in the slot can be calculated as,

$$\hat{\psi}_{c1,s} = N_c \frac{\hat{\Phi}_{t1,s}}{2\sin(p\frac{\delta}{2})} = \frac{N_c}{p} \hat{B}_{s1} l_s r_s \tag{3.56}$$

The amplitude of the fundamental flux linkage of phase *a* due to MMFs of stator windings in the ideal case (which is identical to the case of double-layer full pitch distributed windings with number of slots per pole per phase *q* equal to 1) can be calculated as,

$$\hat{\psi}_{a1,s\_ideal} = \frac{2Q}{3} \hat{\psi}_{c1,s} = \frac{2QN_c}{3p} \hat{B}_{s1} l_s r_s = 4qN_c \hat{B}_{s1} l_s r_s \tag{3.57}$$

where Q is the number of slots and q is the number of slot per pole per phase.

Substituting (3.50), (3.57) and (3.49) into (3.44), we obtain the fundamental winding factor as

$$K_{w1} \equiv \frac{\hat{\psi}_{a1,s}}{\hat{\psi}_{a1,s\_ideal}} = \frac{\hat{N}_{a1}\pi}{4qN_c} = k_{B1} \frac{\pi}{4q} \tag{3.58}$$

where k_{B1} is the factor corresponding to the first harmonic in equation (3.38).

Note that with the machine having the fundamental component different to the torque-producing component, the k_{B1} in the above equation is replaced by the k_{Bk} corresponding to the torque-producing component.

3.4.5. Inductances of Stator Windings

The inductances of stator windings include the self-inductance L_{aa}, the mutual inductance L_{ab}, the slot leakage inductance L_{slot}, the end leakage inductance L_{end} and the harmonic leakage inductance L_h (or the differential leakage inductance or the belt leakage) [Lip 1996], [Han 1994].

For the initial design, it is assumed that the harmonic leakage inductance is negligibly small. The inductance calculation is going to present as follows.

The self-inductance of phase *a* can be calculated as [Lip 1996], [Ref 2006],

$$L_{aa} = \frac{\psi_{aa}}{i_a} = \frac{\mu_0 l_s r_s}{g'_{eff}} \frac{\int_0^{2\pi} N_a(\theta_s) F_{sa}(\theta_s) d\theta_s}{i_a} = \frac{\mu_0 l_s r_s}{g'_{eff}} \int_0^{2\pi} N_a^2(\theta_s) d\theta_s \tag{3.59}$$

The mutual inductance between phase *a* and *b* can be calculated as,

$$L_{ab} = \frac{\psi_{ba}}{i_a} = \frac{\mu_0 l_s r_s}{g'_{eff}} \frac{\int_0^{2\pi} N_b(\theta_s) F_{sa}(\theta_s) d\theta}{i_a} = \frac{\mu_0 l_s r_s}{g'_{eff}} \int_0^{2\pi} N_a(\theta_s) N_b(\theta_s) d\theta \tag{3.60}$$

The slot leakage inductance per phase, corresponding to slot leakage flux as shown in Figure 3.4b, for double-layer windings can be calculated as well-known equation (3.61) [Sah 2001], [Ref 2008b], [Lip 1996]

$$L_{slot} = \frac{Q}{3} 4 N_c^2 l_s P_s \tag{3.61}$$

where, Q is number of slots and P_s is the specific slot permeance function calculated as follows,

$$P_s = \mu_0 \left[\frac{h_s}{3w_s} + \frac{h_1}{(w_{s2} + w_{s3})/2} + \frac{h_0}{b_s} \right] \tag{3.62}$$

where h_s is the slot height (approximately equal to the height of tooth h_t), w_s is the equivalent slot width $w_s=(w_{s1}+w_{s2})/2$, and h_o is the slot opening height and b_s is slot opening width as shown in Figure 3.4a.

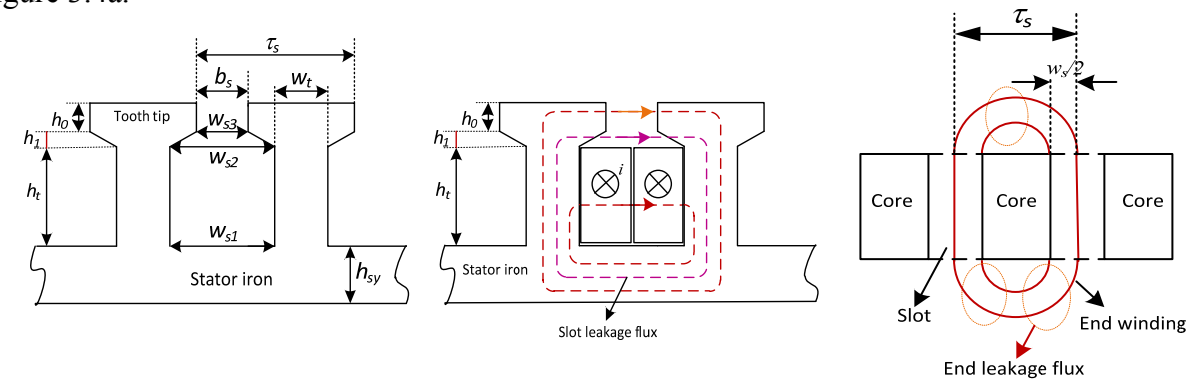

a) b) c)

Figure 3.4. a) Main dimensions of stator iron, b) illustration of slot leakage flux, c) illustration of end leakage flux.

The well-known equation of phase end leakage inductance corresponding to the end leakage flux (as shown in Figure 3.4c) for double-layer windings can approximately be written as [Han 1994], [Sah 2001],

$$L_{end} = \frac{N_{coil}}{6} N_c^2 \mu_0 \tau_s \ln\left(\frac{\pi\tau_s^2 / 4}{(h_s w_s / 2)}\right) \tag{3.63}$$

where N_{coil} is the number of coils of the PM machine.

The leakage inductance can be expressed as

$$L_l = L_{slot} + L_{end} \tag{3.64}$$

The main synchronous inductance L_m concerning airgap flux linkage can be calculated as [Fit 2002]

$$L_m = L_{aa} - L_{ab} \tag{3.65}$$

The synchronous inductance L_s can be written as [Fit 2002],

$$L_s = L_m + L_l \tag{3.66}$$

3.4.6. Examples

To demonstrate the calculation of the magnetic flux density, the winding function and inductances from the equations established above, we are going to consider some fractional-slot concentrated-winding PM machines with slot/pole combination of 3/2, 6/5, 6/7 and 9/8. At the end of this subsection, a summary of formulas for calculating the flux density produced by MMFs and inductances corresponding to different slot and pole combinations is given.

3.4.6.1. Example 1: The PM Machine with a Slot/Pole Combination of 3/2

a) Fundamental Flux Density due to MMFs

Figure 3.5a shows a section of a PM machine with a slot/pole combination of 3/2 as well as flux contour produced by the MMF of phase *a*. Assuming electric current of phase *a* is equal to its amplitude and the electric current direction is shown in Figure 3.5a. Figure 3.5b presents the distribution of flux density of phase *a* along the air gap circumference; this will be explained in details as follows. Figure 3.5c shows the turn function of phase *a*. The positions in the air gap, which opposite the tooth surface of phase *a*, the turn function has a value equal to the number of turns per tooth N_c and the sign of the turn function is "+" because the flux goes out the tooth surface. At other positions, the turn function is equal to zero. To explain the distribution of flux density along the air gap as shown in Figure 3.5a, an equivalent magnetic circuit for a section of

the PM machine as shown in Figure 3.6 is used. Then the result is compared to the calculation of the distribution of flux density in the air gap using the equation (3.24).

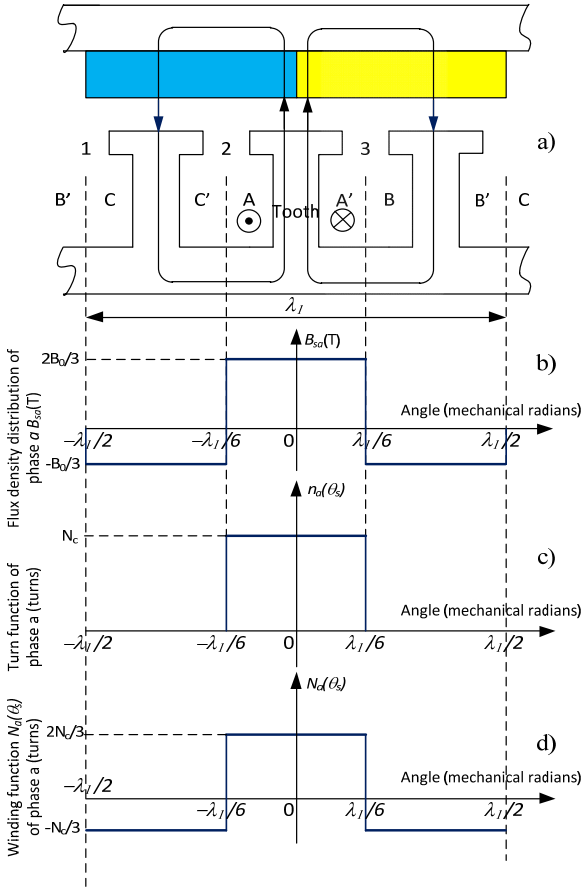

Figure 3.5. a) A section of the PM machine, b) Illustration of flux density distribution due to MMF of phase *a*, c) Turn function of phase *a*, d) Winding function of phase *a* of the PM machine with a slot/pole combination of 3/2, where N_c is the number of turns per tooth.

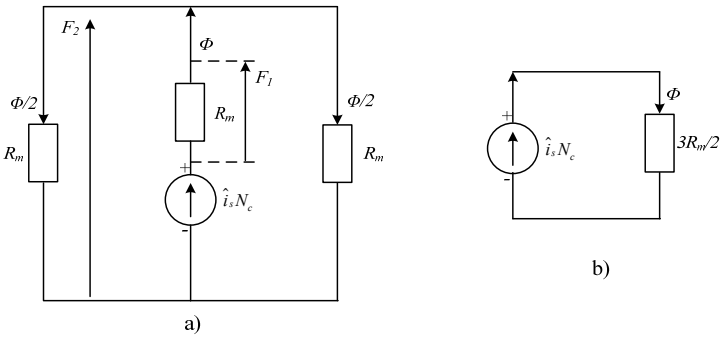

Figure 3.6. a) Equivalent magnetic circuit for a section (as Figure 3.5a) of a PM machine with a slot/pole combination of 3/2, magnetization produced by MMF of phase *a* alone; b) Simplifying the magnetic circuit.

The total reluctance R_m of the magnet and the air gap per slot pitch in Figure 3.6a can be calculated as,

$$R_m = \frac{l_m / \mu_{rm} + g_{eff}}{\mu_0 \tau_s l_s} = \frac{g'_{eff}}{\mu_0 \tau_s l_s}; \quad g'_{eff} = (l_m / \mu_{rm} + g_{eff}) \tag{3.67}$$

where, μ_{rm} is the relative permeability of the magnet, g_{eff} is the effective air gap length, and l_m is the thickness of the magnet.

From Figure 3.6, we obtain

$$F_1 = \frac{2}{3}\hat{i}_s N_c; \quad F_2 = -\frac{1}{3}\hat{i}_s N_c \tag{3.68}$$

According to Ampere's law, we can write this as,

$$F_1 = \frac{B_1}{\mu_0} g'_{eff}; \quad F_2 = \frac{B_2}{\mu_0} g'_{eff} \tag{3.69}$$

where, B_1 is the mean air gap flux density at positions opposite the tooth surface of phase *a*, B_2 is the mean air gap flux density at positions opposite the tooth surface of phase *b* or *c*; these flux densities are due to the MMF of phase a alone.

From the above equations, we obtain

$$B_1 = \frac{2\mu_0}{3g'_{eff}}\hat{i}_s N_c; \quad B_2 = -\frac{\mu_0}{3g'_{eff}}\hat{i}_s N_c \tag{3.70}$$

The flux density B_0 is defined as,

$$B_0 \equiv \frac{\mu_0}{g'_{eff}}\hat{i}_s N_c \tag{3.71}$$

Equation (3.70) can be rewritten as,

$$B_1 = \frac{2B_0}{3}; \quad B_2 = -\frac{B_0}{3} \tag{3.72}$$

Therefore, the distribution of flux density in the air gap due to current-carrying windings of phase *a* alone can be shown as in Figure 3.5b.

The amplitudes of the space harmonic components of air gap flux density in the Fourier series (3.31) can be calculated as,

$$\hat{B}_{sak} = \frac{2}{\lambda_1} \int_{-\lambda_1/2}^{\lambda_1/2} B_{sa}(\theta_s) \cos(\frac{2\pi}{\lambda_1} k\theta_s) d\theta_s = \frac{2}{k\pi} B_0 \sin(k\frac{\pi}{3}) = k_{Bk} B_0 \tag{3.73}$$

$$k_{Bk} = \frac{2}{k\pi} \sin(k\frac{\pi}{3}) \tag{3.74}$$

Above, we calculated flux density in the air gap due to the MMF of phase a. Hereafter, the flux density in the air gap due to three-phase MMF is deducted.

The fundamental flux density in the air gap due to three-phase MMFs alone can be written as,

$$B_{s1}(\theta_s) = \frac{3}{2} \hat{B}_{sa1} \cos(p\theta_s - \omega t) = \frac{3\sqrt{3}}{2\pi} \frac{\mu_0}{g'_{eff}} N_c \hat{i}_s \cos(p\theta_s - \omega t) = \hat{B}_{s1} \cos(p\theta_s - \omega t) \tag{3.75}$$

The amplitude of fundamental flux density in the air gap due to there-phase MMFs can be written as,

$$\hat{B}_{s1} = \frac{3}{2} k_{B1} B_0 = \frac{3\sqrt{3}}{2\pi} B_0 \tag{3.76}$$

Figure 3.5c presents the turn function of phase *a*. Once the turn function has been obtained, the winding function can be calculated according to the equation (3.20), as shown in Figure 3.5d. We can obtain the same result of the distribution of the air gap flux density of phase *a* by using the equation (3.24) instead of using the equivalent magnetic circuit.

b) Inductances

The self-inductance of phase *a* is calculated as,

$$L_{aa} = \frac{\mu_0 l_s r_s}{g'_{eff}} N_{\lambda_1} \int_{-\lambda_1/2}^{\lambda_1/2} N_a^2(\theta_s) d\theta_s = \frac{4\pi}{9} \frac{N_c^2 \mu_0 l_s r_s}{g'_{eff}} \tag{3.77}$$

The mutual inductance between phase *a* and *b* is calculated as,

$$L_{ab} = \frac{\mu_0 l_s r_s}{g'_{eff}} N_{\lambda_1} \int_{-\lambda_1/2}^{\lambda_1/2} N_a(\theta_s) N_b(\theta_s) d\theta_s = -\frac{2\pi N_c^2}{9} \frac{\mu_0 l_s r_s}{g'_{eff}} \tag{3.78}$$

As can be seen, the mutual inductance is equal to one-half of the self-inductance, i.e., L_{ab}=-L_{aa}/2.

3.4.6.2. Example 2: The PM Machines with Slot/Pole Combinations of 6/5 and 6/7

In this subsection, two PM machines are examined, namely the 24 slots/ 20 poles PM machine and the 24 slots/ 28 poles PM machine. Because these PM machines have the same stator and windings, the results presented below are for both PM machines [Ref 2008b]. The procedures to

calculate the distribution of flux density in the air gap and inductances for these PM machines are similar to those in the Example 1. The main results are given in the following.

Figure 3.7a presents a section of the PM machine with 24 slots and 20 poles with electrical excitation for phase *a* alone. While Figure 3.7b presents the winding function of phase *a* and the distribution of flux density in airgap due to the MMF of phase *a* alone. From this figure, the flux density and inductances can be delivered as follows.

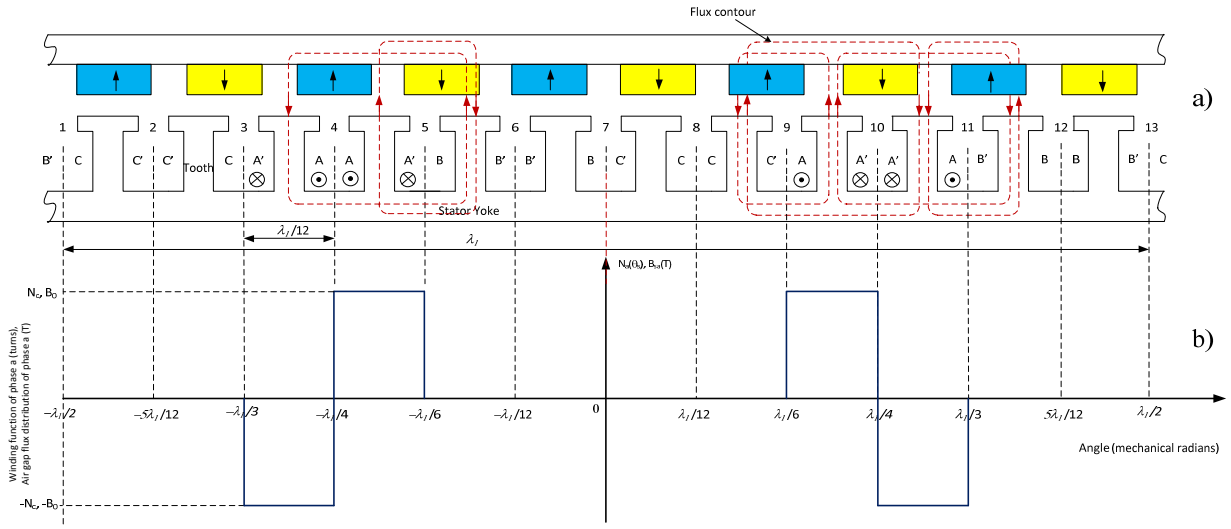

Figure 3.7. a) A section of the PM machine with 24 slots and 20 poles, b) The winding function of phase *a* as well as the distribution of flux density in the air gap due to the MMF of phase *a* alone.

The amplitudes of the space harmonic components of the air gap flux density of phase *a* is

$$\hat{B}_{sak} = \frac{2}{k\pi}\left[2\sin(k\frac{\pi}{2}) - \sin(\frac{k\pi}{3}) - \sin(\frac{2k\pi}{3})\right]\frac{\mu_0}{g'_{eff}}\hat{i}_s N_c = k_{Bk}B_0 \tag{3.79}$$

The amplitudes of harmonic flux density in the air gap due to the three-phase MMFs is

$$\hat{B}_{sk} = \frac{3}{2}\hat{B}_{sak} = \frac{3}{k\pi}\left[2\sin(k\frac{\pi}{2}) - \sin(\frac{k\pi}{3}) - \sin(\frac{2k\pi}{3})\right]\frac{\mu_0}{g'_{eff}}\hat{i}_s N_c \tag{3.80}$$

The self-inductance of phase *a* is calculated as,

$$L_{aa} = \frac{\mu_0 l_s r_s}{g'_{eff}}\int_0^{2\pi} N_a^2(\theta_s)d\theta_s = \frac{\mu_0 l_s r_s}{g'_{eff}} N_{\lambda_1}\int_0^{\lambda_1} N_a^2(\theta_s)d\theta_s = \frac{2\pi}{3}\frac{N_c^2\mu_0 l_s r_s}{g'_{eff}} \tag{3.81}$$

The mutual inductance between phase *a* and *b* is calculated as,

$$L_{ab} = \frac{\mu_0 l_s r_s}{g'_{eff}} \int_0^{2\pi} N_a(\theta_s) N_b(\theta_s) d\theta_s = \frac{\mu_0 l_s r_s}{g'_{eff}} N_{\lambda_1} \int_0^{\lambda_1} N_a(\theta_s) N_a(\theta_s + \frac{\lambda_1}{3}) d\theta_s = 0 \tag{3.82}$$

3.4.6.3. Example 3: The PM Machine with a Slot/Pole Combination of 9/8

Figure 3.8a presents a section of the PM machine with 27 slots and 24 poles, while Figure 3.8b presents the winding distribution and flux density distribution of phase *a* of this machine. The calculation is similar to that in the Example 1. The calculation results for this machine are presented as follows.

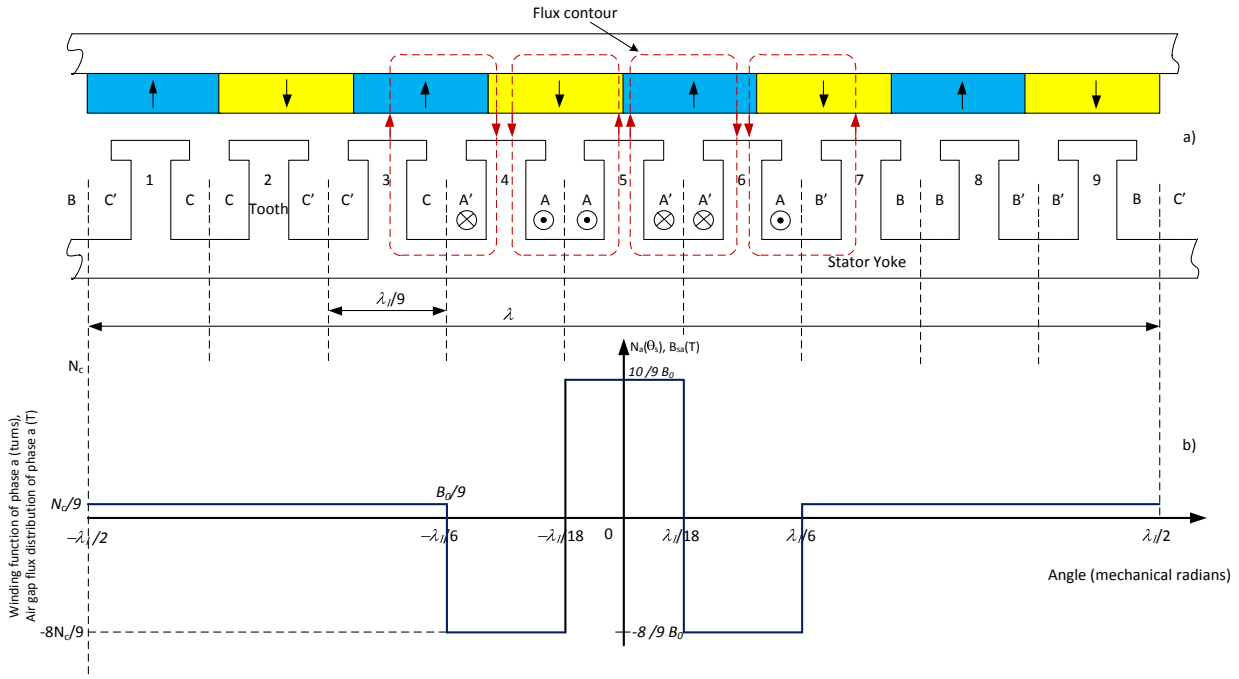

Figure 3.8. a) A section of the PM machine with 27 slots and 24 poles, b) The winding function of phase *a* as well as the distribution of flux density in the air gap due to the MMF of phase *a* alone.

The amplitudes of the space harmonic components of the air gap flux density of phase *a* are

$$\hat{B}_{sak} = \frac{2}{k\pi}\left[2\sin(k\frac{\pi}{9}) - \sin(\frac{k\pi}{3})\right]\frac{\mu_0}{g'_{eff}}\hat{i}_s N_c = k_{Bk} B_0 \tag{3.83}$$

The amplitudes of the space harmonic flux density in the air gap due to three-phase MMFs are

$$\hat{B}_{sk} = \frac{3}{2}\hat{B}_{sak} = \frac{3}{k\pi}\left[2\sin(k\frac{\pi}{9}) - \sin(\frac{k\pi}{3})\right]\frac{\mu_0}{g'_{eff}}\hat{i}_s N_c \tag{3.84}$$

The self-inductance of phase *a* is

$$L_{aa} = \frac{\mu_0 l_s r_s}{g'_{eff}} \int_0^{2\pi} N_a^2(\theta_s) d\theta_s = \frac{\mu_0 l_s r_s}{g'_{eff}} N_{\lambda_1} \int_0^{\lambda_1} N_a^2(\theta_s) d\theta_s = \frac{52\pi}{81} \frac{N_c^2 \mu_0 l_s r_s}{g'_{eff}} \quad (3.85)$$

The mutual inductance between phase *a* and *b* is

$$L_{ab} = \frac{\mu_0 l_s r_s}{g'_{eff}} \int_0^{2\pi} N_a(\theta_s) N_b(\theta_s) d\theta_s = \frac{\mu_0 l_s r_s}{g'_{eff}} N_{\lambda_1} \int_0^{\lambda_1} N_a(\theta_s) N_a(\theta_s - \frac{\lambda_1}{3}) d\theta_s = -\frac{2\pi}{81} \frac{N_c^2 \mu_0 l_s r_s}{g'_{eff}} \quad (3.86)$$

The main synchronous inductance is

$$L_m = L_{aa} - L_{ab} = \frac{2\pi}{3} \frac{N_c^2 \mu_0 l_s r_s}{g'_{eff}} \quad (3.87)$$

3.4.6.4. Summary of Section 3.46

The main calculation results of the armature flux density and inductances in the above examples, corresponding to typical combinations of slot and pole are summed in the Table 3.1.

In sum, it can be seen from calculation results of inductances that inductance is proportional to the square of the number of turns per tooth, length of stator core and stator radius. It is inversely proportional to the length of the effective air gap.

It can be seen from this table that the main synchronous inductance is not dependent on slot number. This is because when the number of slots increases, the air gap permeance per slot pitch decreases. Therefore, air gap inductance does not change with respect to number of slots, assuming number of turns per tooth are constant. In addition, air gap inductance does not depend on the number of poles. Consequently, the air gap inductance is not dependent on the combination of slot and pole. It should be noted that the equation for calculating inductances is an approximation. To obtain an accurate inductance, nonlinear FEM computation is required.

Table 3.1. Summary of formulas for calculating the armature field and inductances.

N0.	Slot/pole	The amplitudes of the space harmonics of the flux density due to the three-phase MMFs	Inductance expressions
1	3/2	$\hat{B}_{sk}=\frac{3}{k\pi}\sin(k\frac{\pi}{3})\frac{\mu_0}{g'_{eff}}\hat{i}_s N_c$	$L_{aa}=\frac{4\pi}{9}\frac{N_c^2\mu_0 l_s r_s}{g'_{eff}}$ $L_{ab}=-\frac{2\pi}{9}\frac{N_c^2\mu_0 l_s r_s}{g'_{eff}}$ $L_m=\frac{2\pi}{3}\frac{N_c^2\mu_0 l_s r_s}{g'_{eff}}$
2	6/5	$\hat{B}_{sk}=\frac{3}{k\pi}\left[2\sin(k\frac{\pi}{2})-\sin(\frac{k\pi}{3})-\sin(\frac{2k\pi}{3})\right]\frac{\mu_0}{g'_{eff}}\hat{i}_s N_c$	$L_{aa}=\frac{2\pi}{3}\frac{N_c^2\mu_0 l_s r_s}{g'_{eff}}; L_{ab}=0$ $L_m=L_{aa}$
3	6/7	$\hat{B}_{sk}=\frac{3}{k\pi}\left[2\sin(k\frac{\pi}{2})-\sin(\frac{k\pi}{3})-\sin(\frac{2k\pi}{3})\right]\frac{\mu_0}{g'_{eff}}\hat{i}_s N_c$	$L_{aa}=\frac{2\pi}{3}\frac{N_c^2\mu_0 l_s r_s}{g'_{eff}}; L_{ab}=0$ $L_m=L_{aa}$
4	9/8	$\hat{B}_{sk}=\frac{3}{k\pi}\left[2\sin(k\frac{\pi}{9})-\sin(\frac{k\pi}{3})\right]\frac{\mu_0}{g'_{eff}}\hat{i}_s N_c$	$L_{aa}=\frac{52\pi}{81}\frac{N_c^2\mu_0 l_s r_s}{g'_{eff}}$ $L_{ab}=-\frac{2\pi}{81}\frac{N_c^2\mu_0 l_s r_s}{g'_{eff}}$ $L_m=\frac{2\pi}{3}\frac{N_c^2\mu_0 l_s r_s}{g'_{eff}}$

3.5. Total Field

Using the principle of superposition, the total field in air gap can be obtained by summing the field due to the permanent magnets and the field due to MMFs of stator windings alone. Therefore, the total magnetic flux density can be written as,

$$B(\theta_s,\theta_m)=B_g(\theta_s,\theta_m)+B_s(\theta_s) \tag{3.88}$$

We can write the fundamental field as,

$$B_1(\theta_s,\theta_m) = B_{g1}(\theta_s,\theta_m) + B_{s1}(\theta_s) = \hat{B}_1 \sin(p\theta_s - \omega t - \varphi_{B_1}) \tag{3.89}$$

Figure 3.9 shows the total fundamental flux density in a case where the fundamental flux density produced by magnets lags the fundamental flux density due to MMFs alone for π/2. The field distribution is plotted for the maximum amplitude of the stator current at the moment ωt=0. It is shown that the influence of the armature field on the total field in the air gap for the studied PM machine is negligibly small.

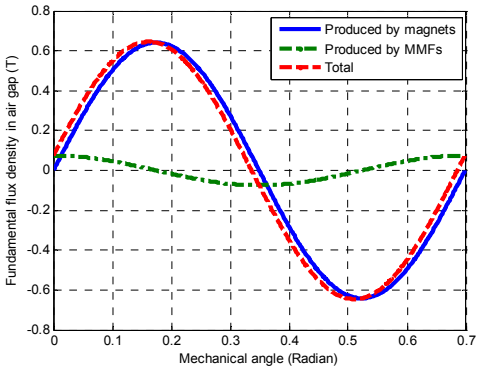

Figure 3.9. Armature reaction of the fundamental flux density in air gap, for the PM machine B.

3.6. Electromotive Force EMF (or Internal Voltage)

As mentioned earlier, the analytical model is only used for the initial design of PM machines, after that the automated nonlinear transient FEM model is used for further adjustment of the design. Therefore, it is only necessary to present the fundamental component of electromotive force (EMF) in this section.

To calculate the EMF of a phase, first we calculate the flux linkage of a phase, which is due to magnets, e.g., phase *a*. This can be calculated as,

$$\psi_{a1,m} = \iint_S n_a(\theta_s) B_{g1}(\theta_s,\theta_m) dA = l_s r_s \int_0^{2\pi} n_a(\theta_s) B_{g1}(\theta_s,\theta_m) d\theta_s \tag{3.90}$$

The instantaneous EMF of phase *a* can be calculated according to Faraday's law as

$$e_{a1} = -\frac{d\psi_{a1,m}}{dt} \tag{3.91}$$

The equation (3.91) is the form in general. It is used to calculate the instantaneous fundamental EMF. However, this depends on the winding function. This causes difficulty when formulating the rms EMF of PM machines with the different combinations of slot and pole. In addition, for

initial design, the attention is paid on the fundamental rms EMF. Therefore, we are going to establish the general form of this quantity in an alternative way as follows.

The fundamental EMF induced in a coil can be calculated according to Faraday's law as

$$\begin{aligned} e_{coil1} &= -N_c \frac{d\phi_{t1,m}}{dt} = N_c p\omega_m \hat{\Phi}_{t1,m} sin(p\omega_m t) = N_c p\omega_m \frac{2}{p} \hat{B}_{g1} l_s r_s \sin(p\frac{\delta}{2}) sin(p\omega_m t) = ... \\ ... &= N_c \omega_m 2\hat{B}_{g1} l_s r_s \sin(p\frac{\delta}{2}) sin(p\omega_m t) = \sqrt{2} E_{coil1} sin(p\omega_m t) \end{aligned} \tag{3.92}$$

Note that the fundamental flux passing a tooth $\phi_{t1,m}$ is calculated from the equation (3.18).

From (3.92), the fundamental rms EMF of a coil can be expressed as,

$$E_{coil1} = \sqrt{2} N_c \omega_m \hat{B}_{g1} l_s r_s \sin(p\frac{\delta}{2}) \tag{3.93}$$

where N_c is the number of turns per coil which are wound on a tooth.

The EMF of a coil is formed from the EMF of two coil sides put in two adjacent slots, so that the fundamental rms EMF of a coil side can be expressed as,

$$E_{s1} = \frac{E_{coil1}}{2\sin(p\frac{\delta}{2})} = \frac{1}{\sqrt{2}} N_c \omega_m \hat{B}_{g1} l_s r_s = N_c \omega_m B_{g1} l_s r_s \tag{3.94}$$

where B_{g1} is fundamental rms flux density in the air gap.

The fundamental rms EMF of a phase for double-layer concentrated windings with a parallel branch can be calculated as,

$$E_1 = 2\frac{Q}{3}.K_{w1} N_c \omega_m B_{g1} l_s r_s = \sqrt{2}.K_{w1} N_w \omega_m \hat{B}_{g1} l_s r_s \tag{3.95}$$

Substituting (3.16) into (3.95), we obtain

$$E_1 = \frac{1}{\sqrt{2}} K_{w1} N_w \hat{\Phi}_{g1} \omega = \pi\sqrt{2} K_{w1} N_w f_1 \hat{\Phi}_{g1} \tag{3.96}$$

where, Q is the slot number, $2Q/3$ is the number of coil sides of a phase, K_{w1} is the fundamental winding factor, N_w is the number of turns of a phase, ω_m is the mechanical angular speed of the rotor, f_1 is the fundamental frequency of EMF, and ω is the electric angular frequency, $\omega = 2\pi f_1 = p\omega_m$.

3.7. Voltage on Load

The instantaneous terminal voltage of phase *a* can be expressed as [Fit 2002],

$$u_a = e_a + L_s \frac{di_a}{dt} + R_s i_a \tag{3.97}$$

where, e_a is the instantaneous electromotive force of phase *a*, and L_s is the synchronous inductance. For the phases remaining, the voltage on load is similarly calculated.

In the equation (3.97), R_s is the winding resistance of a phase which can be calculated as,

$$R_s = \frac{8\rho_{Cu}}{\pi d_{cu}^2} N_w \left(l_s + \frac{\pi}{2} \frac{(\tau_s + w_t)}{2} \right) \tag{3.98}$$

where ρ_{cu} is the Copper resistivity, d_{cu} is diameter of Copper wire, w_t is tooth width, l_s is stator length, and N_w is the number of turns of a phase with a parallel branch.

If only the fundamental component is considered and the reference direction for current is chosen as positive out of the machine terminals, the voltage of phase *a* can be calculated using the following equation, written in the form of the complex number [Fit 2002],

$$\vec{U}_{a1} = \vec{E}_{a1} - j\omega L_s \vec{I}_{a1} - \vec{I}_{a1} R_s \tag{3.99}$$

3.8. Electromagnetic Power

The instantaneous electromagnetic power is calculated as,

$$p_e(t) = e_a i_a + e_b i_b + e_c i_c \tag{3.100}$$

Mean electromagnetic power of the PM machine is approximately calculated as,

$$P_e = mE_1 I_1 \cos\gamma = mE_1 I_1 \sin\beta \tag{3.101}$$

where, *m* is the number of phase, γ is the electrical angle between the fundamental electromotive force of a phase E_1 and the fundamental rms stator current I_1, β is the angular displacement between the fields produced by the magnet and the stator current.

Substituting equation (3.96) into (3.101), we obtain

$$P_e = m\sqrt{2} K_{w1} N_w \omega_m r_s l_s \hat{B}_{g1} I_1 \sin\beta = m\pi K_{w1} f_1 N_w \hat{\Phi}_{g1} \hat{I}_1 \sin\beta \tag{3.102}$$

where, $\hat{I}_1$ is the amplitude of the fundamental current of a phase, $\hat{I}_1 = \sqrt{2} I_1 = \hat{i}_s$.

3.9. Electromagnetic Torque

There are several methods to calculate electromagnetic torque such as Maxwell'stress method, Virtual work method, power balance method, equivalent current sheet method, etc. For calculation of mean electromagnetic torque, the power balance method and equivalent current sheet method are preferred, because of the advantage of their simplicity. In this section, the mean torque expressions are given according to these two methods for the purpose of increasing understanding.

The relation between the instantaneous electromagnetic torque and the instantaneous electromagnetic power is expressed as [Hen 1994], [Sle 1994]

$$T_e(t) = \frac{p_e(t)}{\omega_m} = \frac{e_a i_a + e_b i_b + e_c i_c}{\omega_m} \tag{3.103}$$

Mean torque is calculated as,

$$T_e = \frac{P_e}{\omega_m} = \frac{P_e}{2\pi f_1 / p} \tag{3.104}$$

Substituting (3.102) into (3.104), we obtain

$$T_e = mK_{w1}N_w r_s l_s \hat{B}_{g1}\hat{I}_1 \sin\beta = \frac{mp}{2} K_{w1}N_w \hat{\Phi}_{g1}\hat{I}_1 \sin\beta \tag{3.105}$$

Apart from the method above, the electromagnetic torque can be calculated by means of the equivalent current sheet method [Sle 1992], [Sle 1993]. This method suggests that the stator winding is modelled as equivalent current sheets distributed over the stator slot opening [Hua 2011]. The linear current density or the electric loading is defined as total ampere per stator circumference. The torque-producing component of electric loading (assuming this component is the first harmonic component) can be written as, [Sle 1992], [Mil 1989]

$$K_1(\theta_s) = \hat{K}_1 \sin(p\theta_s - p\omega_m t + \beta) \tag{3.106}$$

where β is the angular displacement between the field produced by the magnet and the stator current, and $\hat{K}_1$ is the amplitude of the current sheet as

$$\hat{K}_1 = K_{w1}\frac{m(2N_w)\hat{I}_1}{2\pi r_s} \tag{3.107}$$

Assuming that only torque-producing components of the air gap flux density and electric loading contribute to mean torque. Therefore, according to Lozent's force method, the mean electromagnetic torque per volume unit can be expressed as [Sle 1992], [Mil 1989], [Pyr 2008]

$$T_V = 2\sigma = \hat{B}_{g1}\hat{K}_1 \sin\beta \tag{3.108}$$

where σ is the shear stress in the air gap, N/m^2.

Mean torque is equal to the air gap volume multiplied by the mean electromagnetic torque per volume as

$$T_e = \pi r_s^2 l_s \hat{B}_{g1}\hat{K}_1 \sin\beta \tag{3.109}$$

When substituting the equation (3.107) into (3.109), we obtain an equation that is identical to the equation (3.105). Two methods for calculating mean torque therefore give the same results.

3.10. Electrical Losses

Electrical losses in a PM machine include Copper loss, rotor eddy current loss and stator iron loss. These losses will be discussed briefly in this section.

3.10.1. Copper Loss

Copper loss is due to current flowing through wire. It is proportional to the resistance of the wire and the square of the current. Copper loss is calculated as

$$P_{Cu} = 3R_s I_1^2 \tag{3.110}$$

In equation (3.110), I_1 is the rms current running in the winding of a phase, R_s is the winding resistance of a phase, which is calculated according to equation (3.98). Note that resistance is a function of temperature as

$$R_{s(T)} = R_{s(20)}[1+\alpha_{Cu}(T-20)] \tag{3.111}$$

where, $R_{s(T)}$ is stator resistance at temperature T, $R_{s(20)}$ is stator resistance at temperature of 20^{o}C, and α_{Cu} is the temperature coefficient of Copper resistance.

3.10.2. Rotor Eddy Current Loss

Rotor eddy current loss in a PM machine includes magnet eddy current loss and rotor yoke eddy current loss. The eddy current losses are caused by the space harmonics of the stator windings, time harmonic current, and stator slotting. The analytical model for calculating rotor eddy current loss was well described in [Pol 2007], [Zhu 2004], so it is not presented here.

3.10.3. Stator Iron Loss

The stator iron loss model for FEM computation in Chapter 7 can also be used for the analytical model. In addition, the analytical model for stator iron loss was also well described by Polinder in [Pol 1998], so there is no need to mention the model here.

3.11. Design Constraint for Magnet Protection against Demagnetization

The PM machine should be designed to be able to withstand a demagnetizing field of the MMFs of current-carrying windings, which might cause partial demagnetization or total demagnetization of magnets. In this section, equations as constraints corresponding to different operations are given for the design of the PM machine in order to protect against demagnetization.

As mentioned in Chapter 2, when the maximum temperature of the magnet is small enough (<100 ^{o}C, this value depends on type of magnet), the demagnetization curve in the second quadrant is considered as a straight line, i.e., there is no knee point on the curve in the second quadrant. In this case, the magnet operates safely under any operating condition at a room temperature, if satisfying the equation that follows,

$$B_d \le B_m - \hat{B}_s \tag{3.112}$$

In the equation (3.112), B_d is the flux density at which the magnet is subject to total demagnetization. This value is about -0.2 T at a temperature of 20 ^{o}C. This value increases with increased magnet temperature. The maximum value of flux density in magnet B_m can be calculated according to equation (3.3), i.e., B_m=$B_{g,0}$. The maximum value of the flux density $\hat{B}_s$ produced in the magnet by the three-phase MMFs of stator windings alone can be approximately calculated by the fundamental value in equation (3.38), i.e., $\hat{B}_s = \hat{B}_{s1}$.

At high magnet temperature, a knee point emerges on the magnetization curve in the second quadrant. If the flux density of the magnet is smaller than that of the knee point, the magnet might be subject to partially demagnetize. In order for the magnet to avoid partially demagnetizing, the value B_d in the equation (3.112) is replaced by the flux density at knee point B_{knee}. In addition, the flux densities B_m and $\hat{B}_s$ are respectively replaced by the equations (3.3) and (3.38). Therefore, we have,

$$B_{knee} \le \frac{l_m}{l_m + \mu_{rm} k_c g} B_r - \frac{3}{2} k_{B1} \frac{\mu_0}{g'_{eff}} N_c \hat{i}_s \quad \text{or} \quad B_{knee} \le \frac{l_m}{\mu_{rm} g'_{eff}} B_r - \frac{3}{2} k_{B1} \frac{\mu_0}{g'_{eff}} N_c \hat{i}_s \tag{3.113}$$

where k_{B1} is the factor corresponding to the first harmonic in equation (3.38).

It should be noted that the remanent flux density of magnet decreases and the flux density of knee point increases with increased temperature of the magnet, as already discussed in Chapter 2.

To protect magnets from the three-phase short circuit, the amplitude of current in the equation (3.113) is replaced by the amplitude of short circuit current. This current is calculated as,

$$\hat{i}_{short} = k_s \frac{\sqrt{2}E_1}{\sqrt{(\omega L_s)^2 + R_s^2}} = k_s \frac{2K_{w1}N_w\omega_m \hat{B}_{g1} l_s r_s}{\sqrt{(\omega L_s)^2 + R_s^2}} \tag{3.114}$$

In equation (3.114), k_s is a factor accounting for the increasing amplitude of short current during the transient of three-phase short circuit. It is a function of ratio of winding resistance to reactance. According to [Cah 2005], [Mor 2007a], [Dub 2001], this factor is approximately equal to the value of 2. The E_1 is the fundamental rms EMF of a phase calculated according to (3.96), L_s is the synchronous inductance calculated as (3.66), and R_s is the stator-winding resistance of a phase calculated according to equation (3.111).

3.12. Sizing Equations

Generator design commonly requires a number of iterative processes so that using analytical equations can give a great insight into change of design parameters. In this section, the sizing equations are given for finding the starting point for the design of the PM machine. The further refinement of the design can be done by FEM computation.

There are many unknown parameters concerning the design of a PM machine so that it is necessary to fix some of them. The remaining parameters are determined by using sizing equations. The fixed parameters are as follows,

1) The number of phases m,
2) Rated torque and power,
3) Rated speed,
4) Rated voltage,
5) Current density J,
6) Number of poles $2p$,
7) Number of slots N_{slot},
8) Air gap length g,
9) Numbers of parallel branches of windings of a phase,
10) Ratio of interior diameter of rotor to length of rotor k_{sh}.
11) Slot opening depth h_0, and
12) Remanent flux density of magnets B_r.

The main sizing equations for the PM machine are summarized in Table 3.2. Once dimensions of the PM machine have been calculated, the volume and mass of components as well as of the whole PM machine can easily be derived, so equations for these quantities are not presented in this thesis.

Table 3.2. Main equations for finding the starting point of the design process of the PM machine.

Description	Expression
Shaping coefficient The coefficient is the ratio of the interior diameter of the rotor D_{ir} to the length of the rotor l_r.	$k_{sh}=D_{ir}/l_r$
Air gap shear stress σ (tangential force) per area unit. Note: σ_m is the value of the shear stress that permanent magnet material can suffer, for NdFeB magnet σ_m around 20-50 kPa. The k_{safe} is safe factor, k_{safe} =2÷3, [Bol 2005], [Hen 1994], [Pyr 2008], [Dor 2011].	$\sigma = \dfrac{0.5T_e}{\dfrac{\pi}{4}D_{ir}^2 l_r} = \dfrac{\sigma_m}{k_{safe}}$
Interior diameter of rotor D_{ir}	$D_{ir} = \sqrt[3]{\dfrac{2T_e k_{sh}}{\pi\sigma}}$
Length of rotor	$l_r=D_{ir}/k_{sh}$
Stator length l_s and stator diameter D_s	$l_s=l_r$, $D_s=D_{ir}$-$2g$
Magnet length in the radial direction Note: Lower mechanical limitation for magnet thickness is 2 mm. Common choice B_{g0} = (50%÷80%)B_r. For example, with B_r = 1.2 T, if $l_m = \mu_{rm}g_{eff}$, B_{g0} = 0.5B_r = 0.6 T; if $l_m = 4\mu_{rm}g_{eff}$, B_{g0} = 0.8B_r = 0.96 T.	$l_m = \dfrac{\mu_{rm} g_{eff}}{B_r / B_{g,0} - 1}$
Magnet width Note: k_m is the ratio of magnet width to pole pitch. For initial design, k_m =0.7÷0.75.	$w_m = k_m \dfrac{\pi D_{ir}}{2p}$
Tooth width w_t Note: The maximum flux density of tooth is in the range of 1.6÷1.8 T. The lower mechanical limitation for stator tooth width is 5 mm.	$w_t = \dfrac{\hat{\Phi}_{t1}}{l_s \hat{B}_{t1}}$
Slot opening	$b_s=2.g$
Stator yoke width h_{sy}	$h_{sy} = B_{g,0} w_m / (2B_{sy})$
The number of turn per phase Note: Assuming one parallel branch.	$N_w = \dfrac{U_1}{\sqrt{2}.K_{w1}\omega_m \hat{B}_{g1} l_s r_s}$
Diameter of Copper wiring d_{cu} Note: Current density J=5 A/mm^2 for natural air cooling and J=10 A/mm^2 for water cooling.	$A_{cu} = I_1/J$ $d_{cu} = 2\sqrt{\dfrac{A_{cu}}{\pi}}$
Average length of a turn l_{Cu}	$l_{Cu} \simeq 2\left(l_s + \dfrac{\pi}{2}\dfrac{(\tau_s + w_t)}{2} \right)$
Slot area A_{slot} Note: Filling factor k_{fill}.	$A_{slot} = \dfrac{2N_c A_{cu}}{k_{fill}}$
Slot top width Note: see Figure 3.4 for explanation of meaning of dimensions. Q is the number of slots. D_s is the stator diameter.	$w_{s2} = \dfrac{\pi(D_s - 2h_0 - 2h_1)}{Q} - w_t$
Slot bottom width	$w_{s1} = \sqrt{w_{s2}^2 - 4\pi\dfrac{A_{slot}}{Q}}$
Slot height h_s	$h_s = \dfrac{2A_{slot}}{w_{s1} + w_{s2}}$
Rotor yoke thickness h_{ry} Flux density of rotor yoke B_{yr} is in the range of 1.2÷1.8 T. This depends on the type of material in rotor yoke.	$h_{ry} = \dfrac{B_{g,0} w_m}{2B_{ry}}$

3.13. Influence of Magneto-Motive Force on Rotor Eddy Current Loss

The magneto-motive force of windings relates to the current-carrying conductor and configuration of windings. This influences electromagnetic torque, torque ripple, rotor eddy current loss, etc. By comparing MMF-harmonics of different windings, a rough comparison of eddy current losses in rotors during load can be made. In this way, the feasible combination of slot and pole numbers can be chosen for minimizing rotor eddy current loss. In addition, analysis results of harmonic components of MMF will be used to explain the calculation in Chapter 8. Therefore, in this section, MMF distribution and the harmonic components of typical winding configurations are investigated.

Again, it is assumed that the flux in the air gap due to the MMF is perpendicular to the surface of the stator. The MMF gets a positive value if the flux comes out of the tooth. On the other hand, the MMF gets a negative value if the flux goes into the tooth. The current direction in the coil and the direction of tooth flux produced should satisfy the corkscrew rule. Moreover, the slot opening effect is disregarded for more transparency in the analysis of MMFs. This assumption is to separate the influence of the slotting effect and the MMF harmonic components on rotor eddy current loss of the PM machine.

Five typically selected PM machines, namely machine 1 with 24-slot/16-pole, machine 2 (the reference machine B as mentioned in Chapter 2) with 27-slot/18-pole, machine 3 with 24-slot/20-pole, machine 4 with 27-slot/24-pole and machine 5 with 24-slot/28-pole, corresponding to slot/pole combinations of 3/2, 3/2, 6/5, 9/8 and 6/7 are used in this study. All PM machines have the same number of winding-turns per tooth.

The waveform of three-phase MMFs of each PM machine can be obtained by using equation (3.26). The MMFs are obtained when the current of phase *a* is equal to the amplitude $\hat{i}_s$, while the currents of phase *b* and *c* are equal to $-\hat{i}_s/2$, i.e., $i_a=\hat{i}_s$, $i_b=i_c=-\hat{i}_s/2$. The MMFs are normalized to maximum MMF, so the relative value of MMFs is in the range of -1 to 1, making comparison easy.

The analytical three-phase MMF and the harmonic component of the typical PM machines with concentrated windings are presented in Figure 3.10 to Figure 3.12. The MMFs of 27-slot/18-pole and the 24-slot/16-pole machines are nearly the same, because the machines have the same slot and pole combination, so that only the latter is presented in Figure 3.10. The MMFs of the 24-slot/20-pole PM machine (as shown in Figure 3.11) and the 24-slot/28-pole PM machine are identical, because they have the same slot number and winding layout.

As can be seen from Figures 3.10 to 3.12, the three-phase MMF of PM machines with concentrated windings has high harmonic components that include both odd and even harmonic components. During normal operation, the torque-producing component of MMF ideally rotates in synchronism with the rotor magnet field. Their interaction creates the electromagnetic torque of a PM machine. The rest of MMF-components cause undesired effects. As can be seen from Figure 3.10 for machine 1, the 1st (the fundamental, also torque-producing), 2nd, 4th, 5th, 7th and 8th are the dominant space harmonics. However, only the 1st space harmonic interacts with the magnet field to produce continuous torque. This is shown in Figure 3.11 for machine 3 with the 24-slot/20-pole combination that the 1st (sub-harmonic), 5th (torque-producing), 7th, 17th and 19th are the dominant space harmonics. The MMF-distribution of machine 5 is also presented in Figure 3.11, however, the 7th harmonic is the torque-producing component and the 1st and 5th components are the sub-harmonic. The amplitude of the 5th sub-harmonic is higher than that of the 7th torque-producing component. Therefore, it is predicted that machine 4 will have a high rotor eddy current loss during load. In the case of machine 4 (presented in Figure 3.12) the 1st (sub-harmonic), 2nd (sub-harmonic), 4th (torque-producing), 5th, 13th and 14th are the dominant space harmonics for this winding type. In summary, the MMF of the machines 3, 4 and 5 has sub-harmonics, while the MMFs (see Figure 3.10) of conventional PM machines (machine 1 and machine 2) do not have them. On the other hand, the MMF-harmonic amplitude of machines 3, 4 and 5 are generally higher than the traditional ones. Therefore, it is predicted that machines 3, 4 and 5 will have higher rotor eddy current loss than the conventional machines. It is predicted that machine 5 will have the highest rotor eddy current loss because of very high amplitude of sub-harmonics. Machines 4 (having two sub-harmonic components) and machine 3 (having a sub-harmonic) are predicted to have the second and the third highest rotor eddy current loss, respectively.

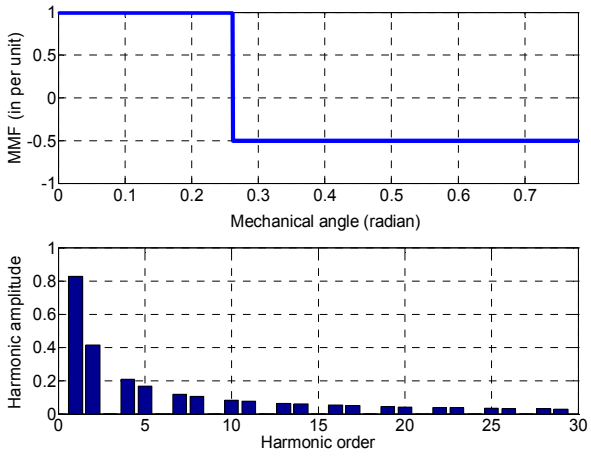

Figure 3.10. Three-phase MMF and the harmonic components of the 24-slot and 16-pole PM machine.

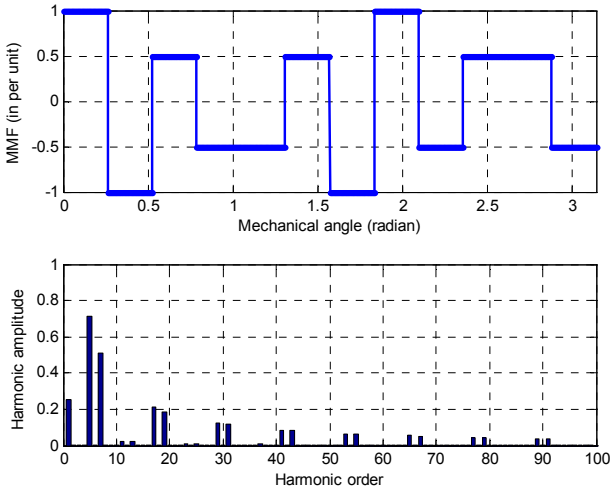

Figure 3.11. Three-phase MMF and the harmonic components of the 24-slot and 20-pole PM machine.

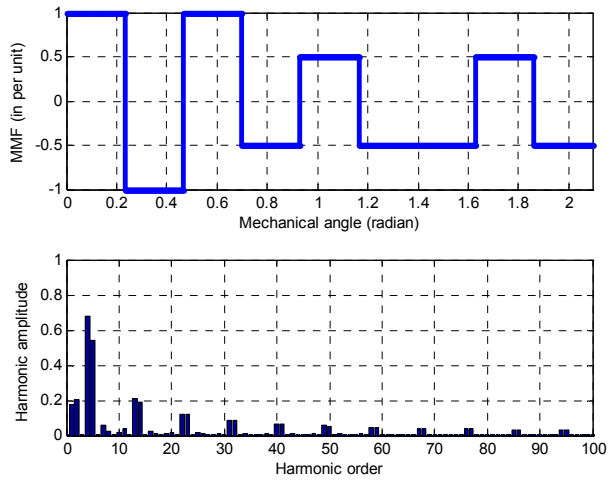

Figure 3.12. Three-phase MMF and the harmonic components of the 27-slot and 24-pole PM machine.

3.14. Conclusions

In this chapter, the analytical model for fast analysis and the initial design of the PM machine were presented. For initial design purposes, the researcher paid attention to the fundamental component rather than the harmonic components. The principle of superposition has been used for calculation of the magnetic field. Accordingly, the magnetic fields in the air gap and magnets were separately calculated for two cases, namely the magnetic field produced by magnets and the magnetic field due to current-carrying windings. The total magnetic field was obtained by adding the two magnetic fields.

The equations of air gap flux density produced by magnets, flux per pole and flux passing through a tooth were derived. Based on these equations, internal voltage expression of the PM machine can be calculated.

The armature field and other armature quantities such as the turn function, the winding function, the winding factor, MMFs and inductances were investigated. The distribution of flux density due to current-carrying windings alone and the three-phase MMFs in the air gap can be calculated through the winding function instead of using equivalent magnetic circuit. This helps to make the calculation of the magnetic field in air the gap more convenient.

The equations of self-inductance, mutual inductance and main synchronous inductance of PM machines with different combinations of slot and pole were presented and summed in Table 3.1. It was shown that the PM machine with a slot and pole combination of 3/2 has a mutual inductance equal to a half of the self-inductance. The PM machines with slot and pole combinations of 6/5 and 6/7 have no mutual inductance, while the PM machine with a slot and pole combination of 9/8 has a mutual inductance much smaller than the self-inductance.

General equations for calculating electromotive force, voltage, mean electromagnetic power, mean electromagnetic torque and losses were given in Section 3.6 to Section 3.10. These equations can be used for analysis of PM machines with different combinations of slot and pole. For increasing insight into the relation of mean electromagnetic torque and other quantities, mean torque equations were given according to the two methods, namely the power balance method and the equivalent current sheet method.

The design constraints for the design of the fractional-slot concentrated winding PM machine with magnets protected from demagnetization were investigated in Section 3.11. In addition, equations were developed for different operation modes such as maximum torque and three-phase short-circuit at room temperature or critical temperature of magnets.

The sizing equations for initial design of the PM machine were derived. The main sizing equations were summarized in Table 3.2.

To select a concentrated winding layout for a PM machine, the MMF harmonic component is an important criterion, as is the fundamental winding factor. The MMF-harmonic component is important because it influences rotor eddy current loss. The rotor eddy current loss of PM machines due to the MMFs was predicted in Section 3.13 after the MMF harmonics of different layouts of concentrated windings were compared. This provided a quick insight into the influence of winding configurations on rotor eddy current loss.

CHAPTER 4

NUMERICAL MODEL

4.1. Introduction

The analytical model for initial design, which provides a quick insight into the effect of design parameter variations was developed and described in Chapter 3. The main disadvantage however, is that the model is not very accurate. This is because it is hard to take slotting, fringing, and magnetic saturation effects into account. Therefore, a FEM model, based on the analytical model, is required for refining the design. Stationary FEM is sufficient for taking into account slotting, fringing, and saturation effects, but transient FEM including rotor motion is required for calculating eddy current loss. In this chapter, the focus is on developing an automated nonlinear transient FEM model including rotor motion of PM machines with concentrated windings.

The transient FEM based model is known to be accurate in calculation. It is, however, time-consuming. It can take days to do the design optimization. Especially, the three-dimension transient FEM (3D-FEM) model takes hours to compute the performance of a PM machine corresponding to an electric cycle if using a personal computer. In the near future when personal computers become more powerful, the 3D-FEM based design optimization of PM machine will likely still be time-consuming. Therefore, in this thesis, almost all results are obtained from the 2D-FEM simulation.

In this chapter, first of all, equations of electromagnetic field, flux linkage, and internal voltage are derived for FEM computation. Automated-nonlinear-transient-FEM-program including rotor motion is developed. The nonlinear transient FEM model including rotor motion is coupled with the circuit model. This results in a field-circuit coupled model. The method for a FEM program which converges and runs faster during deep magnetic saturation is also discussed. The demagnetization model is developed to ensure that the designed PM machine avoids demagnetization. Finally, conclusions are drawn. An overview of main contents of this chapter is presented in the following flowchart.

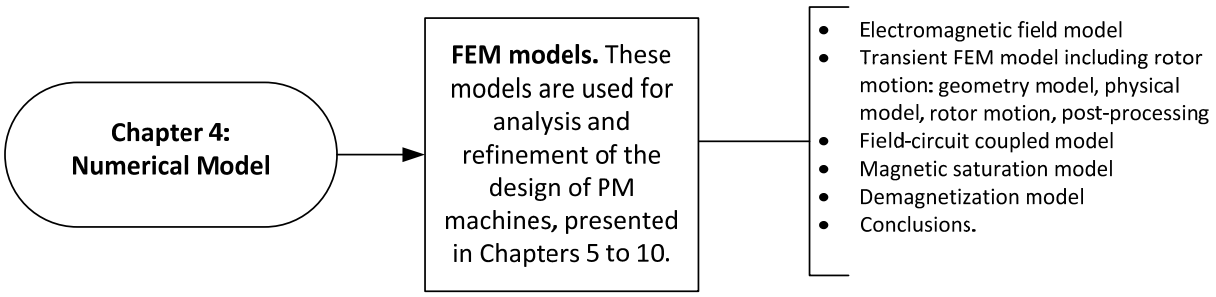

Figure 4.1. Outline of this chapter.

4.2. Electromagnetic Field Model

4.2.1. Governing Electromagnetic Field Equation

In general, the electromagnetic field equation of the domain of a PM machine in two dimensions can be written as [Pyr 2008], [Jab 2004], [Com 2010]

$$\nabla\times(\mu^{-1}(\nabla\times\vec{A}_z-\vec{B}_r))+\sigma\frac{\partial\vec{A}_z}{\partial t}=\vec{J}_{s,z}-\sigma\nabla\varphi \tag{4.1}$$

where, $\vec{A}_z$ is the magnetic vector potential in the z-direction, $\vec{B}_r$ is the vector remanant flux density of magnets, $\vec{J}_{s,z}$ is the current density of external source in the z-direction, φ is the electric scalar potential, μ is the permeability of the material, and σ is the electric conductivity. With nonlinear material, μ is a function of the flux density.

4.2.2. Flux Linkage and Induced Voltage

The flux linkage ϕ through a turn of a winding and the induced voltage e of a turn can be calculated in 2D-FEM as [Jab 2004], [Pyr 2008]

$$\phi=\frac{L}{S}\left(\iint_{\Omega^+}A_z d\Omega-\iint_{\Omega^-}A_z d\Omega\right) \tag{4.2}$$

$$e=-\frac{\partial\phi}{\partial t} \tag{4.3}$$

where L is the length of the conductor, Ω^+ and Ω^- are integration areas corresponding the go and return sides of equivalent conductors of the stator windings, and S is cross section area of the equivalent conductor.

4.3. Finite-Element-Model for PM Machines

In this section, firstly, a concept in the form of flow chart, based on the transient FEM model including rotor motion is proposed for the design and analysis of the PM machines. Then, procedures for establishing a two-dimension transient FEM program including rotor motion will be presented. Finally, a three-dimension FEM model is briefly introduced.

4.3.1. Proposed Flow Chart for Analysis and Design of PM Machines

In Figure 4.2, we propose a concept in form of a flow chart for analyzing and designing permanent magnet machines. When using the concept presented in the flow chart for analyzing a certain PM machine, the repeating branch in the left of the flow chart could be ignored. According to the flow chart, FEM software such as COMSOL® is linked with Matlab® and program runs on Matlab. Dimensions of the PM machine (pole number, teeth dimension, permanent magnet dimension, etc) are initial data for calculating the coordinates of the points. Then, Matlab program draws the necessary lines or arcs or circle necessary and lastly edits them. In this way, the geometry modeling of the PM machine is automatically made. The boundary conditions and the nonlinear transient FEM program including rotor motion can also be fully done by a script based on Matlab's command set. It can therefore save time in the analysis and design of electric machines. Truly, in order to solve the optimization problems, the designers have to adjust dimensions of the machine constantly. This procedure is time consuming and stressful for the designer if he does not use the automated FEM program. The nonlinear transient FEM program including rotor motion will be used for surveying performances of concentrated winding exterior rotor PM machines in this chapter and the next chapters.

4.3.2. 2D Transient FEM Model Including Rotor Motion

FEM model can implement for the whole PM machine. However, in order to FEM program runs faster and takes less memory, the symmetrical property or anti-symmetrical property of a PM machine should be utilized. If so, instead of simulation for whole of the PM machine, FEM analysis only needs to do for one section. For example, utilizing symmetrical property of the reference PM machine B with 27 slots and 18 poles, only a section corresponding to one ninth of the PM machine is simulated. Main procedures to establish FEM simulation for the PM machines are presented as follows.

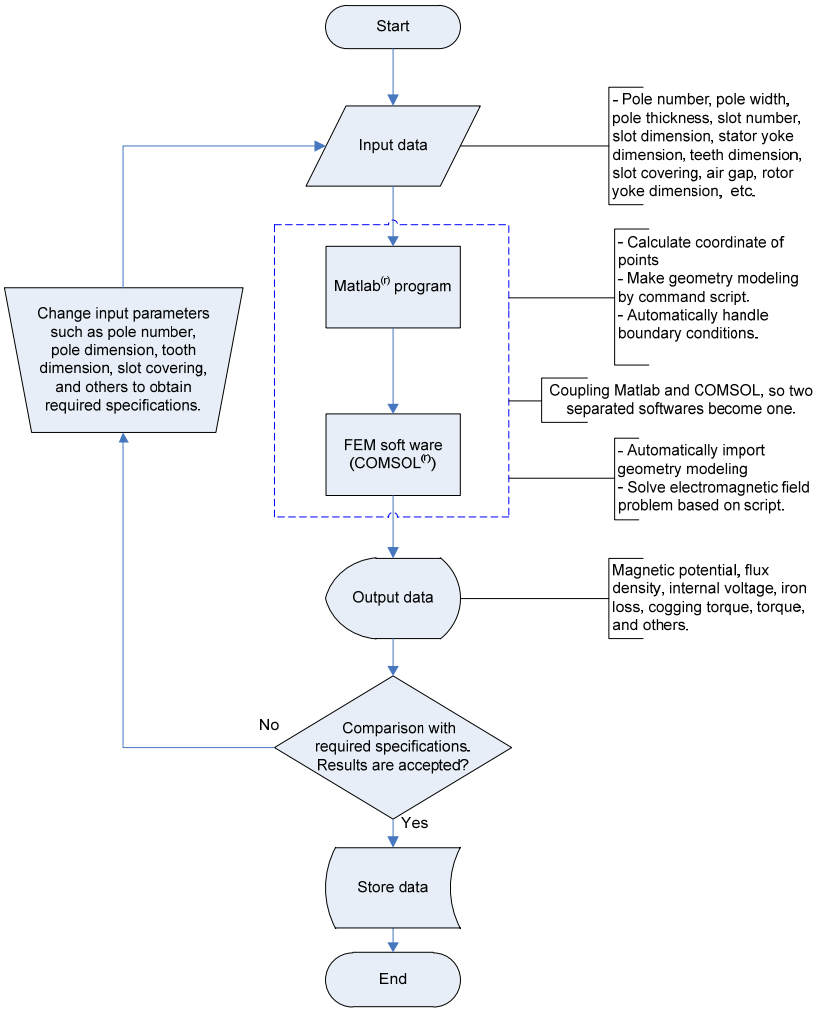

Figure 4.2. Flow chart for analysis and design of PM machines based on nonlinear transient FEM including rotor motion.

4.3.2.1. Geometry Model

Geometrical model can be made by script or using user interface of FEM software, or a combination. However, in order to make the program more flexible, it is suggested that all steps of the program should be taken by script. Figure 4.3 presents geometry of a section of the reference PM machine B of which the main dimensions were presented in Chapter 2.

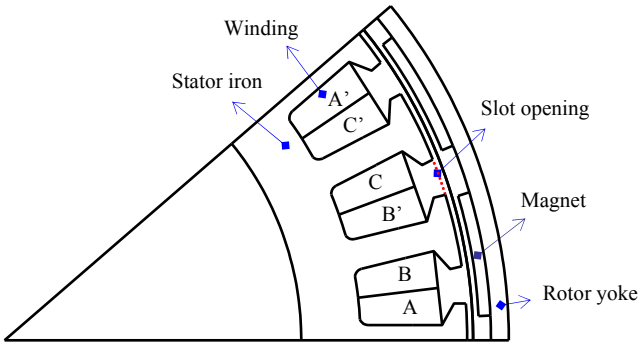

Figure 4.3. Geometry of a section of the reference PM machine, where A-A', B-B' and C-C' represent the three-phase coils.

4.3.2.2. Physical Model

a) Winding Model

This section illustrates method used to make a model for windings of a 27-slot/18-pole PM machine. This concept can be extended to apply to other winding configurations.

Windings of the reference PM machine have 27 coils. Each phase has nine coils, which are divided in to three parallel branches. Therefore, each branch of a phase has three coils connected in series. The three-phase winding system is a star connection.

The electric angle between adjacent slots is 120^{o}. Thus, the structure of windings has order: AA', BB', CC'..., where A, B and C represent conductors and A', B' and C' represent the return conductors of phase *a*, *b* and *c* respectively. Each coil is approximately modeled by an equivalent concentrated turn. Electric current of the equivalent concentrated turn in the FEM model should be satisfied the equation, $i=i_r.N_c$; where, i_r is rated electric current running in a coil, N_c is the turn number of a coil, and i is the equivalent electric current that is setup in the model. Current density $J_{s,z}$ in equation (4.1) is set up in the model as $J_{s,z}=i/S$, where S is a cross-section of the equivalent conductor in the model.

b) Magnet Model

The direction of magnetization of the permanent magnets of the studied PM machine is in the radial, so it can be modeled in the xy-coordinate with the root of co-ordinate at the centre of the PM machine. This can be expressed as,

$$\vec{B}_r = sgn(\vec{B}_r)\,|\,B_r\,|\left(\frac{x}{\sqrt{x^2+y^2}},\frac{y}{\sqrt{x^2+y^2}}\right) \tag{4.4}$$

where, 'sgn' is the signal function, $sgn(\vec{B}_r)=1$ if the vector $\vec{B}_r$ goes into the surface of the magnet and $sgn(\vec{B}_r)=-1$ if the vector $\vec{B}_r$ comes out of the surface of the magnet.

c) Boundary Condition

There are some types of boundary conditions used in the FEM model as shown in Figure 4.4. They are described as follows.

- Continuity boundary conditions (continuity of the tangential component of the magnetic field): $\vec{n}\times(\overrightarrow{H_1}-\overrightarrow{H_2})=0$, where $\vec{n}$ is the normal vector of the point on the boundary.
- Magnetic insulation: $A_z=0$.
- Periodic conditions: For continuity-periodic boundary conditions, we have an equation $A_{src} = A_{dst}$, where A_{src} and A_{dst} are the vector magnetic potential of the source boundary and the destination boundary respectively.
- Identity pairs: For symmetrical sectors, we have $A_{src}(\theta)=A_{dst}(\theta-s2\pi/n_{sec})$, where s=0,1,2…, n_{sec} is the number of sections, and θ is the mechanical angle in the stator reference.

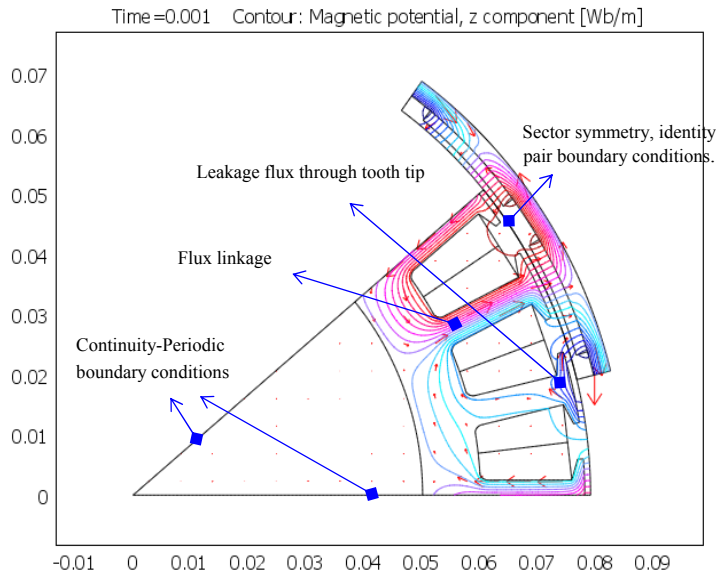

Figure 4.4. The magnetic vector potential contours of the PM machine and boundary conditions, during no-load.

d) Rotor Motion

To take into account rotor motion, the Arbitrary Lagrangian-Eulerian (ALE) method is used [Jab 2004]. When using the method, the meshes of the motion part are not deformed [Com 2010]. The

FEM model is divided into two parts, namely motion part (rotor) and stationary part (stator). The motion and stationary parts are linked together using the symmetrical identity pairs. During computation, the moving part slides over the stationary part at the rotor speed.

4.3.2.3. Meshing

The number of mesh points influences the accuracy of numerical calculations. If meshes are coarse (the number of degree of freedom is low), the computation accuracy is low. The FEM program with a coarse mesh however takes less time than that with a finer mesh. Normally, the FEM program is made in compromise between accuracy and time-consuming. Meshes of the air gap layer need to be small enough to guarantee the accuracy. The mesh of the rotor area should also be made fine enough to catch eddy current induced in it. Regarding the domains are less important i.e., the air hollow inside the stator, meshes can be made rougher to program running faster or remove from the model as done in Chapter 10. Figure 4.5 is an example illustrating the technique used to make meshes for the FEM model of the reference PM machine with 27slots and 18 poles.

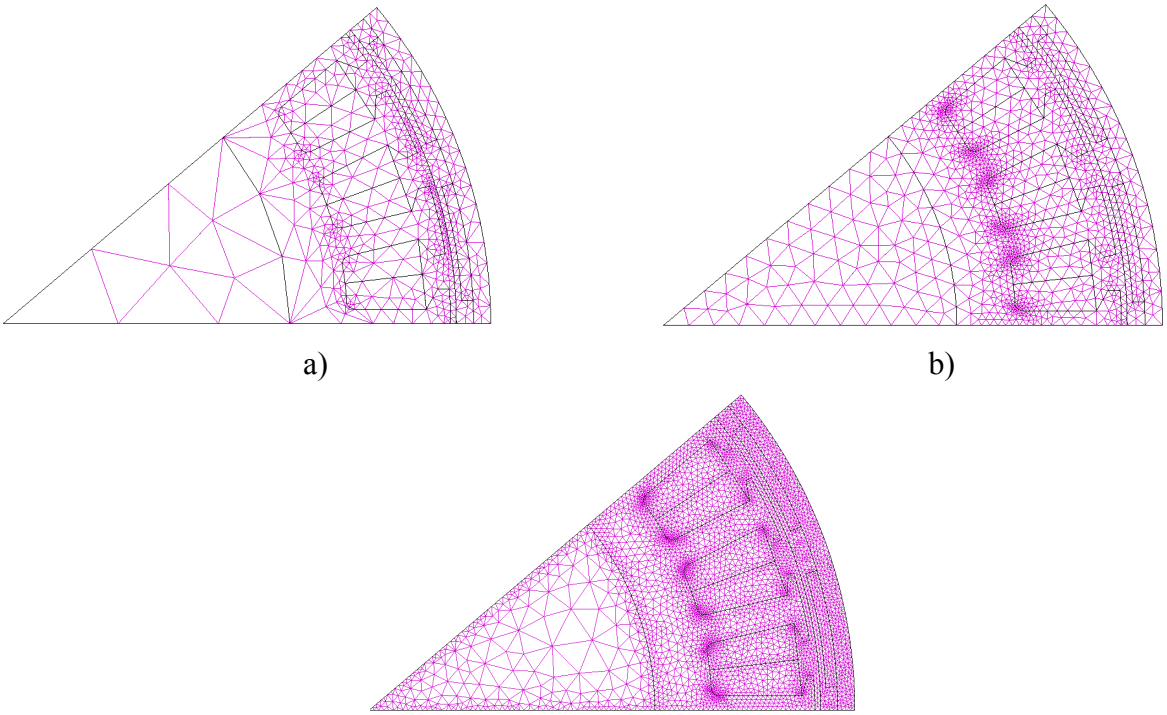

Figure 4.5. FEM meshes of a section of the reference PM machine B: a) coarse meshes, b) intermediate meshes, c) fine meshes for important subdomains, preferred in this study.

4.3.2.4. Solving

For time-stepping procedures, there are two main parameters: simulated time interval and number of time-steps. Normally, the time length is equal to the time cycle of the fundamental internal voltage. However, in the certain cases, the time length can be shortened so that less time is consumed during simulation. Meanwhile, the number of steps is determined according to our testing experience for the specific case. If the time step is too large, it leads to an increase in errors in the post computation. For the reference PM machine, the number of time steps is about 200.

For a non-linear transient FEM program, an efficient solver is the Newton-Raphson method with the Jacobian matrix updated on every iteration. In order for the program to converge, the FEM program must go through several steps: first, the program is solved with the iron permeability constant in stationary mode to get the initial point for the nonlinear stationary mode; then, it is solved with a BH-curve in the stationary mode to get the initial point for transient mode; and finally, the program runs with the BH-curve in transient solution.

4.3.2.5. Post-Processing

Once the vector magnetic potential has been found by solving equation (4.1), the flux density, induced voltage, electromagnetic torque, eddy current loss, and stator iron loss of a PM machine can be derived. These procedures are called post-processing. Figure 4.6a shows the FEM simulation of the entire reference PM machine, while Figure 4.6b shows the FEM simulation of a section of the PM machine. The FEM model for a section uses identity boundary conditions and periodic boundary conditions, therefore the electromagnetic field of this section is identical to that of other sections, and it represents the whole of the PM machine. More results of the post-processing will be presented in the sections below and in the next chapters.

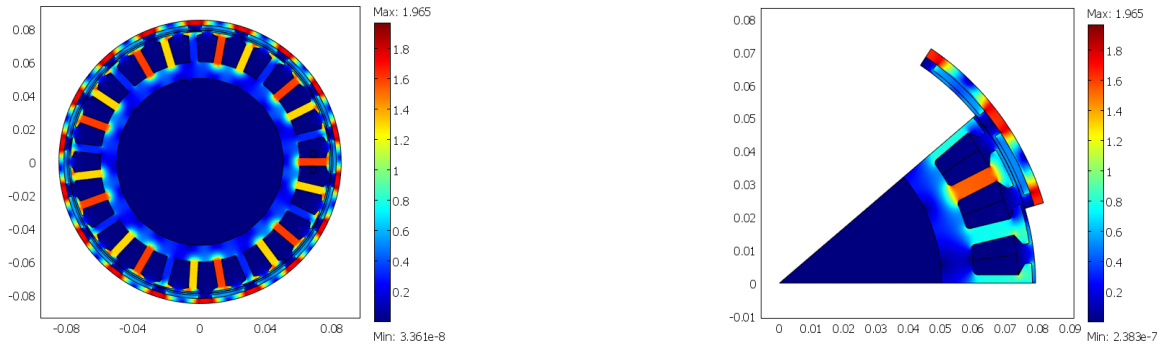

a) b)

Figure 4.6. FEM simulation of a 27-slot/18-pole PM machine B during no-load: a) FEM model for whole of the PM machine, b) FEM model for only one section corresponding to one ninth of the PM machine.

4.3.3. 3D-FEM Model

A three-dimension FEM (3D-FEM) model is apparently more accurate than a 2D-FEM model. A 3D-FEM model takes the end effects of winding and magnet into account, which are neglected in the 2D-FEM model. However, a stationary 3D-FEM computation with multiple rotor positions and a transient 3D-FEM computation are very time-consuming. They require a powerful computer with a large memory and high speed processors. For design optimization, a large number of iterations are required to find the optimal solution. Therefore, at present, the 3D-FEM model is not suitable for design optimization. On the other hand, the comparison of simulation and experimental results in Chapter 10 shows that the 2D transient FEM including rotor motion is sufficiently accurate for calculating magnetic field, voltage, torque, and stator iron loss. Therefore, in this thesis, almost all results are extracted from the 2D transient FEM model.

Figures 4.7 and 4.8 present the 3D-distribution of flux density of a 27-slot/18-pole PM machine during no-load using the stationary 3D-FEM computation. Figure 4.7 depicts the entire PM machine, while Figure 4.8 depicts a section only.

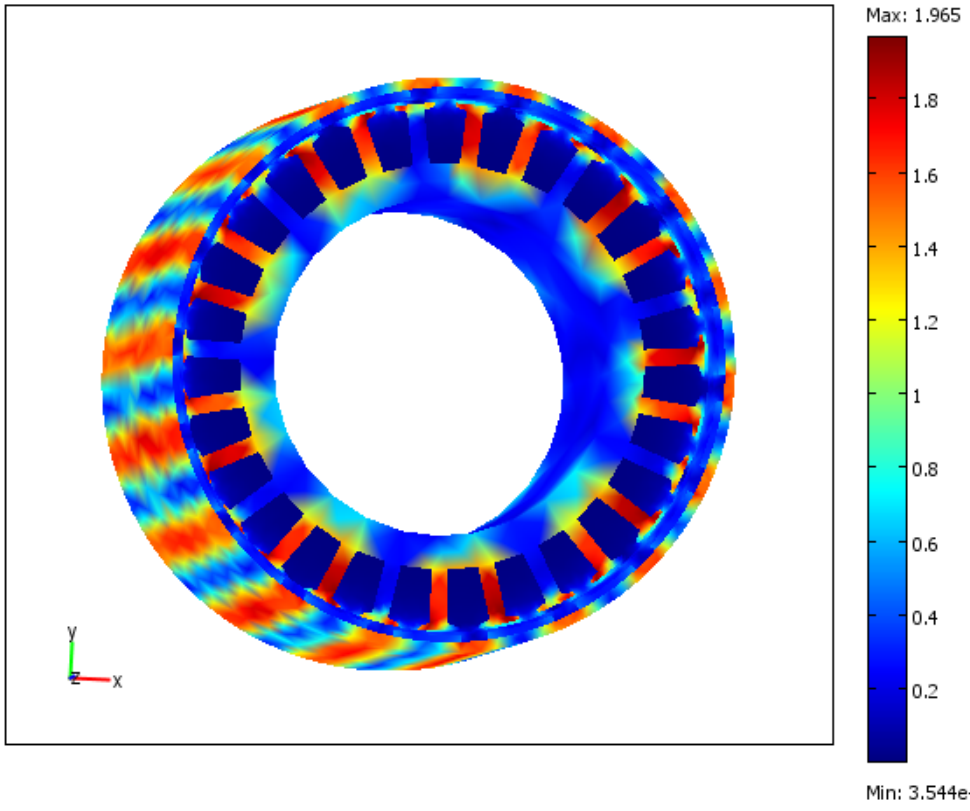

Figure 4.7. The 3D-distribution of no-load flux density in a 27-slot/18-pole PM machine.

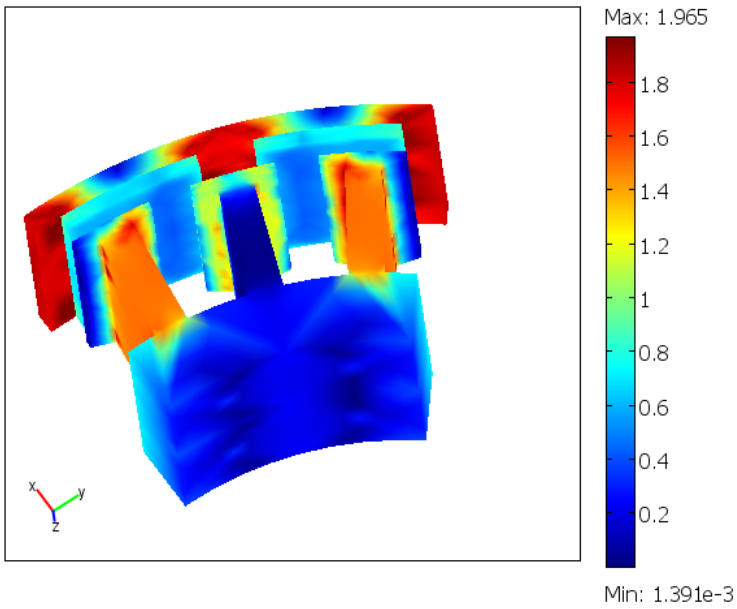

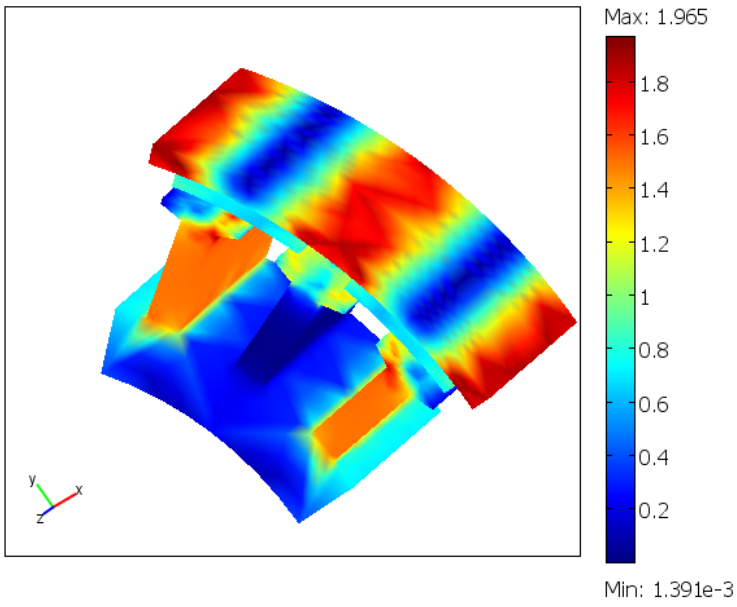

Figure 4.8. The 3D-distribution of no-load flux density in a section of a 27-slot/18-pole PM machine.

4.4. 2D-Field Circuit Coupled Model

a) Field-Circuit Coupled Model for Calculating Eddy Current

To calculate magnetic vector potential in magnets in 2D-FEM and to satisfy equation (4.5), i.e. eddy current circulation in the magnet, it is necessary to solve equation (4.1) coupled with the circuit equation (4.6),

$$\iint_S \vec{J}_{e,z} dS = \iint_S \left\{ \sigma(-\frac{\partial \vec{A}_z}{\partial t} - \nabla \varphi) \right\} dS = 0 \tag{4.5}$$

or

$$\vec{I}_{i,z} + \vec{I}_{u,z} = 0 \;\; => \;\; \vec{J}_{i,z} + \vec{J}_{u,z} = 0 \tag{4.6}$$

where,

$$\vec{J}_{i,z} = \frac{\vec{I}_{i,z}}{S_m} = -\frac{1}{S_m} \iint_S \sigma \frac{\partial \vec{A}_z}{\partial t} dS \tag{4.7}$$

$$\vec{J}_{u,z} = \frac{\vec{I}_{u,z}}{S_m} = -\frac{1}{S_m} \iint_S \sigma \nabla \varphi dS \tag{4.8}$$

where S is the surface of integration, S_m is the cross section area of the magnet in the axial direction. $I_{i,z}$ is the induced current in the z-direction and $I_{u,z}$ is the unknown current in the z-direction, $J_{e,z}$ is the total eddy current density in the z-direction, $J_{i,z}$ is the averaged induced current density in the z-direction due to the rotational electric field strength vector and $J_{u,z}$ is the averaged unknown current density in the z-direction due to the electric scalar potential. Instead of applying the gradient of the electric scalar potential $\nabla\varphi$ into equation (4.1), we apply $J_{u,z}$ as an external current density on the domain of the magnet. Once the magnetic vector potential has been found by solving equation (4.1), the averaged induced current density $J_{i,z}$ can be calculated from equation (4.7). Then, $J_{u,z}$ can be found by solving the equation (4.6). We thus arrive at a field-circuit coupled model [Ger 2004], [Lah 2001].

It should be noted that the above equations from (4.5) to (4.8) are only necessary when calculating eddy current loss. Otherwise, the electric scalar potential can be neglected.

b) Field-Circuit Coupled Model for Calculating Performance during Load

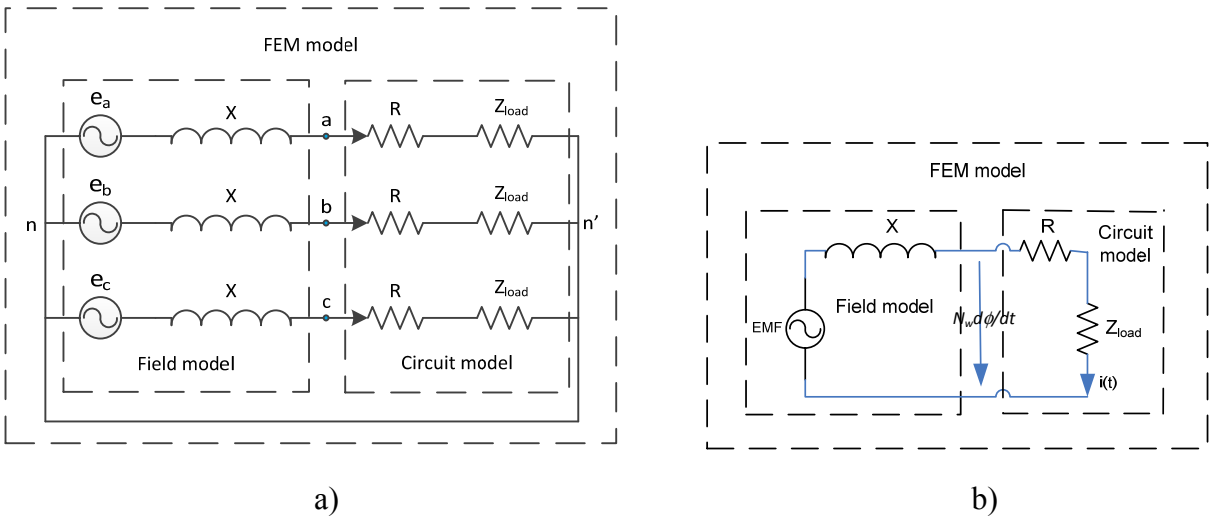

a) b)

Figure 4.9. Principle of field-circuit coupled model; a) three phases; b) one phase.

To take into account the influence of load property (viz., including both current amplitude and current angle) and the winding resistance, a symmetrical three-phase load circuit should be coupled to the FEM electromagnetic model of the three-phase PM machine as shown in Figure 4.9a. This forms the field–circuit coupled model. It is assumed that

- the winding of the PM machine as well as the three-phase load is a star connection; and
- either the neutral points of the winding of the PM machine and load are connected together or the three-phase voltage system is symmetrical, i.e., $u_a+u_b+u_c=0$.

With assumptions above, the principle of the field-circuit coupled model can be applied for the phases separately. The principle is simplified for one phase as shown in Figure 4.9b. In the figure, R is winding resistance of a phase, Z_{load} is impedance of load under test, N_w is the number of turns of a phase assuming that the winding has one parallel branch. Calculation of the slot/pole combination of 3/2 (other combinations of slot and pole can be adapted from the following description) is described as,

(1). The field model is used to calculate total flux ϕ through a tooth

(2). The circuit model is used to calculate the electric current of a phase by solving the following differential equation,

$$i+\frac{L_{load}}{(R+R_{load})}\frac{di}{dt}=\frac{1}{R+R_{load}}N_w\frac{d\phi}{dt} \tag{4.9}$$

where, L_{load} and R_{load} are the inductance and resistance of the load.

(3). The calculated current is applied to stator windings in the FEM model.

4.5. Magnetic Saturation Model

To consider magnetic saturation, either an analytical function of the measured BH curve or a data table of the measured BH curve is used. A transient FEM program using analytical function runs faster than using the data table of the measured BH curve. Because the FEM program using analytical function does not need to interpolate and extrapolate as using the data table of the measured BH curve. In addition, the speed of convergence of the program (using the iteration method of Newton-Raphson) depends on the smoothie and slope of the BH curve. Through our experiments, it was found that the more the analytical function is similar to the measured BH curve, the more time the program takes to run. Therefore, a compromise for this issue can be found by selecting a reasonably analytical function of BH curve. Figure 4.10 illustrates the measured BH curve of iron material and some BH-analytical functions. With the analytical function as shown by curve (4) in Figure 4.10, the FEM program runs fast. When using curves (2) and (3), the FEM program runs more slowly than when using curve (4). If using the data table of the measured BH curve, the program takes 12 minutes to calculate one electric cycle, with configuration of the computer as (2.3 GHz, duo CPU, 3.5GB of RAM). If using the analytical BH curve (4), the program takes 7 minutes. If using the analytical BH curve (3) (or curve (4)), the program takes 8 minutes (9 minutes). Therefore, if 20 iterations are needed to refine results, 60 to 100 minutes will be saved in comparison with using the data table of the measured BH-curve.

In fact, there is always discrepancy between the BH-analytical function and the measured BH curve, so the solution using the analytical function always has certain error. However, it can be used when the air gap length and/or magnet thickness are big enough such as in flywheel applications. Figure 4.11 compares simulation and experimental results of internal voltage, using different BH curves for stator iron lamination in simulation. Generally, simulation and experimental results are in good agreement regarding amplitude. When playing with simulation it is shown that magnetic saturation in the stator iron influences simulation results more than magnetic saturation in rotor yoke does.

The FEM programs of a PM machine always work well with the data table of the measured BH curve in static solution. A static FEM model can also be used to calculate performance characteristics of a PM machine. It is especially useful in the case of problems which are difficult to solve in dynamic mode, for instance, the analysis of a PM machine with eccentric rotor. However, it is consumed time to calculate one cycle of internal voltage using this method and rotor eddy current effect is not taken into consideration.

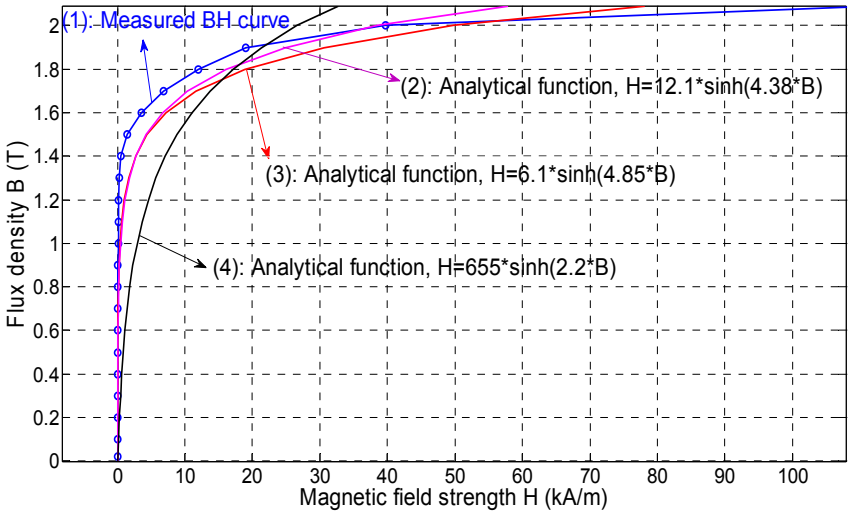

Figure 4.10. BH curve models of lamination iron.

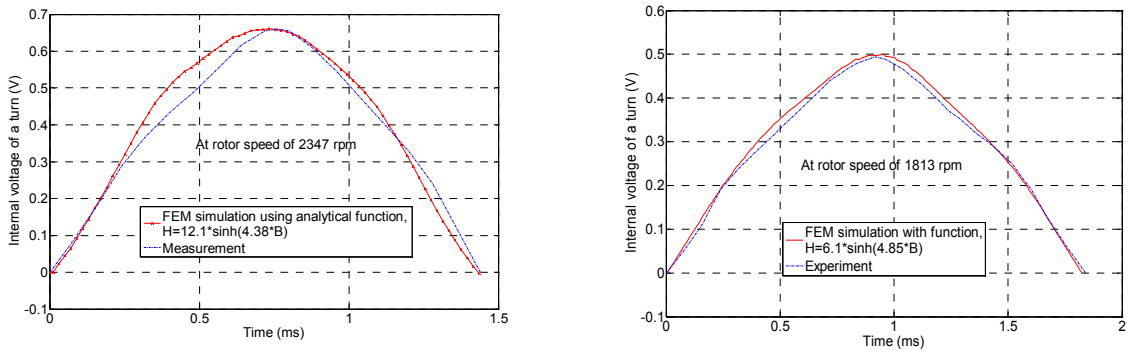

a) b)

Figure 4.11. Comparison of simulation and experiment of internal voltage of a turn, using the BH-analytical function.

4.6. Demagnetization

In this section, first, demagnetization issues will be discussed. Then, the approach to demagnetization analysis is investigated. Finally, some demagnetization analyses for the PM machine B are presented.

The armature reaction in a PM machine can cause the partial or total demagnetization of the magnets. In normal operation, the current is limited by the control drive so that if the magnet thickness and coercivity were sufficiently large, there is no risk of demagnetization. However, abnormal operating conditions such as short circuit can produce large current, which may be

several times larger than the rated current. Therefore, it is important to assess demagnetization of the magnet in the worst case. The worst case is assumedly associated with the maximum working temperature and the transient of the three-phase short circuit. The maximum temperature of magnets in the small-scale ship application is limited at 150°C. At this temperature, the knee point of the demagnetizing characteristic of Neodymium magnets comes into existence. For example, in the Figure 4.12, the knee point of magnet material Neorem 576a at 150 °C has the coordinate of 560 kA/m and 0.3 T.

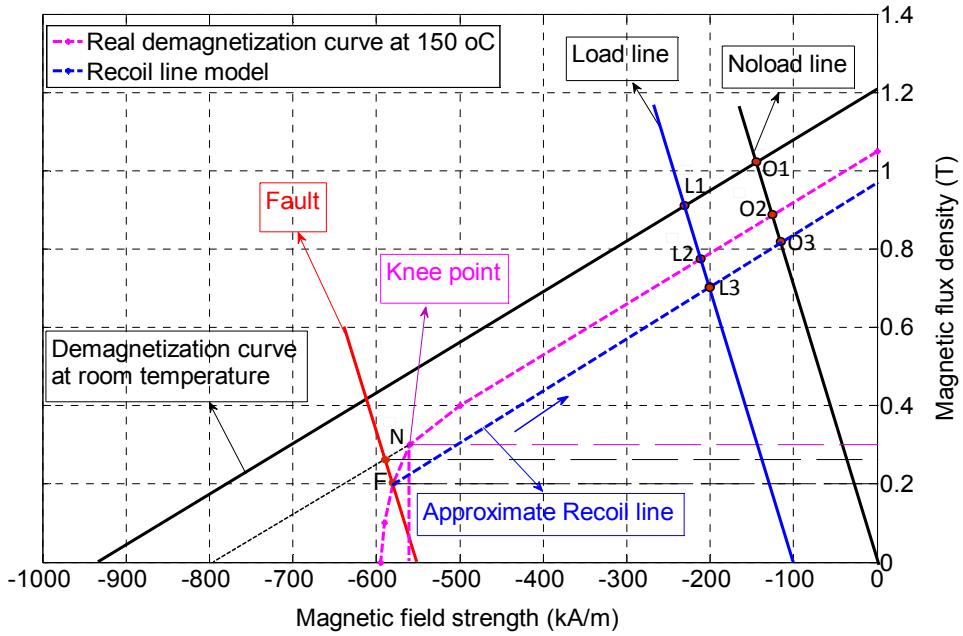

Figure 4.12. Demagnetization curve at different temperatures of a Neodymium magnet (Neorem 576a).

In order to ensure that magnet is not partially demagnetized, the intersection of the load line and the demagnetization curve should be higher than knee point N at maximum working temperature, for example in Figure 4.12, working point L2 is higher than the knee point N. For simplicity, the linear model is chosen for checking the demagnetization of the designed PM machines. At room temperature, the BH curve in the second quadrant is modeled as a straight line that is determined by remanent flux density and intrinsic coercivity. When the magnet temperature is high enough, the knee point emerges on the BH curve in the second quadrant. In this case, the BH curve in second quadrant is modeled as straight line that is determined by remanent flux density and coordinate of knee point at the working temperature. In this section, the distribution of flux density on surface of magnet with respect to time and mean flux density of a magnet (calculated as equation (4.10)) are used to assess the demagnetization level of the magnet. If the flux density in any area of a magnet is smaller than that of knee point, the magnet

suffers partial/totally demagnetization. The mean of radial flux density in the magnet at a certain time is calculated as,

$$B_{mean} = \frac{1}{S_m} \iint_S B_n dA \tag{4.10}$$

where, S_m is the area of the cross-section of the magnet, S is integration surface, and B_n is the normal (radial) component of flux density.

Some analyses of the 27slots/18 poles PM machine B during different operation conditions are presented as follows. Note that the worst operation condition is defined as: three-phase short circuit and maximum working temperature of magnet of 150 ^{o}C.

Figure 4.13 shows the flux density distribution on the surface of a magnet at different times, during three-phase short circuit, using a demagnetization curve at 150^{o}C. To implement the simulation of the three-phase short circuit, a field-circuit coupled model is used. The FEM model is linked to a three-phase winding resistor. It is shown from Figure 4.13 that in the area of dark-blue, the magnet is subject to partial demagnetization, because its flux density is smaller than that of knee point of 0.3 T. Figure 4.14 presents the mean flux density of south-pole magnet (the first magnet) and north-pole magnet (the second magnet). At time instants, the mean flux density is smaller than that of knee point. This means that the working point is lower than the knee point, for instance point F in Figure 4.12, so that almost the whole area of the magnet is subject to partial demagnetization. Even when the mean flux density of the magnet is greater than the flux density of knee point, some areas of the magnet probably have a flux density smaller than that of knee point; so the magnet still suffers partial demagnetization. Therefore, it is suggested that the FEM simulation of flux density distribution in magnets (as shown in Figure 4.13) should always be carried out in order to check and make sure that the flux density of all points in magnets of the designed PM machine should be higher than that of the knee point.

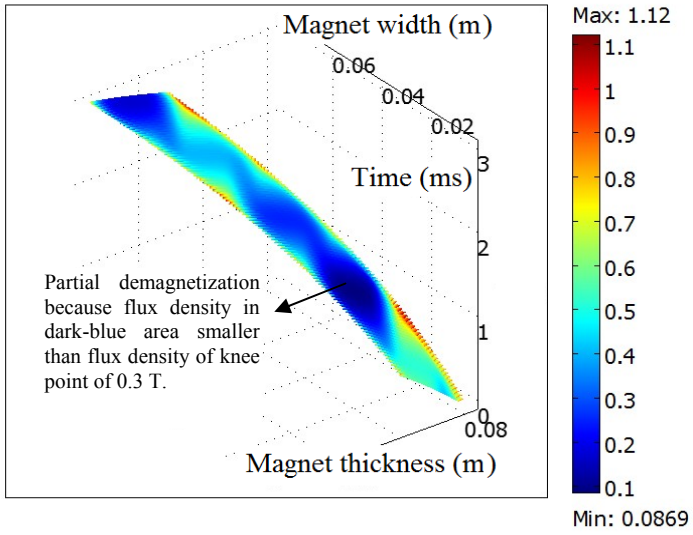

Figure 4.13. Radial flux density distribution of the magnet for partial demagnetization analysis, at different times, during three-phase short circuit, at a magnet temperature of 150 ^{o}C, with a remanent flux density of 1.05 T at 150 ^{o}C.

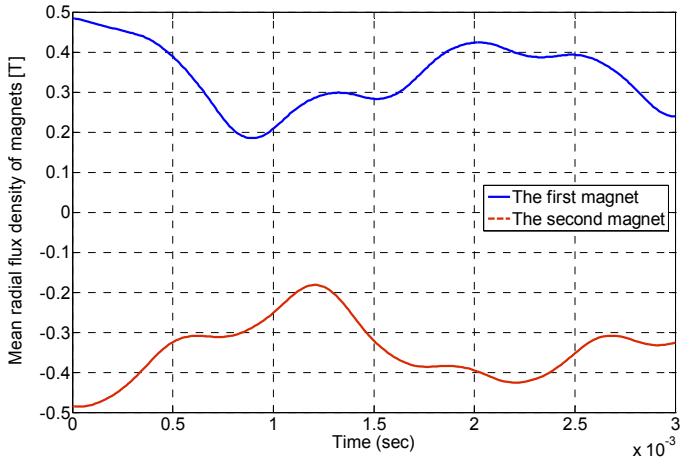

Figure. 4.14. Mean radial flux density for assessment of magnet demagnetization during the worst-scenario: three-phase short circuit and the magnet temperature of 150 ^{o}C.

Figure 4.15 presents the results of magnet demagnetization analysis during three-phase short circuit, at room temperature, with a remanent flux density of 1.2 T. At room temperature, there is no knee point in the demagnetization curve. Therefore, under these working conditions, the magnet is safe from demagnetization, because the flux densities of all points in the first magnet are positive.

Figure 4.16 and Figure 4.17 present demagnetization analyses at operation modes of maximum torque and rated current; the working temperatures of magnets are respectively at 150 ^{o}C and room temperature. It is shown that magnets are safe from demagnetization in the operation modes because of the flux density is greater than that of the knee point.

Comparing Figure 4.14 and 4.16b shows that the armature reaction during three-phase short circuit strongly distorts the curve of mean flux density.

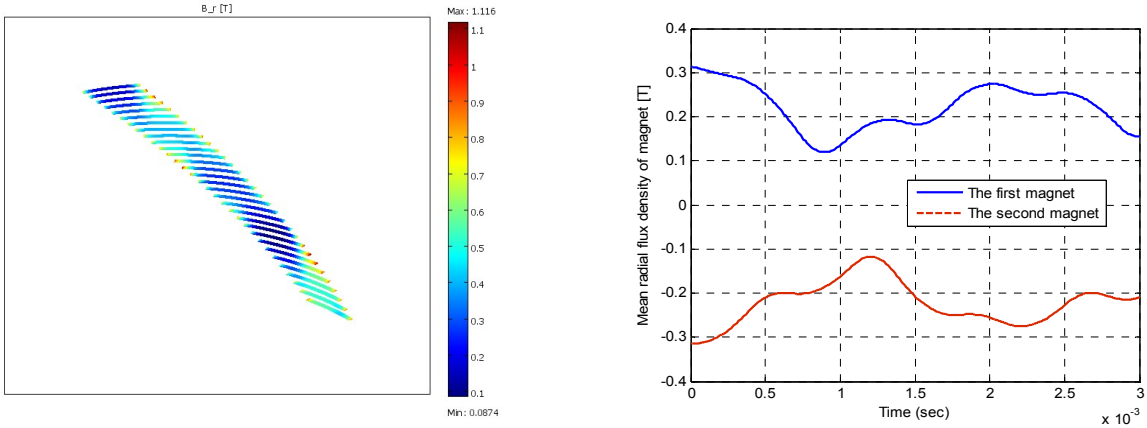

a) b)

Figure 4.15. Demagnetization analysis at different times during three-phase short circuit, room temperature, a remanent flux density of 1.2 T: a) distribution of flux density in the first magnet, b) mean flux density of magnets.

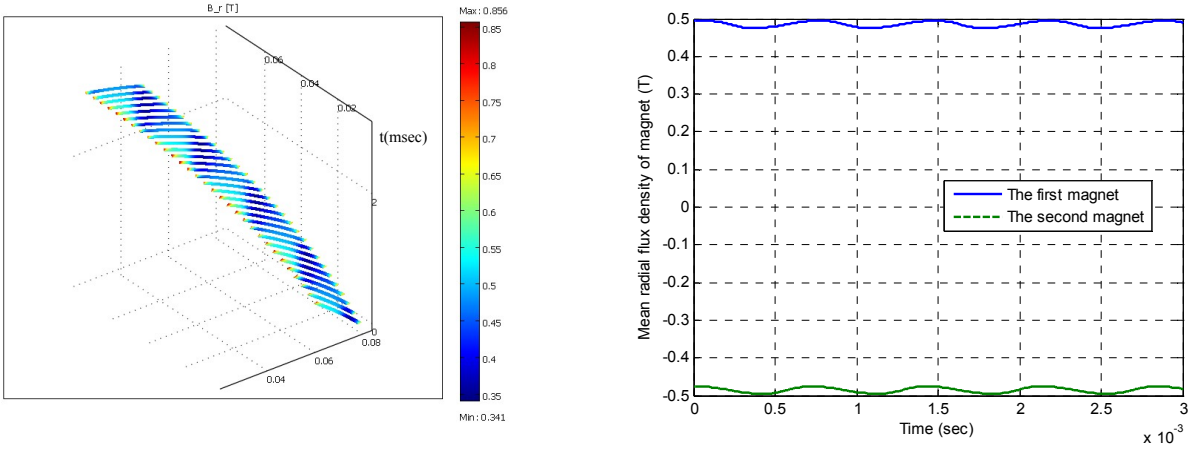

a) b)

Figure 4.16. Checking magnet demagnetization at a maximum torque current angle of 90 degrees, a magnet temperature of 150 ^{o}C, a remanent flux density of 1.05 T at 150 ^{o}C: a) Radial flux density distribution, b) mean radial flux density.

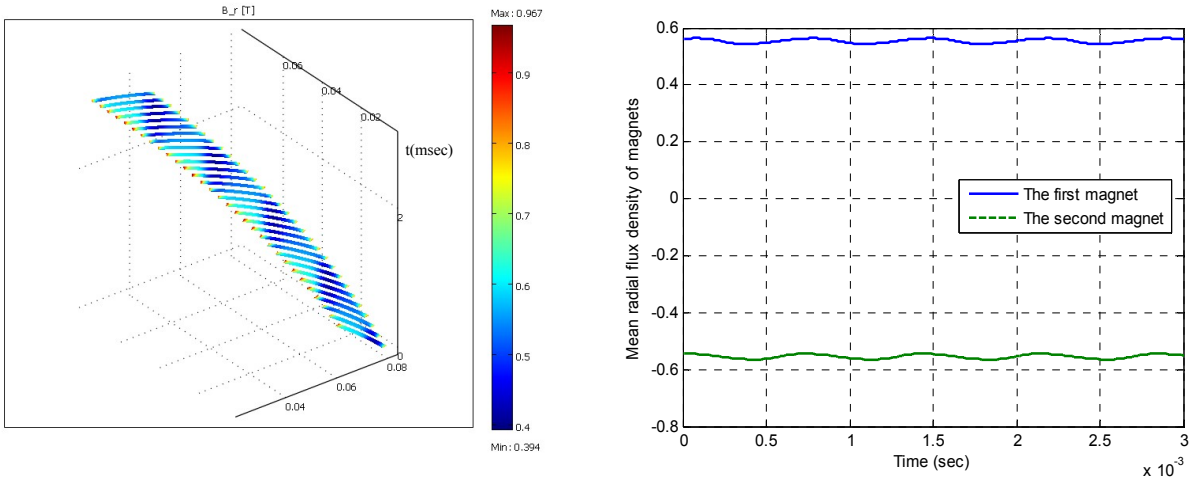

a) b)

Figure 4.17. Checking magnet demagnetization at a maximum torque current angle of 90 degrees, room temperature (in this case, there is no knee point in the demagnetization curve) and a remanent flux density of 1.2 T: a) radial flux density distribution, b) mean radial flux density.

4.7. Conclusions

In this chapter, the nonlinear transient FEM model including the rotor motion for the design and analysis of the PM machines is presented. Equations for calculating the magnetic field, flux linkage, and internal voltage are given.

A concept in the form of a flowchart, based on the transient FEM model including rotor motion is developed for analyzing and designing the PM machine. According to the concept, the geometry model, boundary conditions, and FEM computations are made automatically. Therefore, the program is very flexible and the design parameters of the PM machine can be changed easily.

The non-linear FEM model including rotor motion coupled to a circuit model is developed. This results in the field-circuit coupled model. Resistance of windings is taken into account in the FEM simulation to ensure the accuracy of the model. The model is used to analysis the PM machine during the three-phase short circuit. The FEM model and the program therefore form an efficient tool for the analysis and design of the PM machine.

The magnetic saturation model and solvers are discussed. These ensure that the FEM program is convergent and runs faster during deep magnetic saturation.

A demagnetization model is developed to assess the demagnetization of magnets. This is to ensure that the designed PM machine is safe during the worst operating conditions.

CHAPTER 5

SLOTTING EFFECT AND HYBRID MODEL

5.1. Introduction

The development of the FEM model of PM machines with concentrated windings was described. In this chapter, the FEM model is used to study the influence of the slotting on the distribution of magnetic fields in air gap and magnets, the flux linkage and the internal voltage of PM machines. A new hybrid model combining a static FEM model with an analytical model (presented in Chapter 3) is developed for the design of the PM machines.

Although there are several authors investigated the influence of the slotting effect, most authors have focused on the influence of the slotting effect on the magnetic field in air gap [Car 1926], [Zhu 1993b], [Zhu 2002], [Zhu 2010], [Daj 2010], [Lub 2010], [Jia 2011], [Che 2011a]. A comprehensive study of the influence of the slotting effect on the magnetic field in magnets, flux linkage, internal voltage, cogging torque, torque ripple, mean torque, rotor eddy current loss, and stator iron loss of the fractional slot PM machine with concentric windings is rather rare, especially at small slot opening. In the case of small slot opening, leakage flux passing through tooth tips is significant. In addition, several questions concerning slotting effect are not mentioned or not described in details in literature. For example,

- Does current literature of slotting effect for PM machines have limitations?
- What is the relation between voltage and slot opening?
- What is the relation between mean torque and slot opening?
- What is the relation between rotor eddy current loss and slot opening: linear or nonlinear, how can the relation be plotted?
- How about frequency of eddy current at a point in the magnet due to slotting effect? Which parameters does this depend on? Which positions in the magnet have high eddy current density?.

These questions motivate us to further study the slotting effect using static FEM as well as nonlinear transient FEM computation including rotor motion, which is known as the only accurate and effective method for predicting the performances of PM machines.

In this chapter, only the effect of slotting on the magnetic field, flux linkage, and internal voltage will be studied. The traditional literature about slotting effect will be evaluated. The slotting effect on cogging torque, torque ripple, mean torque, stator iron loss, and rotor eddy current loss will be investigated in the next chapters.

The results of research described in this chapter show that the traditional literature about the slotting effect has limitations in predicting the performances of PM machines at small slot opening. A calculation method of correction factors for slotting effect, fringing effect and magnetic saturation are proposed to improve the analytical model for the design of the PM machine. The analytical model and the static FEM model are linked together. This results in a proposed hybrid model with increased accuracy when compared to the analytical model and accelerates the design optimization process when compared to the transient FEM model. The hybrid model along with its program developed in this chapter has the ability to do automated sizing. It will be used for the design of PM machines in small-scale ship application. The relation of flux linkage and internal voltage to slot opening width are given. This has never been mentioned in the literature by other authors. As a result, the analysis provides the insight into the influence of the slotting effect on the performance of PM machine.

This chapter is organized as depicted in the flowchart in Figure 5.1. First, the slotting effect on the magnetic field in the air gap and magnets, flux linkage, and internal voltage is investigated. Next, Carter factor expressions in literature are evaluated by comparing them to FEM computations. The limitation of the traditional approach of slotting effect is recognized and discussed. Subsequently, the method for calculating the correction factor of slotting effect and magnetic saturation is investigated. The hybrid model for improving the design of PM machines is proposed. Afterwards, the analytical model, hybrid model, linear transient FEM model, and nonlinear transient FEM model are compared. Finallly, the conclusion of this chapter is drawn. The PM machine B is used as the reference PM machine for analyses.

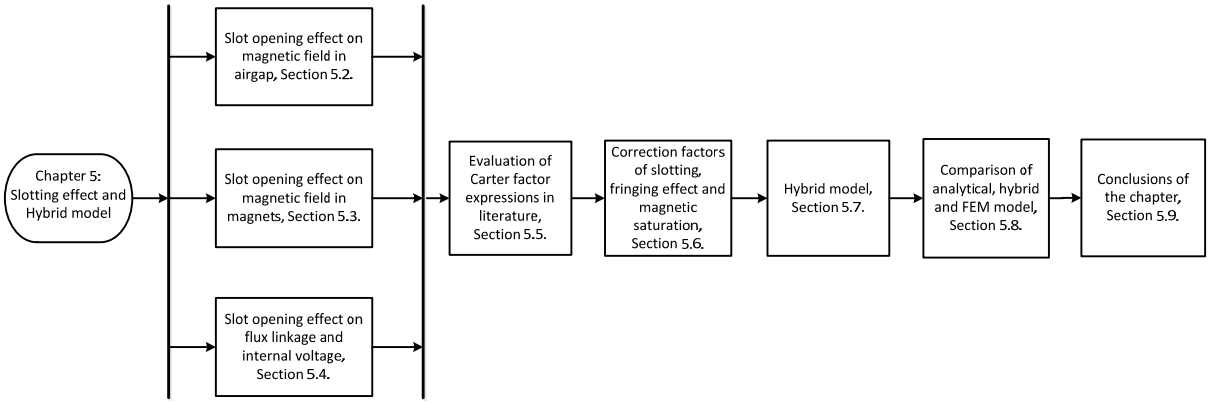

Figure 5.1. The organization of this chapter.

5.2. Influence of Slot Opening on Distribution of the Magnetic Field in Air gap

Slotting influences the magnetic field of the air gap in two ways. Firstly, it reduces the average magnetic flux per pole and secondly, the slotting affects the distribution of the flux in the air gap, see Figure 5.2 and 5.3. As a result, slotting leads to inhomogeneous flux density in the air gap. At the positions opposite slot opening with low permeability, flux density is smaller than that at the positions opposite teeth with high permeability. The inhomogeneity of the air gap flux density results in voltage ripple, cogging torque or torque ripple.

Figure 5.2 shows calculation results of the radial flux density in the middle of the air gap for cases of full-open slot, semi-open slot and closed slot during noload. Magnetic saturation is taken into account by using a measured BH-curve. Clearly, the slotting effect on the flux density increases when the slot opening increases the air gap reduces by about 20% of the value of the closed slot, and the radial flux density waveform is highly distorted. With closed slot, the air gap flux density is homogeneous along the circumferential magnets.

The air gap flux density can be represented as a function of radius, stator angle (mechanical angle in the stator coordinate) and rotor angle [Zhu 1993b], [Hol 2007]. Figure 5.3 illustrates the radial flux density in the air gap with different air gap radii of the reference machine B during noload. As can be seen, when radius increases the slotting effect reduces, but it is still significant. The air gap flux density at positions corresponding to the edge of stator teeth gets sharp peak. This is known as slot edge effect.

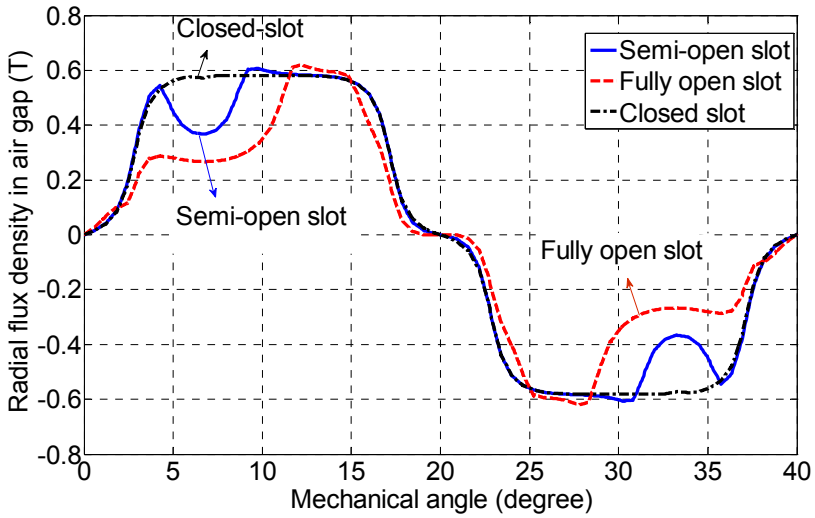

Figure 5.2. The radial flux density in the middle of the air gap for full-open slot, semi-open slot and closed slot during noload.

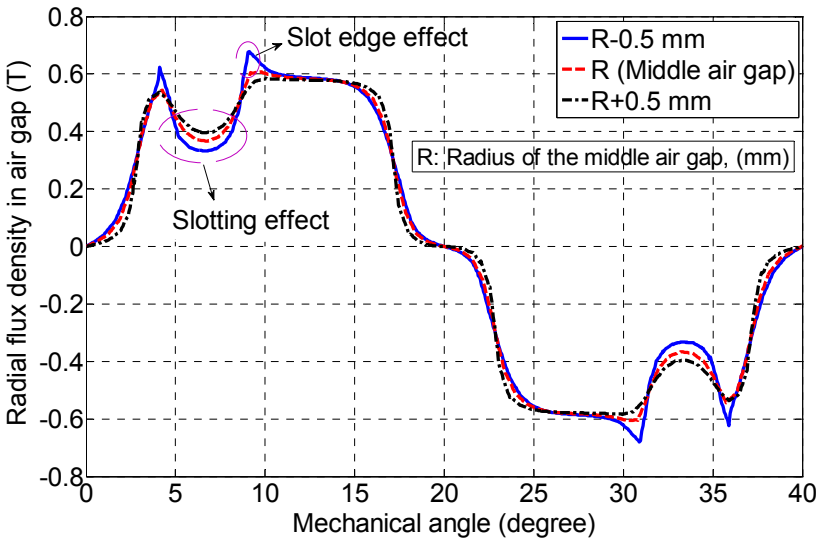

Figure 5.3. The radial flux density in the air gap vs. mechanical angle, at different air gap radii, for semi-open slot machine B.

5.3. Influence of Slot Opening on Distribution of Magnetic Field in Magnets

In this section, the distribution of flux density in magnets is presented. Figure 5.4 illustrates the radial flux density in the magnets and the air between adjacent magnets. The effects inside the magnets can be divided into slotting effect, magnet edge effect, and the others that are not influenced by the effects. It can be seen that due to the effect of leakage flux at the edges of the magnets, the magnet flux density reaches peak value at the edges. For the outside of the magnet,

i.e., the air between adjacent magnets, the edge effect can also be explained similarly. However, the direction of the leakage flux density in the air between adjacent magnets inverts the direction of the leakage flux inside the magnet. Therefore, the flux density waveform at the magnet edges in Figure 5.4 has a jumping step from positive value to negative value and inverse. In addition, it can be seen from this figure that the edge effect is negligibly small at the arc on the surface of magnet.

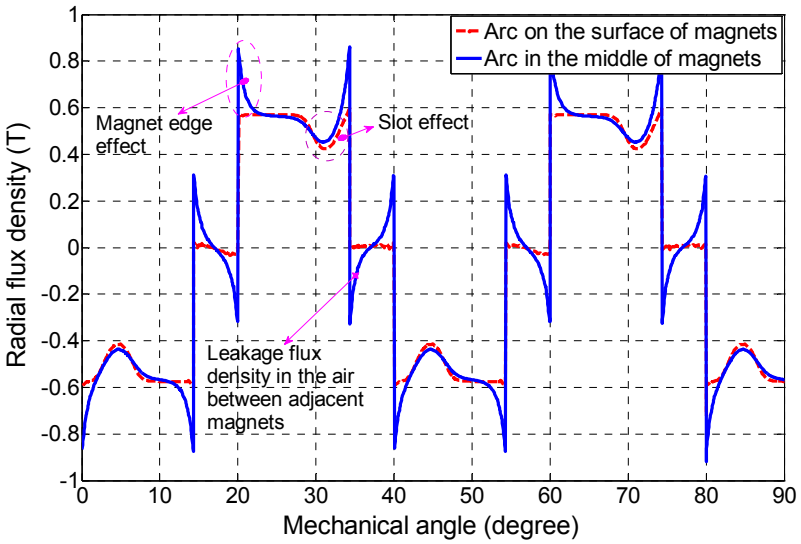

Figure 5.4. Radial flux density in the magnets and the air between adjacent magnets for in the case of a semi-open slot PM machine.

Figure 5.5 and Figure 5.6 present the radial flux density in the middle of the magnets for cases of full-open slot and semi-open slot for no-load and load, respectively. It can be seen that with full-open slot PM machine, magnet flux density is distorted more strongly than is the case in the semi-open slot PM machine. Therefore, the predicted eddy current loss of the former is higher than that of the latter. Compared to no-load, there is a small change in radial flux density of magnets at edges during load as shown in Figure 5.6. However, the waveform of the radial flux density during load is generally similar to that of no-load, so the armature reaction for the reference machine B is small.

The edge effect produces high flux density at the edge of magnets, while the slotting effect causes variation of flux density in magnets. Therefore, the combination of slotting effect and edge effect of magnet can be one of reasons that lead to higher magnet eddy current loss. Design optimization of magnet dimension and slot opening width is therefore recommended to reduce the effects and magnet eddy current loss.

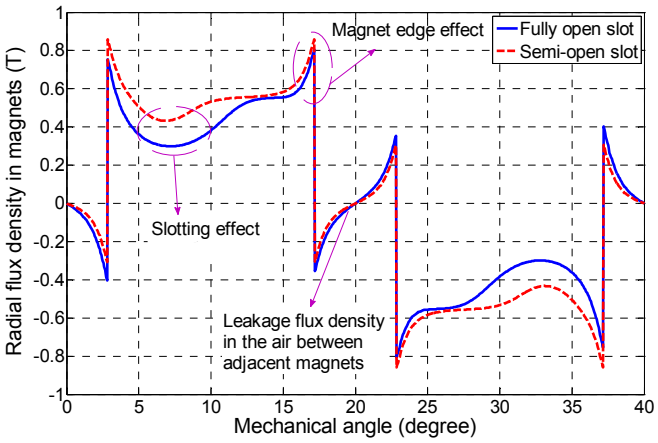

Figure 5.5. Radial flux density in the magnets and the air between adjacent magnets for in the following cases: full-open slot and semi-open slot PM machine, during no-load.

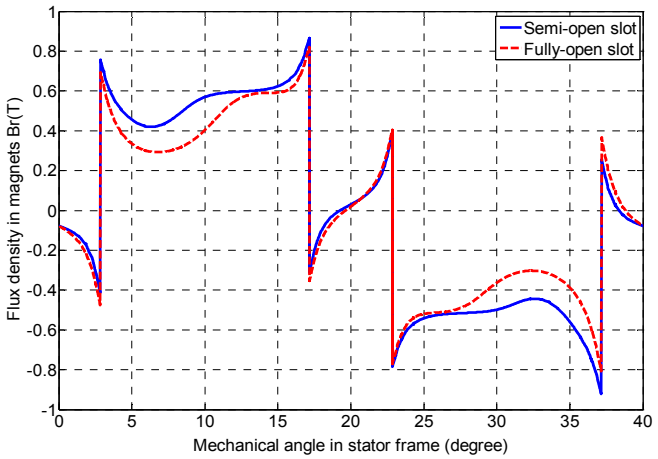

Figure 5.6. Radial flux density in the magnets and the air between adjacent magnets in the following cases: full-open slot and semi-open slot PM machine, during load.

5.4. Influence of Slot Opening on Flux Linkage and Internal Voltage

In Chapter 4, transient FEM model and equations for calculating flux linkage and internal voltage were given. In this section, the equations are used to calculate flux linkage and internal voltage. Figure 5.7 presents flux contour simulation of fully open slot (Figure 5.7a), semi-open slot (Figure 5.7 b) and closed slot (Figure 5.7 c and d) PM machines. Figure 5.8 shows the simulated results of the turn internal voltage of a fully open slot PM machine. The internal voltage waveforms in Figure 5.8 are not sinusoidal. The internal voltage of a turn in the middle of slot and that in the bottom of slot are identical. Nevertheless, the internal voltage of a turn in the top tooth is highly distorted by the flux that only goes through the top of the tooth and does not go through stator back iron.

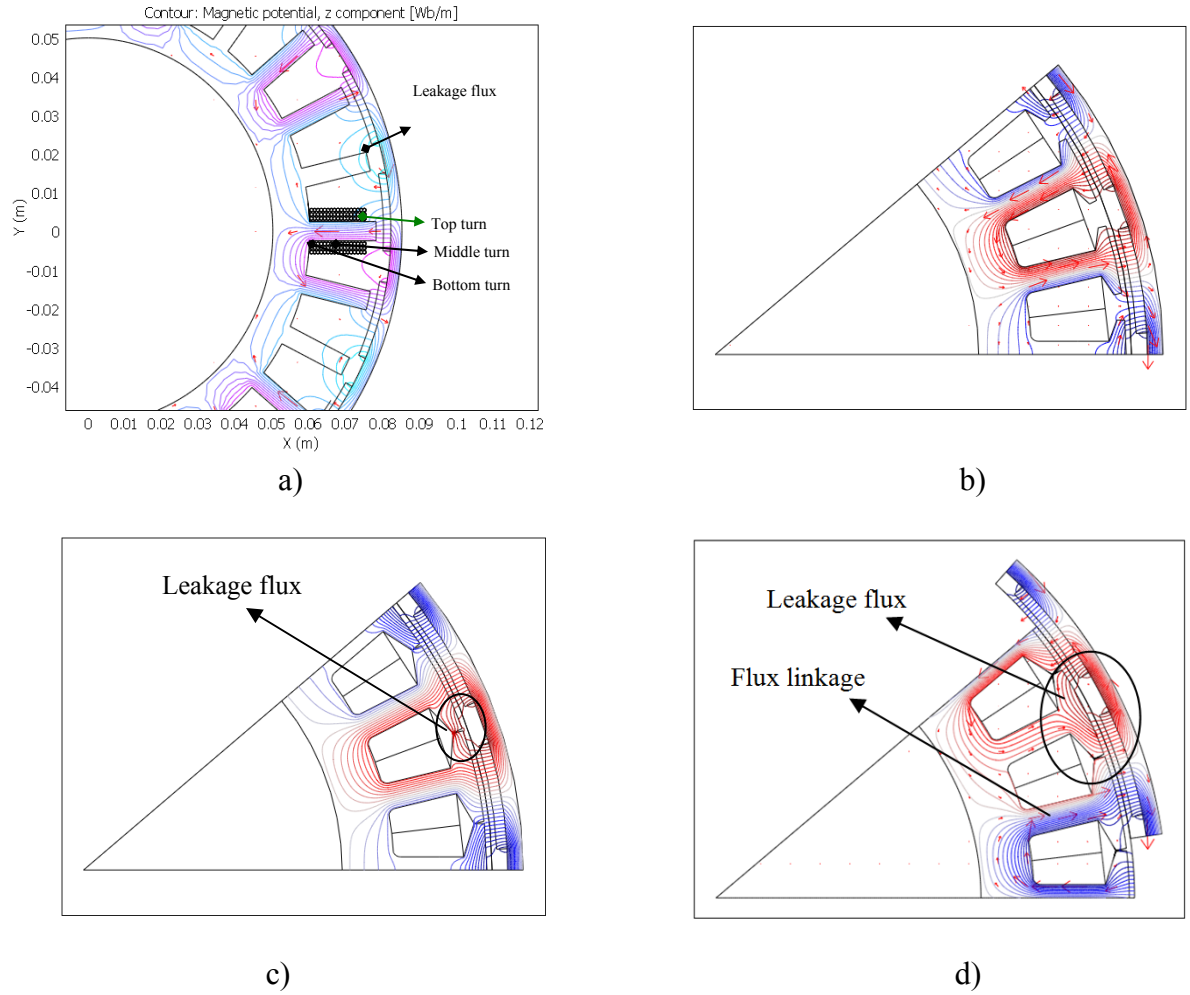

Figure 5.7. Contour of flux: a) fully open slot; b) semi-open slot; c, d) closed-open slot PM machine.

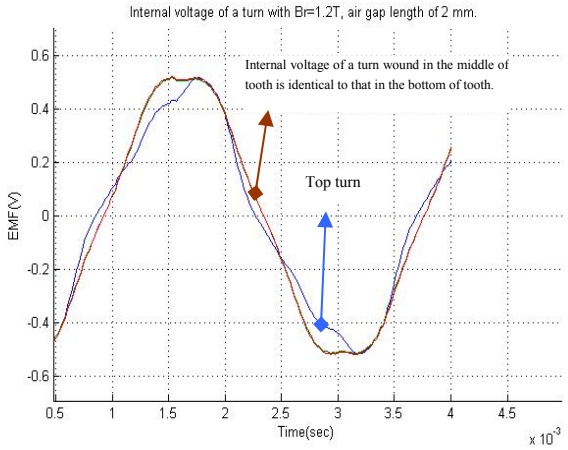

Figure 5.8. Internal voltage (EMF) of a turn in the top, middle, and bottom of a tooth, of fully open-slot PM machine, at speed of 2347 rpm.

Figure 5.9 compares the internal voltage waveforms of a full-open slot, a closed slot, and a semi-open slot PM machine. It is shown that slot opening affects the internal voltage amplitude significantly. If slot opening is large, the flux linkage through tooth will be small. Therefore, the internal voltage amplitude will be small and PM machine will need more turn numbers to reach the rated voltage. When slot-opening width is small, leakage flux passing through tooth tips increases, flux linkage decreases and internal voltage amplitude also decreases. Because of the slot-opening effect as mentioned above, the slot opening should be designed for maximum internal voltage amplitude. Figure 5.10 compares flux linkage waveforms with different slot opening width. It can be seen that although internal voltage waveform is not sinusoidal, the flux linkage is nearly sinusoidal. This is because the voltage equals the derivative of flux linkage with respect to time.

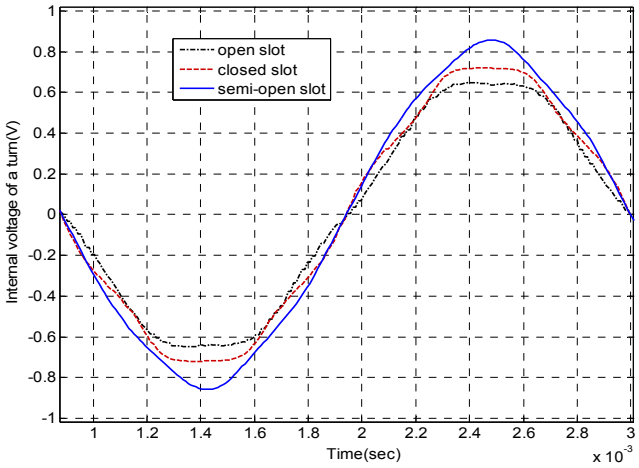

Figure 5.9. Internal voltage vs. slot opening, at speed of 3150 rpm.

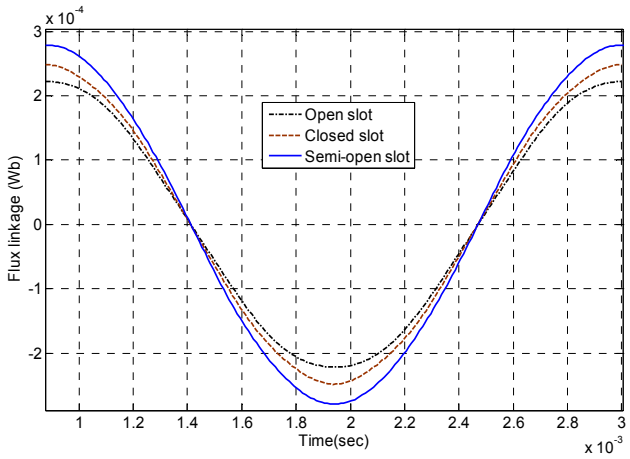

Figure 5.10. Flux linkage of a turn vs. slot opening, at speed of 3150 rpm.

Figure 5.11 presents the relation between the flux linkage amplitude of a turn and a slot opening, while Figure 5.12 presents the relation between the maximum internal voltage of a turn and the slot opening; during no-load, calculated by the transient FEM model including rotor motion. Magnetic saturation is taken into account in all calculations, except for in the few cases shown in Figure 5.11 and 5.12. The internal voltage reaches a maximum value at slot opening of around 4 mm in the case of magnetic saturation. With the slot opening width in the range of 0 to 4 mm, (the so-called range of small slot opening), both internal voltage and flux linkage amplitudes decrease when the slot opening decreases. With the slot opening greater than 4 mm, internal voltage and flux linkage amplitude decrease when the slot opening increases. It is also shown in Figure 5.12 that the permeability of stator steel strongly affects voltage amplitude. When the permeability of steel increases, voltage amplitude increases. In addition, the range of small slot opening is lower when relative permeability of steel increases. Looking at the distribution of flux in Figure 5.7 c and d, especially leakage flux passing through tooth tips, we see that the range of small slot opening always exists even when ideal steel with infinite relative permeability is used.

On the contrary, regarding analytical models using the Carter factor, when slot opening decreases, the Carter factor decreases. Thus, air gap flux density increases and internal voltage increases. Therefore, the trend of internal voltage calculated by transient FEM is different from the trend of internal voltage if calculated by conventional analytical models at small slot opening. The reason is that analytical models do not consider the influence of the leakage flux, which goes through tooth tips as shown in Figure 5.7c and d. Moreover, the leakage flux does not go through windings, so it does not induce voltage in windings.

Referring back to Figure 5.2, it can be seen that when slot opening decreases, the mean flux density in the air gap increases. Therefore, if we use flux density in the air gap to derive internal voltage, voltage amplitude will increase with the decrease of slot opening. It can be concluded that if air gap flux density is used to calculate the internal voltage of the radial-flux PM machine with slotted stator as is done by conventional analytical models using Carter's theory or the theory of the equivalent current sheet, they are not possible to account for the decrease of internal voltage at small slot opening. This is the limitation of conventional literature of the slotting effect, in the range of small slot opening, using Carter factor and air gap flux density to calculate internal voltage. In fact, a slot opening should be big enough to put windings into slots. Analytical design models using the Carter factor to account for slotting effect might therefore be acceptable for rough design. In the next section, the Carter factor expressions found in literature will be evaluated by comparing them to FEM computation.

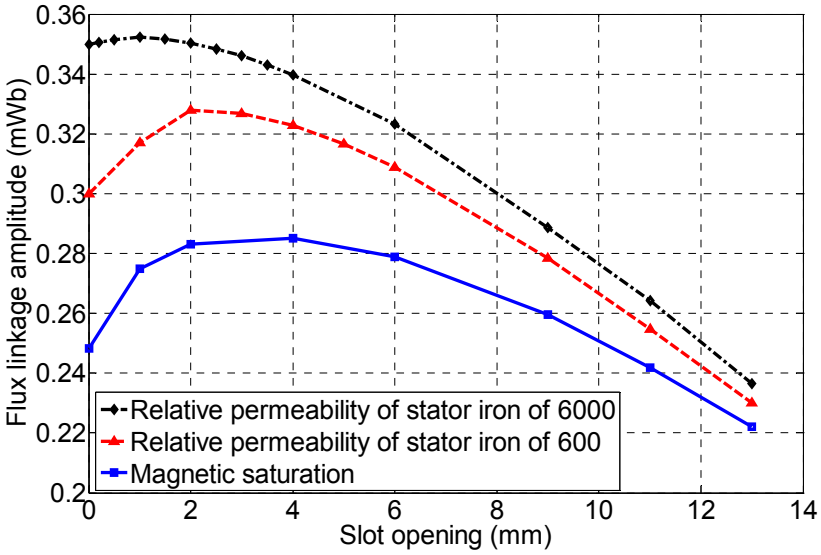

Figure 5.11. Flux linkage amplitude of a turn vs. slot opening, at speed of 3150 rpm during no-load.

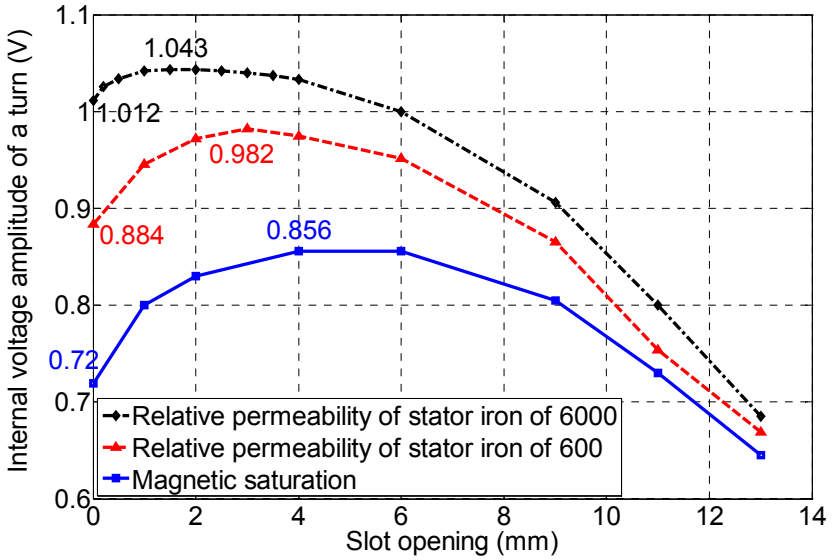

Figure 5.12. Influence of slot opening on maximum voltage of a turn during no-load.

5.5. Evaluation of Carter Factor Expressions Found in Literature

In the prior section, it is shown that the literature of slotting effect has limitation at small slot opening. When the slot opening is large enough, the Carter factor might be used. In this section, the Carter factor expressions found in literature are evaluated by comparing them with FEM computations.

In the conventional analytical design model of slotted PM machine, the Carter factor is important. This factor influences the calculated results for the air gap flux density, voltage, etc. The electromagnetic force, electromagnetic torque, and voltage are normally calculated based on the magnetic field of the air gap. Thus, if the accuracy of the air gap flux density is improved, the analytical model accuracy will also be improved. There are many expressions for the Carter factor in literature, which leads to confusion. The Carter factor expressions are evaluated by comparing to FEM computations to find the most suitable expression for design and analysis of PM machines considered in this study.

For the sake of clarity, we will define three correction factors. First, the FEM slotting factor or FEM Carter factor is a factor accounting for slotting effect and calculated by static FEM computation at a single rotor position. Second, the FEM fringing factor is a factor accounting for the fringing flux of the magnet (as shown in Figure 5.13) and calculated by FEM computation at a single rotor position for a closed slot PM machine. Third, the correction factor calculated by FEM including both the slotting and fringing effects is called the total FEM correction factor k_{tol_sf}.

For the sake of comparison of Carter factor expressions and the FEM Carter factor, we have to separate the slotting effect and the fringing effect of magnets in FEM calculation, as follows.

First, it is necessary to explain the fringing phenomenon. The fringing effect of a magnet is a field phenomenon in which the corners of the flux density in the air gap due to the magnet become rounded and the flat tops become narrower, as shown in Figure 5.14, curve (1). Curve (1) is the flux density in the air gap including fringing effect with zero slot opening width, calculated by FEM. Curve (2) is also flux density in the air gap calculated by analytical method, but not including fringing effect. Curve (3) is mean flux density of points opposite the magnet, derived from curve (1). The fringing effect causes the decrease of mean air gap flux density per pole as well as internal voltage. However, the fringing effect reduces the amplitude of harmonic components making air gap flux density and voltage more sinusoidal.

Similarly to slotting effect, the fringing effect can be taken into account by using a fringing correction factor. When the slot-opening width is equal to zero, the slotting factor is equal to one, so the fringing factor can be calculated by FEM computation. The FEM fringing factor is calculated according to equation (3.8) (in Chapter 3), in which flux density in the air gap is calculated by FEM computation for the PM machine with zero slot opening width. As a result, the FEM fringing factor has a value of 1.06. The FEM fringing factor depends on air gap length and the dimension of the magnet. The FEM slotting factor (or FEM Carter factor, curve (7) in Figure 5.15) is therefore equal to the total FEM correction factor k_{tol_sf} (curve (6) in Figure 5.15)

minus the FEM fringing factor of 1.06 plus 1. The relation of correction factors can be expressed as [Car 1926]

$$k_{tol\_sf} = k_C + k_{fringing} - 1 \tag{5.1}$$

where k_{tol_sf} is total FEM correction factor accounting for both slotting effect and fringing effect, k_C is FEM Carter factor, and $k_{fringing}$ is FEM fringing factor.

Figure 5.15 shows correction factors versus slot opening. Curves (1) to curve (5) are respectively calculated corresponding to the equations from equation (3.9) to (3.13). The total FEM correction factor including slotting effect and fringing effect is depicted by curve (6). It is calculated according to equation (3.8). In the analytical equations of the Carter factor, the fringing effect of the magnet is neglected. Therefore, when the slot opening approaches zero, the Carter factor approaches the value of one. However, the fringing effect of magnets is included in the FEM calculation, so that curve (6) is greater than one, even when the slot-opening width reaches zero. Note that since radial flux density is calculated at the arc in the middle air gap, the edge effect of slot opening can be neglected as can be seen in Figure 5.2.

It can be seen from Figure 5.15 that the analytical Carter factor, curves (1), (3), and (4) and the FEM Carter factor, curve (7) follow a similar trend, but the value is significantly different. Curves (1) and (3) are almost the same. Curves (2) and (7) match in the case of a slot opening width smaller than 9 mm, otherwise the discrepancy increases as the slot opening increases. The curves (5) and (7) match, but the trend is a bit different when the slot opening is over 12 mm. In summary, the curve (5) is the closest to the FEM Carter factor. The fringing effect is significant so that it is recommended that it should be considered in the design of PM machines.

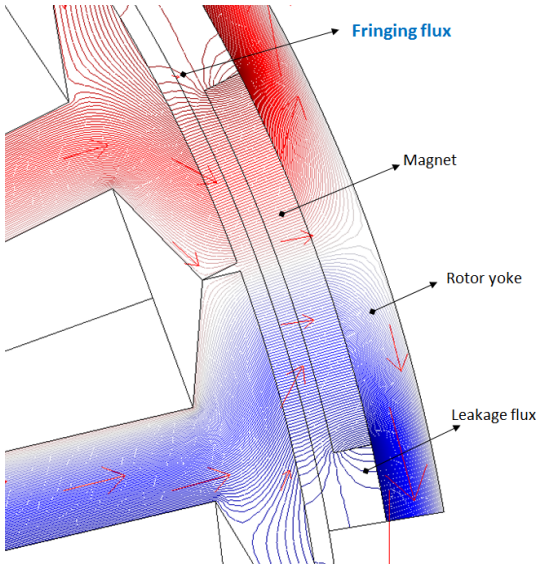

Figure 5.13. Demonstration of fringing flux of magnet.

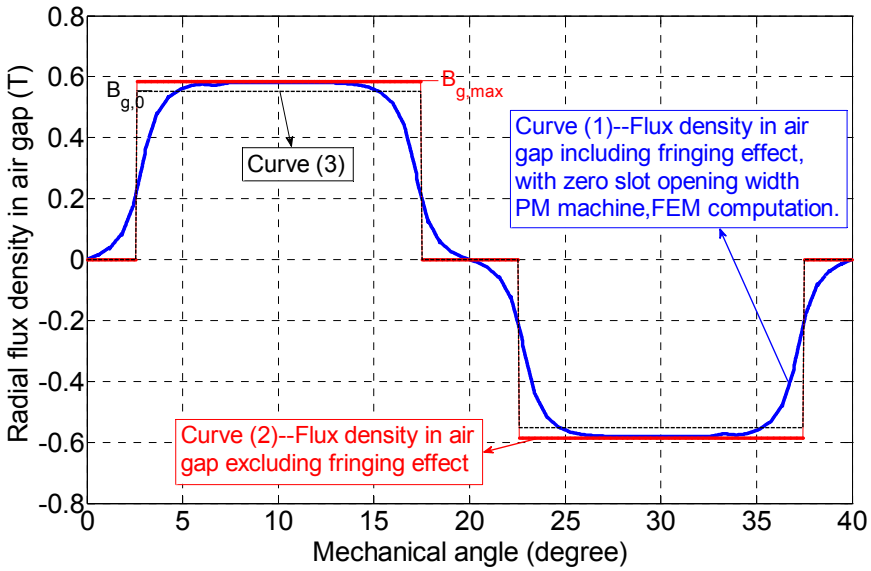

Figure 5.14. Illustration of flux density in air gap with and without the fringing effect of magnet, excluding the slotting effect.

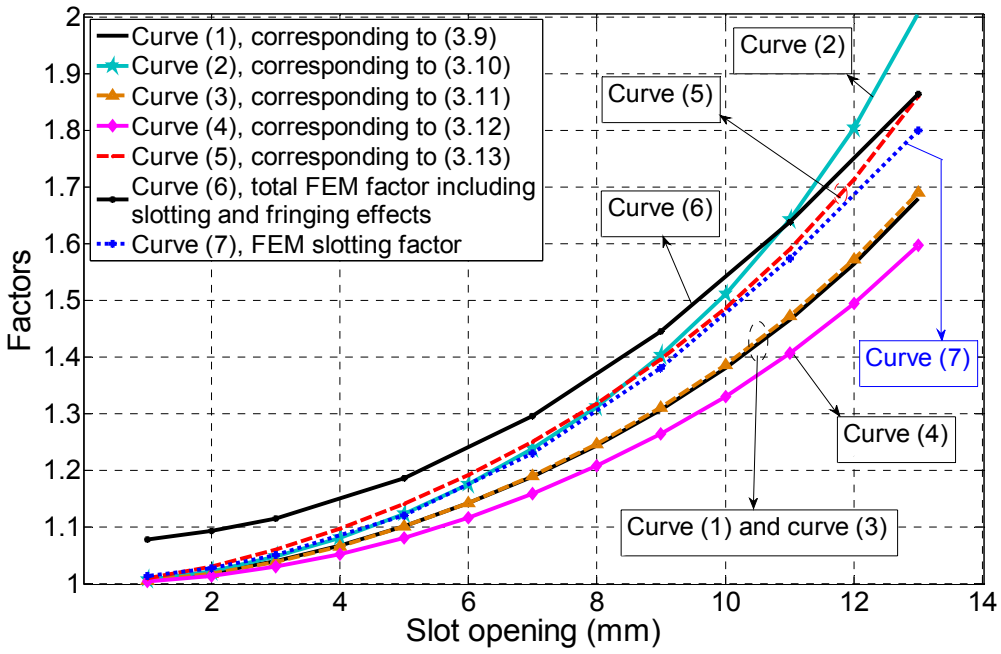

Figure 5.15. Comparison of Carter factor calculated by FEM and analytical expressions.

5.6. Total Correction Factor of Slotting, Fringing and Magnetic Saturation Effects

In the previous section, correction factors of slotting and fringing effects were investigated. In this section, the correction factor of magnetic saturation and the total correction factor

accounting for all of slotting, fringing, and magnetic saturation effects, which is based on FEM computation, are investigated. Different methods to calculate the correction factor of magnetic saturation are discussed.

Because the permeability of iron reduces during magnetic saturation, the leakage flux passing through tooth tips increases in comparison with the case of the unsaturated circuit, while air gap flux density and flux linkage decrease. Therefore, the voltage induced in the windings decreases.

To improve the analytical model, we can use an effective air gap (equivalent air gap) to take into account the magnetic saturation influence on reducing air gap flux density and voltage. The saturation correction factor is defined as,

$$k_{sat} = B_{g\,mean\_unsat} / B_{g\,mean\_sat} = g_{eff\_sat} / g = 1 + \Delta g_{sat} / g, \quad \Delta g_{sat} = g_{eff\_sat} - g \tag{5.2}$$

where, $B_{g\,mean\_unsat}$ and $B_{g\,mean\_sat}$ are respectively mean flux density in the air gap corresponding to FEM simulations of unsaturated and saturated magnetic circuit; and g_{eff_sat} is equivalent air gap accounting for magnetic saturation effect.

The total correction factor accounting for slotting, fringing, and magnetic saturation effects can be defined as,

$$k_{tol} = g_{eff\_tol} / g = 1 + (\Delta g_{sf} + \Delta g_{sat}) / g \tag{5.3}$$

$$k_{tol} = k_{tol\_sf} + k_{sat} - 1 \tag{5.4}$$

where, g_{eff_tol} is the total effective air gap length accounting for the slotting, fringing and magnetic saturation effects; Δg_{sf} and Δg_{sat} are the increase of air gap length due to slotting and fringing effects and magnetic saturation effect, respectively; k_{tol_sf} is the total correction factor accounting for slotting and fringing effects.

Figure 5.16 shows a comparison of flux density in the middle of air gap during linear magnetic circuit and saturated magnetic circuit for two cases: no-load (Figure 5.16a) and load (Figure 5.16b). From the air gap flux density, the correction factors k_{tol_sf}, k_{sat}, and k_{tol} can be calculated. An example of the factors during no-load is shown in Figure 5.17. In this figure, the factor k_{tol_sf} is calculated as presented in the Section 5.5, while the correction of magnetic saturation k_{sat} is calculated according to equation (5.2). The total correction factor k_{tol} is calculated according to equation (5.4). Note that the total correction factor can be calculated directly from the air gap flux density in the case of magnetic saturation. However, the magnetic saturation correction factor based air gap flux density cannot account for the reduction of flux linkage and internal voltage in the range of small slot opening due to leakage flux passing through tooth tips as explained in Section 5.4. In addition, when stator iron is saturated, the

decrease of flux linkage is greater than the decrease of air gap flux density, because of the increase of leakage flux through tooth tips. Hence, the correction factor of magnetic saturation based on tooth flux density might results in more accurate results than the correction factor of magnetic saturation based on air gap flux density. Hereafter, the correction factor of magnetic saturation based on tooth flux density will be discussed and compared to the correction factor of magnetic saturation based on air gap flux density.

Figure 5.18 shows correction factors versus slot opening. The correction factor of slotting and fringing effects is identical to that in Figure 5.17. The correction of magnetic saturation is calculated according to equation (5.2), but based on flux density of tooth, instead of using air gap flux density as in Figure 5.17. The correction factor of magnetic saturation in Figure 5.18 is greater than that in Figure 5.17, especially in the range of small slot opening. This is because leakage flux passing through tooth tips increases and flux linkage decreases during magnetic saturation. It should be noted that in calculation, the rotor position is chosen so that the magnet is centred on the tooth so the flux density of the tooth will reach the maximum value. It can be seen from Figure 5.18 that when the slot opening is larger than about 4 mm, the total correction factor is increases with respect to the increase of slot opening. However, in the range of slot openings smaller than 4 mm, the total factor increases with respect to the decrease of slot opening. The method calculating the correction factor of magnetic saturation based on tooth flux density therefore results in more accurate results in the range of small slot opening than the methods using the correction factor of magnetic saturation based on air gap flux density. This means that in the range of small slot opening, calculated voltage decreases when slot opening decreases.

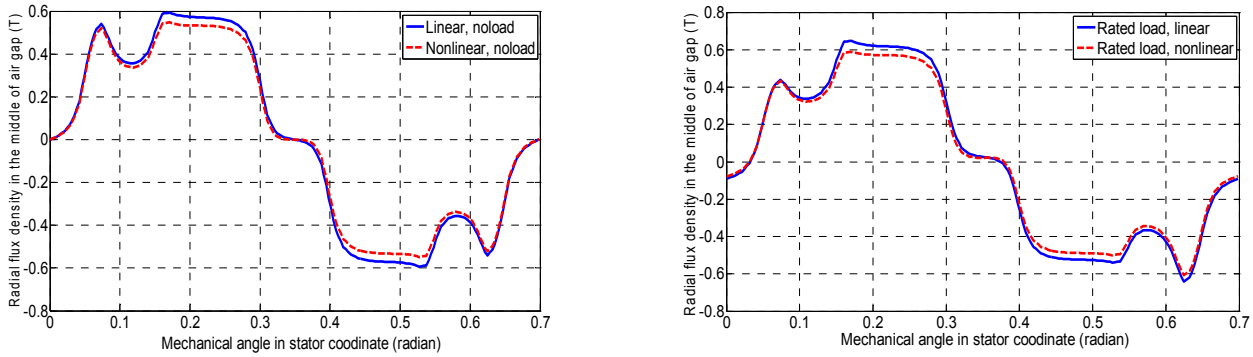

a) b)

Figure 5.16. Radial flux density in the middle of air gap of the PM machine B with slot opening of 6mm, a) during noload, b) during load.

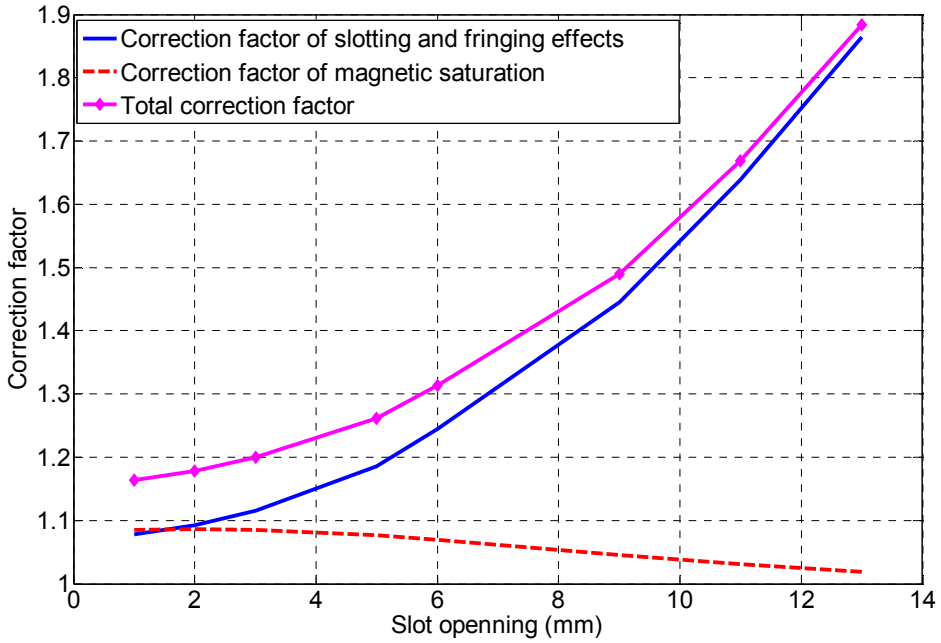

Figure. 5.17. Correction factors of slotting and fringing effects, correction factor of magnetic saturation, and total correction factor vs. slot opening, with magnetic saturation correction factor calculated based on air gap flux density.

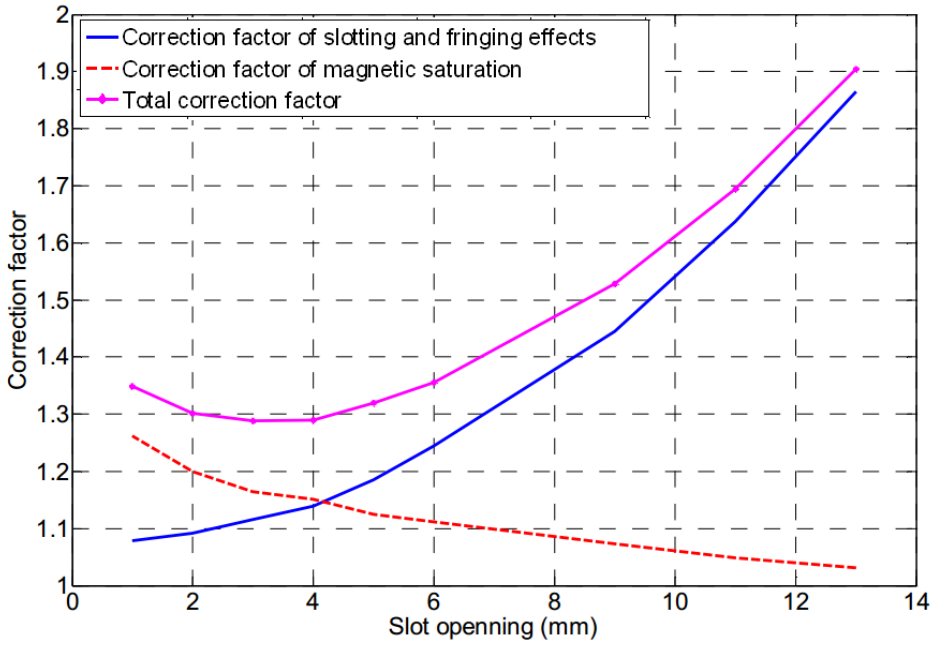

Figure 5.18. Correction factors of slotting and fringing effects, correction factor of magnetic saturation, and total correction factor vs. slot opening, with magnetic saturation correction factor calculated based on tooth flux density.

To apply correction factors in the design of PM machines, the factors should be calculated automatically for different dimensions of PM machine. An improved model for the design of PM machines will be proposed in the next section to implement this idea.

5.7. Hybrid Model – An Improvement on the Analytical Model

In the previous section, the correction factors of slotting and fringing effect and magnetic saturation are presented. The analytical model is improved by using the correction factor. However, for design optimization, we need a model that can automatically calculate correction factors for any geometry of PM machine. In this section, a new model and a process for the design of PM machines is proposed.

The analytical model and the static FEM model with single rotor position are coupled during the design process to generate a third model, the so-called "hybrid model". First, the static linear FEM model with single rotor position is used to calculate flux density in a selected tooth at a selected rotor position. Next, the correction factor of slotting and fringing is calculated. The rotor position is chosen so that the magnet and the tooth are centred; therefore the tooth flux density reaches the maximum value. Then, the static nonlinear FEM model with the same rotor position as the linear FEM model is used to calculate tooth flux density. Afterwards, the correction factor of magnetic saturation is ratio of the tooth flux density in the case of the linear FEM simulation to the tooth flux density in the case of the nonlinear FEM simulation. Finally, the total correction factor is calculated according to equation (5.4).

To implement the concept, a static FEM program is developed based on scripts. The program can automatically create the geometry model and handle boundary conditions. The static FEM program with single rotor position is a subprogram that is called by the main program to calculate correction factors.

A design process using the hybrid model for the design of PM machines is proposed as shown in Figure 5.19. This is a type of multi-level design including four steps: specifying input specifications, preliminary design, and the design of PM machine based on the hybrid model, and refining the design by using nonlinear transient FEM including rotor motion. The hybrid model replaces the traditional model based on the analytical model. The hybrid model utilizes the fast calculation advantage of the analytical model and the accuracy of the FEM model. The hybrid model takes into account slotting effect, fringing effect and magnetic saturation. It therefore reduces the time used for the design of PM machines in comparison with the FEM model as well as improves accuracy in comparison with the analytical model. In the next section,

the hybrid model will be compared with the analytical model and the nonlinear transient FEM model including rotor.

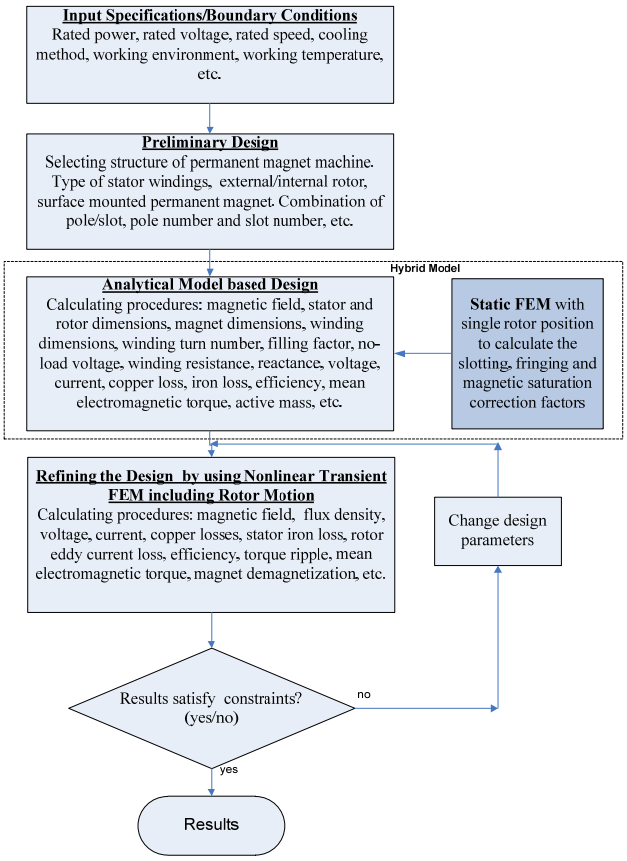

Figure 5.19. A proposal design process including a new hybrid model and automated transient FEM including rotor motion for design of PM machines.

5.8. Comparing Analytical, Hybrid and FEM Models of PM Machines

Table 5.1 presents calculation results of the reference PM machine B with different design models at a rated rotor speed of 3150 rpm. While Table 5.2 estimates the calculation error of models, normalized to the non-linear transient FEM model. It must be noted that the electric power of the PM machine in the design model is kept constant. This means that if the calculated voltage increases, the calculated electrical current and copper loss will decrease. There are three models used for comparison, namely,

+ Model 1--analytical model: Equations for computation were presented in Chapter 3 and the Carter factor is calculated according to equation (3.11) in Chapter 3.

+ Model 2--hybrid model: Correction factors accounting for slotting, fringing, and magnetic saturation effects are calculated by the static FEM model with single rotor position. The analytical model and the static FEM model are coupled.

+ Model 3: Nonlinear transient FEM model including rotor motion is used for calculation.

The main results are shown in the Table 5.1 and 5.2 and these show that the hybrid model is an improvement on conventional analytical design model. The hybrid model and the nonlinear FEM model show a fair agreement.

It should be noted that maximum flux density of tooth and rotor yoke can be calculated directly by static FEM, instead of using the analytical model. However, in the Table 5.1 the hybrid model presented still uses analytical method to calculate the flux density. This is to show the influence of correction factors on the improvement of the analytical model.

In conclusion, using the hybrid model not only improves the design model in terms of accuracy, but also increases the reliability of the model in comparison with the analytical model. It also significantly reduces time cost in comparison with the transient FEM model.

Table 5.1. Comparison of analytical model, hybrid, and FEM models, with fixed output power.

Parameters	Analytical model	Hybrid model	Nonlinear transient FEM model
Correction factors of slotting/fringing/magnetic saturation	1.19 / 1 / 1	1.19 / 1.06 / 1.1	none
Line to line voltage (V)	194	180	177
Maximum flux density of rotor yoke (T)	1.81	1.69	1.67
Maximum flux density of stator tooth (T)	1.93	1.62	1.64

Note: The flux density is calculated for points in the middle of rotor yoke, and tooth.

Table 5.2. Estimation of calculation errors of models, normalized to non-linear transient FEM model.

	Analytical model	Hybrid model
Voltage error (%)	9.7	1.9
Tooth flux density (%)	17.9	1
Flux density of stator tooth	8.3	-1.2

5.9. Conclusions

In this chapter, the influence of slot opening on the distribution of flux density in magnets and air gaps was investigated. The edge effect of magnets and slot opening were also discussed. From studying the distribution of flux density in magnets, it was found that the combination of slotting effect and edge effect of magnets produces strong variation of flux density in magnets (Figure 5.4, 5.5 and 5.6), which can cause large magnet eddy current loss.

The relations of flux linkage and internal voltage to slot opening were evaluated. It was shown that the conventional literature of the slotting effect has a limitation in the range of small slot opening. During the traditional approach using air gap flux density to calculate voltage, the Carter factor creases while slot opening decreases. Therefore, voltage amplitude is increases. However, in the range of small slot opening, when the slot opening increases, the leakage flux passing through tooth tips increases and flux linkage is decreases as shown in Figure 5.11, leading to the decrease of voltage as shown in Figure 5.12. This has never been described in literature before. Thus, the study gives new insight into the influence of slot opening on flux linkage and voltage at small slot opening.

A method for separating slotting effect and fringing effect in FEM computation was proposed. Therefore, the Carter factor expressions found in literature were evaluated by comparing analytical calculation with FEM calculation to find the most suitable expression for the design of PM machines. Method for calculating correction factors of slotting, fringing, and magnetic saturation effects was investigated.

A hybrid model was proposed, which combines the analytical and the static FEM model with single rotor position. The hybrid model took slotting effect, fringing effect and magnetic saturation into account. This model was validated by comparing it to transient FEM computation, which was validated by experiments in Chapter 10. The hybrid model utilizes the fast calculation advantage of the analytical model and the accuracy of the FEM model. It therefore reduces the time needed for the design of PM machines in comparison with the FEM model as well as improves accuracy in comparison with the analytical model. In addition, a design process including the new hybrid model and automated transient FEM including rotor motion was proposed as shown in Figure 5.19.

CHAPTER 6

OPTIMAL ELECTROMAGNETIC TORQUE PERFORMANCES

6.1. Introduction

In Chapter 5, the influence of the slotting effect on magnetic field, flux linkage and internal voltage was investigated. In this chapter the influence of the slotting effect as well as other design parameters on mean torque, cogging torque and torque ripple is studied.

A major problem in the design of permanent magnet machines is the need to reduce cogging torque and torque ripple. Torque ripple is an inherent property of slotted PM machines, which causes mechanical vibration, acoustic noise, and decreases the life span of the machines [Dos 2007], [Ayd 2008], [Isl 2009]. A large number of applications therefore require minimized cogging torque and minimized torque ripple [Ash 2011], [Che 2010], [Wan 2010a], [Cho 2009], [Yan 2006].

There are three main components of electromagnetic torque in a PM machine, namely [Zhu 2000], [Isl 2009], [Bia 2002]: 1- mutual torque, caused by the interaction of the magnet and the armature field; 2- reluctance torque, which is due to rotor saliency producing variations of air gap reluctance with respect to rotor position; and 3- cogging torque, which is a result of the interaction between the permanent magnet field and the slotted stator. The torque quality can be improved by reducing torque ripple in mutual torque and reducing cogging torque. The average electromagnetic torque can be increased by salvaging reluctance torque.

Cogging torque and torque ripple elimination are highly challenging issues during the design of slotted PM machines. Several methods are reported in literature [Bia 2002], [Moh 2004], [Isl 2009], [Ayd 2008], [Ash 2011], [Che 2010], [Wan 2010a], [Fei 2010], [Cho 2009], [Yan 2006] to reduce cogging torque and torque ripple. Selecting the combination of slot and pole, fractional slot, dummy slot, air gap variation, skew of the magnet or stator, step-skew of the magnet, the design of magnet pole arc, the design of slot opening, PM shifting, and rotor eccentricity are well known techniques for reducing cogging torque.

The combination of slot and pole, slot opening and pole width are specifications that have great influence on mean torque, peak-peak cogging torque and torque ripple [Bia 2002], [Isl

2009]. By selecting the correct combination of slot and pole and the design optimization of slot opening and pole width, cogging torque can be reduced significantly without causing manufacturers any additional problems and without increasing costs as happens when other methods are used. The influence of slotting on the electromagnetic torque of slotted PM machines has not been reported in detail in literature. Therefore, the influence of slotting and other design parameters such as combination of slot and pole and magnet width on cogging torque, torque ripple and mean electromagnetic torque will be investigated in this chapter.

In this Chapter, the performances of electromagnetic force and torque of the PM machine B are analyzed. Mean torque performance is also presented as a function of the current angle and the current amplitude. A proposed process to estimate the influence of the combination of slot and pole on cogging torque is presented. Peak-peak cogging torque and torque ripple are presented as functions of the slot opening and magnet width. In addition, the relation between mean torque and slot opening is investigated. This is not covered in literature. The analysis gives insight into the change and relation of design parameters to torque performance. Most numerical calculation results of torque in this chapter use Maxwell's stress tensor method embedded in a nonlinear transient FEM simulation, however, they are also compared to those using the Virtual work method in a few cases, [Pyr 2008], [Dan 2005], [Pos 2005].

6.2. Maxwell's Stress Tensor

According to Maxwell's stress theory, the vector magnetic field strength $\vec{H}$ between objects in a homogeneous region (e.g. air) creates a vector stress $\overrightarrow{\sigma_F}$ on the object surface [Pyr 2008]. The stress can be divided into normal (radial) component and tangential component, [Pyr 2008]

$$\sigma_{Fn} = \frac{1}{2}\mu_0(H_n^2 - H_t^2) = \frac{1}{2\mu_0}(B_n^2 - B_t^2) \tag{6.1}$$

$$\sigma_{Ft} = \mu_0 H_n H_t = \frac{1}{\mu_0} B_n B_t \tag{6.2}$$

where H_n and H_t are the normal and tangential components of the vector magnetic field strength, B_n and B_t are respectively the normal and tangential components of the vector flux density, μ_0 is permeability of air.

In a 2D-FEM model, the attractive force (normal force or radial force) F_n and moving force (tangential force) F_t are calculated as,

$$F_n = \frac{1}{2\mu_0}\iint_S (B_n^2 - B_t^2)dS = \frac{L}{2\mu_0}\oint_l (B_n^2 - B_t^2)dl \tag{6.3}$$

$$F_t = \frac{1}{\mu_0}\iint_S B_n B_t dS = \frac{L}{\mu_0}\oint_l B_n B_t dl \tag{6.4}$$

where, S is the integration surface that is a flat surface chosen in the center of the air gap, L is the stator length, and l is the integration contour, which is chosen at the center of the air gap.

The cogging torque and electromagnetic torque of a PM machine can be calculated using Maxwell's stress tensor as, [Gue 2008], [Bia 2002], [Pyr 2008]

$$T = \frac{1}{\mu_0}\iint_S rB_n B_t dS \tag{6.5}$$

where, B_n and B_t are respectively the normal and tangential components of the flux density, μ_0 is the permeability of the air, and r is the radius. In the two dimensions FEM calculation, $r=sqrt(x^2+y^2)$.

In the 2D-FEM model, the formula below is normally used instead of equation (6.5) to approximately calculate electromagnetic torque,

$$T = \frac{L}{\mu_0}\oint_l rB_n B_t dl \tag{6.6}$$

where, L is rotor axial length, and contour l is chosen at the central air gap for calculating the line integral [Bia 2002].

According to [Pyr 2008], [Bia 2005], instead of equations (6.5) and (6.6), it is possible to compute the average value of the electromagnetic torque over the entire air-gap surface. The torque can therefore be calculated as

$$T = \frac{L}{\mu_0 g}\iint_S rB_n B_t dS \tag{6.7}$$

where, g is air gap length and S is the double integral in the air gap area constituted by the layers between the stator and the rotor. It should be noted that the equation (6.7) is only valid in a homogeneous region so that the air gap should be divided into three layers and the electric conductivities of stator iron and magnets are set to zero during simulation. Calculated results according to equations (6.6) and (6.7) will be compared in the next section.

6.3. Analysis of Electromagnetic Force and Torque

In this section, electromagnetic force and torque of the 27-slot, 18-pole PM machine with concentrated windings (i.e., the reference machine B) are investigate, during noload and load.

6.3.1. During No-load

Figure 6.1 shows cogging torque versus rotor angle with different methods using Maxwell's stress tensor, equation (6.7) and the Virtual work method. As can be seen, the results calculated by different methods, are almost the same. The peak – peak cogging torque is about 1.2 Nm. With the 27 slots and 18 poles, the number of periods of cogging torque per pole pair N_p is *6* and number of periods of cogging torque per slot N_s is 2.

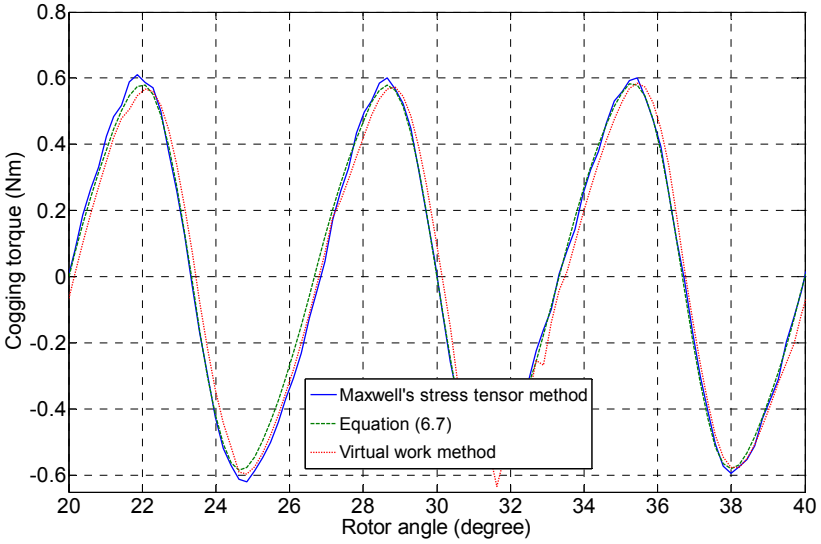

Figure 6.1. Cogging torque vs. rotor angle, with linear magnetic calculation according to different methods, at speed 3150 rpm.

It is confirmed from FEM analysis that the accuracy of the torque calculation mainly depends on three factors. First, the discretization meshes should be sufficiently fine to be able to solve the air gap magnetic field accurately; otherwise, some unexpected ripple on the torque performance due to numerical error can arise. Secondly, the integration contour position has to be chosen carefully. For Maxwell's stress tensor the air-gap is divided into two layers, which correspond to the stator air-gap and the rotor air-gap. The integration contour should be in the centre of air gap. The proximity of the integration contour nearby the stator steel or magnet can lead to errors in the torque calculation. The method using equation (6.7) calculating cogging torque converges to the Maxwell's stress tensor with the integration contour in the centre of the air gap. Third, the order of the shape functions in FEM computation also influences computation accuracy. The second order elements are a good choice for torque computation.

6.3.2. During Load

In this subsection, tangential force and electromagnetic torque during load are investigated. In addition, the mean torque is presented as a function of current angle and current amplitude.

Figure 6.2 shows tangential force and electromagnetic torque versus rotor angle at a rated current and a current angle of 90 degrees (current angle is the angular displacement between the vector fundamental field produced by the magnet and the vector stator current). Figure 6.3 shows the electromagnetic torque of the PM machine B versus time, with sinusoidal current, electric current angle of 90 degrees, and different current amplitude I_m. The electric current angle is the angle between the vector stator current and the *d*-axis of the rotor field coordinate. Compared to the fundamental internal voltage frequency (presented in Chapter 5), torque frequency is 6 times higher. The number of the torque ripple and the number of cogging torque in a time interval are the same. This is due to the fact that torque ripple arises from the interaction between the magnetic field of the magnets and the stator slotting.

It can be seen from Figure 6.4a that the mean electromagnetic torque is presented as a function of current angle, but the waveform is not sinusoidal, due to magnetic saturation. The waveform is distorted more when electric current increases (increasing magnetic saturation level). Besides, the peak of maximum average torque is not located at point with a current angle of 90 degrees, but it biases an angle of about 1.5 electric degrees (for k_i=1.25). When the electric current is small, the torque waveform with respect to rotor angle is nearly sinusoidal. It is symmetrical through the vertical axis at 90 degrees. Figure 6.4b presents mean electromagnetic torque versus current angle and current amplitude. It shows that when the current amplitude is smaller than the rated current, the electromagnetic torque is nearly linear with current amplitude. However, when current amplitude is higher than the rated value, the relation becomes nonlinear.

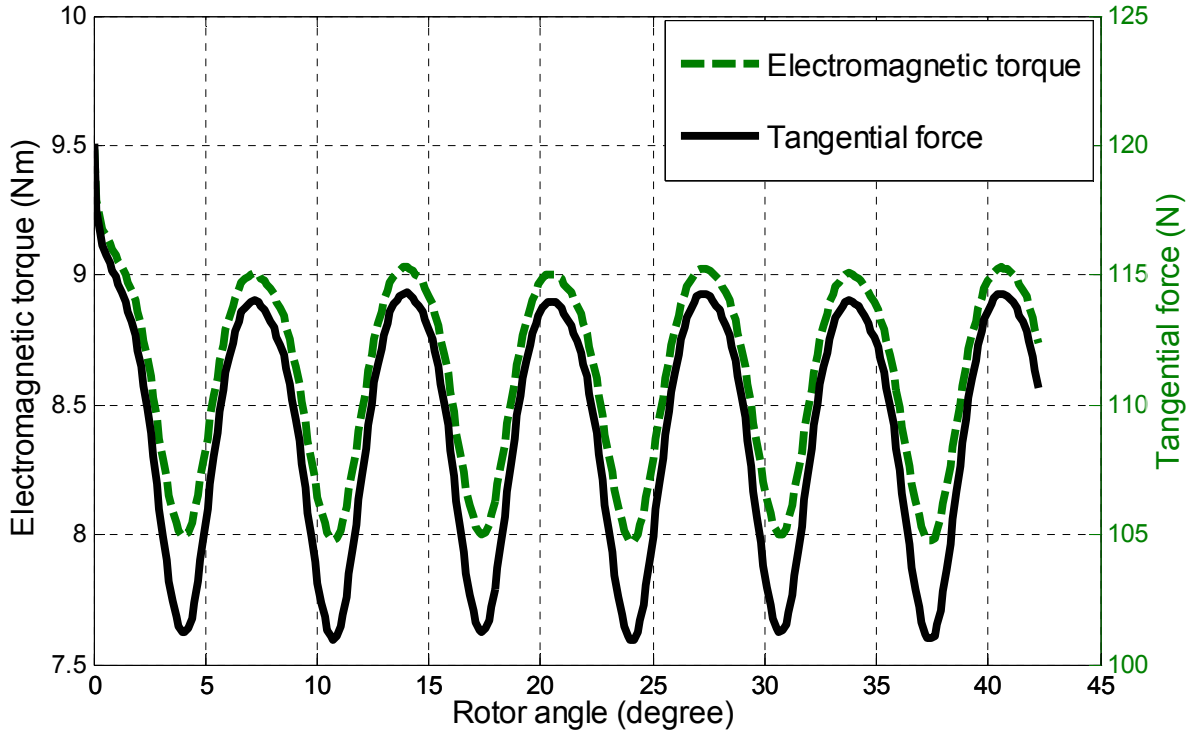

Figure 6.2. Electromagnetic torque and tangential force versus rotor angle.

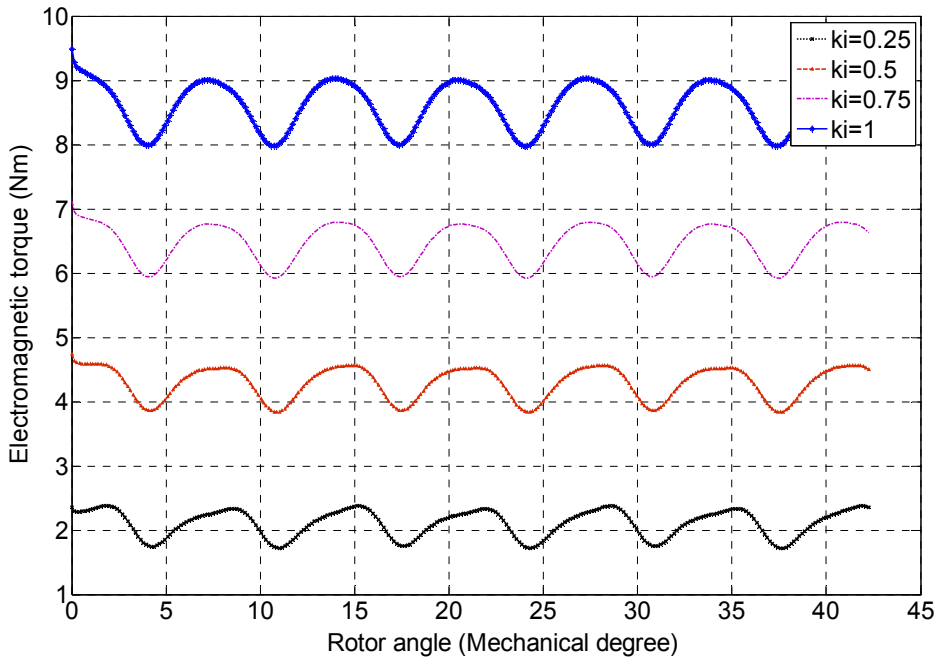

Figure 6.3. Electromagnetic torque versus rotor angle, with a current angle of 90 degrees, where k_i is ratio of current amplitude to rated current amplitude.

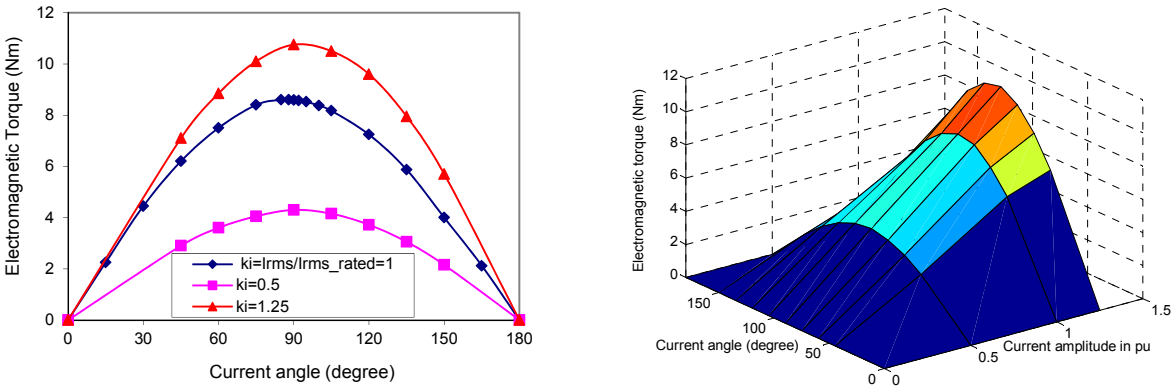

a) b)

Figure 6.4. Mean electromagnetic torque versus current angle and current amplitude.

6.3.3. Influence of Magnetic Saturation on Electromagnetic Torque

Figure 6.5 compares electromagnetic torques of the 27-slot and 18-pole PM machine during linear magnetic circuit and magnetic saturation. In the case of the linear magnetic circuit, the relative permeability of the rotor yoke and stator iron lamination are 300 and 600 respectively. As can be seen, both the mean electromagnetic torque and torque ripple strongly depend on magnetic saturation. Torque ripple with linear magnetic circuit is larger than that of magnetic saturation. The mean electromagnetic torque in the case of magnetic saturation is 15% smaller than that of linear magnetic circuit. It is therefore suggested that magnetic saturation always needs to be taken into account in electromagnetic force and torque calculation [Mad 2003], [Kim 2010].

Figure 6.6 shows the mean electromagnetic torques of the 27-slot and 18-pole PM machine calculated for linear and nonlinear magnetic circuits. If a linear magnetic circuit is assumed, the mean electromagnetic torque waveform versus current angle is sinusoidal. This means that the performance is symmetrical over a vertical axis at 90 degrees. However, in the case of non-linear magnetic circuit, the performance is unsymmetrical and peaks at a current angle of 89 degrees.

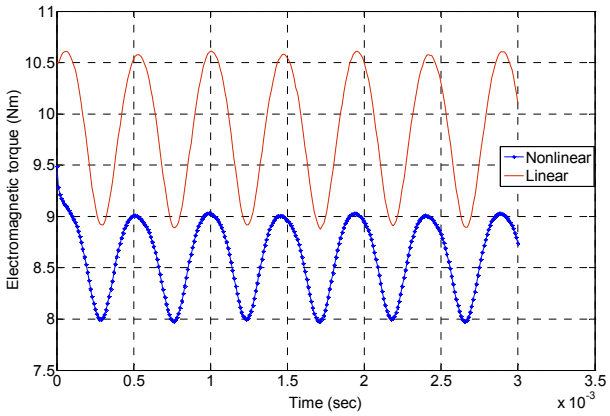

Figure 6.5. Electromagnetic torques versus time, with I_{rms}=10 A, at a current angle of 90 degrees. Comparing electromagnetic torques of linear magnetic circuit and magnetic saturation.

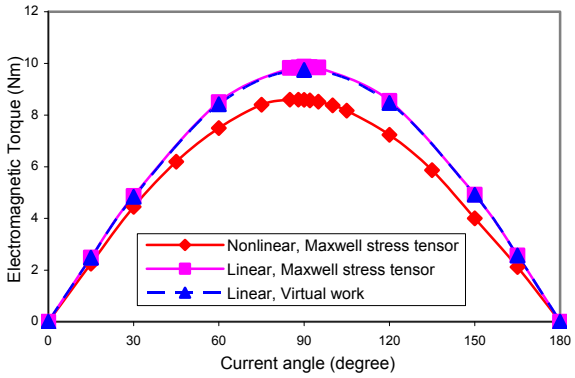

Figure 6.6. Electromagnetic torques versus current angle, the PM machine B. Electric current applied in windings is the same in both cases of nonlinear calculation and linear magnetic calculation.

6.4. Influence of Design Parameters on Cogging Torque during No-load

In this section, the influence of slot and pole combinations on the cogging torque is presented first. Afterwards, the influence of slot opening and magnet width on cogging torque is investigated. Finally, peak–peak cogging torque is presented as a function of both slot opening and magnet width.

6.4.1. Influence of Slot and Pole Combination on Cogging Torque

In this subsection, the influence of the slot and pole combination on the peak-peak cogging torque is investigated. A new process is proposed to evaluate the influence of pole number, slot number, and combination of slot and pole on peak-peak cogging torque.

The cogging torque can be described using a Fourier series expansion as [Bia 2002],

$$\tau_{cog}(\theta_m) = \sum_{k=1}^{\infty} T_k \sin(kN_s Q\theta_m + \varphi_k) \tag{6.8}$$

where Q is the number of the slots, N_s is the number of cogging torque periods per slot, θ_m is mechanical angle position of the rotor, φ_k is initial angle of the harmonic component k^{th}.

The slot/pole combination must be selected at the beginning of design process in order to reduce the cogging torque and meet other requirements such as minimizing eddy current loss. Selecting the right slot/pole combination can efficiently reduce cogging torque. For example, the analysis in Figure 6.7 shows that the peak-peak cogging torque of the modular PM machines with 24-slot/20-pole, 24-slot/22-pole, 24-slot/26-pole and 24-slot/28-pole is small enough, while that of conventional PM machines with 24-slot/16-pole and 27-slot/18-pole combinations are significant. For fair comparison of cogging torque, the PM machines have the same ratio of slot opening/slot pitch and pole width/pole pitch as well as the same stator and rotor diameters. Magnetic saturation is taken into account. It should be noted that magnetic saturation strongly influences cogging torque. For example, during linear simulation, the peak-peak cogging torque of two machines with 27slots/18poles and 24slots/16poles are nearly the same, as shown in Figure 6.8, because they have the same combination of slot and pole. However, when magnetic saturation is taken into account the peak-peak cogging torque of the two machines differ, as shown in Figure 6.7.

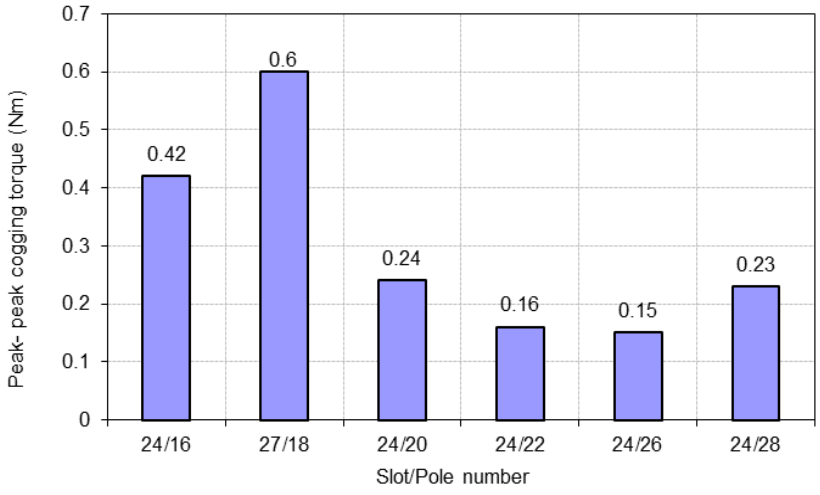

Figure 6.7. Influence of slot/pole combination on cogging torque, with magnetic saturation taken into account.

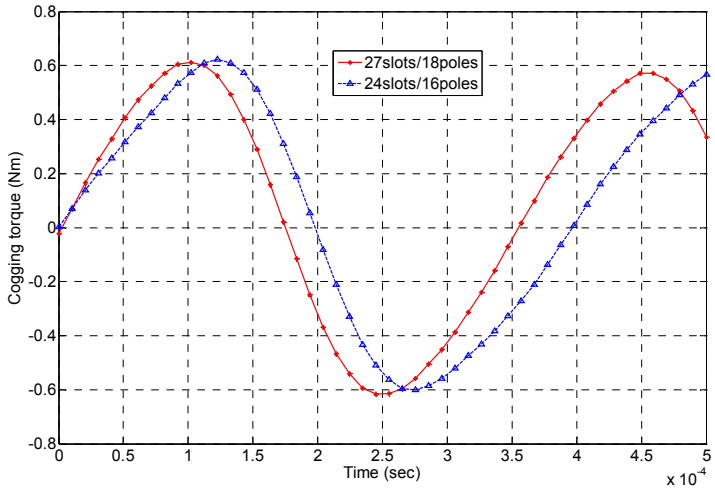

Figure 6.8. Cogging torque of two machines with 27slots/18poles and 24slots/16poles, with linear simulation.

To evaluate the peak-peak cogging torque, the following terminologies are used.

- The number of periods of the cogging torque per mechanical revolution (CPMR) depends on the number of slots and poles. For a rotor with identical poles, equally spaced around the rotor and linear iron, the CPMR is computed as [Bia 2002], [Bia 2005], [Moh 2004], [Hwa 2006], [Isl 2009]

$$CPMR = LCM(Q,2p) \tag{6.9}$$

  where, *LCM* stands for the least common multiple, Q is slot number and p is the number of pole pairs.

- The number of cycles of cogging torque per pole pair is calculated as [Bia 2002], [Moh 2004],

$$N_p = CPMR/p \tag{6.10}$$

- The number of cycles of cogging torque per slot is calculated as, [Moh 2004], [Isl 2009]

$$N_s = CPMR/Q = 2p/GCD(Q,2p) \tag{6.11}$$

  where, *GCD* stands for the greatest common divisor.

Note that if PM machines have the same slot number per pole per phase, they have the same N_p as well as the same N_s. Moreover, we have the fact that $LCM(Q,2p).GCD(Q,2p)=2pQ$.

Table 6.1 gives comparison results of the peak-peak cogging torque and the indexes used to evaluate the peak-peak cogging torque of typical PM machines with fractional slots.

Table 6.1. Comparison of the cogging torque and the index of PM machines.

Combination of slot/pole	Slot number, Q	Pole number, $2p$	LCM (Q,$2p$)	GCD (Q,$2p$)	N_p	N_s	T_{p-p} (Nm)
3/2	24	16	48	8	6	2	0.42
3/2	27	18	54	9	6	2	0.65
6/5	24	20	120	4	12	5	0.24
12/11	24	22	264	2	24	11	0.16
12/13	24	26	312	2	24	13	0.15
6/7	24	28	168	4	12	7	0.23

Based on the analysis results in Table 6.1 and the calculation results of Hwang in [Hwa 2006], a process to evaluate the peak-peak cogging torque of PM machines is proposed as follows.

- The number of periods of cogging torque per slot N_s is the most significant index to evaluate the peak-peak cogging torque. The greater the N_s, the smaller the peak-peak cogging torque. When the N_s of any combinations of slot and pole is equal, the number of periods of cogging torque per pole N_p becomes the index for evaluation.
- The greater the N_p, the smaller the peak-peak cogging torque. When both the N_s and N_p of any combinations of slot and pole are identical, the GCD becomes the index for evaluation.
- The smaller the GCD, the smaller the peak-peak cogging torque. When the indexes N_s, N_p and GCD of any combinations of slot and pole are equal, the LCM is the index for comparison of the peak-peak cogging torque.
- The greater the LCM, the lower the peak-peak cogging torque.

6.4.2. Cogging Torque as Function of Slot Opening

Figure 6.9 shows cogging torque versus time and slot opening, corresponding to a certain magnet width/pole pitch of 0.72 (of the reference PM machine B). As can be seen from Figure 6.10, the peak–peak cogging torque strongly depends on the slot opening. In general, the variation of cogging torque with respect to slot opening is hard to predict because the edge effect of magnet and slot opening, combination of slot and pole, magnet width, and magnetic saturation [Liu 2008], [Zhu 2010], [Bia 2002] influence cogging torque. In Figure 6.10, the peak–peak cogging toque varies from 0 to 1.9 Nm. The zero peak-peak cogging torque is at a closed slot opening. This is because air gap reluctance reaches a constant value when the slot opening width becomes zero. In addition, cogging torque is proportional to the derivative of air gap reluctance with respect to rotor angle. However, in practice, slot opening width should be great enough to place windings, so the slot opening for minimum peak-peak cogging torque is 5 mm. By presenting

peak–peak cogging as a function of slot opening, a slot opening can be selected for minimum cogging torque.

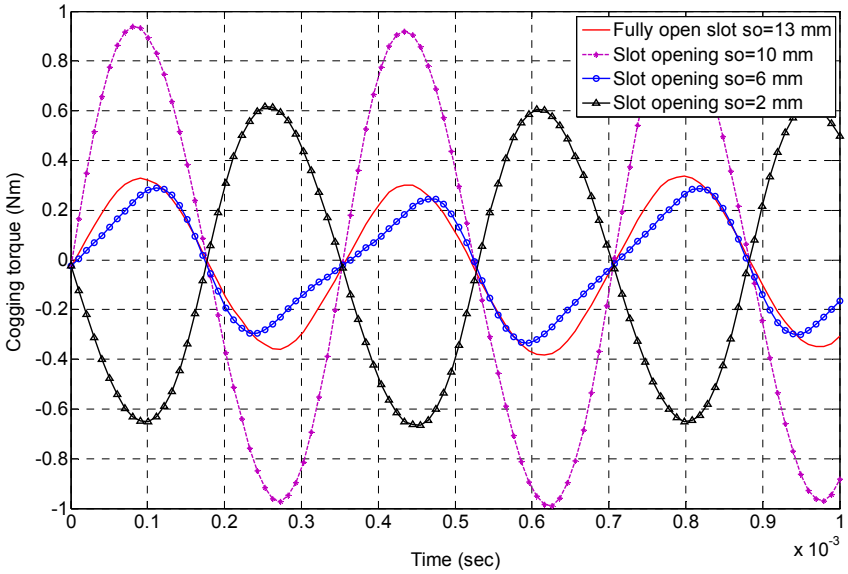

Figure 6.9. Cogging torque versus time and slot opening, with the ratio of magnet arc width to pole pitch equal to 0.72, magnetic saturation taken into account for both stator and rotor.

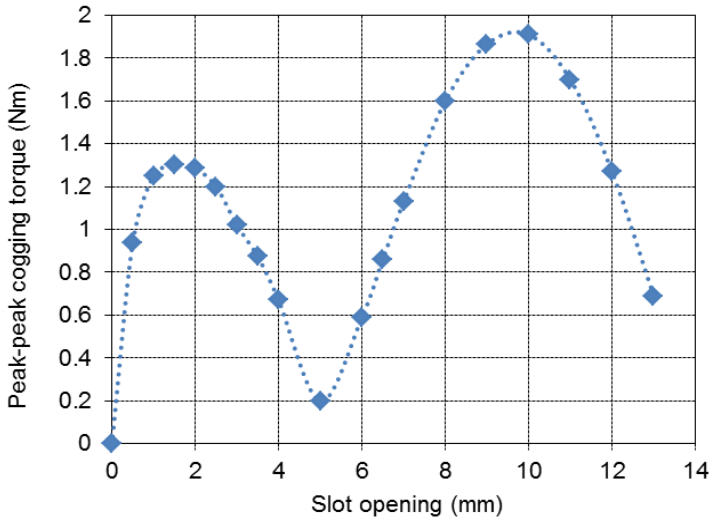

Figure 6.10. Peak – peak cogging torque versus slot opening, with the ratio of magnet arc width to pole pitch equal to 0.72.

6.4.3. Cogging Torque as Function of Magnet Width

Figure 6.11 presents cogging torque versus time and magnet width with a slot opening of 6 mm. Figure 6.12 shows the peak–peak cogging torque as a function of magnet width/pole pitch. The peak-peak cogging torque varies in a wide range from 0.25 Nm to 5.58 Nm with respect to a magnet width/pole pitch variation of 0.5 to 1. It has a minimum value of 0.25 Nm at a magnet width/pole pitch of 0.73. When the magnet width/pole pitch is greater than 0.73, the peak-peak cogging torque increases fast. It peaks at a magnet arc of 1. The calculation results are in agreement with those found in the literature [Liu 2008], [Fei 2010].

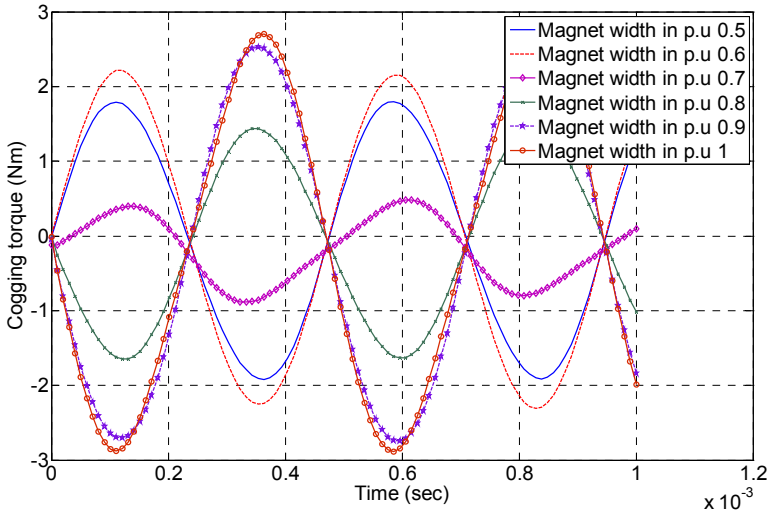

Figure 6.11. Peak – peak cogging torque versus time and magnet width, with slot opening of 6 mm, the reference PM machine B.

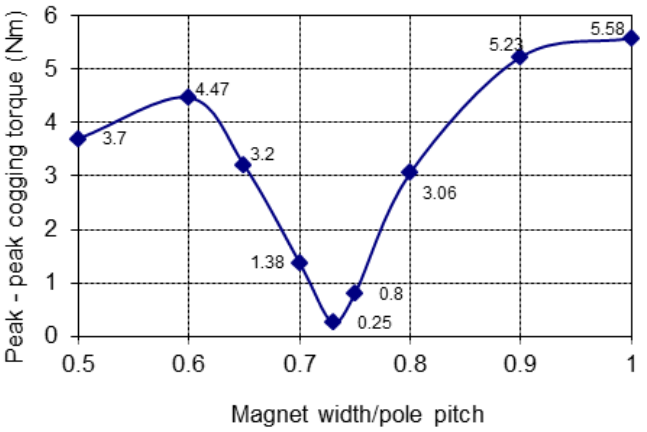

Figure 6.12. Peak – peak cogging torque versus magnet width, with slot opening of 6 mm, the reference PM machine B.

6.4.4. Cogging Torque as Function of Slot Opening and Magnet Width

Figure 6.13 presents the peak – peak cogging torque as a function of slot opening and magnet width. Clearly, the cogging torque, slot opening, and magnet width relation is complex. The global value for minimizing peak – peak cogging torque is found around the point with the coordinate (slot opening, magnet width, peak-peak cogging torque) = (6mm, 0.73, 0.25Nm).

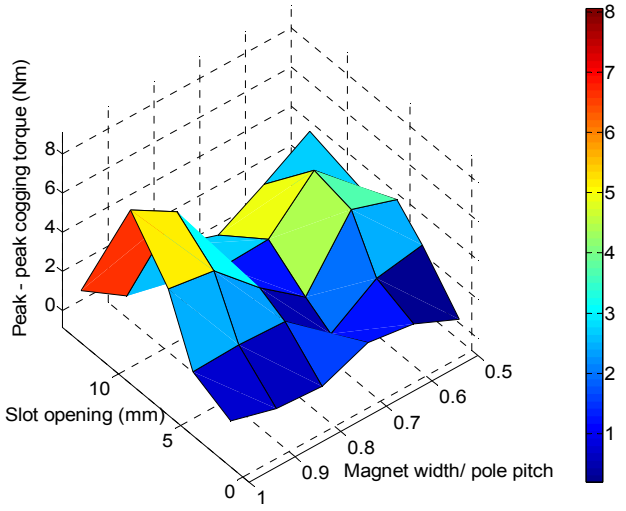

Figure 6.13. The peak – peak cogging torque versus slot opening and magnet width.

6.5. Influence of Slot Opening and Magnet Width on Torque during Load

In this section, the influence of slotting and magnet width on torque ripple and mean torque is investigated. Slot opening and magnet width are optimized for minimizing torque ripple. The relation between mean torque and slot opening is investigated. This has not been mentioned in literature before. Magnet width is optimized for minimizing torque ripple and maximizing mean torque.

6.5.1. Torque Ripple versus Slot Opening

Torque ripple is the difference between the highest peak and the lowest peak of electromagnetic torque. Figure 6.14 presents torque ripple versus slot opening, corresponding to a magnet width/pole pitch of 0.72 (of the reference PM machine). As can be seen the torque ripple varies in a wide range from 0.73 to 2.15 Nm. The smallest value of torque ripple corresponds to a slot opening of about 4 mm, while a peak of 2.15 Nm is reached at a slot opening of 9 mm. By presenting torque ripple as a function of slot opening, a slot opening can be selected for minimizing torque ripple. It can be seen that torque ripple is at a minimum at a slot opening different from the value where peak-peak cogging torque is at a minimum. Nevertheless, the two

optimal values are not too far apart. Hence, a slot opening selected within two optimal points can achieve minimum torque ripple and minimum peak-peak cogging torque at the same time.

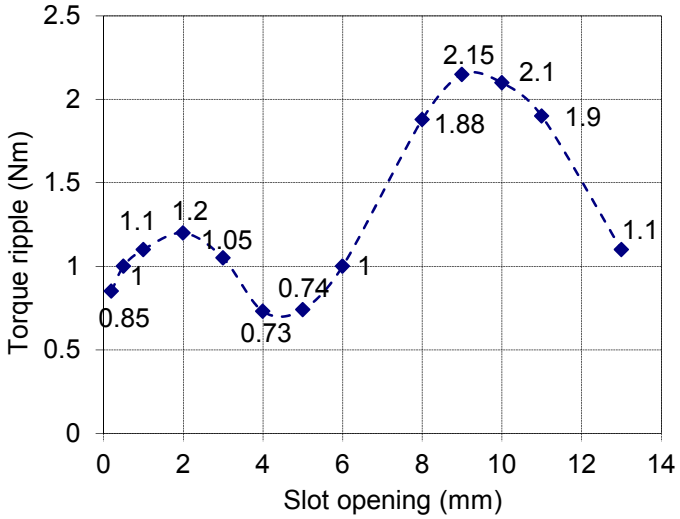

Figure 6.14. Torque ripple vs. slot opening, at a current angle of 90 degrees and rotor speed of 3150 rpm.

6.5.2. Mean Electromagnetic Torque versus Slot Opening

Figure 6.15 presents the mean electromagnetic torque versus slot opening for rated current, at a current angle of 90 degrees. As can be seen, slot opening affects mean electromagnetic torque significantly. If a slot opening is larger than 4mm, the flux linkage decreases in Figure 5.11, Chapter 5. Therefore, the mutual torque due to the interaction of magnetomotive force and magnet field reduces. Thus, mean electromagnetic torque also decreases when the slot opening increases.

With a slot opening smaller than 4 mm, the leakage flux across tooth tips increases and flux linkage decreases. Thus, mean torque reduces when the slot opening decreases. This has not been described in literature before. It has been mentioned in literature that when a slot opening decreases, flux density in the air gap increases so that mean electromagnetic torque increases as shown in equation (3.105), Chapter 3. However, in the range of small slot opening, leakage flux through tooth tips increases. This causes the decrease of flux linkage and mean electromagnetic torque. Based on the performance presented in Figure 6.15, a slot opening can be selected for maximizing mean electromagnetic torque. If we reconsider the performance of internal voltage versus slot opening as shown in in Figure 5.12, Chapter 5, for the case of magnetic saturation, we see that voltage reaches its maximum value at the same slot opening width as maximum mean torque.

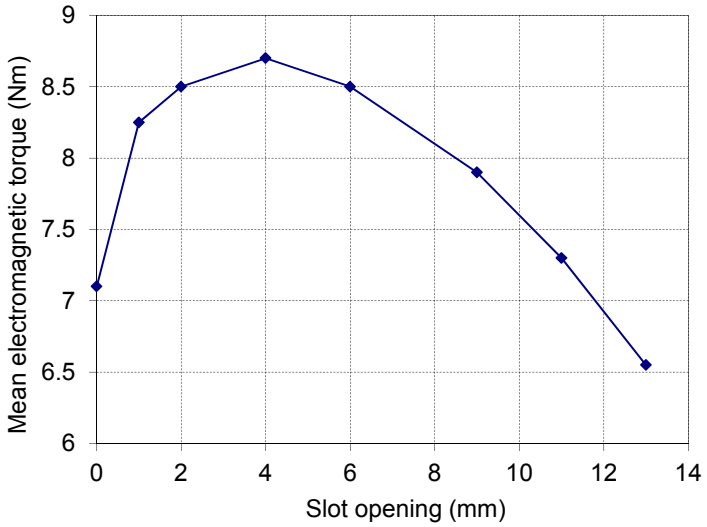

Figure 6.15. Mean electromagnetic torque vs. slot opening, at a current angle of 90 degrees.

6.5.3. Influence of Magnet Width on Torque Ripple and Mean Torque

Analysis results of torque ripple and mean electromagnetic torque are presented in Figures 6.16a and 6.16b. They show that torque ripple depends very much on magnet arc width. It varies from 0.7 Nm to 5.5 Nm, i.e., corresponding to from 7.5% to 62% of its mean electromagnetic torque. It reaches a minimum value at a magnet arc width of 0.73 (i.e., 131.4 electric degrees). When magnet arc width comes into full-size, the peak-peak cogging torque is quite high. Additionally, with a magnet arc width in the range of 0.7 and 1, the mean torque only changes with a narrow margin of about 5%. When magnet arc reaches 1, the mean torque reduces slightly due to the increasing leakage flux between two adjacent poles. However, when the magnet arc width is smaller than 0.7, mean torque significantly reduces in accordance with the reduction of magnet arc width. Generally speaking, the variation rule of torque ripple with respect to magnet arc width is difficult to predict and present in an expression, because it depends on many design variables: number of poles, slot/pole combination, magnetic saturation level, etc. Interestingly, the waveform of torque ripple versus magnet arc width (see Figure 6.16a) is nearly similar to that of peak-peak cogging torque versus magnet arc width (as shown in Figure 6.12). Therefore, magnet width can be selected for minimizing torque ripple and at the same time minimizing cogging torque.

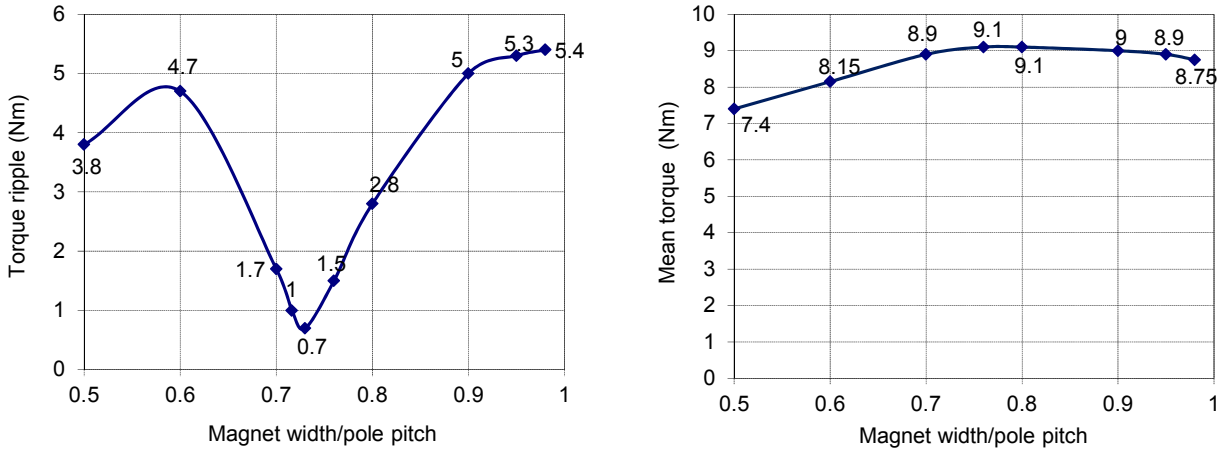

a) b)

Figure 6.16. Torque performances with fixed slot opening and ampere-turn: a) Torque ripple vs. magnet width/pole pitch, b) mean electromagnetic vs. magnet width/pole pitch.

6.5.4. Torque Ripple as Function of Slot Opening and Magnet Width

Figure 6.17 presents torque ripple as function of slot opening and magnet width. Torque ripple minimizes at coordinate [slot opening (mm), magnet width/pole pitch, torque ripple (Nm)]=[6, 0.73, 0.7]. Meanwhile, at these optimal parameters of minimal torque ripple, mean electromagnetic torque only reaches 8.8 Nm, which is smaller than the maximum mean torque of 9.1 Nm.

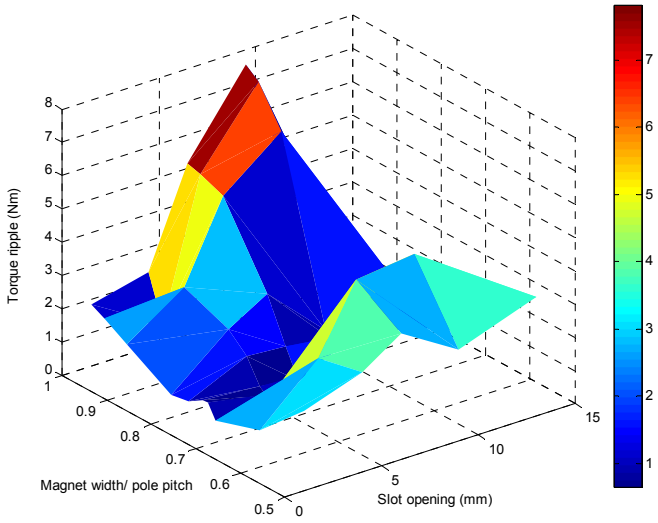

Figure 6.17. Torque ripple versus slot opening and magnet width.

6.5.5. Mean Torque as Function of Slot Opening and Magnet Width

Figure 6.18 presents mean electromagnetic torque as a function of slot opening and magnet width. Mean electromagnetic torque maximizes at the coordinate (slot opening (mm), magnet width/pole pitch, mean torque (Nm))=(6, 0.76, 9.1). If the magnet width/pole pitch of 0.72 is retained and the slot opening is varied, the characteristic performance of mean torque and slot opening becomes what is depicted in Figure 6.15, so Figure 6.15 is an individual case of what is depicted in Figure 6.18. A program based on the transient FEM model is developed to find the main design parameters such as slot opening and magnet width for maximizing torque. The algorithm used to solve the optimization problem is the direct search which is available in the Optimization Toolbox of Matlab®.

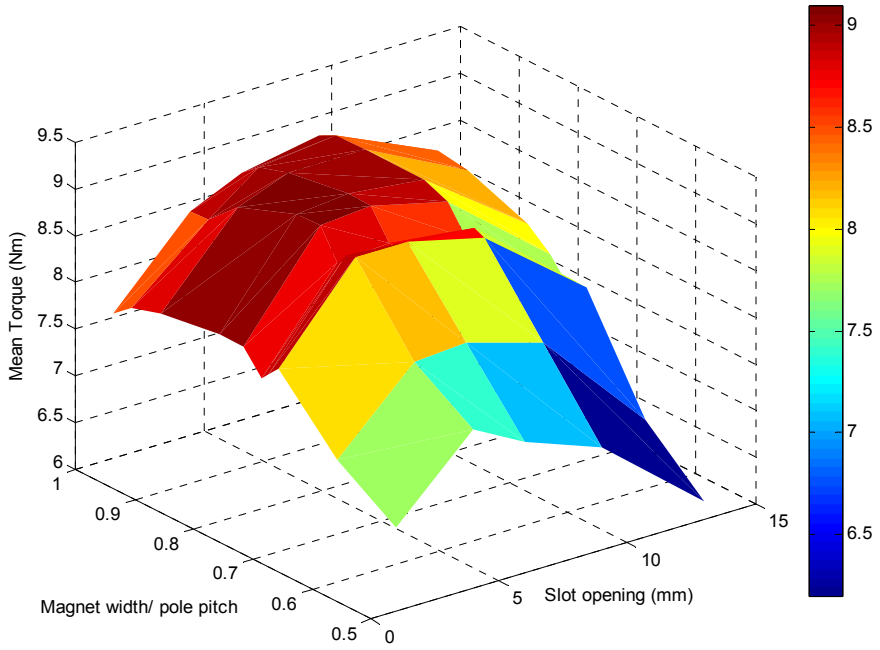

Figure 6.18. Mean electromagnetic torque versus slot opening and magnet width.

6.6. Conclusions

In this chapter, an approach to perform nonlinear transient FEM analysis including rotor motion for the calculation of electromagnetic force and torque is proposed. The study results show that cogging torque and electromagnetic torque are very sensitive to magnetic saturation. It is suggested that magnetic saturation should always be taken into account in the calculation of electromagnetic torque.

A process to evaluate the cogging torque is proposed. It is found that the number of cycles of cogging torque per slot N_s and the number of cycles of cogging torque per pole N_p are the first and second most important indexes used to evaluate cogging torque. The greatest common divisor GCD plays a less important role than the number of cycles of cogging torque per slot N_s and the number of cycles of cogging torque per pole N_p in estimating cogging torque, while, the least common multiple LCM is the least important in comparison with the other indexes. The smaller the number of cycles of cogging torque per slot N_s and the greatest common divisor GCD, the smaller the peak-peak cogging torque. The greater the number of cycles of cogging torque per pole N_p and the least common multiple LCM, the smaller the peak-peak cogging torque.

The influence of design parameters on cogging torque, torque ripple and mean torque was investigated. Cogging torque and torque ripple are presented as a function of slot opening and magnet width. The analysis helps increase insight into the influence of design parameters on electromagnetic torque performances.

The relation between mean electromagnetic torque and slot opening is investigated. The performance presented in Figure 6.15 can be used to choose slot openings for maximizing mean electromagnetic torque. The relation between torque and slot opening has not been described in literature before. It was known in theory that mean electromagnetic torque increases when slot openings decrease. However, in the range of small slot openings, leakage flux through tooth tips is increases when slot openings decrease. This causes the decrease of flux linkage passing through stator windings and of mean electromagnetic torque.

It is interesting to point out that the optimal magnet arc width for minimum peak-peak cogging torque and minimum torque ripple, with a fixed slot opening width are identical, as shown in Figure 6.12 and 6.16a . However, the optimal slot openings for minimizing peak–peak cogging torque and for minimizing torque ripple, with a fixed magnet arc pole, are different, although they are not very dissimilar, as shown in Figure 6.10 and 6.14

Selecting the right combination of slot and pole and optimizing major design parameters such as pole width and slot opening are an efficient way to minimize the peak-peak cogging torque or torque ripple.

CHAPTER 7

IRON LOSS MODELING AND ANALYSES

7.1. Introduction

In Chapter 5, the influence of slotting effect on magnetic field, flux linkage, and internal voltage was investigated. In Chapter 6, the influence of the slotting effect on cogging torque, torque ripple and mean torque was studied. In this chapter, the influence of the slotting effect on rotor eddy current loss and stator iron loss will be studied.

The rare-earth sintered magnets, e.g., Samarium-Cobalt (SmCo) or Neodymium-Iron-Boron (NdFeB) are electrical conductors with high conductivity. Thus, the eddy current losses produced in the magnets and rotor yoke take a significant part of the total losses and cannot be neglected.

The rotor eddy current losses of PM machine were studied by using analytical models [Pol 1999], [Dah 2005], [Zhu 2004], [Wan 2010b] based on assumptions such as either linear magnetic circuit or ignoring slotting effect. Transient FEM simulations were studied in [Kaw 2006], [Car 2008], [Yam 2010]. Nevertheless, there are not too many detailed studies, which include all of the following: magnetic saturation, influence of slot opening, operation modes and segmented magnets on the distribution of the rotor eddy current density and the rotor eddy current losses of exterior rotor PM machines with concentrated windings.

In this chapter, a non-linear transient two-dimensional FEM (2D-FEM) model including the motion of the rotor is used to study rotor eddy current losses. Loss in stator iron-core is also modeled and calculated. The 2D-FEM model is not as time-consuming as 3D-FEM model. The 3D model is not suitable for design optimization because numerous repetitive computations are required to find the optimal solution. In fact, the 2D-FEM eddy current computation is not as accurate as the 3D computation, but this can be limited by using the equivalent electric resistance of the conductor, instead of using the real one. The equivalent electric resistance is a function of the real electric resistance, dimensions of conductor, and conductor temperature [Ruo 2010]. Therefore, the goal of this chapter is to develop an automated 2D-FEM program to calculate rotor eddy current loss as well as stator iron loss for the design optimization of PM machines.

The distribution of eddy current density in magnets is investigated. The influence of slot opening and magnet segmentation as well as working modes of PM machine on eddy current loss is addressed. The method used allows the monitoring of the eddy current losses in the rotor as a function of time, rotor speed, load, and stator slot opening. The method therefore constitutes an indispensable FEM-tool in the design of PM machines taking the rotor eddy current loss into account. This method is able to make geometry model and to handle boundary conditions automatically, and to make calculated results of rotor eddy current loss more visual, but just in the 2D model.

7.2. Rotor Eddy Current Loss Formula

The eddy current density can be calculated by the following equations [Kaw 2006], [Pyr 2008]

$$\overrightarrow{J_e} = \sigma \overrightarrow{E_e} \tag{7.1}$$

$$\nabla \cdot \overrightarrow{J_e} = 0 \tag{7.2}$$

Since the eddy current circulates in its conductor, the equation (7.2) is required.

The influence of the end effect is neglected in the 2D model, thus the magnetic vector potential $\overrightarrow{A}$, the electric vector field strength $\overrightarrow{E_e}$ and the vector current density $\overrightarrow{J_e}$ only have component in the z-direction, so that $\overrightarrow{E_e} = E_z \overrightarrow{e_z}$, $\overrightarrow{A} = A_z \overrightarrow{e_z}$, and $\overrightarrow{J_e} = J_z \overrightarrow{e_z}$. The instantaneous eddy current loss in the magnets and the rotor yoke is calculated with the following equation [Zhu 2004],

$$P_{edd}(t) = \int_V \frac{|J_e|^2}{\sigma} dV = L \iint_S \frac{|J_{ez}|^2}{\sigma} dS \tag{7.3}$$

where, S and L are the cross section area and the length of conducting region in the z-direction, respectively. And V is the volume of the electrical conducting region in which the eddy current J_e is induced.

7.3. Rotor Losses of a Semi-Open Slot PM Machine

The eddy current loss dominates in the rotor domain. It is much larger than the rotor hysteresis loss, because the frequency of the eddy current is large enough. The rotor eddy current loss is

caused by slot opening, Magneto Motive Force (MMF)-winding harmonics, and time harmonics of the phase current. In this section, the distribution of the eddy current density and its loss are surveyed by using the 2D transient FEM model including rotor motion. Magnetic saturation is taken into account by applying BH curve. The rotor eddy current losses are calculated for the reference PM machine B with concentrated windings, 27 slots/18 poles, slot opening of 6 mm and the rated rotor speed of 3150 rpm. The rotor losses are calculated for both no load and load.

7.3.1. Rotor Eddy Current Loss during No-load

The rotor eddy current loss during no load is due to the existence of slot opening. The flux density distribution in the magnets of a slotted PM machine is not homogeneous (as presented in Chapter 5). It is stronger at positions opposite the teeth and weaker under the slot opening. When the rotor moves, the eddy current is induced in the magnets and the rotor back iron.

Figure 7.1 presents the surface plot of the eddy current density in the rotor, at time of 0.1 ms. As can be seen large values of eddy current density in magnets is situated under slot opening.

Figure 7.2 and Figure 7.3 show the distribution of the eddy current density in magnets as a function of mechanical angle (in stator reference frame) and radius. The mechanical angle θ_m of a point in the magnets at time t is defined as $\theta_m = \omega.t + \theta_0$, where ω is the angle speed of rotor and θ_0 is mechanical angle of the point in the magnets at time t=0. At positions in magnets opposite slot opening, the eddy current density changes rapidly with respect to variations of the radius and mechanical angle. At time of 0.1 ms, it reaches its highest value at points on the surface of magnets and the opposite slots (about 13 degrees for the first magnet and 26.5 degrees for the second magnet). It decreases, while the arc radius increases. Inversely, at positions under teeth, the eddy current density is nearly unchanged when the radius and mechanical angle change.

Figure 7.4, Figure 7.5, and Figure 7.6 show the magnetic vector potential, flux density and eddy current density at a point in the middle of magnet with respect to time. As can be seen, the magnetic vector potential and the eddy current density at a point with respect to time have the same frequency. The fundamental frequency of the eddy current density f_e at a point is equal to the product of the slot number Q per pole pair (Q/p) and the fundamental frequency of the rotating field ($p.n/60$), thus,

$$f_e = Q\frac{n}{60} = \frac{Q}{p}f \tag{7.4}$$

where, f is the fundamental frequency of the rotating field, p is the number of pole pairs, Q is the number of slots, and n is rotation of the rotor per minute.

The eddy current density frequency is dependent on slot number per pole pair, so that it is called the slot frequency. For example, the ratio of the number of slots to the number of poles is 3/2, hence the fundamental frequency of the eddy current at a point is greater than that of the rotating field by factor of three.

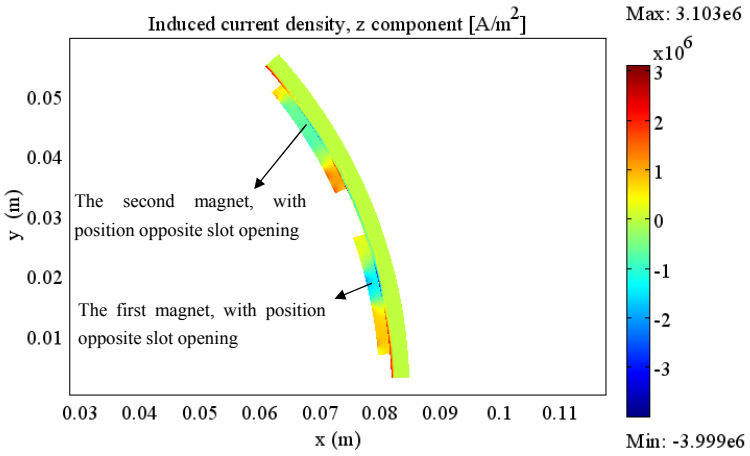

Figure 7.1. Eddy current density map in magnets and rotor yoke at time of 0.1ms, with rotor speed of 3150 rpm, during no-load.

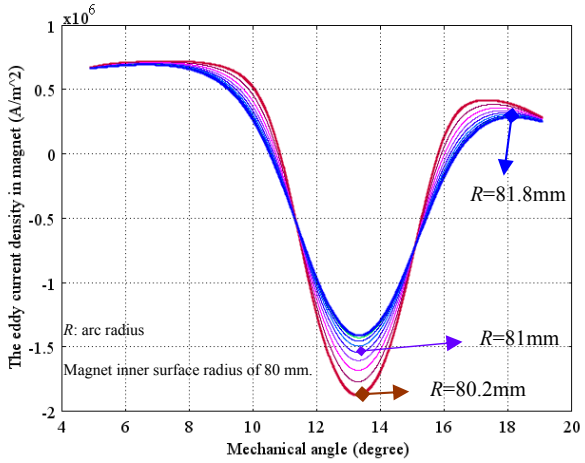

Figure 7.2. Eddy current density in the first magnet versus mechanical angle (in the stator reference frame), at time of 0.1ms, during no-load simulation, corresponding to arc radius in range of R=80.2:0.2:81.8 mm.

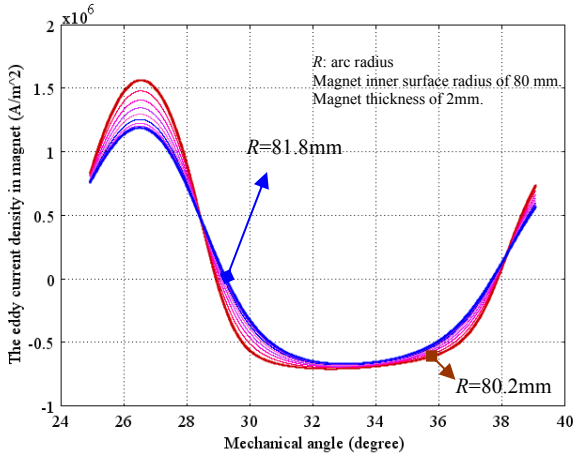

Figure 7.3. Eddy current density in the second magnet versus mechanical angle (in the stator reference frame), at time of 0.1 ms, during no-load simulation, corresponding to arc radius in range of R=80.2:0.2:81.8 mm.

Figure 7.7 presents the amplitude of harmonic components of the eddy current density waveform standardized to the fundamental frequency of the rotating field *f*. As can be seen, the dominant harmonic components in the eddy current density are the third, sixth and ninth of the fundamental frequency of the rotating field *f*; or the first, second, and third multiples of the fundament frequency of the eddy current density *3f* [Ama 2005]. The PM machine has 18 poles, the rated speed of 3150 rpm, and the rated frequency of 472.5 Hz. Hence, the fundamental frequency of the rotor eddy current density is 1417.5 Hz. As a result, the rotor eddy current loss is significant.

As frequency increases, electric current begins to move from an equal distribution through the conductor cross section toward a layer close to the outer surface of conductor. This phenomenon is known as the skin effect. The thickness of the layer is called the skin depth. Figure 7.8 presents the variation of the skin depth normalized to half of the magnet width versus the harmonic order. It is evident that, for most of the dominant harmonics, the skin depth is much greater than half of the magnet width, which indicates that the influence of skin depth is negligibly small.

Figure 7.9 shows the instantaneous eddy current losses with respect to time. The eddy current loss of the rotor back iron is much smaller than that of the magnets. This is because the rotor back iron is farther from the air gap than the magnets, so that the eddy current density in the rotor back iron due to slot opening effect is smaller.

The eddy current loss in the magnets and rotor back iron is proportional to square of the eddy current density. Therefore, the fundamental frequency of the eddy current loss is twice that of the eddy current density, i.e., six times bigger than that of the rotating magnetic field.

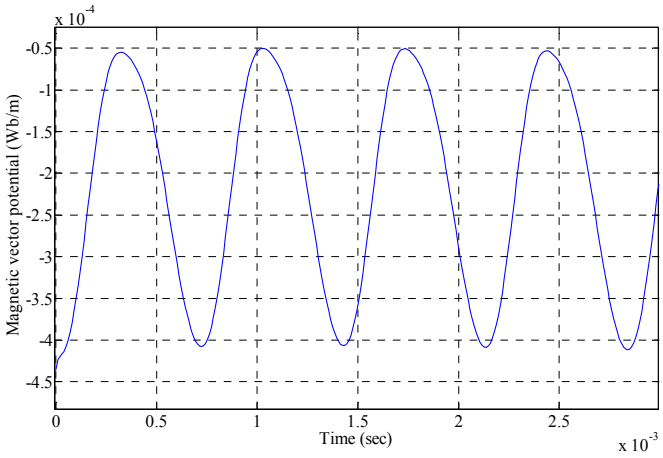

Figure 7.4. Magnetic vector potential in the middle of the first magnet during no-load.

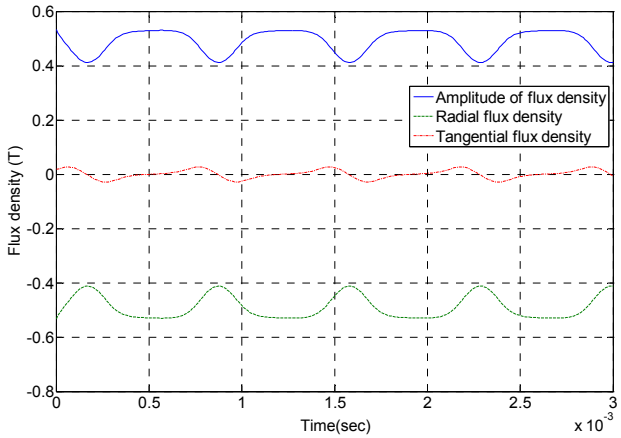

Figure 7.5. Flux densities in the middle of the first magnet during no-load.

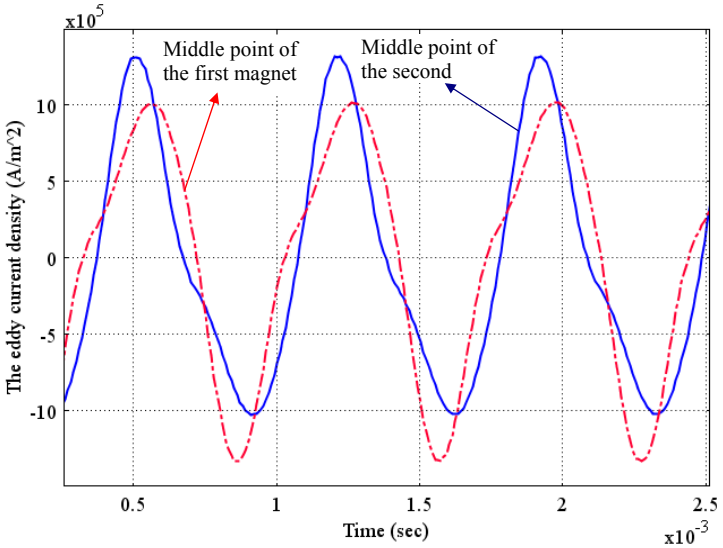

Figure 7.6. Eddy current density of points in the middle of magnets vs. time.

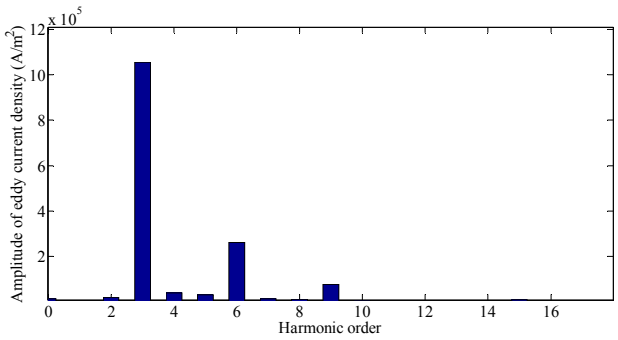

Figure 7.7. Amplitude of harmonic components of the eddy current density of a point in the middle of the first magnet.

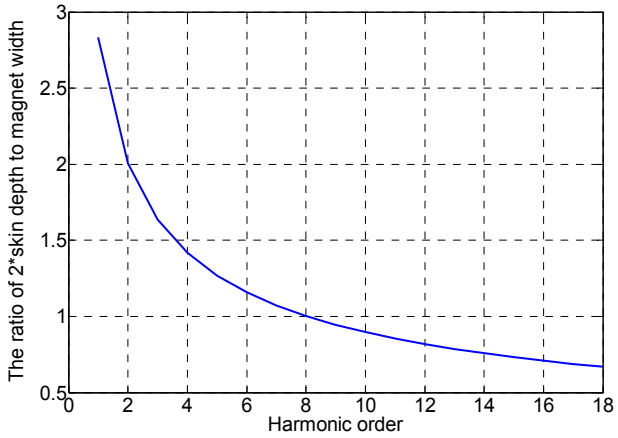

Figure 7.8. Skin depth as a function of harmonic order normalized to half of magnet width.

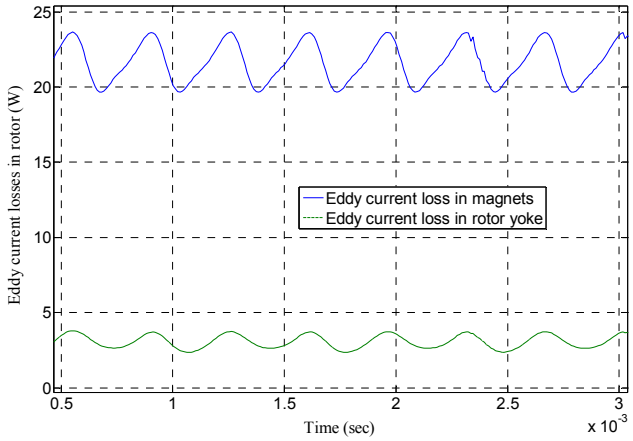

Figure 7.9. The instantaneous the eddy current losses in the magnets and rotor yoke at the rated rotor speed of 3150 rpm, during no load.

7.3.2. Rotor Eddy Current Losses with Load

During ideally sinusoidal current load, the eddy current losses in the rotor are due to stator slot opening and magnetomotive force (MMF) winding harmonics.

The eddy current loss caused by slot opening is calculated during no-load, which is mentioned in the foregoing section.

The eddy current loss due to MMF winding harmonics is calculated by means of setting up remanent flux density in magnets to zero. Meanwhile, there is rated armature current running in the windings. The magnetic field in this case is therefore generated by the armature current only. There is no magnetization of magnets in this case, so it is shortly called un-magnetization [Tot 2004], [Car 2008].

Figure 7.10 presents the results of calculating rotor eddy current losses with load. During calculation, it is assumed that the electric current of stator windings is sinusoidal. The eddy current losses in the rotor are shown as a function of the armature electric current amplitude I_a and the electric current angle β. The electric current angle is the angle between the vector stator current and the *d*-axis of the rotor field coordinator. Thus, the armature current is related to the *d*-axis current I_d and *q*-axis current I_q as $I_d=I_a.cos\beta$ and $I_q=I_a.sin\beta$. The horizontal axis in Figure 7.10 is the stator current amplitude in per unit (pu). It changes from zero to twice the rated current amplitude. The eddy current losses in the rotor are calculated for two typical operating modes. One is the maximum torque operation mode with a current angle of 90 degrees. The other is the operation mode with a current angle of 135 degrees.

As can be seen, the eddy current losses in both operating modes are greater than the eddy current losses during no load. The eddy current losses increase when the current amplitude increases. For the second operation mode, the rotor eddy current loss is 1.2 times higher than that of the maximum torque operation mode and 2.85 times higher than that of the no-load operation mode.

The rotor eddy current loss during the second operation mode might be expected to be lower than that during no-load, because of the demagnetizing armature reaction effect in the *d*-axis. In fact, however, the inverse occurs. This is because the concentrated winding-carrying current produces high amplitude and high frequency harmonic magnetic field in the *d*-axis in the air gap. The *d*-axis armature reaction of flux density harmonics leads to high frequency and harmonic losses in magnets and rotor yoke [Ziv 2006].

The eddy current density waveforms of the middle point of the first magnet are presented in Figure 7.11. They are calculated separately, corresponding to three cases namely, un-magnetization, no-load, and rated load with a current angle of 135 degrees. The term of un-magnetization can understand as the remanent flux density of magnets is assumed to be zero so

the field in the machine is produced by MMFs only. It is shown from Figure 7.11 that because of magnetic saturation, the magnet eddy current density at rated load is higher than the sum of the magnet eddy current density due to slotting and the magnet eddy current density due to MMFs alone.

It can be seen from Figure 7.12 that the eddy current loss in magnets due to MMF winding harmonics alone is much higher than that in rotor yoke. Figure 7.13 compares the eddy current losses in magnets and rotor yoke with rated current and a current angle of 135 degrees. As can be seen, because the influence of magnetic saturation, the total rotor eddy current loss at rated load is not equal to the sum of the losses calculated separately during no load as shown in Figure 7.9 and un-magnetization of magnets as shown in Figure 7.12.

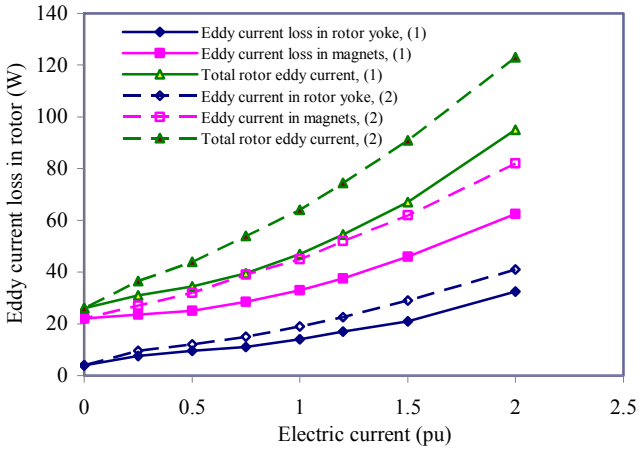

Figure 7.10. Rotor eddy current losses v.s. load current. Operating modes: (1)--Current angle of 90 degrees, the maximum electromagnetic torque. (2)--Current angle of 135 degrees.

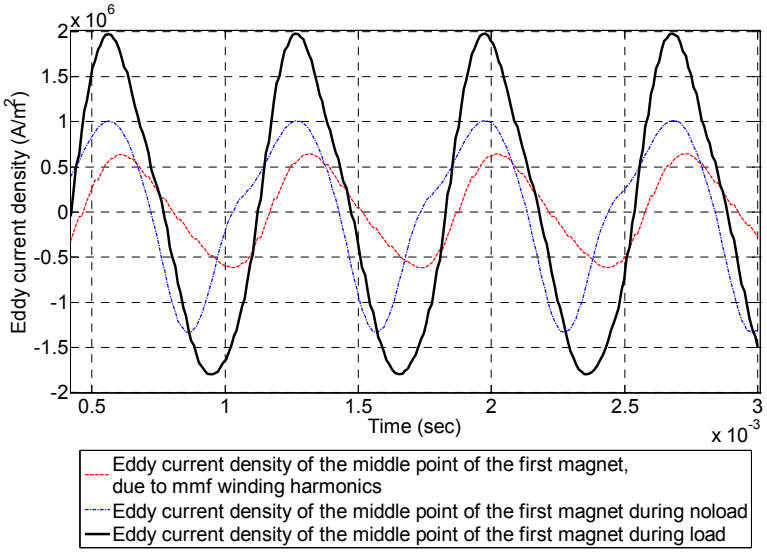

Figure 7.11. Eddy current densities of the middle point of the first magnet, calculated for three separated cases: un-magnetization, no-load, and rated load with current angle of 135 degrees.

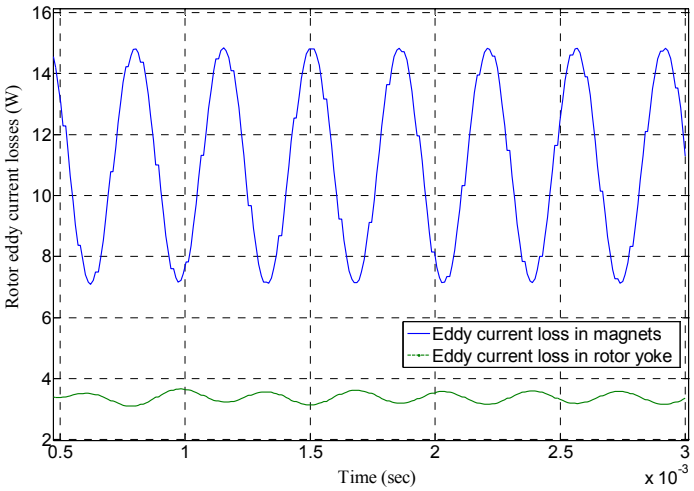

Figure 7.12. Eddy current losses in rotor due to MMF winding harmonics alone, at a current angle of 135 degrees, during un-magnetization of magnets.

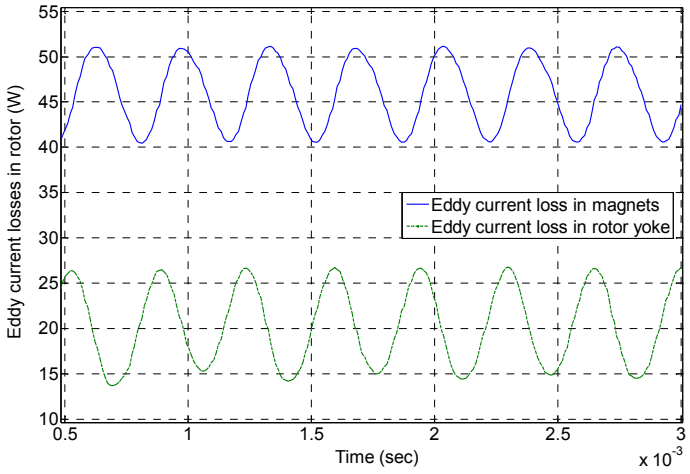

Figure 7.13. Eddy current losses in rotor with a rated current and a current angle of 135 degrees.

7.4. Influence of Slot Opening on Magnet Eddy Current Loss

To study the influence of slot opening on the rotor eddy current losses, the electric current in stator windings is setup to zero. Therefore, the rotor eddy current losses are only caused by slot opening. The rotor eddy current loss due to MMF harmonic components and the time harmonic components of stator current is equal to zero during no load.

7.4.1. Semi-Open Slot versus Fully Open Slot at 3150 rpm

Figure 7.14 shows eddy current density distribution of the middle arc of magnets. Figure 7.15 compares the eddy current density of points in the middle of the first magnet. It is shown that the

maximum value of the eddy current density of the middle point of the magnet of the fully open slot PM machine is greater by 2.4 times than that of the semi-open slot PM machine. As a result, the mean value of the eddy current loss of the fully open slot PM machine is greater by ~5.5 times than that of the semi-open slot PM machine (more information about this comparison can be found in Figure 7.28).

The maximum value of the magnet eddy current density increases when the slot opening increases. However, the frequency of the eddy current density at a point is constant when the slot opening dimension changes, i.e., the frequency is not dependent on slot opening dimension. This is because the frequency of the eddy current density is only dependent on the number of slots per pole pair.

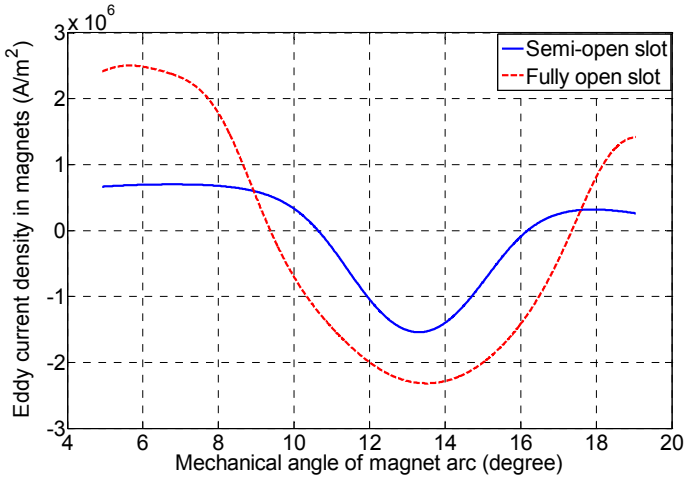

Figure 7.14. Eddy current density distribution of arcs in the middle of magnets v.s. mechanical angle, at time of 0.1 ms.

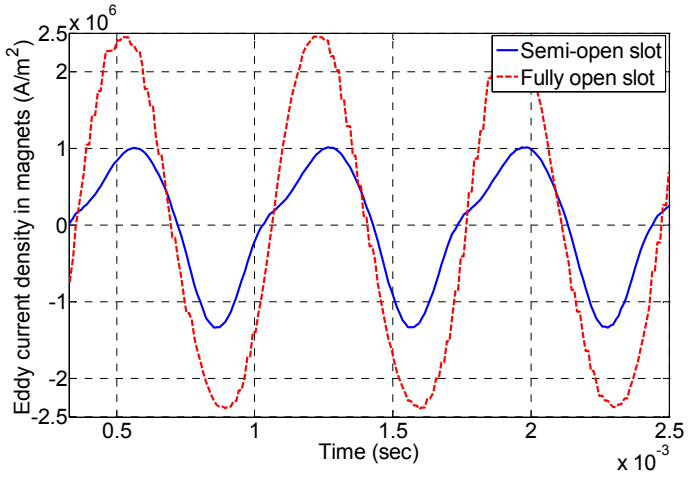

Figure 7.15. Eddy current density of the middle points of magnets v.s. time.

7.4.2. Rotor Iron Losses as Function of Slot Opening at 3150 rpm

Figure 7.16 presents the eddy current losses in magnets and rotor yokes as well as the total rotor eddy current loss as a function of slot opening at the rated speed of 3150 rpm. As can be seen, when the slot opening is smaller than 3 mm, the eddy current losses are negligibly small. With slot openings greater than 3 mm, the eddy current losses increase rapidly, when slot openings increase. Figure 7.16 also shows that the eddy current loss in magnets dominates the total eddy current loss in the rotor. The rotor eddy current loss increases when the slot opening decreases. However, the internal voltage only reaches maximum value at a certain slot opening. If the slot opening is too big or too small, the flux linkage will decrease and the internal voltage will not reach maximum value (see Figure 7.16) Thus, slot openings need to be designed to compromise between maximizing internal voltage and minimizing the total eddy current loss. With this criterion, the optimal slot opening that can be chosen from Figure 7.16 is 4 mm. Figure 7.17 compares rotor eddy current loss during no load and load (at rated current and maximum torque current angle). It can be seen that compared to no load, rotor eddy current loss during load increases significantly. This is caused by the MMF of current-carrying windings.

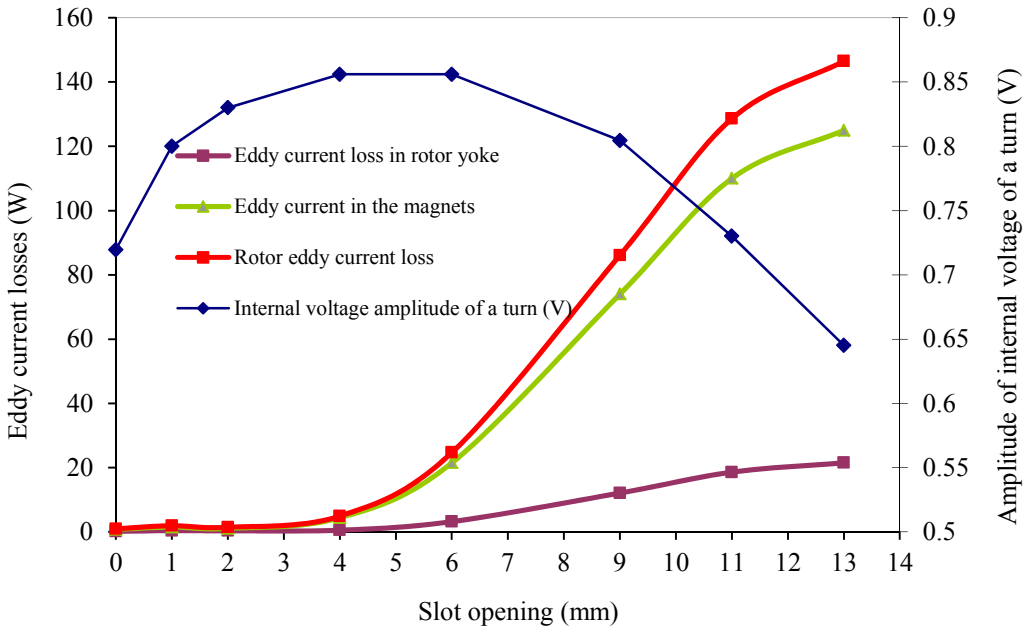

Figure 7.16. a) Rotor eddy current losses vs. slot opening, b) internal voltage amplitude of a turn vs. slot opening, at rated speed of 3150 rpm, during noload.

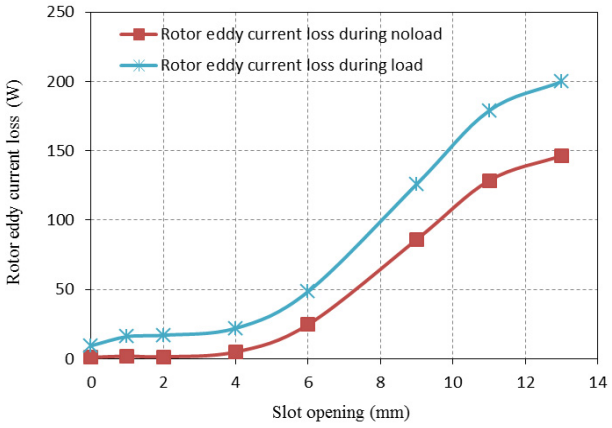

Figure 7.17. Mean rotor eddy current losses vs. slot opening, at the rated speed of 3150 rpm.

7.5. Stator Lamination Iron Loss

In this section, the stator iron loss model and a method of extracting the loss coefficients using the Epstein test data of the manufacturer are presented.

7.5.1. Extracting Iron Loss Coefficient using the Manufacturer's Epstein Test

The stator iron losses in W/kg can be explained by using three well known components, namely, the hysteresis loss, the classical eddy current loss and the excess loss as

$$P_{Fe} = P_h + P_c + P_{ex} \tag{7.5}$$

For the sinusoidal flux density, the steel lamination iron loss in W/kg can be written as [Ros 2007], [Den 1999],

$$P_{Fe} = k_h f B_m^{\beta} + k_e f^2 B_m^2 + k_{ex} f^{1.5} B_m^{1.5} \tag{7.6}$$

where,

+ k_h is the hysteresis coefficient which depends on the material and B_m is the maximum flux density. The exponent β is the Steinmetz constant; for the grades of silicon steel laminations, it is in the range of 1.8 to 2.2. The factors k_h and β are obtained by the curve fitting method by utilizing the Epstein test data of the manufacturer.

+ k_e is the eddy current coefficient, which is calculated as, [Den 1999]

$$k_e = \frac{\pi^2 d^2 \sigma}{6\gamma_{Fe}} \tag{7.7}$$

where, σ is the electric conductivity of the steel lamination; γ_{Fe} is the weight density of the material; and d is the thickness of the steel lamination.

+ The excess loss (anomalous loss) constant k_{ex} can firstly be obtained from the Epstein test, then it is corrected from the experiment iron loss of the PM machine at a given frequency.

Figure 7.18 shows the curve fitting of the manufacturer's Epstein test for estimating the factors. It shows that the curve-fitting approximates well with the data of the Epstein test of the manufacturer. Based on the manufacturer's data, the coefficients are calculated according to the curve-fitting method, i.e., k_h= 0.02452, β=2, k_{ex} = 2.22*10^{-14}. The eddy current coefficient is calculated by using (7.7), k_e=0.01963.

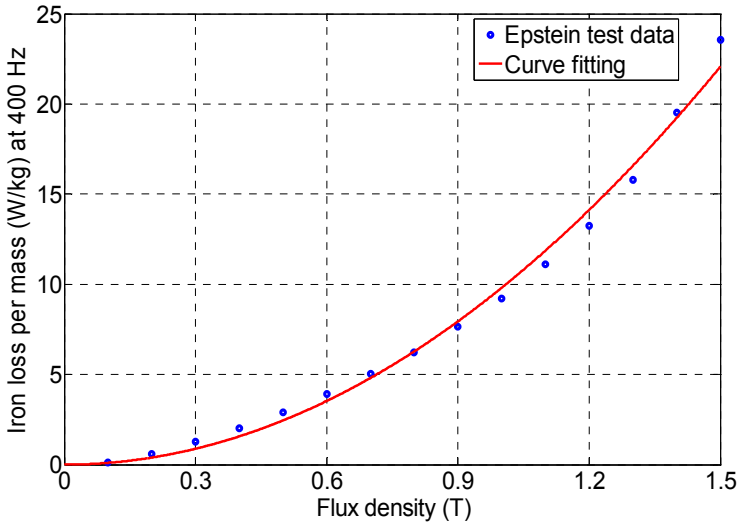

Figure 7.18. Using the curve fitting method to estimate iron loss factors, results in k_h= 0.02452, β=2, k_e=0.01963, k_{ex} = 2.22*10^{-14}.

7.5.2. FEM Stator Iron Loss Model

Using the FEM model, the instantaneous stator iron loss in W/kg is calculated as [Den 1999],

$$P = k_h f B_m^{\beta} + \frac{k_e}{2\pi^2}\left(\frac{dB}{dt}\right)^2 + k_{exc}\left(\frac{dB}{dt}\right)^{1.5} \tag{7.8}$$

where k_{exc} is the excess loss factor. The factor accounts for increasing iron loss due to the manufacturing process of the stator of the machine and the difference between flux distribution in the ideal Epstein test and real PM machine. The factors k_h and k_e are assumed the same as in the section above.

The excess loss factor k_{exc} is can be obtained by combining the experimental iron loss and the FEM calculation at a given rotor speed. The formula used to calculate k_{exc} at certain value of Ampere-turn and rotor speed can be expressed as [Den 1999],

$$k_{exc} = \frac{P_{\exp} - mean\left\{k_h f B_m^{\beta} + \frac{k_e}{2\pi^2}(\frac{dB}{dt})^2\right\}}{mean\left\{(dB/dt)^{1.5}\right\}} \tag{7.9}$$

where, P_{exp} is the experimental stator iron loss at a certain value of Ampere-turn and rotor speed.

The hysteresis loss P_h in a volume V is presented is presented by the well-known equation [Ros 2007], [Den 1999],

$$P_h = \int_V \gamma_{Fe} k_h B_m^{\beta} f dV \tag{7.10}$$

The instantaneous classical eddy current loss in a volume is calculated as,

$$P_C(t) = \int_V \sigma \frac{d^2}{12}\left(\frac{dB(t)}{dt}\right)^2 dV \tag{7.11}$$

where, d is lamination thickness, σ is the electric conductivity and $B(t)$ is the instantaneous flux density.

The instantaneous excess eddy current loss in a volume is calculated as,

$$P_{ex}(t) = \int_V \gamma_{Fe} k_{exc}\left(\left|\frac{dB(t)}{dt}\right|\right)^{3/2} dV \tag{7.12}$$

where, k_{exc} is the excess eddy current loss coefficient estimated by a combination of experiment and FEM calculation as equation (7.9).

Table 7.1. Coefficients for calculating the stator iron loss.

Hysteresis coefficient	k_h	0.02452
Classic eddy current loss coefficient	k_e	0.01963
Excess loss coefficient	k_{exc}	0.0002746

Table 7.1 shows calculation results of iron loss coefficients. By using these factors, stator iron loss of the PM machine is calculated at different rotor speeds. A comparison of simulation and experimental results of the iron loss of the PM machine A is presented in Chapter 10. It shows good agreement. It is shown from calculation results that stator excess loss is 1.6 times higher than the total loss of the stator hysteresis loss and the stator classical eddy current loss, at rotor speed of 3000 rpm. The measured iron loss of the PM machine is 2.6 times higher than the iron loss calculation if using the data of the Epstein test alone. Therefore, the excess loss should always be taken into account during the iron loss calculation.

7.6. Influence of Rotor Speed and Slot Opening on Rotor and Stator Iron Losses

Figures 7.19 to 7.21 present the eddy current losses of rotor yoke and magnets and total rotor eddy current loss as a function of both slot opening and rotor speed. As can be seen, the rotor eddy current losses caused by slot opening increase according to the increase of the rotational rotor; because the magnitude of the eddy current is proportional to the time derivative of the air gap flux density.

As can be seen, with a closed slot, the rotor eddy current losses due to slot opening can be negligible. Over the whole range of operating speed, the rotor eddy current losses increase when the slot opening increases. They reach peak value at a fully open slot. With a fully open slot as well as a nearly fully open slot, the rotor eddy current loss has the potential to cause overheating and demagnetize the magnets.

Figure 7.22 presents the computational results of stator iron loss versus rotor speed and slot opening. It is shown that the stator iron loss corresponding to a slot opening of 4 mm is the highest. As mentioned before, with this slot opening, flux linkage and internal voltage also reach a peak. When the slot is fully open, stator iron loss reaches a minimum but rotor eddy current loss reaches a peak. The total iron loss of the rotor and stator reaches its maximum with fully open slot and reaches its minimum with a closed slot, as shown in Figure 7.23.

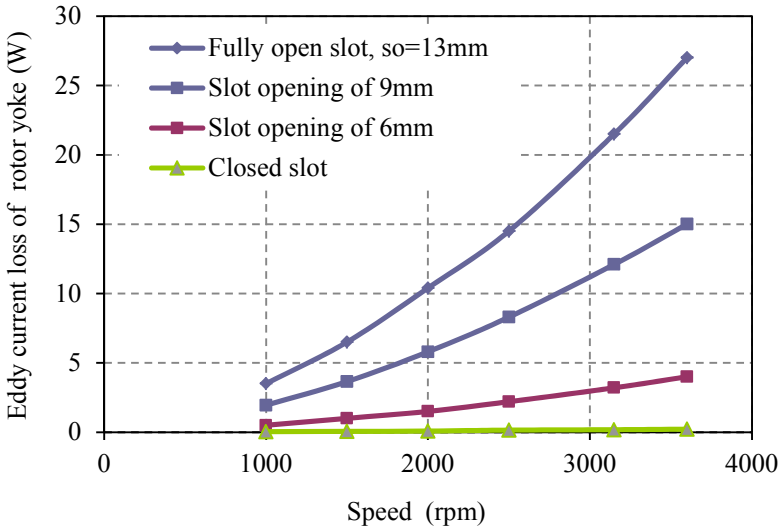

Figure 7.19. Eddy current losses in rotor yoke vs. rotor speed and slot opening, during noload.

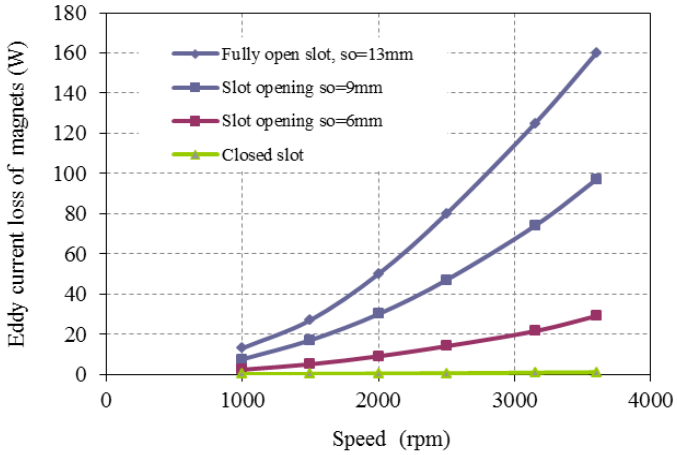

Figure 7.20. Eddy current losses in the magnets vs. rotor speed and slot opening, during noload.

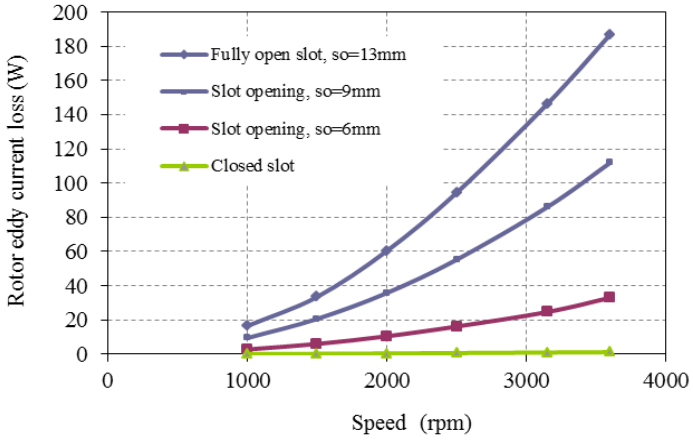

Figure 7.21. Total rotor eddy current loss vs. rotor speed and slot opening, during noload.

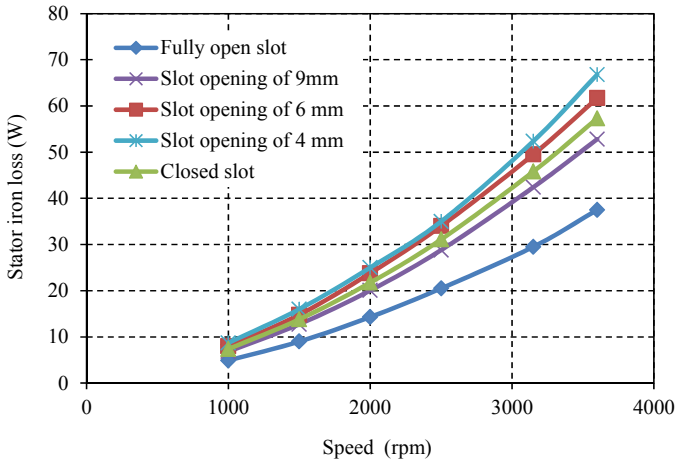

Figure 7.22. Stator iron loss vs. rotor speed and slot opening, during noload.

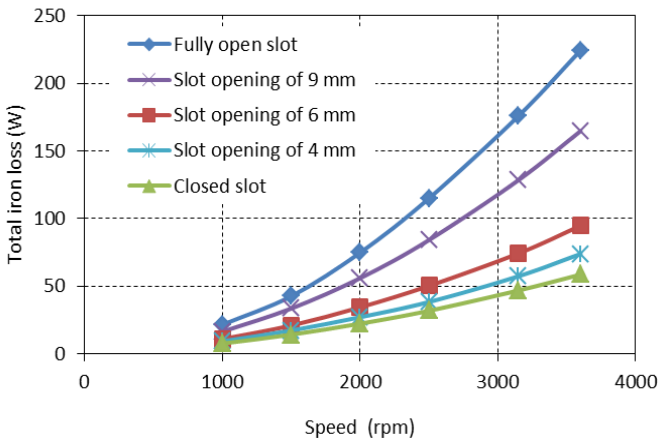

Figure 7.23. Total iron loss of rotor and stator vs. rotor speed and slot opening, during noload.

Figure 7.24 depicts losses versus slot opening at rotor speed of 3150 rpm, during no-load. We see that stator iron loss decreases when slot-opening width is greater than 4 mm. This is because flux linkage decreases as shown in Figure 5.11, Chapter 5. With slot opening in the range of 1 mm to 4 mm, stator iron loss is nearly constant. Because the decrease of iron losses in stator teeth and stator back iron due to the decrease of flux linkage is compensated by the increase of iron loss in tooth tips due to the increase of leakage flux through tooth tips. In the case of slot opening of 0 to 1 mm, the decrease of flux linkage due to the increase of leakage flux through tooth tips leads to the decrease of stator iron loss. When slot-opening width is large (greater than 7 mm), rotor eddy current loss is dominant in total iron loss of the stator and rotor. Conversely, when slot-opening width is small (smaller than 7 mm), stator iron is dominant in the total iron loss.

Figure 7.25 shows losses versus slot opening at rotor speed of 3150 rpm, during rated load. It can be seen from Figure 7.24 and Figure 7.25 that the stator iron loss does not change so much from no-load to load. This is because the armature field is small, comparing to the field produced by magnets. However, rotor eddy current loss increases significantly. This leads to the total iron loss of rotor and stator during load significantly increases in comparison with the total iron loss during noload.

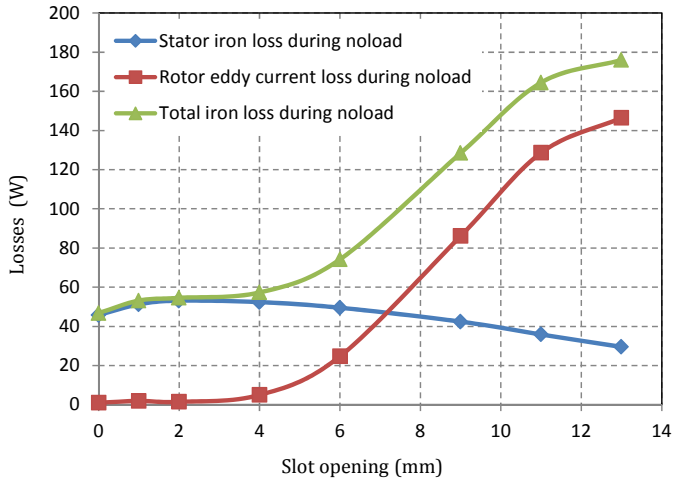

Figure 7.24. Losses vs. slot opening during noload.

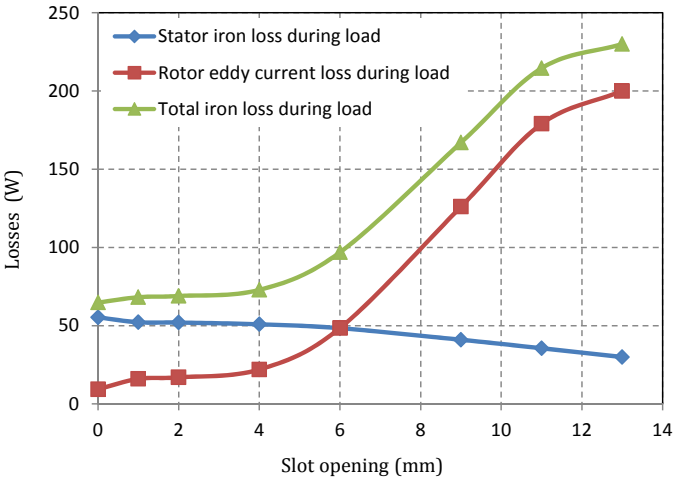

Figure 7.25. Losses vs. slot opening during rated load and maximum torque current angle.

7.7. Magnet Segmentation Effect

To reduce magnet eddy current loss, magnets are divided into segmentations in the radial direction as shown in Figure 7.26 and Figure 7.27, [Yam 2010], [Yam 2009]. Calculation results of the magnet eddy current loss of semi-open slot and fully open slot PM machines with different magnet segmentation number are presented in Figure 7.28. It can be seen in this study that the magnet segmentation method is very efficient to reduce eddy current loss in PM machines. Eddy current loss reduces quickly when the number of segmentation increases. For example, with three segmentations, the magnet eddy current loss of a fully open slot PM machine decreases by five times in comparison with that of single block magnet, i.e. from 125 watts to 25 watts. When the segmentation number reaches seven, the magnet eddy current loss is negligibly small.

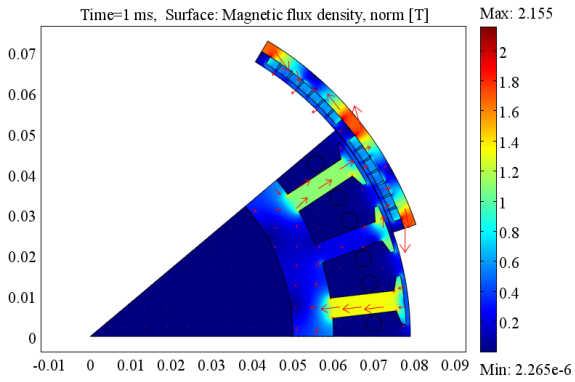

Figure 7.26. The 2D-FEM model of the semi-open slot PM machine with seven-segmentation magnet, with non-linear transient solution at time of 1 ms and a speed of 3150 rpm.

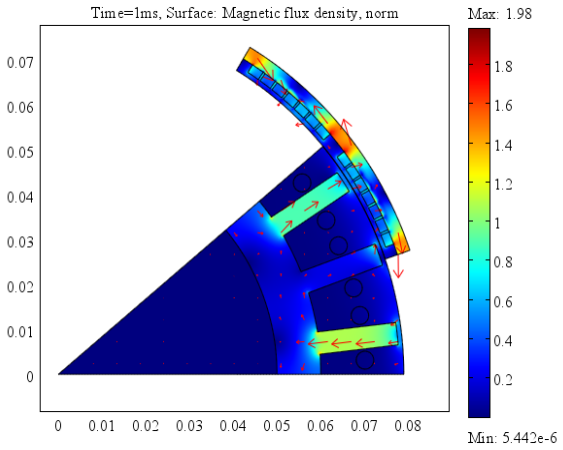

Figure 7.27. 2D-FEM model of a fully open slot PM machine with seven-segmentation magnets, with non-linear transient solution at a time of 1 ms and a speed of 3150 rpm.

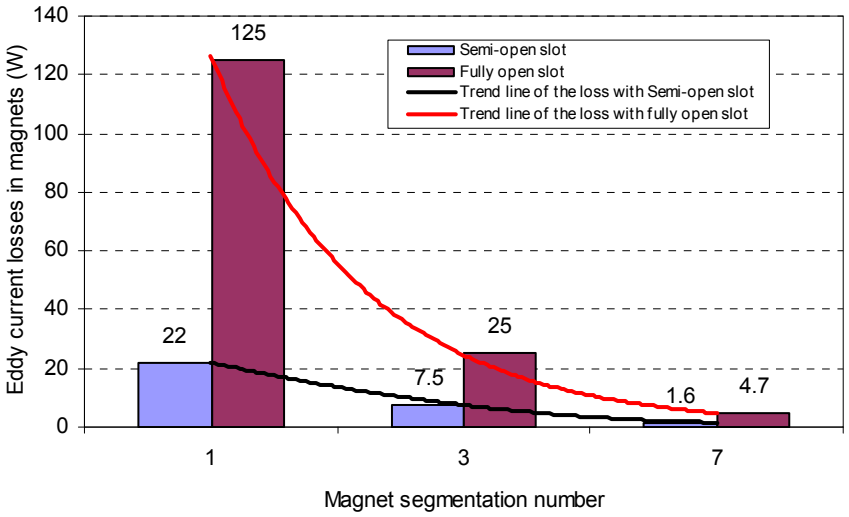

Figure 7.28. Eddy current losses in magnets vs. magnet segment number.

7.8. Conclusions

The distribution of the eddy current density and eddy current loss in the rotor of a concentrated winding PM machines in a flywheel was studied in this chapter. The two-dimension transient FEM model including rotor motion was used for this study, while magnetic saturation was taken into account for both stator iron and rotor back iron. The FEM simulated results show that the eddy current density in magnets reaches peak value at the position under slot opening.

The influence of slot opening on the eddy current loss in magnets, rotor back iron, and stator iron loss was also investigated. The results show that in the case of fully opened slots, the eddy current loss in the magnets becomes large enough to potentially overheat the magnets and demagnetize them. The maximum value of the eddy current density of the middle point of the magnet of the fully open slot PM machine is greater by 2.4 times than that of the semi-open slot PM machine B. As a result, the mean value of the eddy current loss of the fully open slot PM machine is greater by about 5.5 times than that of the semi-open slot PM machine B (Figure 7.28). The proposed approach and analysis results can be used to select the slot opening that minimizes rotor eddy current losses while maximizing the internal voltage (Figure 7.16).

The maximum value of the magnet eddy current density increases when the slot opening increases. However, the frequency of the eddy current density at a point is unchanged when the slot opening dimension changes, i.e., the frequency is not dependent on slot opening dimension, but dependent on the number of slots per pole pair. The fundamental frequency of eddy current at a point is equal to the product of slot number per pole pair and the fundamental frequency of the rotating field. The dominant harmonic components of the eddy current density of magnets are the first, second, and third order of the fundamental frequency of the eddy current density.

The rotor eddy current losses during load are investigated in two typical operation modes, namely the maximum torque operation with a current angle of 90 degrees and a current angle of 135degrees. The rotor eddy current loss of the second operation mode is 1.2 times higher than that of the maximum torque operation mode and 2.85 times higher than that of the no-load operation mode.

To explain the cause of eddy current loss in magnet, the loss is calculated separately for three cases, namely, un-demagnetization of magnets (i.e., eddy current loss due to the MMF winding harmonics alone), no-load, and rated load. Calculation results for the PM machine B shown that the eddy current loss of magnets due to the slotting effect takes account for about two third the total eddy current loss during rated load and the remaining part is due to the MMF winding harmonics. However, because of the influence of magnetic saturation, the total rotor eddy current

loss at rated load is not equal to the sum of the losses calculated separately on no load and un-magnetization of magnet.

The segmentation of magnets for the reduction of eddy current loss was investigated. The result shows that the magnet segmentation method is an efficient way to reduce magnet eddy current loss. With only three magnet segmentations, the eddy current loss of magnets is reduced significantly, by about 3-5 times. With seven magnet segmentations, magnet eddy current loss can be negligibly small, as shown in Figure 7.28.

A stator iron loss model was developed. Two steps must be taken to estimate the coefficients. During the first step, the coefficients are calculated according to curve-fitting method of the data of the manufacturer and equation (7.7). During the second step, the excess loss (anomalous loss) coefficient is corrected from the experiment iron loss of the PM machine at a given frequency.

The method used in this Chapter allows for the monitoring of the eddy current losses in the rotor as a function of time, rotor speed, operating mode and stator slot opening. It therefore constitutes an indispensable tool in the design of PM machines taking the eddy current losses in the rotor into account.

CHAPTER 8

CIRCUIT THERMAL MODEL

8.1. Introduction

In Chapter 3 and 7, the electromagnetic model was developed to calculate the losses (the thermal sources). In this chapter, a thermal model is built and investigated. Afterwards, the thermal model and electromagnetic model are coupled to result in a multi-physic model for the design of PM machines taking into account temperature constraint.

Why do we need a thermal model? High temperatures can damage the electrical insulation of windings and demagnetize the magnets. With a thermal model, the temperature of points in a PM machine can be estimated without measurements or with a minimum of measurements. Therefore, the cost in time and money of the design will be reduced. The thermal model can also be used to estimate key temperatures for protecting PM machines, optimal working operations and design optimization, considering temperature constraints.

Why a circuit thermal model? The circuit thermal model or lumped-parameters thermal model is well known as an effective and accurate methodology to estimate temperatures of electric machines [Haf 2010], [Fan 2010], [Ner 2008], [Bog 2003], [Mel 1991]. It is easy and fast to change the parameters of the thermal model. However, FEM thermal simulation or computational fluid dynamics (CFD) are accurate, but very time-consuming. In fact, an exact evaluation of heat transfer coefficients could require a series of CFD computations. This however requires large computational effort and expertise in the field of fluid dynamics [Ner 2008], [How 2011]. Fortunately, the evaluation of the convection coefficients for both natural and forced convections can be done accurately enough by using the correlations for Nusselt number found in the literature [Chi 1996], [Oze 2000], [Rou 2007], [Ner 2008], [Sta 2008], [How 2012]. Therefore, the circuit thermal model of PM machines is preferred in this study.

Coupling the thermal model and the electromagnetic model: The circuit thermal model for the induction machines, reluctance machine and interior rotor PM machines can be found in [Mel 1991], [Bog 2003], [Ref 2004], [Rou 2007]. However, the complication level of the thermal model depends on the complication level of the geometry. Besides, the electromagnetic transient

FEM computation coupled thermal model for the exterior rotor PM machine with concentrated windings with complicated geometry such as cooling plates at both the stator hollow and end side, metal bolts through the stator in the axial direction and spokes in the stator hollow has not yet been investigated in literature properly. Therefore, this is addressed in this chapter.

Approach of this chapter: Many parts of a PM machine can be assumed like the hollow cylinder, so the thermal model of a hollow cylinder is considered as the fundamental when establishing a conduction thermal model of parts of the PM machine [Mel 1991], [Pur 2006], [Pyr 2008]. The thermal model of the entire PM machine is formed by connecting the thermal models of adjacent parts through the contacting conduction thermal resistance and/or the convection and/or radiation thermal resistance. The thermal model is created with the following assumptions: heat flows are independent in radial and axial directions; thermal capacitance and heat generation are uniformly distributed in each part of the PM machine; and the lateral sides of the PM machine are open.

Organization of this chapter: Thermal model system is described in Section in Section 8.2. Next, the circuit thermal model of conductive parts is presented in Section 8.3. Then, the convective/radiative heat transfer from the PM machine to the environment is investigated in Section 8.4. Afterwards, the simulation method of thermal model and the principle of coupling thermal model and electromagnetic FEM model are discussed in Section 8.5. Result of thermal simulation in Simulink Matlab® is compared to the experimental result in Section 8.6. The solution for improving the heat transfer from the machine to the environment is proposed in Section 8.7. Finally, conclusions are drawn in Section 8.8.

8.2. Thermal Model of System

The PM machine is divided into separate geometrical sections, as shown in Figure 8.1, each section has own thermal model. The circuit thermal model of a section is connected to the thermal model of neighbouring sections through thermal resistances such as conductive or radiative or convective thermal resistances to from the thermal model of the whole PM machine. The studied PM machine system can be divided into the following twelve sections as,

(1)-Shaft; (2)-Stator yoke; (3)-Stator teeth; (4)-Stator slot winding; (5)-End winding; (6)-Air gap; (7)-Permanent magnets; (8)-Rotor yoke; (9)-Outer rotor frame (flywheel); (10)-Frame end side; (11)-Interior parts of stator hollow; and (12)-Cooling plate.

However, for simplified thermal model, the frame end side and shaft are ignored in the thermal model depicted in Figure 8.2. This machine is mounted on a wall by bolts, which keep the machine at a certain distance from to the wall. The frame end side of the PM machine is open.

Therefore, this machine has both end sides open. It is shown from experiment that the temperature differences in the end sides are negligible.

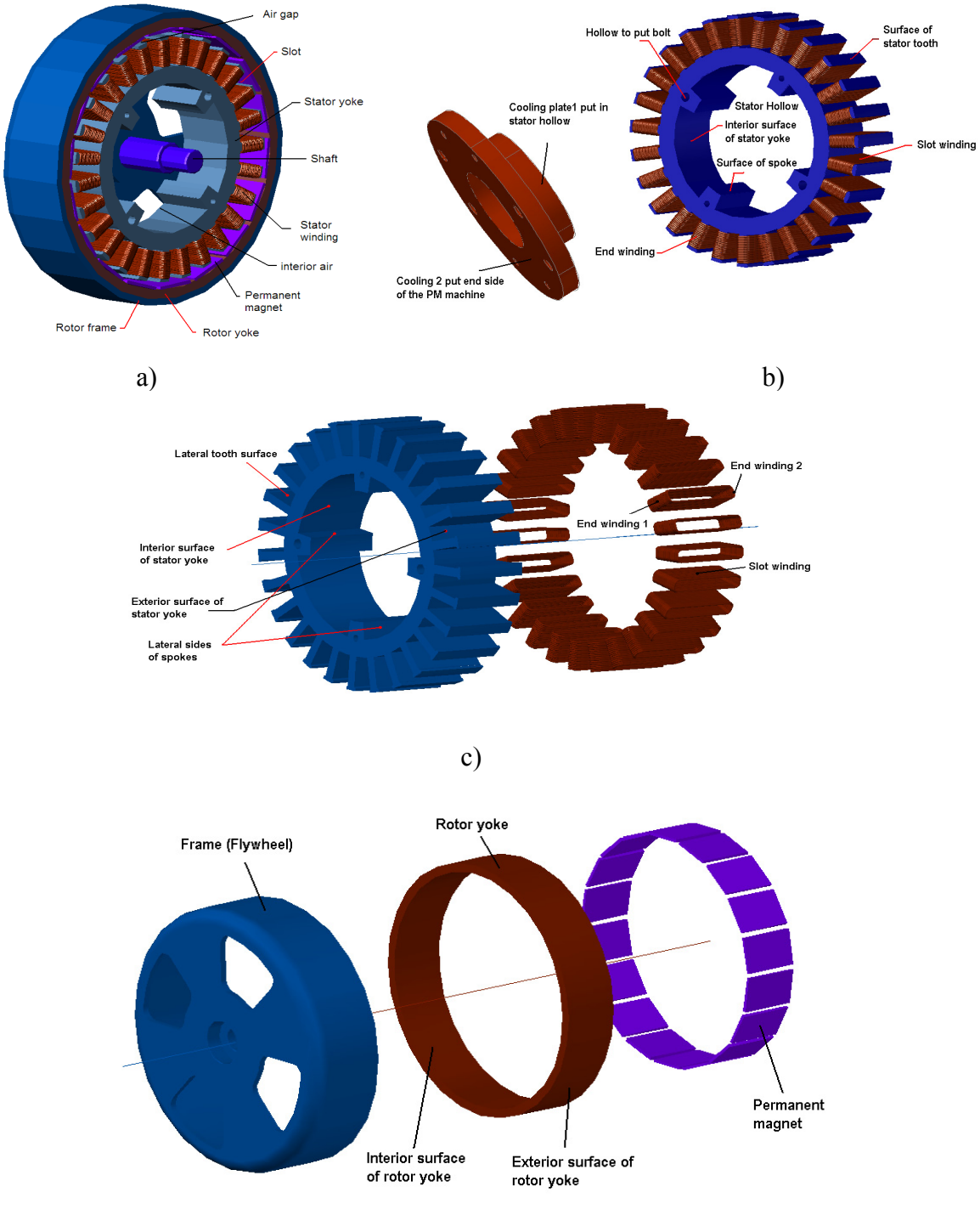

Figure 8.1. Configuration of a PM machine system: a) 3D geometry, b) Cooling plate and stator, c) Stator core and windings, d) Parts of rotor.

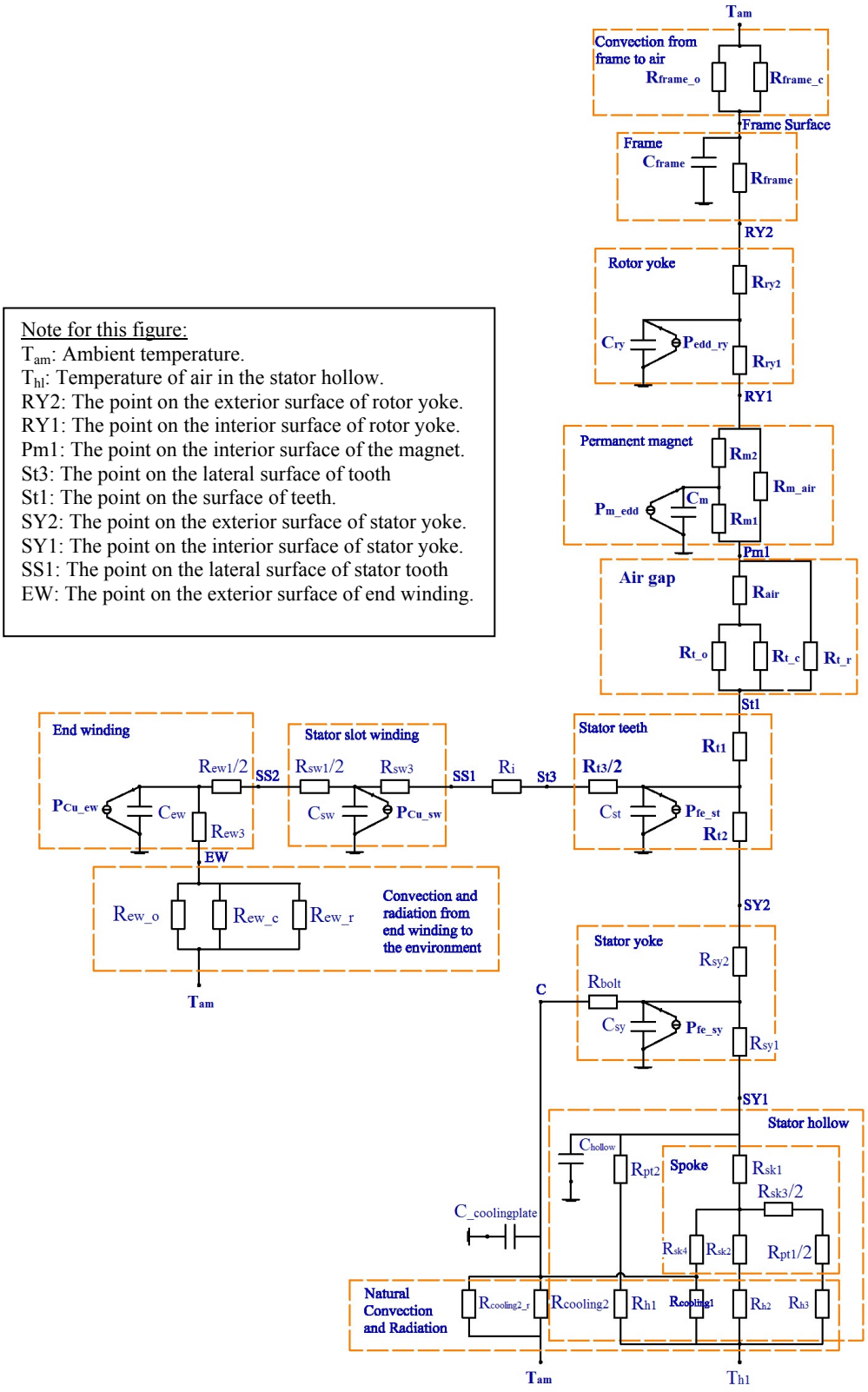

Figure 8.2. Full thermal model of the entire PM machine.

Figure 8.2 presents the full thermal model of the PM machine. The thermal parameters of the thermal model of the PM machine B are shown in Table 8.1, in which convection thermal resistances are calculated at a rotor speed of 720 rpm.

Table 8.1. Parameters of thermal model of PM machine B.

Parameter	Symbol	Value	Unit
Stator Yoke			
Radial conduction thermal resistance of the stator yoke lower half part	R_{sy1}	0.0132	K/W
Radial conduction thermal resistance of the stator yoke upper half part	R_{sy2}	0.0144	K/W
Conduction thermal resistance of bolts	R_{bolt}	2.90	K/W
Thermal capacitance of the stator yoke	C_{sy}	442.7	J/K
Stator Teeth			
Conduction thermal resistance of the stator teeth upper half part	R_{t1}	0.0705	K/W
Conduction thermal resistance of the stator teeth lower half part	R_{t2}	0.0705	K/W
Conduction thermal resistance between the internal stator teeth and lateral tooth surface in slot	R_{t3}	0.0054	K/W
Thermal capacitance of stator teeth	C_{st}	311.3	J/K
Air gap			
Natural convection thermal resistance from surface stator to air in the air gap	R_{t_o}	9.866	K/W
Forced convective thermal resistance from stator surface to air in the air gap	R_{t_c}	2.278	K/W
Radiation thermal resistance from tooth surface to rotor	$R_{t\ r}$	18.885	K/W
Conduction thermal resistance of air gap	R_{air}	2.032	K/W
Slot Winding			
Conduction thermal resistance between slot winding and end winding 1	R_{sw1}	0.0368	K/W
Conduction thermal resistance between slot winding and end winding 2	R_{sw2}	0.0368	K/W
Conduction thermal resistance between the internal slot winding and interior surface of slot winding	R_{sw3}	0.0412	K/W
Thermal resistance of insulation layer between slot winding and tooth	R_i	0.098	K/W
Thermal capacitance of slot winding	C_{sw}	142.8	J/K
End Winding			
Conduction thermal resistance between internal end winding and slot winding	R_{ew1}	0.0126	K/W
Conduction thermal resistance between internal end winding and slot winding	R_{ew2}	0.0126	K/W
Conduction thermal resistance between internal end winding and the exterior surface of end winding	R_{ew3}	0.1285	K/W
Thermal capacitance of end winding	C_{ew}	45.5	J/K
Natural convective thermal resistance from end winding to air.	$R_{ew\ o}$	5.928	K/W
Forced convective thermal resistance from end winding to air.	$R_{ew\ c}$	1.314	K/W

Radiation thermal resistance from the end winding to the environment	R_{ew_r}	12.690	K/W
Permanent Magnet			
Radial conduction thermal resistance of the magnet lower half part	R_{m1}	0.0068	K/W
Radial conduction thermal resistance of the magnet upper half part	R_{m2}	0.0067	K/W
Thermal resistance of air between adjacent magnets	$R_{m\ air}$	10.63	K/W
Thermal capacitance of magnets	C_m	120.3	J/K
Rotor Yoke			
Radial conduction thermal resistance of the rotor yoke lower half part	R_{ry1}	0.0038	K/W
Radial conduction thermal resistance of the rotor yoke upper half part	R_{ry2}	0.0039	K/W
Thermal capacitance of rotor yoke	C_{ry}	450.7	J/K
Rotor Frame (flywheel)			
Radial conduction thermal resistance of the frame	R_{frame}	0.0036	K/W
Thermal capacitance of frame	C_{frame}	346.1	J/K
Natural convective thermal resistance from outer surface of frame to air.	R_{frame_o}	6.6605	K/W
Forced convective thermal resistance from outer surface of frame to air.	R_{frame_c}	1.2319	K/W
Interior Components of Hollow Cylinder			
Radial conduction thermal resistance of the spoke upper half part. The subscript “sk" stands for spoke	R_{sk1}	0.1449	K/W
Radial conduction thermal resistance of the spoke lower half part	R_{sk2}	0.3029	K/W
Conduction thermal resistance between internal spoke and the lateral spoke	R_{sk3}	0.1112	K/W
Radial conduction thermal resistance of the spoke lower half part in contact with cooling plate 1	R_{sk4}	0.4039	K/W
Conduction thermal resistance of the plastic layer at the lateral side of the spoke. The subscript “pt" stands for plastic	R_{pt1}	1.1905	K/W
Conduction thermal resistance of the plastic layer at the interior surface of the stator yoke	R_{pt2}	0.2803	K/W
Natural convection thermal resistance from surface of hollow to air	R_{h1}	12.49	K/W
Natural convection thermal resistance from spoke surface to air	R_{h2}	59.40	K/W
Natural convection thermal resistance from lateral sides of the spoke to air	R_{h3}	25.90	K/W
Cooling Plate			
Natural convection thermal resistance of cooling plate 1	$R_{cooling1}$	11.960	K/W
Natural convection thermal resistance of cooling plate 2	$R_{cooling2}$	8.299	K/W
Radiation thermal resistance from cooling plate 2 to wall	$R_{cooling2\ r}$	30.784	K/W
Thermal capacitance of whole cooling plate	$C_{coolingplate}$	402.4	J/K

8.3. Models of Thermally Conductive Parts

8.3.1. Thermal Model for Shaft and Shall Bearing

Figure 8.3a presents a sketch of a rotor shaft and its thermal model. The thermal model as shown in Figure 8.3b has three thermal resistances: R_1 is the axial conduction thermal resistance from the point of contact (S) of shaft and ball bearing to the point of contact (S1) of shaft and the end side frame; R_2 is convection thermal resistance from the shaft surface to air in the stator hollow; and R_3 is the total of thermal resistances of from ball bearing to the metal wall and from the metal wall to air. The ball bearing is mounted on a large Aluminum wall and the convection thermal resistance R_2 at rated rotor speed is so small, so the heat due to mechanical loss is almost discharged to air through R_2 and R_3. Therefore, the influence of mechanical friction loss on the temperature of windings and magnets of the PM machine is ignored. The thermal model of the shaft is not included in thermal model of the whole PM machine.

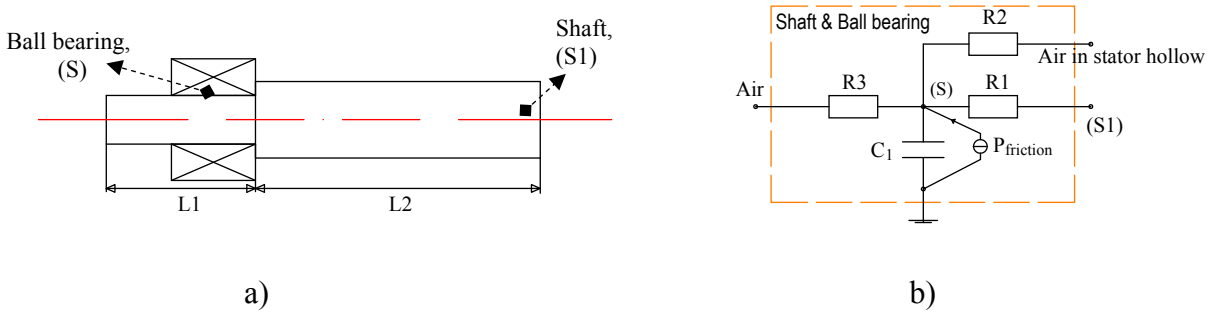

a) b)

Figure 8.3. a) Sketch of shaft and ball bearing, b) Thermal model of shaft; where, (S) is the point of contact of the shaft and ball bearing and (S1) is the point of contact of the shaft and the end side frame.

8.3.2. Thermal Model of Stator Yoke

The stator yoke is a hollow cylinder made by numerous iron laminations, so that heat transfer in the axial direction is much smaller than in the radial direction. However, there are four bolts in the axial direction of the stator yoke, which are connected to a cooling plate (called “cooling plate 2”) put at the end side of the PM machine. This causes heat transfer in the axial direction to increase significantly. Therefore, the thermal resistance of bolts R_{bolt} should be included in the thermal model of the stator yoke. The thermal model of the stator yoke is presented in Figure 8.4.

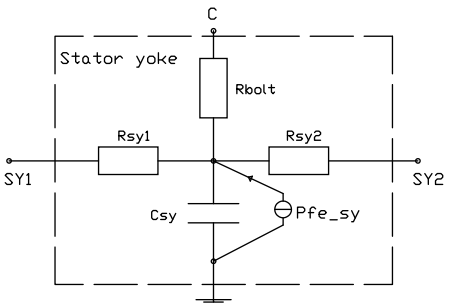

Figure 8.4. Thermal model of the stator yoke, where (SY1) is the point on the interior surface of the stator yoke, (SY2) is the point on the exterior surface of the stator yoke and (C) is the point connected to the cooling plate 2.

The parameters of the thermal model in Figure 8.4 can be calculated as [Bog 2003]

$$R_{sy1} = \frac{1}{2\pi k_{iron} L_s} \ln\left(\frac{D_1}{D_m}\right) \tag{8.1}$$

$$R_{sy2} = \frac{1}{2\pi k_{iron} L_s} \ln\left(\frac{D_m}{D_2}\right) \tag{8.2}$$

where, D_1 is the outer diameter of rotor yoke, D_2 is the inner diameter of stator yoke and $D_m=(D_1+D_2)/2$.

Thermal capacitance of the stator yoke is calculated as,

$$C_{sy} = mc_p = \rho c_p V = \left(\rho_{iron} c_{iron} n l_l + \rho_{air} c_{air} (L_s - n l_l)\right) \pi (D_1^2 - D_2^2)/4 \tag{8.3}$$

where, n is the number of iron laminations, l_l is thickness of iron lamination, k_{iron} is the thermal conductivity of iron k_{iron}=30 (W/m/K), ρ_{iron} is the mass density of iron ρ_{iron}=7700 (kg/m^3), c_{iron} is the specific heat of iron c_{iron}=490 (J/kg/K), ρ_{air} is the air mass density ρ_{air}=1.18 (kg/m^3), and c_{air} is the air specific heat c_{air}=1012 (J/kg/K) at 27^{0}C.

8.3.3. Thermal Model of Stator Teeth

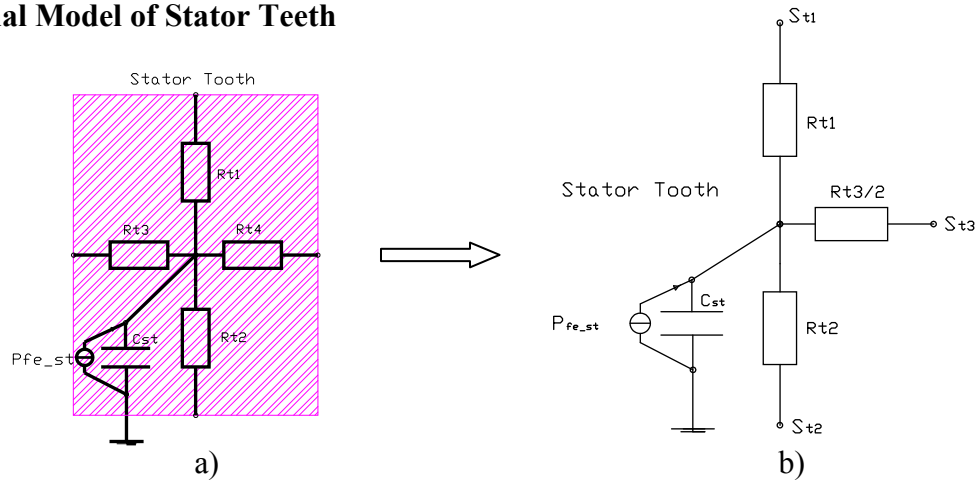

Figure 8.5. Thermal model of Stator teeth, where S_{t1} is the point on the surface of the stator tooth, S_{t2} is the point contacting with the stator yoke, and S_{t3} is the point linking to the stator slot.

The stator core is made from numerous iron laminations, so that thermal conductive resistance in the axial direction is smaller than in the radial and transverse directions. Therefore, heat transfer in the axial direction can be neglected in the equivalent thermal model. Figure 8.5a is a thermal model of stator teeth, while Figure 8.5b is the simplified thermal model.

Thermal resistances are calculated as,

$$R_{t1} = R_{t2} = \frac{h_t / 2}{k_{iron} L_s W_t} \frac{1}{z} \tag{8.4}$$

$$R_{t3} = R_{t4} = \frac{W_t / 2}{k_{iron} L_s h_t} \frac{1}{z} \tag{8.5}$$

where, h_t, W_t, L_s, z, and k_{iron} are respectively height, width of tooth, stator length, number of teeth and thermal conductivity of iron lamination. Note that the number of teeth of the PM machine is equal to the number of slots, i.e., N_t=Q=z.

The thermal capacitance is calculated as,

$$C_{st} = \left(\rho_{iron} c_{iron} n l_l + \rho_{air} c_{air} (L_s - n l_l)\right) h_t W_t z \tag{8.6}$$

where, ρ_{iron} and ρ_{air} are mass density of iron and air, and c_{iron} and c_{air} are the specific heat of iron and air.

The iron loss of all of the stator teeth P_{fe_st} is calculated by a transient FEM.

8.3.4. Thermal Model of the Stator Slot Winding

Figure 8.6 depicts a part of the cross section of the stator. The windings in the slot are trapezoidal. For the purposes of modeling, the shape is transformed into an equivalent rectangular with a height equal to the height of the tooth and its width equal to the mean value of slot width [Mel 1991]. Therefore, slot winding is modeled as a solid rectangular with thermal conductivity in the axial direction equal to thermal conductivity of Copper. Thermal conductivity in other directions is equal to the varnish thermal conductivity multiplied by a factor F greater than 1, [Bog 2009], [Mel 1991], [Pur 2006]. According to experimental results in [Pur 2006], the factor is a function of filling factor. With a filling factor of 0.2 to 0.8, the factor F is from 1.5 to 10. Because of the very high thermal conductivity of Copper windings in the axial direction, a large amount of heat flux from slot winding goes to the end winding and is released to the air at the end sides of the machine by convection. A large amount of heat is transferred from the slot winding to the stator tooth. Therefore, it is only necessary to model heat transfer from slot winding to the end winding and stator tooth. The thermal model is depicted in Figure 8.7.

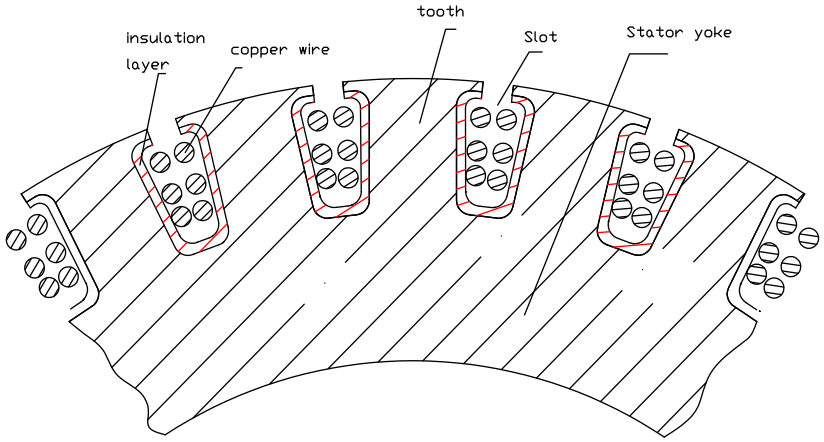

Figure 8.6. A part of the stator cross section.

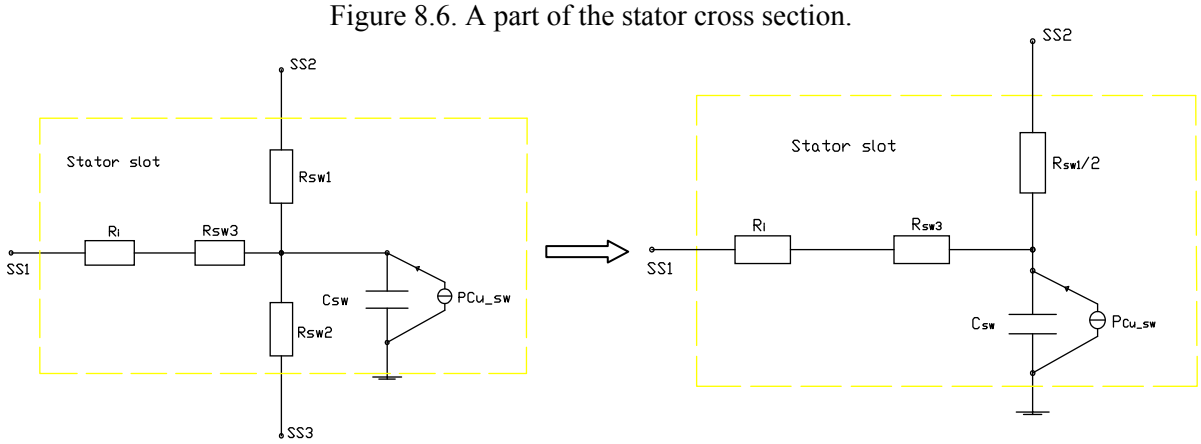

Figure 8.7. Thermal model for the stator slot winding. SS1 is the point between the stator slot and stator tooth, SS2 and SS3 are the points at the end sides of the stator slot winding.

The thermal conductive resistance in the axial direction from the slot winding to the end winding is

$$R_{sw1} = R_{sw2} = \frac{L_s / 2}{k_{Cu}(N_c A_{Cu})} \frac{1}{2z} \tag{8.7}$$

where, k_{Cu} is Copper thermal conductivity, k_{Cu}=401 (W/m/K) at 27°C, N_c is the number of turns per coil and A_{Cu} is the cross section area of wiring, $A_{Cu} = \pi d_{Cu}^2 / 4$.

The thermal conductive resistance from the centre of slot winding to the electric insulation layer between slot windings and teeth is

$$R_{sw3} = \frac{W_s / 2}{F k_v h_t L_s} \frac{1}{2z} \tag{8.8}$$

The thermal conductive resistance of the electric insulation layer is

$$R_i = \frac{d_i}{k_i h_t L_s} \frac{1}{2z} \tag{8.9}$$

where, W_s is equivalent slot winding width, d_i is the thickness of plastic electric insulation, d_i=0.5 mm, and k_i is the thermal conductivity of electric insulation material, k_i=0.15 (W/m/K),and k_v is the thermal conductivity of the insulating varnish layer, k_v= 0.18 (W/m/K) at 27°C.

The thermal capacitance of slot winding is

$$C_{sw} = c_{Cu} m_{sw} z = 2 c_{Cu} \rho_{Cu} N_c A_{Cu} L_s z \tag{8.10}$$

where, c_{Cu} is the thermal specific heat of Copper, c_{Cu} = 385 (J/kg/K) at 20°C, ρ_{Cu} is the mass density of Copper, ρ_{Cu} =8950 (kg/m^3), and m_{sw} is the mass of a slot winding.

Copper power loss of slot windings is

$$P_{Cu\_sw} = z R_{sw} I^2 \tag{8.11}$$

In equation (8.11), the slot winding electrical resistance is

$$R_{sw} = \rho_{Cu} \frac{2 N_c L_s}{A_{Cu}} \tag{8.12}$$

where, ρ_{Cu_20} is the Copper resistivity of 1.7241 10^{-8} (Ωm) at 20°C, and Copper resistivity at temperature T is calculated as $\rho_{Cu\_T} = \rho_{Cu\_20}\{1+\alpha(T\text{-}20)\}$, with the Copper thermal coefficient of resistance α=0.0039.

8.3.5. Thermal Model of the End Winding

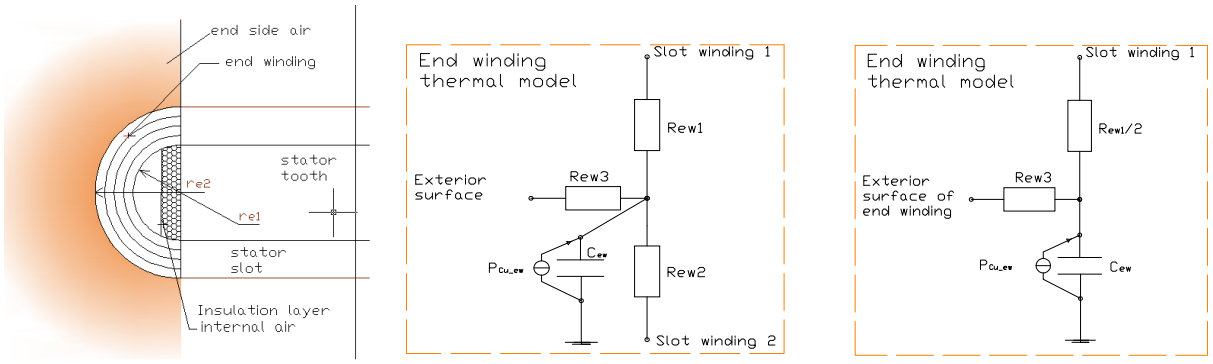

a) b) c)

Figure 8.8. a) End winding view, b) Thermal model of the end winding, c) Simplified thermal model of end winding.

To establish a thermal model of end windings, the following assumptions are made:

- ✓ The end winding is considered as a homogeneous solid cylinder.
- ✓ Heat transfer between the end winding and slot winding has a thermal conductivity equal to that of Copper.
- ✓ Heat transfer from end winding to the end side of the tooth is neglected, because thermal conductivities of end windings, iron laminations in the axial direction and the electric insulation layer are so poor.
- ✓ Thermal conductivity of the equivalent cylinder in its radial direction is equal to F times the conductivity of the varnish k_v, [Mel 1991], [Pur 2006].
- ✓ The conductive heat transfer of the equivalent cylinder in its axial direction is neglected. This is because of the poor thermal conductivity of the varnish of Copper wires and the small area of the cross section.
- ✓ Two end sides of a coil are assumed symmetrical. This assumption can be applied to PM machines as the lateral sides of the frame are open. This is confirmed from the temperature measurements.

Figure 8.8 presents thermal model of end winding. Thermal resistances are calculated as follows.

The thermal conductive resistance between end winding and slot winding is

$$R_{ew1} = R_{ew1} = \frac{1}{2z} \frac{l_e / 2}{k_{Cu}(N_c A_{Cu})} \tag{8.13}$$

The thermal resistance between middle end windings (i.e., middle equivalent cylinder) and exterior surface of end winding (i.e., surface of equivalent cylinder) is

$$R_{ew3} = \frac{1}{2z}\frac{1}{\pi F k_v h_t}\ln(\frac{r_{e2}}{r_m}) \tag{8.14}$$

where, $r_m=(r_{e1}+ r_{e2})/2$, and r_{e1} and r_{e2} are interior and exterior radii of the equivalent cylinder of the end winding. The specifications such as F, k_v, k_c, A_{Cu} are calculated in the same way as that of the slot winding.

The average end winding length is

$$l_e = \pi(r_{e1}+r_{e2})/2 \tag{8.15}$$

where $r_{e1}=W_t/2$, $r_{e2}=(W_t+2N_{layer}\, d_{Cu}+2d_i)/2$, and h_t and W_t are respectively the height and width of a tooth and N_{layer} is the number of winding layers.

The thermal capacitance of end winding is

$$C_{ew} = 2zm_{ew}c_{Cu} \tag{8.16}$$

$$m_{ew}=A_{Cu}N_c\, l_e \rho_{Cu} \tag{8.17}$$

where, m_{ew} is the mass of an end winding, A_{Cu} is Copper wire cross sectional area, $A_{Cu} = \pi d_{Cu}^2 / 4$.

End winding loss is

$$P_{ew}=2zR_{ew}I^2 \tag{8.18}$$

The electrical resistance of end winding is

$$R_{ew} = \frac{\rho_{Cu} N_c l_e}{A_{Cu}} \tag{8.19}$$

8.3.6. Heat Transfer in Air Gap

The thermal model of the air gap is divided into two parts, namely the thermal model for heat transfer between stator surface and the air gap and the thermal model for the heat transfer between air gap and rotor. Heat transfer from the stator surface to the air gap is modeled as a turbulent fluid flow as shown in Section 8.4.4. The airflow in the air gap is assumed to have a velocity equal to that of a point on the surface of a magnet. The velocities of the rotor and fluid in the air gap are almost the same, so the heat transfer between them is modeled as the thermal conduction according to the method of the authors in [Rou 2007], [Bog 2003]. Conductive thermal resistance between the air gap and the rotor is calculated for an air cylinder as follows [Bog 2003], [Cen 1997],

$$R_{air} = \frac{1}{2\pi k_{air} L_s} \ln\left(\frac{D_{os} + 2g}{D_{os} + g}\right) \tag{8.20}$$

where D_{os} is the outer stator diameter and g is the air gap length.

8.3.7. Thermal Model of the Permanent Magnet

Magnets are assumed to produce a cylinder, including two parts in a pole pitch, namely, magnet and air as shown in Figure 8.9a. Therefore, the thermal model of magnets has two parallel braches as shown in Figure 8.9b.

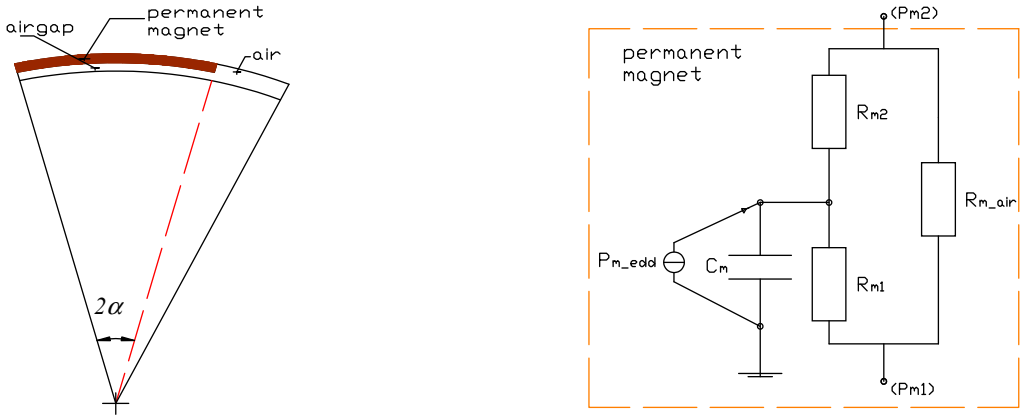

a) b)

Figure 8.9. Thermal resistance of permanent magnet. (Pm1) and (Pm2) are respectively the point on the interior and interior surface of the magnet.

Thermal conductive resistances of magnets are

$$R_{m1} = \frac{\pi}{2\alpha} \frac{1}{2\pi k_{pm} L_m} \ln\left(\frac{r_{pm}}{r_{ipm}}\right) \tag{8.21}$$

$$R_{m2} = \frac{\pi}{2\alpha} \frac{1}{2\pi k_{pm} L_m} \ln\left(\frac{r_{opm}}{r_{pm}}\right) \tag{8.22}$$

$$R_{m\_air} = \frac{\pi}{\pi - 2\alpha} \frac{1}{2\pi k_{air} L_m} \ln\left(\frac{r_{opm}}{r_{ipm}}\right), \; r_{pm} = (r_{ipm} + r_{opm})/2 \tag{8.23}$$

where, L_m is the length of the magnet in the axial direction, r_{opm} is the outer radius of the permanent magnet, r_{ipm} is the inner radius of the permanent magnet, r_{pm} is the mean radius of magnet, k_{pm} is the conductive heat transfer of the magnet, k_{pm} =9 (W/m/K) for the Neodymium magnet.

The thermal capacitance of magnets is

$$C_m = c_{pm} m_{pm} = c_{pm} \rho_m 2pW_m t_m L_m \tag{8.24}$$

where, W_m, t_m, L_m is the width, thickness, and length of the permanent magnet in the axial direction respectively, ρ_m is the mass density, and c_{pm} is the specific heat of the magnet.

The eddy current loss of permanent magnets is calculated by a transient FEM model as presented in Chapter 7.

8.3.8. Thermal Model of the Rotor Yoke

The rotor yoke is a hollow cylindrical with assuming that heat transfer in the axial direction of rotor yoke is so small, so that the thermal model is presented as Figure 8.10 and the thermal conductive resistances are calculated as follows,

$$R_{ry1} = \frac{1}{2\pi k_{ry} L_{ry}} \ln(\frac{D_{ry1}}{D_{rym}}) \tag{8.25}$$

$$R_{ry2} = \frac{1}{2\pi k_{ry} L_{ry}} \ln(\frac{D_{rym}}{D_{ry2}}) \tag{8.26}$$

$$D_{rym}=(D_{ry1}+ D_{ry2})/2 \tag{8.27}$$

The thermal capacitance is

$$C_{ry} = \rho_{ry} c_{ry} \pi (D_{ry1}^2 - D_{ry2}^2) L_r / 4 \tag{8.28}$$

where, ρ_{ry} is mass density, c_{ry} is specific heat, and D_{ry1} and D_{ry1} are respectively the outer and inner diameter of the rotor yoke.

The eddy current loss of the rotor yoke P_{edd_ry} is calculated by a transient FEM model.

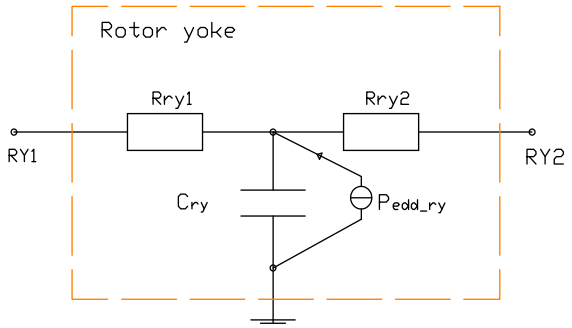

Figure 8.10. Thermal model of rotor yoke. RY1 and RY 2 are respectively the points on the exterior and interior surface of the rotor yoke.

8.3.9. Thermal Model of the Frame (Flywheel)

Assume that the heat transfer in the axial direction is negligible. The frame is considered as a cylinder, so its thermal resistance and capacitance in the radial direction is [Bog 2003],

$$R_{frame} = \frac{1}{2\pi k_{frame} L_f} \ln\left(\frac{D_{f1}}{D_{fs2}}\right) \tag{8.29}$$

$$C_{frame} = \rho_{frame} c_{frame} \pi (D_{frame1}^2 - D_{frame2}^2) L_{frame} / 4 \tag{8.30}$$

where, k_{frame} is the thermal conductivity of frame material, L_f is frame length, D_{f1} is the outer diameter of the frame, D_{f2} is the inner diameter of the frame.

8.3.10. The Thermal Model for Interior Parts of Stator Yoke

The thermal model of the interior parts of the stator yoke includes the thermal resistor of covering plastic, thermal resistor of spokes and the thermal convection from these surfaces to the air in the hollow. Figure 8.11a predicts a cross section of the stator and emphasizes the internal parts of the stator hollow. Figure 8.11b presents a thermal model for the internal parts of the stator hollow.

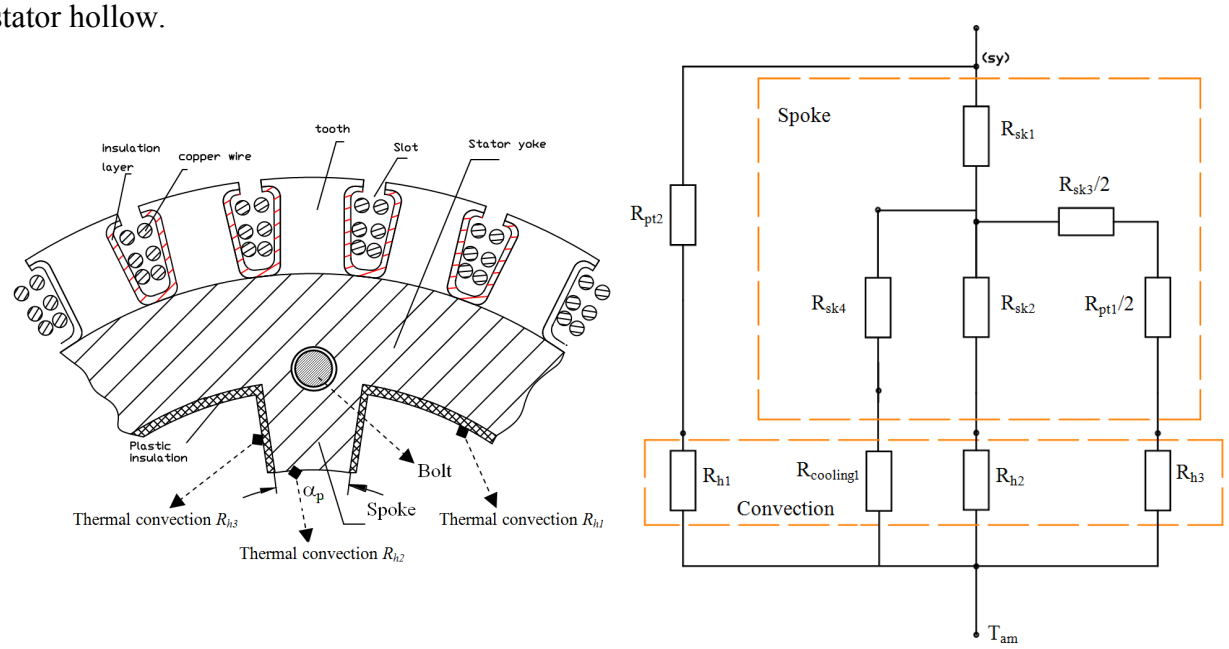

a) b)

Figure 8.11. a) Cross section illustrating interior parts of the stator hollow, b) thermal model of interior parts of the stator yoke. The subscript of thermal resistors means that "sk" stands for spoke, "pt" stands for plastic.

a) Thermal Model for Spokes

Assume that the spoke heat transfer on the axial direction is negligible. Heat transfer is only in the radial direction. This is because the stator is made of iron laminations. The thermal resistances of all spokes are

$$R_{sk1} = k_p \frac{1}{2\pi k_{iron} L_s} \ln(\frac{D_{sk1}}{D_{sk}}) \tag{8.31}$$

$$R_{sk2} = k_p \frac{1}{2\pi k_{iron} (L_s - L_c)} \ln(\frac{D_{sk}}{D_{sk2}}) \text{ , } D_{sk} = (D_{sk1} + D_{sk2})/2 \tag{8.32}$$

$$R_{sk3} = \frac{t_{sk}/2}{n_p k_{iron} L_s H_{sk}}; \qquad R_{pk4} = k_p \frac{1}{2\pi k_{iron} L_c} \ln(\frac{D_{sk}}{D_{sk2}}) \tag{8.33}$$

$$k_p = \frac{2\pi}{n_p \alpha_p} \tag{8.34}$$

where, n_p is the spoke number; D_{sk1}, D_{sk2}, and D_{sk} are the outer, inner, and mean diameter of the spoke respectively; L_s and L_c are the length of stator and cylinder cooling, and t_{sk} and H_{sk} are the average thickness and height of the spoke respectively.

b) Thermal Resistance of Plastic Covering Spoke

$$R_{pt1} = \frac{1}{n_p} \frac{d_{pt}}{k_{pt} L_s H_{sk}} \tag{8.35}$$

where k_{pt} is the thermal conductivity of the plastic and d_{pt} is the thickness of the plastic.

c) Thermal Resistance of Plastic Covering Surface of Interior Stator Yoke

$$R_{pt2} = \frac{d_{pt}}{(2\pi - n_p \alpha_p) k_{pt} r_{is} L_s} \tag{8.36}$$

where r_{is} is the interior radius of the stator yoke.

8.4. Heat Transfer to the Environment

8.4.1. Radiation and Convection Heat Transfer

Heat transfer from the PM machine to the environment is done by the thermal convection and radiation. The following are the main equations for calculating the heat transfer.

a) Radiation Heat Transfer

The thermal radiation can be described by the Stefan-Boltzmann equation as, [Ner 2008]

$$P_{rad} = e\sigma(T_1^4 - T_2^4) \tag{8.37}$$

where P_{rad} is the power transferred by radiation per unit area, e is the emissivity of the surface choosing the value of 0.5 and σ is the Stefan-Boltzmann constant, $5.67*10^{-8}$ ($W.m^{-2}.K^{-4}$). And T_1 and T_2 are the temperature of the surfaces in Kelvins.

The radiation heat transfer between surfaces can be modelled by the equivalent thermal resistance as, [Ner 2008]

$$R_{rad} = \frac{1}{\alpha_{rad} A} \tag{8.38}$$

where, A is area of the surface and α_{rad} is the equivalent radiation coefficient defined as,

$$\alpha_{rad} = \frac{P_{rad}}{(T_1 - T_2)} \tag{8.39}$$

Some radiation thermal resistances are calculated in order to compare them with forced convection thermal resistances as follows,

- Radiation heat transfer from end windings to wall and other objects,
- Radiation heat transfer between the stator surface and the interior rotor surface, and
- Radiation heat transfer from the cooling plate to the wall.

The calculation results of radiation thermal resistances are shown in the Table 8.1. The radiation heat transfer of the other parts can be ignored, because of the low temperature gradient of the parts.

b) Convection Heat Transfer

The convective heat transfer between the surfaces of an object and air is modelled by a convection thermal resistance R_c which is calculated as,

$$R_c = \frac{1}{hA} \tag{8.40}$$

where, h is the heat transfer convection coefficient, A is the area of the surface.

There are some convection thermal resistors are included in the thermal model of the PM machine as follows,

- The natural thermal convection from the interior surface of the hollow to the air in the stator hollow,
- Thermal convection from the frame of rotor to the air,

- Thermal convection from surface of the end windings to the air,
- Thermal convection from the tooth surface to the air gap,
- Thermal convection from the shaft to the air in the stator hollow, and
- Thermal convection from cooling plate to the air.

Detailed description of how to calculate the natural and forced convection coefficients and convection thermal resistances will now be given.

8.4.2. Natural Convection Heat Transfer from Interior Stator Surface to Air

Assume that the effect of the rotating shaft on thermal convection in the hollow is negligible. This is because the shaft surface is smooth and its diameter is small in comparison with hollow diameter. The surface of the stator hollow can be divided into two parts, namely the interior surface of the stator yoke and the surface of the spoke.

a) Convection Thermal Resistance from the Interior Surface of Stator Yoke to Air

The interior surface of the stator yoke is divided in to four sections, which are separated by the spokes. Each of the section is approximated as a rectangular surface. The mean Nusselt number of the natural heat transfer can be therefore approximately calculated according to an empirical correlation as, [Cen 1997], [Rou 2007],

$$N_{uD} = \left\{ 0.825 + \frac{0.378 R_a^{1/6}}{\left[1 + (0.492 / \mathrm{P_r})^{9/16}\right]^{8/27}} \right\}^2 \tag{8.41}$$

where R_a is the Rayleigh number and P_r is the Prandtl number.

The Prandtl number for quiescent air can be written as, [Cen 1997]

$$P_r = \frac{c_p \mu}{k_{air}} \tag{8.42}$$

where c_p is specific heat, μ is the dynamic viscosity of air, and k_{air} is the thermal conductivity of air.

Thermal convection coefficient and convection thermal resistance can be expressed as, [Cen 1997]

$$h_s = \frac{N_{uD} k_{air}}{\delta} \tag{8.43}$$

$$R_{h1} = \frac{1}{h_s A_s} \tag{8.44}$$

The Rayleigh number R_a can be calculated as, [Cen 1997]

$$R_a = G_r.P_r = \frac{g\beta(T_s - T_\infty)\delta^3}{\upsilon^2} P_r \tag{8.45}$$

where, G_r is the Grashof number, g is gravitational acceleration, υ is kinematic viscosity of the fluid, T_s is surface temperature, T_∞ is temperature of air, β is coefficient of volume expansion, $\beta \approx 1/\{(T_s+T_\infty)/2\}$, δ is the characteristic length of the geometry with $\delta = A_s/P_s$, A_s is the area of the surface and P_s is periphery of the surface, and k_{air} is the thermal conductivity of the air.

b) Convection Thermal Resistances of Spoke

The convection thermal resistance R_{h2} from the surface of spokes to the air in the hollow can be calculated in a similar way as in the section above, i.e., Section 8.4.2a. However, the mean Nusselt number is calculated as follows, [Cen 1997]

$$N_{uD} = (N_{uD1} + N_{uD2})/2 \tag{8.46}$$

The Nusselt number N_{uD1} for an upper surface of a hot plate can be calculated as, [Cen 1997],

$$N_{uD1} = 0.54 Ra^{1/4} \tag{8.47}$$

The Nusselt number N_{uD2} for the lower surface of a hot plate can be calculated as, [Cen 1997],

$$N_{uD2} = 0.27 Ra^{1/4} \tag{8.48}$$

Convection thermal resistance R_{h3} from the plastic surface covering the spokes to the air is also calculated as in Subsection 8.4.2a. However, the characteristic length δ is equal to the height of the spoke.

8.4.3. Convective Heat Transfer from Frame of Rotor to Air

The convective heat transfer from the frame to the air can be divided into two, namely natural convection and forced convection. The natural convection does not depend on rotor speed. Forced convection however depends on rotor speed. At high rotor speed, forced convection is dominant, while at rotor stand still, heat transfer is the result of natural convection. The convection coefficients will be presented as follows. Once the thermal coefficients have been obtained, the convection thermal resistance can easily be calculated according to equation (8.40).

a) Natural Convection Coefficient

The natural convection coefficient of the frame is calculated based on the formula for the horizontal cylinder as follows,

$$h_{o\_r} = \frac{N_{uD\_o} k_{air}}{D_{or}} \tag{8.49}$$

where, N_{uD_o} is the Nusselt number of the natural convection and D_{or} is the exterior diameter of rotor.

The Nusselt number can be calculated as, [Cen 1997], [Rou 2007], [Bej 1993],

$$N_{uD\_cylinder} = (0.6 + 0.387 R_a^{0.166} (1 + 0.721 P_r^{-0.5625})^{-0.296})^2 \tag{8.50}$$

b) Forced Convection Coefficients

The mean convective heat transfer coefficients of the rotor frame to air [Oze 2000] can be calculated as $h_r = N_{uD} k_{air} / D_{or}$.

The Prandtl number constant is calculated as $P_r = c_p \mu / k_{air}$, where μ is the dynamic viscosity of air.

The Reynolds number is calculated as, [Oze 2000], $R_e = \omega D_{or}^2/(2\upsilon) = \pi n D_{or}^2/(60\upsilon)$, where ω is angular rotation velocity (rad/s) and n is rotation per minute.

The Nusselt number N_{uD} can also be calculated according formula in [Rou 2007] as

$$N_{uD}=0.3+0.62 Re^{0.5} P_r^{0.333} (1+0.000392 R_e^{0.625})^{0.8} (1+0.543 P_r^{-0.667})^{-0.25} \tag{8.51}$$

8.4.4. Convective Heat Transfer from Tooth Surface to Airgap

It is assumed that heat flow is only transferred from tooth surface to the air gap in the radial direction. As mentioned, the velocity of air in the air gap is considered as equal to that of a point on surface of magnet [Rou 2007]. Therefore, the main coefficients can be calculated as follows.

The Reynolds number can be calculated as $R_e = \omega D_{ir}^2 / (2\upsilon) = 2\pi n / 60 D_{ir}^2 / (2\upsilon)$, where D_{ir} is the interior diameter of rotor and n is rotation of rotor per minute .

The Nusselt number can be calculated for a turbulent flow between the air gap and the stator surface as follows, [Kre 2000], [Rou 2007]

$$N_{uD} = 0.0296 R_e^{4/5} P_r^{1/3} \tag{8.52}$$

The mean convective heat transfer coefficient from the tooth surface to the air gap is calculated as

$$h_s = \frac{N_{uD} k_{air}}{D_{os}} \tag{8.53}$$

8.4.5. Convection Thermal Resistance from End Winding to Air

The rotor operates as a fan for cooling end windings. Therefore, according to the concept in [Rou 2007], it is assumed that the velocity of the air at area of end windings is considered as equal to the velocity of air in the air gap.

a) Natural Convection

Natural convective thermal resistance R_{ew_o} from end winding to air can be calculated as,

$$R_{ew\_o} = \frac{1}{2zh_{ew}A_{ew}}; \quad A_{ew} = \pi d_{ew} h_t / 2 \tag{8.54}$$

$$h_{ew} = \frac{N_{uD} k_{air}}{d_{ew}} \tag{8.55}$$

where A_{ew} is the outer surface area of end windings, d_{ew} is the outer diameter of end windings, h_{ew} the thermal convection coefficient of end windings and h_t is height of tooth.

The Nusselt number for a vertical cylinder can be calculated as in equation (8.41), [Cen 1997].

b) Forced Convection

The Nusselt number for a cylinder can be calculated as equation (8.51), while thermal resistance can be calculated according to equation (8.40).

8.4.6. Natural Convection of the Cooling Plate

The cooling plate has two functions. First, it is used to extract heat from the PM machine and release heat to the environment. Second, it is used to mount the stator of the PM machine on the wall. A brass cooling plate is shown in Figure 8.12a. The cooling is divided into two parts. The first part called “cooling plate 1” is put inside the stator hollow as shown in Figure 8.12b. The other part called “cooling plate 2” is put at the end side of the PM machine; this part is connected to four bolts crossing through the stator yoke.

The natural convection of the cooling plate is totally natural convection of the lateral, exterior and interior surfaces of a horizontal cylinder and disc surfaces. Their Nusselt number is calculated corresponding to the surface shapes like the vertical plate and horizontal cylinder, so equations (8.41) and (8.50) can be used for the calculation.

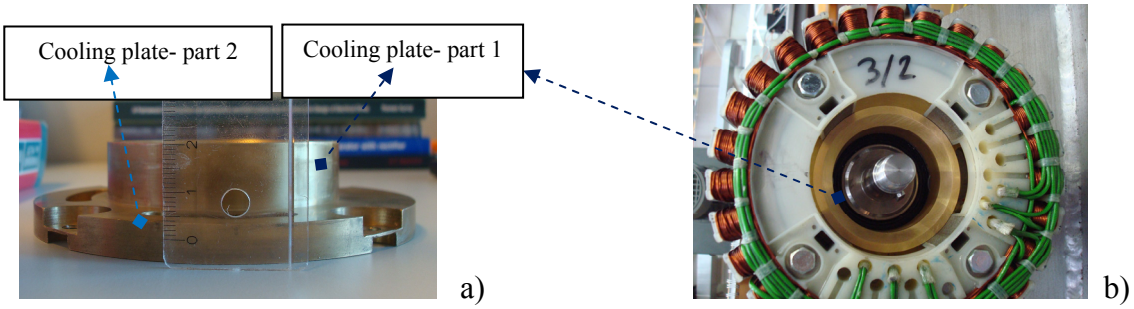

Figure 8.12. a) Cooling plate, b) stator.

8.5. Thermal Model Simulation of a PM Machine

8.5.1. Thermal Model Simulation of the Whole PM Machine

The thermal model of a whole PM machine is formed from the thermal models of components by connecting them together through contacting resistances and/or convection thermal resistance. Figure 8.13 depicts the thermal model simulation program of the whole PM machine B, implemented in Simulink/Matlab®. The thermal simulation program uses capacitors, resistors, and power sources from the library of the Power System Toolbox of Simulink/Matlab®.

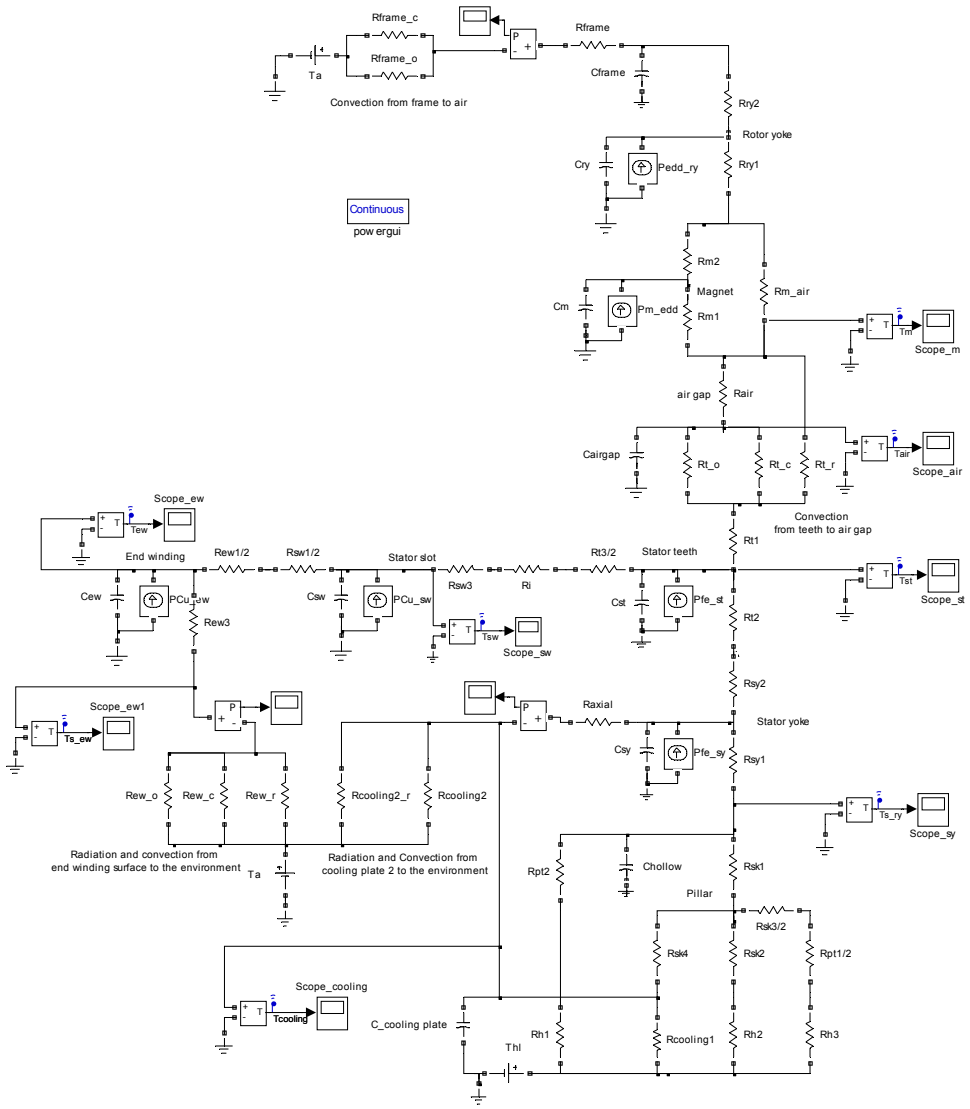

Figure 8.13. Thermal model of the PM machine B simulated in Matlab/Simulink®.

8.5.2. Operating Chart of Simulation Program

Figure 8.14 depicts the concept for writing a thermal analysis program. The power losses of the PM machine are calculated by an automated transient FEM program. A Matlab® command-based sub-program is used to calculate thermal resistances and capacitances. The thermal model is implemented in a Simulink/Matlab® program, which is a sub-program of the main program in m-file Matlab®. The thermal model and its program are flexible, computationally fast as well as visual. The proposed concept allows considering thermal aspects during the iterative automated electromagnetic design process of the PM machine.

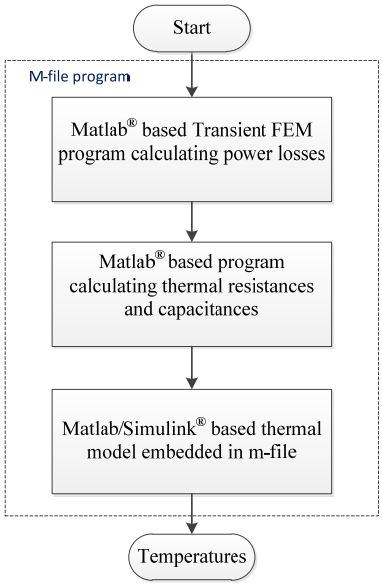

Figure 8.14. Operating chart of simulation program: Thermal model coupling with automated transient FEM model, the program written by Matlab® command set.

8.6. Comparison of Simulation with Experimental Results

Results of measured parameters of the PM machine B during three-phase resistive load are presented in Table 8.2. Figure 8.15 presents measured temperatures of tooth surface, slot winding, end winding, and air near the surface of the stator yoke, while Figure 8.16 presents simulated temperatures. To see the effect on transient temperatures when the electric power of the PM machine changes, we interrupted its three-phase load for a few seconds. Afterwards, the load was again switched on and kept at constant power until the end of the experiment. As a result of the interruption, the temperatures of end winding, slot winding and tooth surface dropped as shown in Figure 8.15. This test is a simple and efficient way to check the sensitivity of thermal sensors during the test to ensure that they are working well. It did not influence the steady-state temperatures of the tested PM machine. For simulation, the electric power and power losses are kept constant, so that the temperature performances increase continuously as shown in Figure 8.16.

For a relevant comparison between simulation and experiment, power losses for thermal simulation are obtained from the experiment. The separated iron loss is based on the ratio of tooth iron loss to total stator iron loss and the ratio of stator yoke iron loss to total stator iron loss, which are obtained from transient FEM simulation. The comparison is done at a low rotor speed with a semi-open slot PM machine, so that rotor eddy current loss is small enough. Table 8.3 compares simulation and experimental results when the temperature reaches a steady state. There

is good agreement. However, in transient operations, it can be found that the temperature of simulation is higher than the measured temperatures. The goal when making the thermal model is to estimate the steady-state temperatures of the slot winding, end winding, magnet, etc for design optimization of PM machines considering the temperature constraint, so there is no motivation to make a more complicated thermal model to get better transient simulation results. However, the reasons for the discrepancy between transient temperature simulation and measurement need to be explained. The discrepancy between transient temperature simulation and the results of experiments can be attributed to the followings:

- The heat transfer in the axial direction of the stator core, rotor iron, air gap, etc is not included in simulation.
- The end side frame, shaft, and ball bearing, which are not included in simulation, increase heat absorption during transient temperature.
- The bolts and nuts cause delay in heat transfer.
- The slotting effect [Mel 1991], [Sta 2008] which increases heat transfer over the smooth surface condition, is not considered.
- The difference between the velocity of the air at different positions in the air gap and end winding is not considered.
- The glue layers between the magnets and the rotor yoke, and between the rotor yoke and the frame can decrease heat transfer.
- Exact data about thermal properties is lacking.

The thermal model is used for design optimization taking into account temperature constraint, so the accuracy of the steady-state temperature is more important than the transient temperature. Therefore, the difference between transient temperatures obtained by simulation and those obtained by experiment can be tolerated. To improve transient thermal simulation, a more detailed thermal modeling is required.

Table 8.2. Measured parameters and losses of PM machine B at steady-state temperatures.

n (rpm)	**I_{rms} (A)**	**$V_{rms\ L-L}$ (V)**	**P_{out} (W)**	**P_{in}(W)**
720	9.13	31.04	490.27	668.03
$P_{Cu}=3.R_{phase}.I^2=$		77.52 W		
$P_{noload}=$		98.97 W		
$P_{mech}=$		73.53 W		
$P_{fe}=$		25.45 W		
$P_{fe}+P_{cu}=$		102.97 W		
$P_{total\ losses}=$		176.50 W		

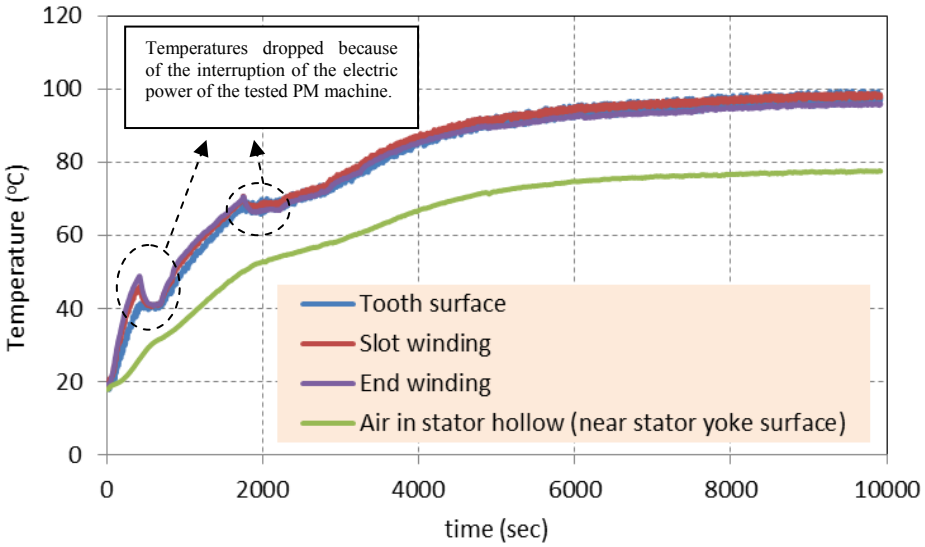

Figure 8.15. Measured temperatures of PM machine B.

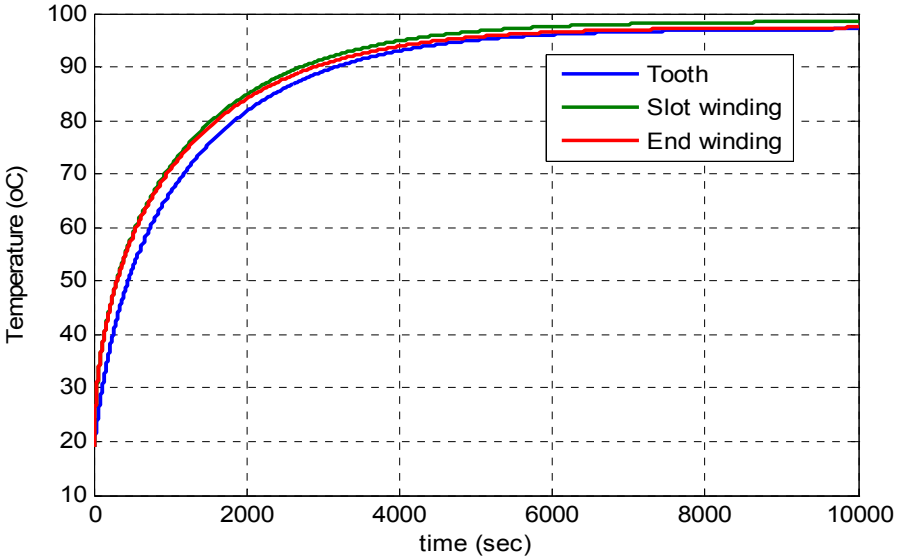

Figure 8.16. Simulated temperatures of PM machine B.

Table 8.3. Comparison of simulation and experimental temperatures at steady-state of PM machine B.

	Tooth surface	Slot winding	End winding	Permanent Magnet
Measurement (°C)	97.5	97.7	96.0	x
Simulation (°C)	96.8	98.5	97.4	40

8.7. Discussion of and Solutions for Improving Heat Transfer

Almost all the heat of the rotating PM machine is released to air from the end windings, rotor frame, and cooling plate. For example in the PM machine B, at rotor speed of 720 rpm, with phase current of 8.13 A, there is a Copper loss of 77.5 W and an iron loss of 25.5 W. According to simulation, the 67 W of the loss is released to air by end windings, 18 W is released to air by the rotor frame, and 18 W is released to air by the cooling plate and the other parts.

In the case of the exterior rotor PM machine, the heat transfer from the rotor to air is very good because of the small forced convection thermal resistance. Moreover, the rotor eddy current loss is not very high. Therefore, the magnet temperature is not high, for instance, at 720 rpm, the temperature of the magnet increases by about 20 ^{o}C. In another example, at a rotor speed of 3150 rpm, there is a Copper loss of 77.5 W, a stator iron loss of 50 W and a rotor eddy current loss of 50 W. In the operating model, the magnet increases the temperature by only 25 ^{o}C and the rotor frame releases up to 60 W to air by forced thermal convection.

At a very low rotor speed or rotor standstill, the forced thermal convection decreases. Natural convection in small parts of the PM machine becomes more significant at low rotor speeds so that a more detailed thermal model may be required.

The thermal convection from the PM machine to air is much higher than the thermal radiation. This is because of the low temperature gradient of inside parts of the machine as well as the low temperature gradient of the parts to objects in the environment. The temperature difference between the rotor surface and objects around it is about 20^{o}C to 30^{o}C, so it is obvious that its radiation heat transfer is negligibly small. Calculation results show that the radiation heat transfers from the stator surface to the rotor and from end windings to the environment are small in comparison to convection heat exchange. At a rated rotor speed of 3150 rpm, radiation thermal resistance from the surface of the end winding to the wall and objects around it is 30 times smaller than the forced convection thermal resistance. At a low rotor speed of 720 rpm, the convection thermal resistance from the surface of the end winding to air is 10 fold higher than the radiation thermal resistance. A similar result was obtained when comparing the radiation heat transfer with the forced convection heat transfer at other surfaces. Therefore, it can be concluded that the radiation heat transfer plays a significant role at very low rotor speed or rotor standstill only. At a high rotor speed around a few thousands rpm as in ship application, the radiation heat exchange is negligible compared with forced convection heat exchange.

The rotor with permanent magnets mounted on its surface functions as a fan, thus a large amount of heat is transferred from end windings to the air. To improve heat transfer from the end

windings to the cooling plate, epoxy should be placed between the end windings and the stator teeth and between the end windings and cooling plate 2. If this is done contact thermal resistance between the end windings and the cooling plate will decrease (this concept has been applied to Machines C and D). Similarly, if epoxy is placed in the slot windings, heat transfer from windings to stator iron will also be improved.

Thermal conductivity of stator iron in the axial detection and made by iron laminations is small, so heat transfer in the axial direction can be neglected. However, the stator yoke has bolts through it. These bolts are connected to a cooling plate. Moreover, the bolts are made of steel, which has high thermal conductivity. This makes thermal conductivity in the axial direction of the system including the stator yoke and bolts increases significantly. Therefore, the use of bolts with high thermal conductivity and low magnetic permeability, and increasing their cross section area can improve heat transfer from the PM machine to the cooling plate. Thermal contact between the stator yoke and bolts also needs to be minimized, for example by using thermal glue.

In this study, the thermal model is only valid for the PM machine with the open lateral space. Otherwise, i.e., the PM machine with an enclosure, a more detailed thermal model of end windings is required; because in this case the PM machine is asymmetrical.

The thermal model in this study is used to estimate the mean temperature of components of the PM machine for design optimization. When studying temperature distribution, a series of CFD computations is required to calculate the distribution of airflow in the air gap and end windings.

When using the water-cooling for the PM machine as shown in Figure 2.17 in Chapter 2, the natural convective thermal resistance R_{h1} in Figure 8.2 should be replaced by an equivalent thermal resistance of the mass transfer of the water-cooling.

8.8. Conclusions

In this chapter, guidelines and methodologies are provided for the selection of suitable thermal equations with different geometries for creating a thermal model network, which takes into consideration special parts of the PM machine with concentrated windings, for instance, bolts, spokes, and cooling plates with a special geometry. The cooling plate is placed both in the stator hollow and at the end side of the machine. The simplified thermal mode in this chapter was made based on the lumped-parameter method and empirical correlation coefficients of thermal

convection found in literature. Thermal parameters can be calculated from the basic information about materials, so that this concept can be applied to the PM machines in the industry.

In the case of an exterior rotor, the rotor is well cooled by forced convection. Moreover, the conduction thermal resistances of the magnet, rotor yoke, and frame are very small. Therefore, the temperature difference between the magnet and the environment is low, about 20^{o}C to 40^{o}C. The risk of magnet demagnetization due to high temperature in normal working operation is low.

A solution for improving heat transfer from the PM machine to air is proposed, that is, improving heat transfer from the machine to the cooling plate by placing epoxy in windings and using bolts put in the axial direction. These methods were applied to Machines C and D.

The thermal model program for combining the electromagnetic transient FEM model and the circuit thermal model is developed. This achieves a fast and accurate temperature computation for the automated electromagnetic design of the PM machine taking into account temperature constraints.

The comparison of simulation and experimental results in the steady-state temperature shows good agreement.

CHAPTER 9

COMPARISON OF MACHINE CONFIGURATIONS

9.1. Introduction

In Chapter 2, electric machines were compared. As a result, the external rotor PM machine with concentrated windings was chosen for the small-scale ship application considered in this thesis. The goal in this chapter is first to compare the performances of PM machines with machines with concentrated windings such as the Ferrite PM machine and the sintered Neodymium PM machine; surface-mounted PM machines and inset PM machines. After that, five promising surface-mounted PM machines with double-layer concentrated windings, having different combinations of slot and pole, namely 24-slot/16-pole, 27-slot/18-pole, 24-slot/20-pole, 27-slot/24-pole and 24-slot/28-pole PM machines, are selected for further comparison to find the most suitable machine for the small-scale ship application. These machines have the number of slots per pole per phase q in a range of 0.25 to 0.5. It should be noted that in order to obtain high winding factor, the number of slots per pole per phase is often chosen in a range of 0.25 to 0.5. Falling out of this range, the winding factor is significantly reduced. The nonlinear transient 2D-FEM model including rotor motion is used to calculate performances of PM machines for comparison.

For practical considerations, the outer stator diameter of PM machines is fixed at 156 mm, the tooth width limited by mechanical issue should be bigger than 5 mm and the filling factor of windings should be smaller than 0.4 for automatically needle-wound windings. The criteria for the selection of generators for ship application are high efficiency and high torque density. In general, power density as well as torque density increases when pole number increases. In equation (3.16), Chapter 3, it was seen that when the number of poles increases, the air gap flux per pole decreases. This leads to the flux passing through rotor back iron, stator tooth, and stator back iron decreasing. Therefore, the dimensions and volume of the machine can be reduced. However, a high number of pole leads to a high slot number, high working frequency, high rotor eddy current loss, and stator iron loss. To compromise between torque density and constraints such as thermal stress, mechanical limitation, efficiency, etc the slot number and pole number of PM machines for this case study should be smaller than 27 and 28 respectively.

9.2. Comparison between Ferrite and Sintered Neodymium PM Machines

The Ferrite magnet has about three times less remanent flux density than the sintered rare-earth magnet, but it costs about ten times less. In this section, a Ferrite PM machine (the PM machine A) is used as benchmark generator for redesigning a sintered Neodymium PM machine for comparison. The flux contour for the two generators is presented in Figure 9.1. In Table 9.1, the main parameters of the two PM machines are compared. Stator core dimension and air gap length of the designed machine are kept the same as those of the benchmark machine to avoid changing mechanical parts when mounting the PM machines on the diesel engine. The internal voltage of the two machines is the same as far as possible. The main dimensions of the Neodymium PM machine such as magnet dimensions and slot opening are optimally designed by using the FEM model. The magnet thickness of 2 mm was designed as thin as possible for high power density and low cost. The sintered Neodymium magnet is 4 times thinner than the Ferrite magnet. Magnet width and slot opening are designed for minimum rotor eddy current loss while maximum terminal voltage and mean electromagnetic torque are as presented in Chapters 5, 6 and 7. The main dimensions of the Ferrite and Neodymium PM machines are compared in Table 9.1.

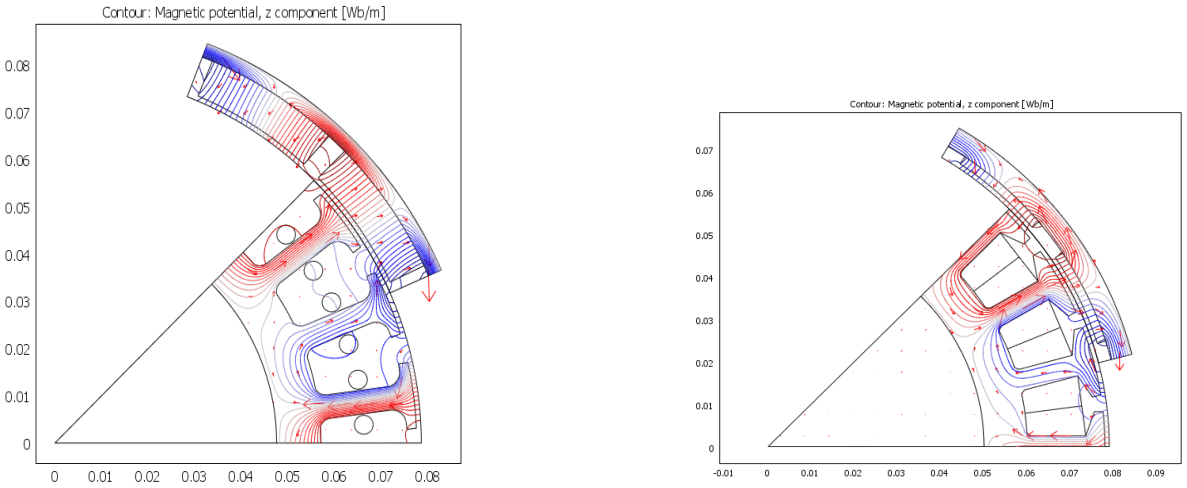

Figure 9.1. Flux contour: a) Ferrite PM machine, b) sintered Neodymium PM machine.

Table 9.1. Comparison of main dimensions of the PM machines.

	Dimensions of the Ferrite PM machine	Dimensions of Neodymium PM machine
Remanent flux density (T)	0.408	1.2
Magnet thickness (mm)	8	2
Magnet width (mm)	27	22.5
Winding diameter (mm)	0.8	0.8
Turn number per tooth	56	38
Slot opening (mm)	6	4
Slot/pole number	24/16	24/16
Outer rotor diameter (mm)	180	172

FEM calculation shows that the performances of the two PM machines are nearly the same. The rotor eddy current loss of the Ferrite PM machine is negligibly small. The rotor eddy current loss of sintered Neodymium magnet is minimized by the small slot opening. It is 15 W during a current loading of 5A and a current angle of 90 degrees. Stator iron loss of the sintered NdFeB machine is higher than that of the Ferrite machine, but the Copper loss of the former is smaller than that of the latter, so the efficiency is nearly the same. Table 9.2 presents the material cost per unit, while Figure 9.2 compares key physical parameters and raw material cost of the Ferrite and Neodymium PM machines, normalized to the parameter of the Ferrite machine. As can be seen, the volume of the NdFeB PM machine only reduces by 9%, this is because the outer stator diameter is fixed. The total cost of the raw Ferrite magnet material is 2.79 lower than that of NdFeB material, while the cost of all the raw materials of the NdFeB PM machine is 1.74 higher than the cost of the materials of the Ferrite machine. The cost of raw material is equal to the product of material mass and material cost per unit. It should be noted that the cost of materials per unit was calculated when the PM machines in this study were manufactured in 2009. The major advantage of the sintered rare earth PM machine compared to the Ferrite one is higher power density. Therefore, the Neodymium PM machine is preferred for the application considered in this study.

Table 9.2. Material cost per unit, when the PM machines in this study were manufactured, in 2009.

	Copper wire	Lamination steel	Steel	Ferrite magnet	Sintered NdFeB
Price [€/kg]	3	1.5	1	5	50

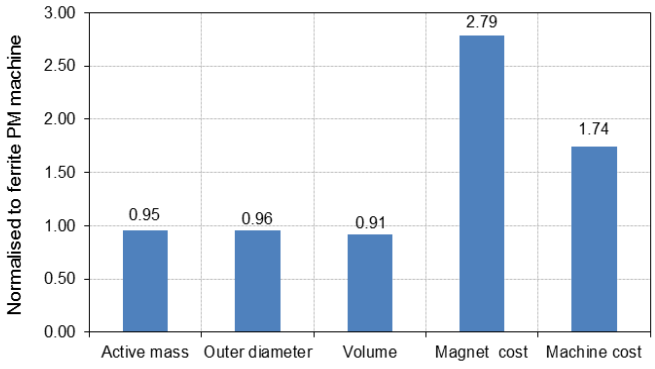

Figure. 9.2. Comparison of key physical parameters and cost of raw materials of a benchmarked Ferrite PM machine and a NdFeB PM machine, normalised to the Ferrite PM machine.

9.3. Exterior Rotor Surface-Mounted PM Machine versus Inset PM Machine

In this section, THE electromagnetic torque of an outer rotor surface-mounted PM machine (the PM machine B, FEM simulation shown Figure 9.3a) and two-inset PM machines (Figure 9.3b and 9.3c) with concentrated windings are compared. The purpose of this work is to provide an answer to the question: is the electromagnetic torque of the inset PM machine improved or not?

For sake of comparison, the structure of these PM machines is almost similar. The inset PM machines are modified from the surface-mounted PM machine by adding iron into the space between adjacent magnets, as in Figure 9.3b.

The nonlinear transient FEM is used for computation. The surface flux density and flux contour are presented in Figure 9.3.

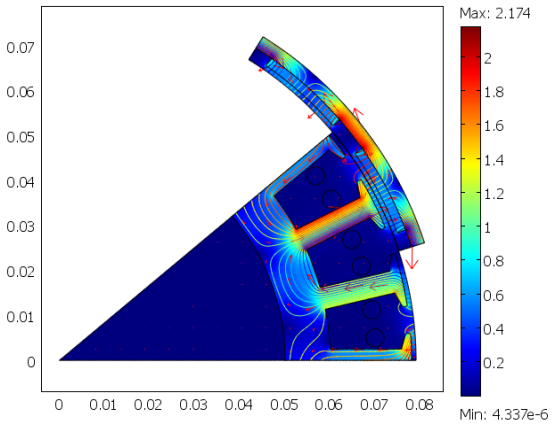

a)

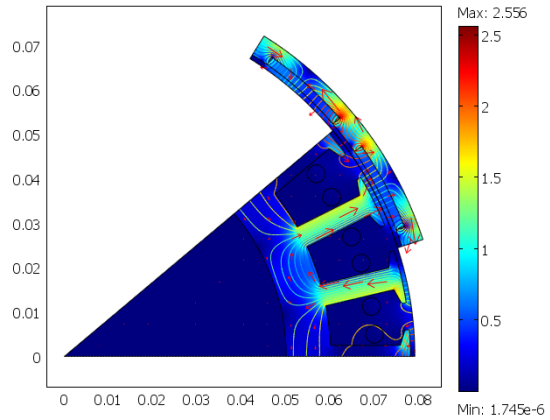

b)

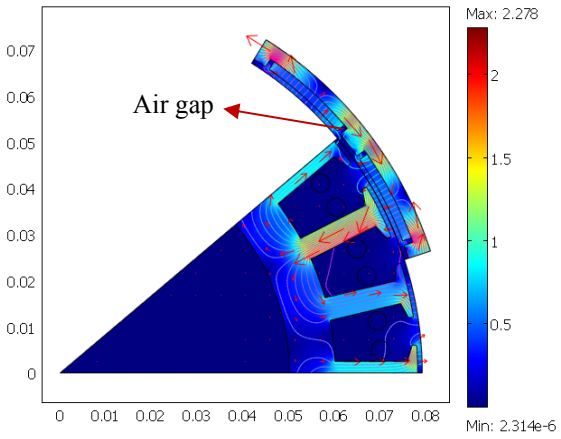

c)

Figure 9.3. FEM simulations for PM machines with 27slots/18poles: a) a surface-mounted PM machine b) an inset PM machine; c) an inset PM machine with air gap insulation layer between magnets and iron.

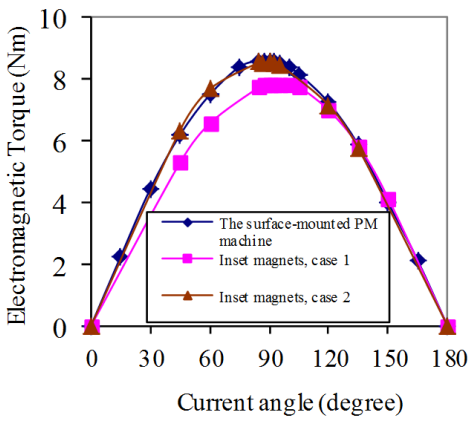

Figure 9.4. Mean electromagnetic torque of the surface-mounted machine B and the inset PM machines versus current angle.

The torque performances of a surface-mounted PM machine and inset PM machines are compared in Figure 9.4. For inset PM machines, there are two cases namely, case1: iron filled between adjacent magnets and case 2: iron filled between adjacent magnets but there is an air gap between the iron and the magnet.

Case 1, the leakage flux between the magnet and the iron significantly increases, as shown in Figure 9.3b and the flux linkage decreases. Moreover, the iron layer between magnets is thin, so reluctance torque is small. As a result, the maximum electromagnetic torque of the inset magnet PM machine is decreased in comparison with that of the surface-mounted PM machine, as shown in Figure 9.4.

Case 2, there is an air gap between the magnet and the iron, as shown in Figure 9.3c. This air gap functions as a magnetic isolation layer so that the leakage flux at edges of magnets reduces and flux linkage going to tooth increases in comparison with case 1. Therefore, the mean electromagnetic torque of the machine in the case 2 is higher than that in the case 1, as shown in Figure 9.4. However, the mean electromagnetic torque is not improved compared with the surface-mounted PM machine, as shown in Figure 9.4, because the iron layers between magnets are thin. This leads to the reluctance torque being negligibly small.

It was found that the inset magnet PM machine might increase mean electromagnetic torque when the iron layers between magnets are thick enough. Magnetic insulation layers, for example, an air gap layer should be inserted between the iron and the magnet to limit leakage flux.

9.4. Comparison between PM Machines with Different Combinations of Slot and Pole

Figure 9.5 and Figure 9.6 depict nonlinear transient 2D-FEM simulation results for the studied PM machines. Figure 9.5a depicts a simulation for machine 1 with 24slots/16poles corresponding to a slot/pole combination of 3/2 (or number of slots per pole per phase q=1/2=0.5). Because of the symmetrical geometry, only a section corresponding to a one-eighth of the machine is simulated. Machine 2 with 27 slots/18 poles corresponding to a slot/pole combination of 3/2, is similar to what was presented in previous chapters. Figure 9.5b is a simulation of half of machine 3 with 24slots/20poles corresponding to a slot/pole combination of 6/5 (q=2/5=0.4). Figure 9.6a is a simulation of one third of machine 4 with 27slots/24poles corresponding to a slot/pole combination of 9/8 (q=3/8=0.375). Figure 9.6b is a simulation of half of machine 5 with 24slots/28poles corresponding to a slot/pole combination of 6/7 (q=2/7=0.286).

Performances of PM machines will be presented in this section for the comparison of electromotive force (EMF), mean torque, rotor yoke iron loss, magnet iron loss, stator iron loss, power density and efficiency. These performances are presented in different forms for comparison.

The load of the generator is a PWM rectifier with a maximum dc voltage of 450V so that the RMS line-to-line voltage is limited to between 180V and 260 V. The comparison of PM machines is done with the same current of 10 A rms and the number of winding turns of each phase is the same. Stator diameter, rotor diameter, air gap length, magnet thickness, ratio of slot opening to pitch slot, and ratio of pole width to pole pitch are the same. Therefore, the materials of all the machines cost nearly the same amount. For sake of clarification, the major dimensions of the five PM machines are given in Table 9.3.

Table 9.3. Major parameters of PM machines studied in this section.

Rated current, [A]	10	Tooth width, [mm]	5
Magnet thickness, [mm]	2	Stator length, [mm]	35
Magnet remanence, [T]	1.2	Outer rotor diameter without flywheel, [mm]	170

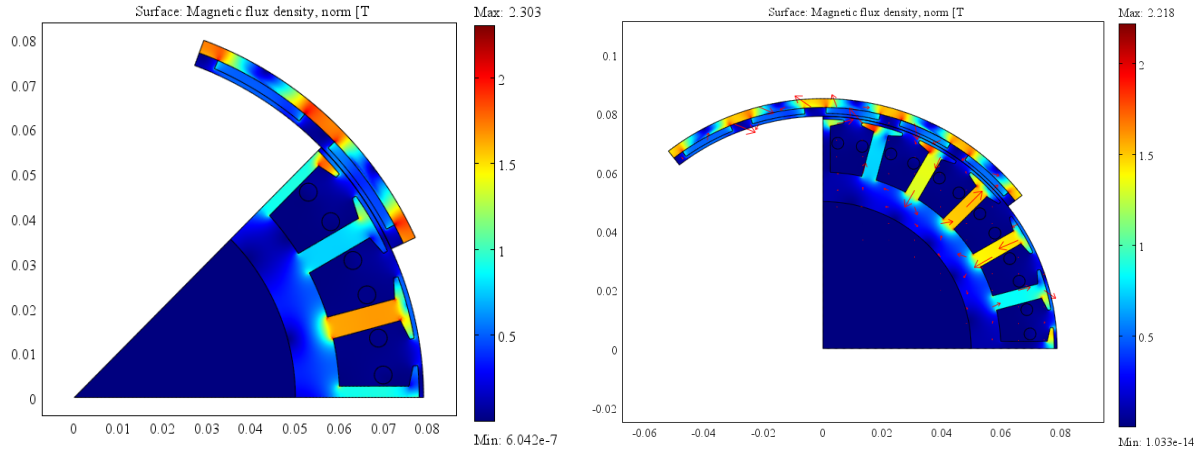

Figure 9.5. FEM simulation: a) the PM machine 1 with 24slots/16poles; b) the PM machine 3 with 24 slots, 20 poles.

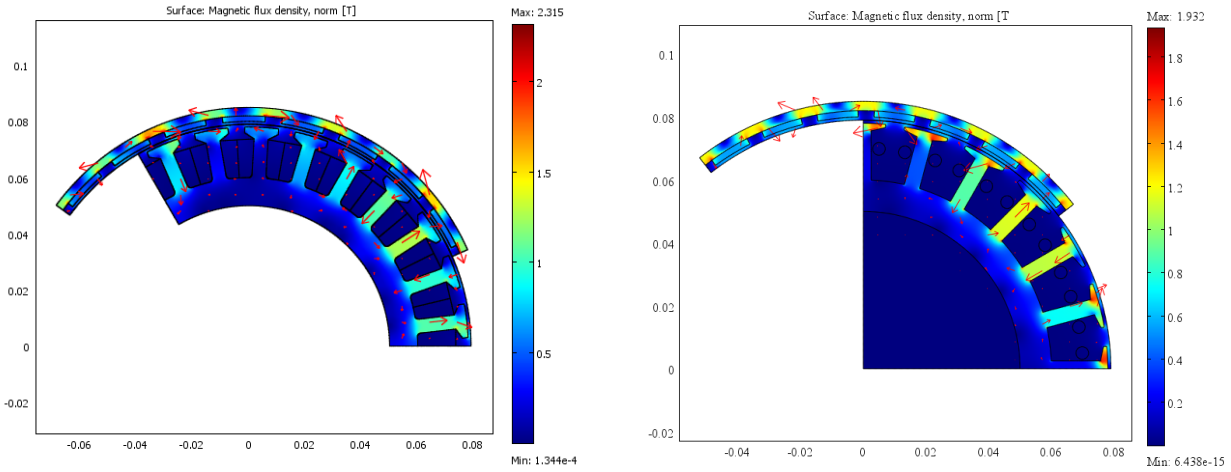

Figure 9.6. FEM simulation: a) the PM machine 4 with 27slots/24poles; b) the PM machine 5 with 24 slots, 28 poles.

9.4.1. No-load Operation

a) Comparison of Internal Voltage (or EMF)

Figure 9.7 presents EMF versus the combination of slot and pole number. For the calculation, PM machines have the same number of turns per phase. The EMF of the 27-slot/24-pole PM machine is greatest, 18% higher than that of the conventional PM machine 1. The results show that EMF depends on not only the winding factor, but also on the pole number. For instance, machines 1 and 5 have the same slot number of 24, when the pole number increases from 16 to 28, the EMF increases by 1.15 times. Machines 1 and 2 have the same winding factor, but when the pole number increases from 16 to 18, the EMF increases by 9%. When the number of poles increases, the PM machine is not as saturated because the air gap flux and flux passing teeth, rotor back iron, and stator back iron decrease.

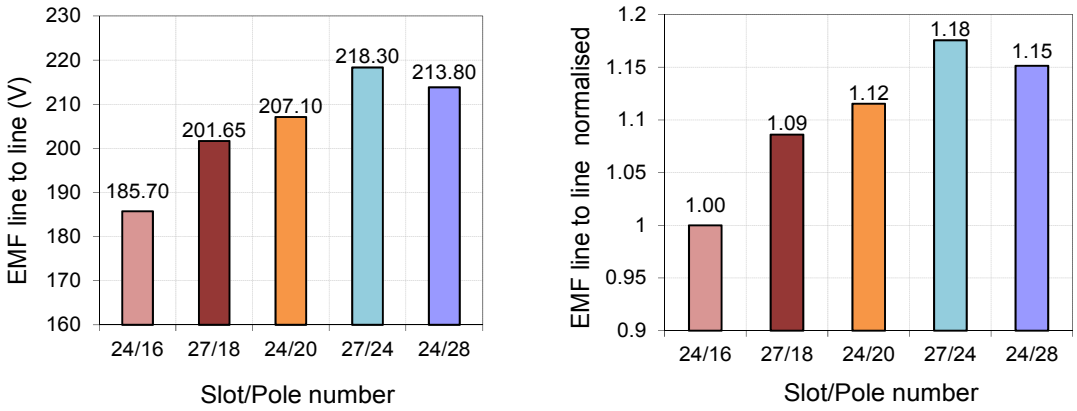

Figure 9.7. a) Electromotive force vs. slot/pole combination; b) EMF normalized to EMF of the PM machine 1 with 24slots/16poles.

b) Comparison of Eddy Current Loss and Stator Iron Loss during noload

Figure 9.8 and Figure 9.9 present losses of the studied PM machines. The rotor eddy current loss of PM machine 4 is the largest, 6.8 times larger than that of the traditional PM machine 1. Clearly, magnet eddy current loss is domninant in rotor loss, significantly higher than rotor yoke loss. The no-load loss of machine 4 is 3.57 times higher than that of reference machine 1.

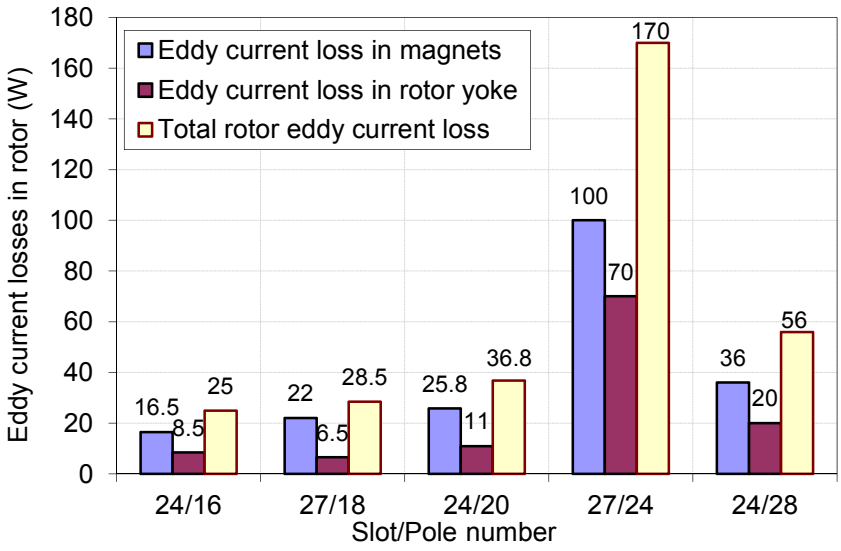

Figure 9.8. Rotor eddy current loss vs. slot/pole number.

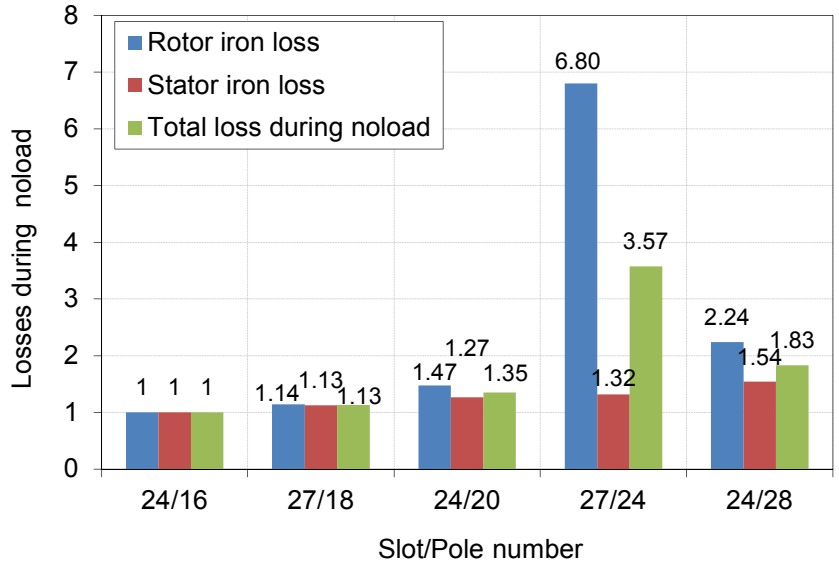

Figure 9.9. Losses vs. slot/pole combination, normalized to the 24-slot/16-pole PM machine.

9.4.2. Load Operation

The nonlinear transient 2D-FEM model including rotor motion is used for computation. The computation was done with the same current of 10 A rms and a current angle corresponding to maximum electromagnetic torque.

a) Comparison of Torque Density

Calculation results of mean electromagnetic torque and the comparison of torque density in Figure 9.10 and Figure 9.11 show that when using the the criterion of maximum torque density, the 24-slot/28-pole PM machine is the best choice. This PM machine has a 26% higher torque density than the reference 24-slot/16-pole PM machine, while the modular 24-slot/20-pole and 27-slot/24-pole PM machine have respectively15% and 16% higher torque density than machine 1. In conclusion, regarding the typical frational slot PM machines with concentrated windings, the torque density of the machine increases when the number of slots per pole per phase decreases.

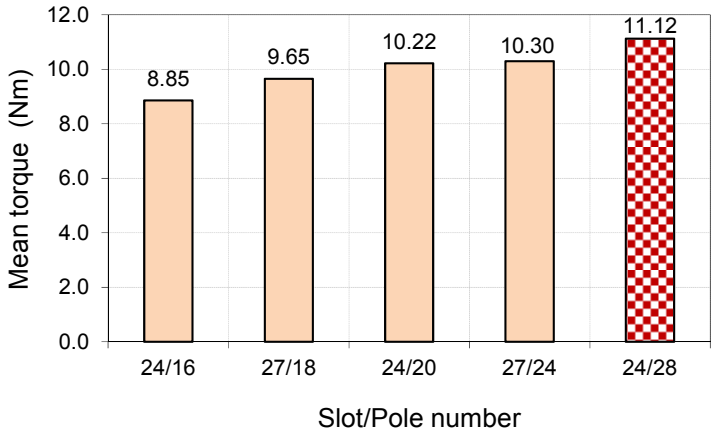

Figure 9.10. Mean torque vs. slot/pole number.

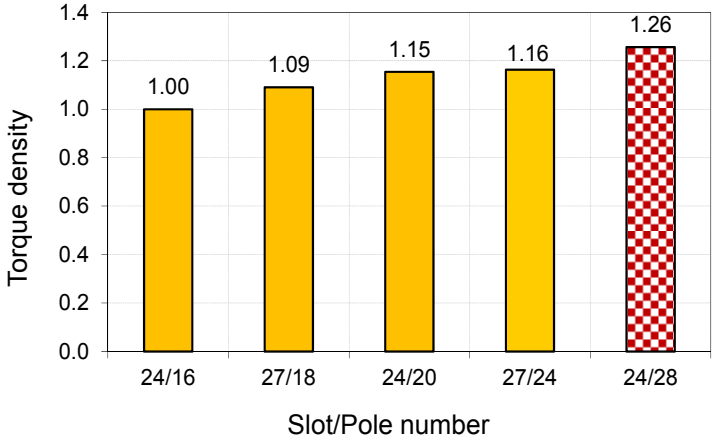

Figure 9.11. Electromagnetic torque density vs. slot/pole, normalized to 24slot/16 pole PM machine.

b) Comparison of Iron Losses during Load and Efficiency

It can be seen from Figure 9.12a that the rotor eddy current losses of the 24-slot/28-pole and 27-slot/24-pole PM machine are very high. During no load, rotor eddy current of the 27-slot/24-pole PM machine is the largest in comparison with the others, as shown in Figure 9.8. However, during load with a rated current of 10A, the rotor eddy current of the 24-slot/28-pole PM machine (machine 5) is the greatest, 5.22 times higher than that of the conventional PM machine 1, as shown in Figure 9.12b. Furthermore, the rotor eddy current on rated load of machine 5 is 4.9 time higher than that during no load. This can be explained by pointing out that the first, fifth, senventeenth and nineteenth harmonic components of MMFs (as shown in figure 3.11, Chapter 3) are the main cause of high rotor eddy current loss in the 24-slot/28-pole PM machine during load.

Calculation results of rotor eddy current loss during load as shown in Figure 9.1, confirm that the use of MMF harmonics to predict rotor eddy current loss in the rough as done in Section 3.13 in Chapter 3, is possible.

It can be seen from Figure 9.8 that the rotor eddy current loss of machine 2 during no load is higher than that of machine 1; this is because machine 2 has a higher working frequency. However, as can be seen from Figure 9.12, the rotor eddy current loss of machine 1 during load is higher than that of machine 2. This is because the two machines have the same number of turns per phase, but machine 1 has a higher number of turns per tooth. The MMF harmonic components play a significant role in causing rotor eddy current loss in machine 1.

Figure 9.13 presents the ratio of loss to input power. It is shown that the rotor eddy current losses of the PM machine 4 and 5 make up the dominant portion of the total loss. It is shown in Figure 9.14 that the efficiency of PM machines 1 and 2 is higher than that of the others. The efficiency of the machine 2 is the highest, reaching 94.12% (excluding mechanical loss). The efficiency of machine 5 is the lowest, only 90.27%, which is about 4% smaller than that of PM machine 2, while the efficiency of the 24-slot/20-pole and 27-slot/24-pole PM machines is respectively 1% and 2.3% smaller than that of PM machine 2. Therefore, regarding the typical frational slot PM machines with concentrated windings, the efficiency of the machines decreases when number of slots per pole per phase decrease.

In short, if the criterion of maximum efficiency is used to select PM machines, the 27-slot/18-pole PM machine 2 is the best choice. In all of PM machines are compared, the 24-slot/20-pole PM machine has neither the highest torque density nor the highest efficiency, but if using multi-criteria that compromise between torque density and efficiency, then it is the best option. If the

magnets of the 24-slot/28-pole PM machine are segmented, it might be a good competitor with the highest torque density and good efficiency.

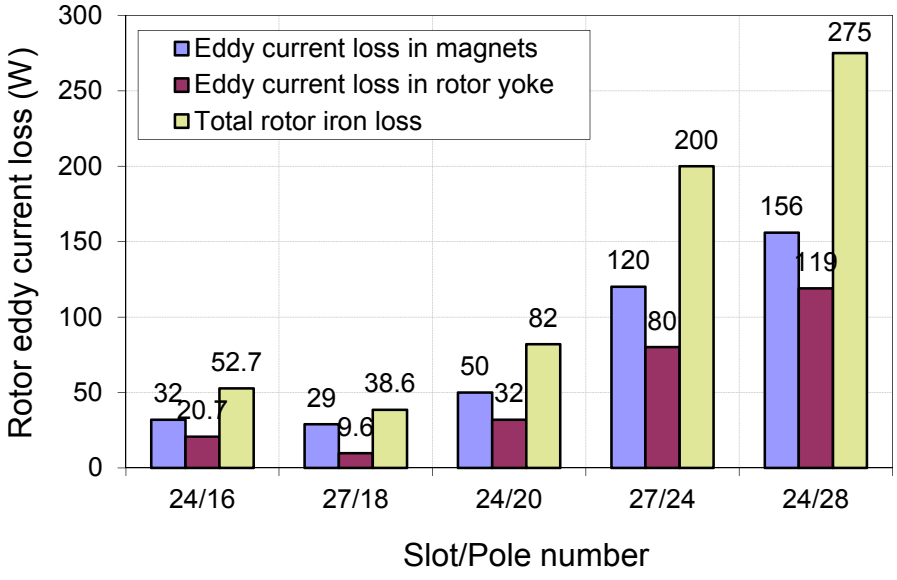

a)

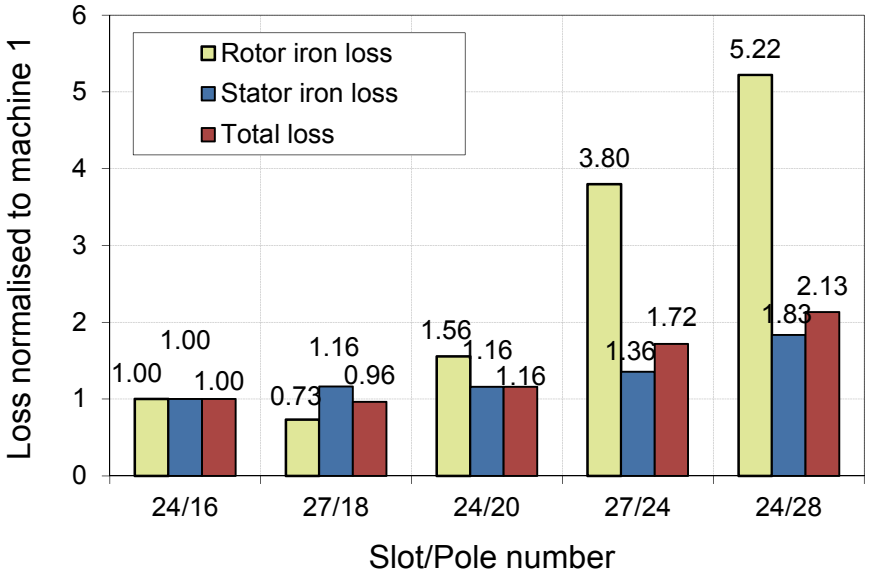

b)

Figure 9.12. a) Comparison of rotor eddy current losses of the PM machines. b) Losses vs. slot/pole combination, normalized to the PM machine 1.

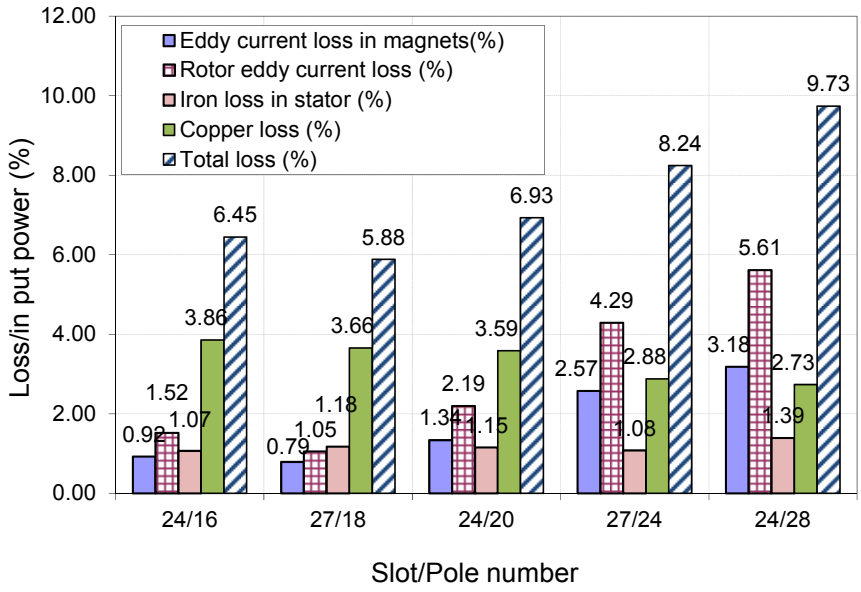

Figure 9.13. Loss/input power of the studied PM machines.

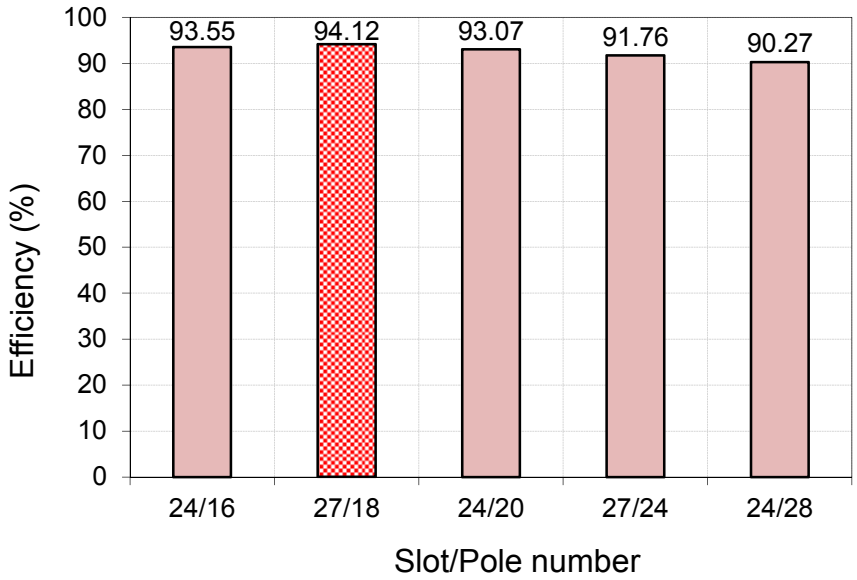

Figure 9.14. Efficiency vs. slot/pole combinations.

9.5. Conclusions

The results of a comparison between a Ferrite PM machine and a Neodymium PM machine show that the thickness of a Neodymium magnet reduces four times in comparison with a Ferrite magnet, but the machine cost of the Neodymium machine is 1.74 times that of the Ferrite

machine. The Neodymium magnet machine is preferred for this application because of its high power density and thin magnets.

Results of a comparison between an external rotor surface-mounted PM machine and external rotor inset PM machines show that the inset magnet machine only increases mean electromagnetic torque when the magnets are thick enough. A magnetic insulation layer, for example an air gap layer should be inserted between the iron and the magnets to reduce leakage flux.

Five promising PM machines, namely the 24-slot/16-pole, 27-slot/18-pole, 24-slot/20-pole, 27-slot/24-pole and 24-slot/28-pole PM machines, corresponding to slot/pole combination of 3/2, 3/2, 6/5, 9/8 and 6/7, were compared. The results are summarized as follows:

- The 24-slot/28-pole PM machine has the highest torque density, 26% higher than that of the 24-slot/16-pole PM machine 1, while the 24-slot/20-pole PM machine has only 15% higher torque density than machine 1.
- The rotor eddy current loss of the 24-slot/28-pole PM machine 5 is the highest, 5.22 times higher than that of the PM machine 1. The efficiency of PM machine 5 is the lowest, about 3.9% lower than that of the 27-slot/18-pole PM machine 2. PM machine 2 has the highest efficiency of the PM machines.
- The 27-slot/24-pole PM machine 4 exhibits very high no load iron loss. This machine has 1% smaller torque density than PM machine 5 and is 2.3% less efficient than PM machine 2.

In conclusion, when using the criterion of maximum torque density, PM machine 5 is the best choice. If the criterion is maximum efficiency, PM machine 2 is the best option. However, when using multi-criteria for compromising between maximum torque density and maximum efficiency, the 24-slot/20-pole PM machine 3 is the best option. If the magnets of the 24-slot/28-pole PM machine are segmented, it might be a good competitor with a high torque density and good efficiency. However, this will increase the overall cost of the machine.

CHAPTER 10

EXPERIMENTAL VALIDATION OF NONLINEAR TRANSIENT FEM MODEL INCLUDING ROTOR MOTION

10.1. Introduction

The nonlinear transient FEM model including rotor motion was developed as described in Chapter 4. The FEM model was used to study the slotting effect on the magnetic field and voltage and this was described in Chapter 5. The model was also used to study the slotting effect on electromagnetic torque (as presented in Chapter 6) and on iron losses (as presented in Chapter 7). In Chapter 9, the model was used to compare performances of PM machines with concentrated windings. In this chapter, the experimental setup and a comparison between FEM simulation and experiments are presented.

By comparing FEM simulation and experimental results, computation models of flux linkage, internal voltage, voltage on load, current, mean electromagnetic, inductance, three-phase short circuit current, and total loss are validated.

In this chapter, four PM machines with concentrated windings are used to validate the FEM model. All the machines have a slot/pole combination of 3/2. Machine A is a 3 kW PM machine with 24 slots and 16 poles. Machine B is 3 kW PM machine with 27 slots and 18 poles. Machine C and D are 9 kW PM machines with 27 slots and 18 poles, which have the same rotor. Machine C is a semi-open slot PM machine, while Machine D is a fully-open slot PM machine. Machine C and D are manufactured to validate slotting effect on internal voltage and iron loss. Note that the material is used in the stator cores of all the PM machines studied. Specifications of all machines were presented in Chapter 2.

10.2. Description of Experiments

The test setup devices comprise a torque sensor, a tachometer, oscilloscope, power analyzer, GPIB (General Purpose Interface Bus) connector and PM generators, as shown in Figure 10.1. The measurement testes performed are captured in the following steps,

(i) No load test without stator
(ii) No load test with stator
(iii) Load test (with resistive load).

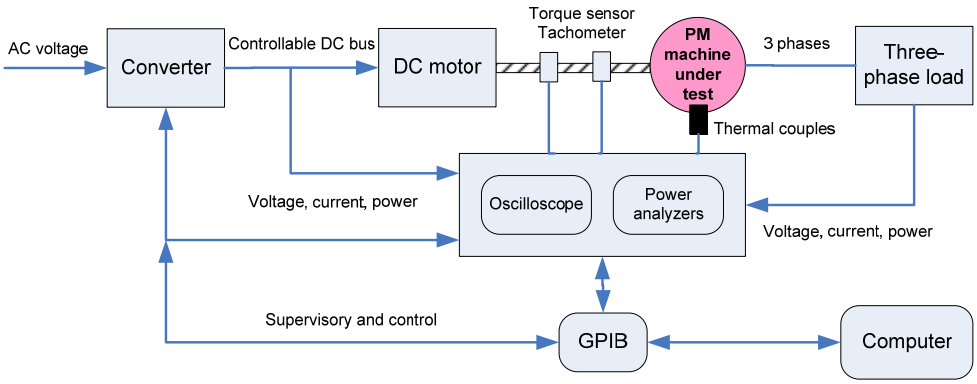

Figure 10.1. Experimental facilities.

The no-load test without stator measures the mechanical losses while the no-load test with stator measures the internal voltage, no-load torque, and no-load loss. The iron loss during no-load is equal to the difference between the no-load losses in (ii) and the mechanical loss in (i). In the load test, voltage, current, torque and speed are measured to give an indication of the total loss and efficiency. The mean electromagnetic torque is equal to the difference between the mean measured torque during load test (iii) and the mean measured torque during no-load test (ii). During load test, there is a symmetrical three-phase resistive load.

10.2.1. Using Machine A for the Validation of the FEM Model

Machine A is a fraction-slot ferrite PM machine with concentrated windings and a slot/pole combination of 3/2. Figure 10.2 presents the rotor, stator, and experimental setup of machine A. The FEM model is a nonlinear transient model coupled with a circuit model as described in Chapter 4. Details of experiments of machine A can be found in [Ani 2007], [Hun 2011].

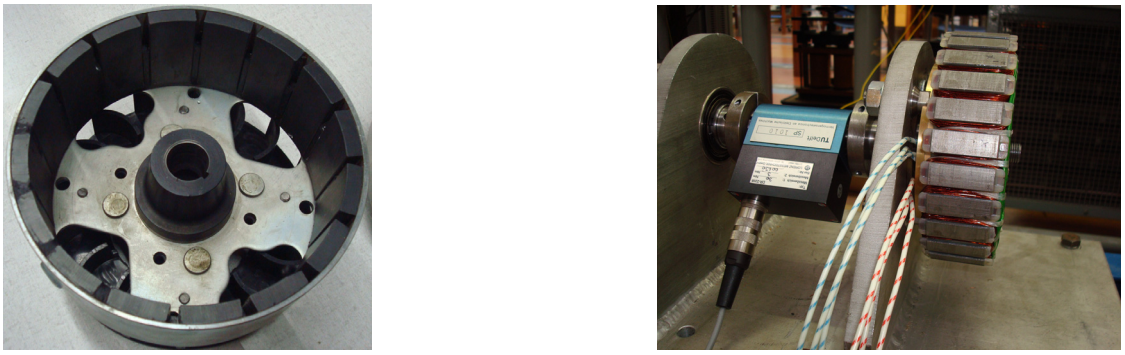

Figure 10.2. Rotor of machine A and test setup.

10.2.2. Using Machine B for the Validation of the FEM Model

Machine B is a 3 kW fractional slot Neodymium PM machine with concentrated windings. Its slot/pole combination is 3/2, which is the same as that of machine A. Figure 10.3 presents the rotor, stator, and setup of this machine.

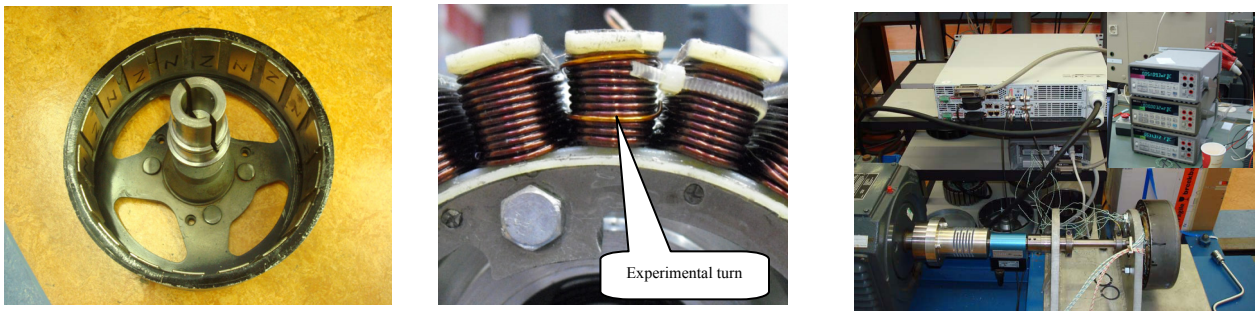

a) b) c)

Figure 10.3. a) Rotor, b) stator, and c) setup of permanent magnet Machine B.

10.3. Experimental Validation of the FEM Model

10.3.1. Experimental Validation of Flux Linkage and Internal Voltage during No-load

Figure 10.3b presents the setup used to measure the internal voltage of a turn and flux linkage through a tooth of Machine B. A turn is wound around a tooth. An oscilloscope is used to measure the voltage at the terminals of a turn at a certain speed of the rotor. Figure 10.4 presents a comparison between simulation and experimental results of flux linkage and internal voltage. The flux linkage is calculated by the transient FEM model according to the equation in Chapter 4, while the internal voltage of a turn is obtained by getting derivative of the flux linkage through a tooth. The measured flux linkage is derived by getting the integration of the measured internal voltage of a turn with respect to time. Results show that even though the internal voltage

amplitude discrepancy between simulation and experiment is about 3.5%, the results of the simulated and measured flux linkage show good agreement in terms of both amplitude and wave form.

Figure 10.5 compares the internal voltage simulation and experimental results of Machine B. Results show that magnetic saturation simulation and experiments are in good agreement with a maximum error of internal voltage amplitude between simulations and experimental results of about 3.5%.

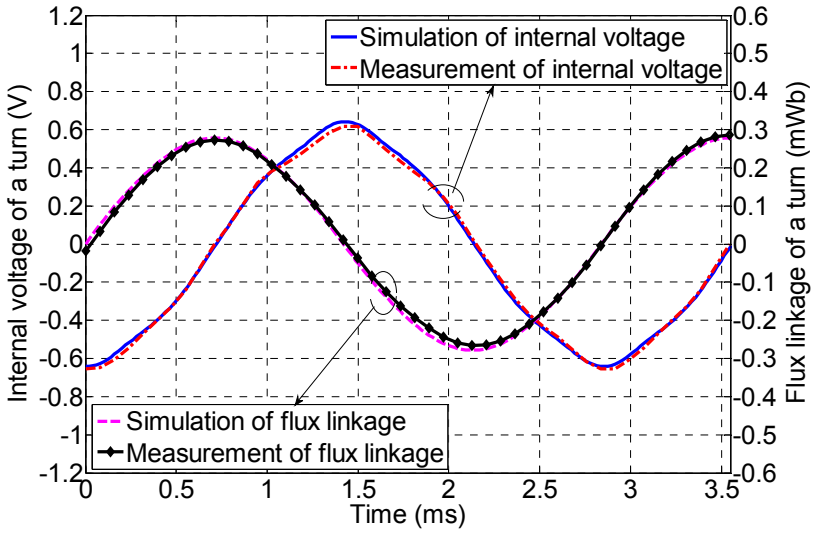

Figure 10.4. Comparison between simulations and experimental results in two cases: internal voltage of a turn and flux linkage of a turn, the semi-open slot PM Machine B at speed of 2347 rpm.

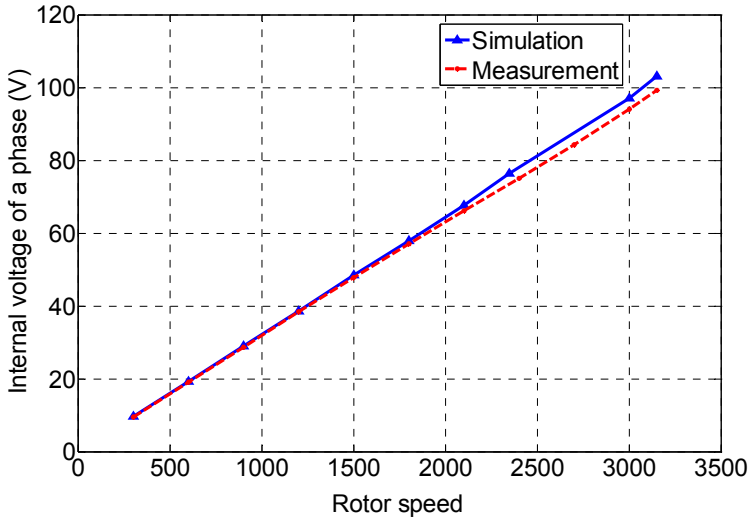

Figure 10.5. Comparing the rms of the internal voltage between simulations and experiments done on the Machine B.

Comparisons done for machine A between internal voltages obtained by simulation and measurement at different rotor speeds are presented in Figure 10.6. They show very good agreement. As can be seen, the increase of voltage is nearly linear to rotor speed.

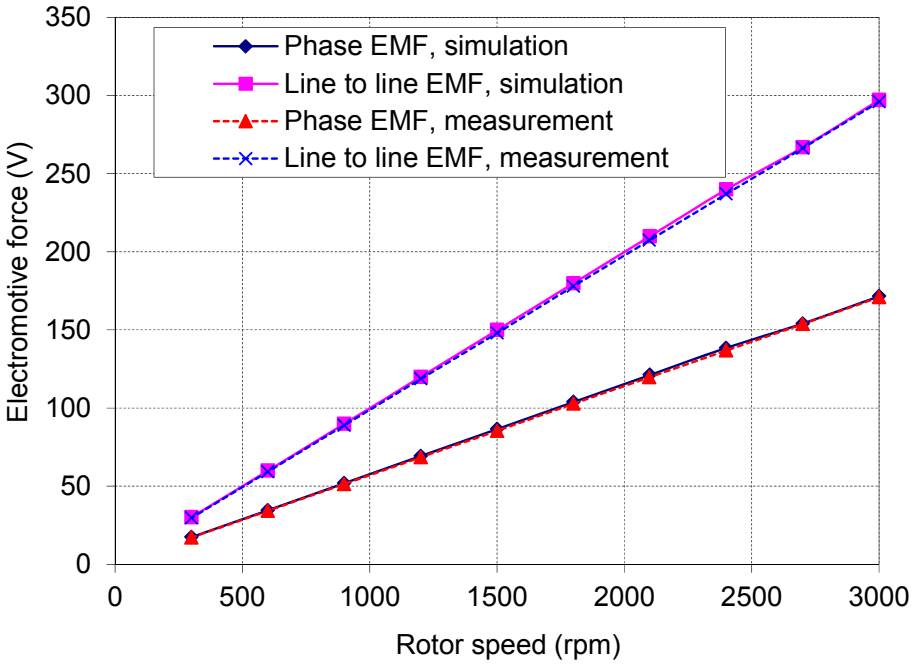

Figure 10.6. Comparison of simulation and experimental results of internal voltage (electromotive force) at different rotor speeds, Machine A.

10.3.2. Experimental Validation of Voltage and Current during Load

Figure 10.7 and Figure 10.8 present the simulation and experimental results done with Machine A regarding voltage and current versus rotor speed. Resistive load is kept constant during the experiment, so when rotor speed increases, voltage and electric current also increase. Figure 10.9 shows the relation between current and load voltage. It can be seen that simulation and experimental results show good agreement.

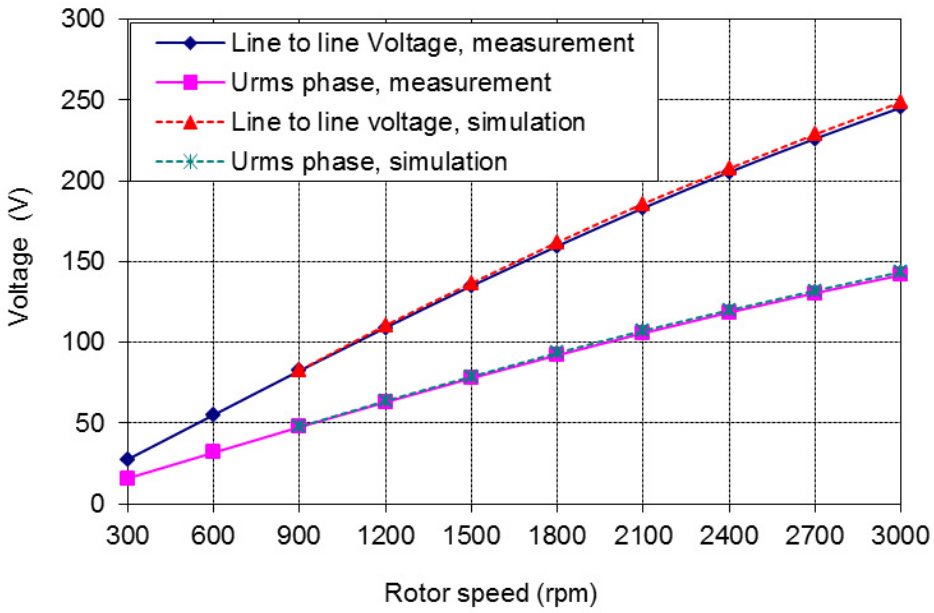

Figure 10.7. Comparison of simulation and measurement of load voltage at different rotor speeds, Machine A.

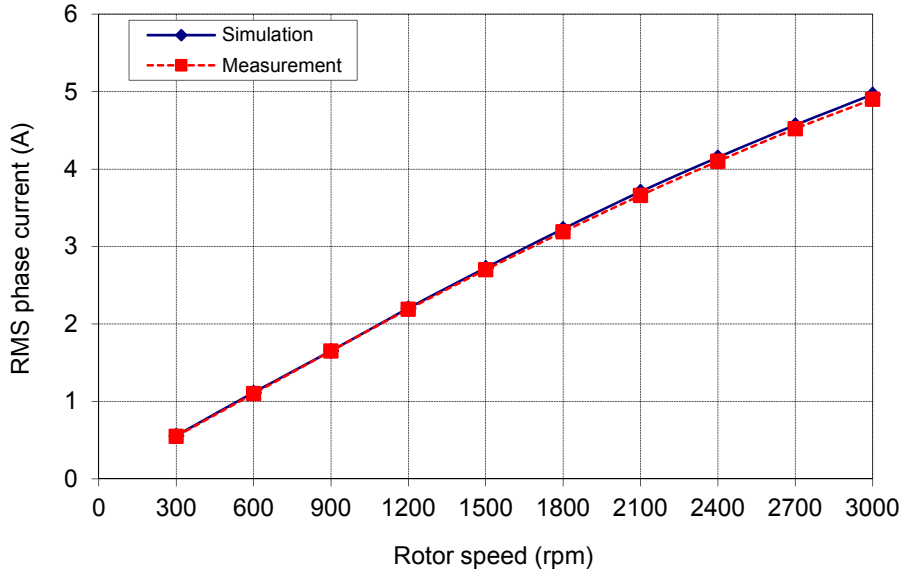

Figure 10.8. Comparison of simulation and measurement of load current at different rotor speeds, Machine A.

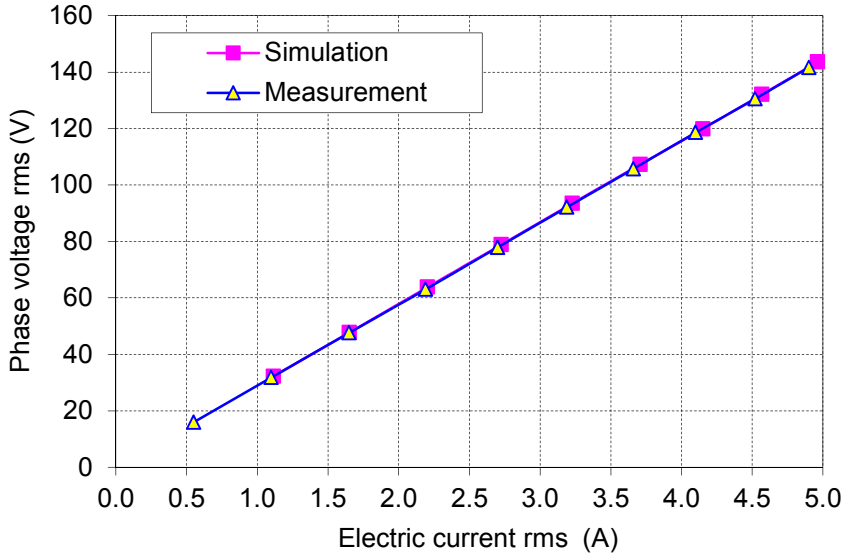

Figure 10.9. Phase voltage vs. load current, Machine A

10.3.3. Experimental Validation of Electromagnetic Torque

Comparisons of mean electromagnetic torque simulation and measurement are presented in Figure 10.10 and Figure 10.11. They show good agreement. In simulation, electromagnetic torque is calculated according to Maxwell's stress tensor method as described in Chapter 6. A torque sensor is used to measure mean electromagnetic torque.

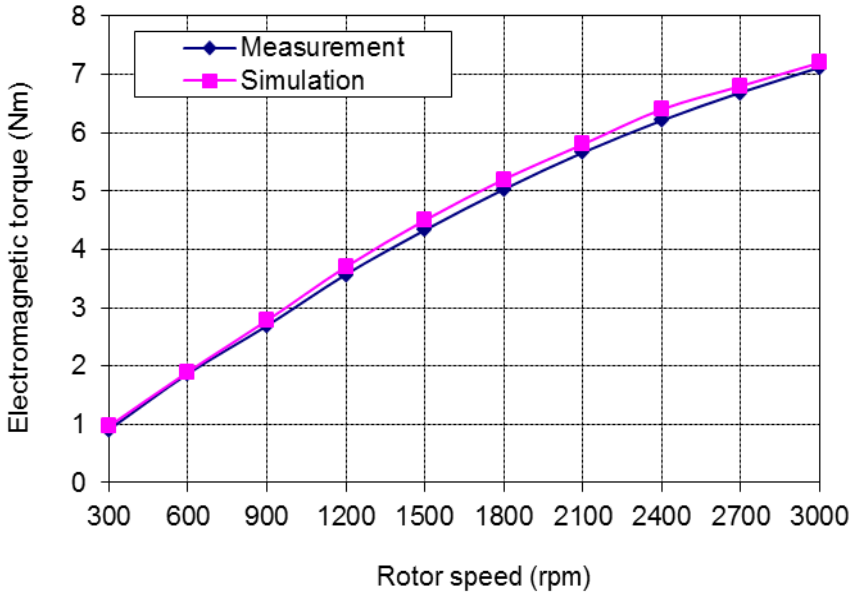

Figure 10.10. Mean electromagnetic torque vs. rotor speed, comparison between simulation and experimental results, Machine A.

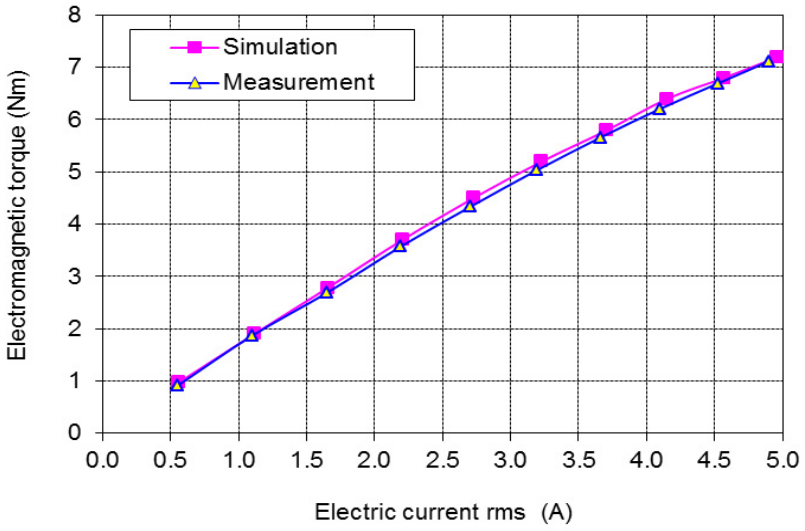

Figure 10.11. Mean electromagnetic torque vs. phase rms current, comparison between simulation and experimental results, Machine A.

10.3.4. Experimental Validation of Iron Loss Model

The modelling and calculation of rotor eddy current loss and stator iron loss were presented in Chapter 7. A comparison of simulation and experimental results of iron loss in Machine A during no-load is shown in Figure 10.12. The results show good agreement. Note that Machine A has thick magnets so that its rotor eddy current loss is small in comparison with the stator iron loss. No independent validation of rotor eddy current loss was done, because this is out of the scope of the study.

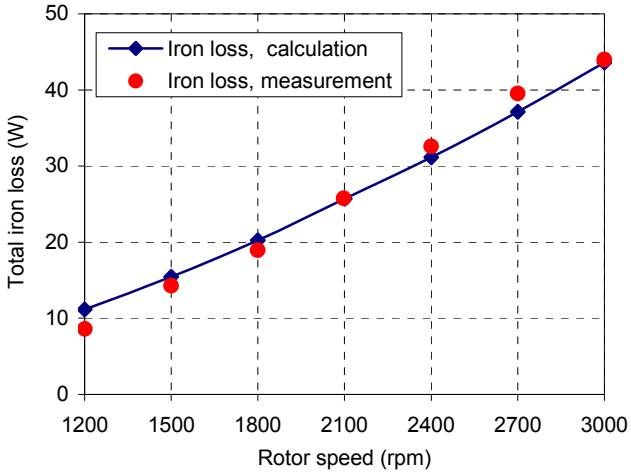

Figure 10.12. Iron loss vs. rotor speed during no-load, comparison of simulation and experimental results of Machine A.

10.3.5. Experimental Validation of Model during Three-Phase Short Circuit

In this section, the simulation and measurement of PM Machine A during three-phase short circuit are compared. Of concern here is the magnet demagnetization discussed in Chapter 4. Terminals of all three-phase winding are shorted together. The rotor speed is increased slowly to a rated speed of 3000 rpm to avoid over transient current due to a sudden short-circuit that may cause the demagnetization of the magnets [Hen 1994]. For this experiment, the short circuit armature current at rated speed is only increased to 1.2 times higher than the rated current. This is because of strong armature reaction in the d-axis direction. The phase-winding resistance of 1.95 Ω is about 10.7 times smaller than the reactance so that current vector (assuming sine-wave) lags behind the electromotive force vector by nearly 90 degrees. This means that the stator current vector is nearly opposite the magnet flux vector so that the total flux linkage through the coil of a phase due to magnet field and current-carrying windings reduces in comparison with no-load. This leads to small voltage drops on the windings of a phase. Therefore, short circuit current is not very high, even though winding resistance is small. For this reason, there is no risk of magnet demagnetization during steady-state short circuit in this PM machine.

In Table 10.1, the simulation and experimental results of the reactance of a phase are shown. These show very good agreement. Impedance is equal to the ratio of phase electromotive force to phase short circuit current at rated rotor speed. Reactance is extracted from phase impedance and resistance.

Table 10.1. Comparison of the simulation and experimental results of Machine A

	I_{short} (A)	Z (Ω)	X (Ω)	L(mH)
Simulation	11.27	15.2	15.1	6.0
Experiment	11.07	15.4	15.3	6.1
Error (%)	1.81	-1.37	-1.39	-1.39

10.3.6. Experimental Validation of Inductance during Load

The reactance (or inductance) of a phase can be calculated from electromotive force and three-phase short circuit current, as discussed in the section above. The alternative method to calculate inductance during resistive load is by using circuit, as depicted in Figure 4.9 (Chapter 4). The phase resistances of windings and load, load current, load voltage can be measured or simulated. Then, voltage dropped on phase reactance can be calculated from electromotive force and voltage dropped on total resistance of winding and load. Finally, inductance is extracted from reactance. However, this method requires several intermediate measurements that can influence the accuracy of inductance. In addition, the dependence of resistance on temperature also

influences accuracy. When comparing the two methods, the discrepancy is about 5%. Figure 10.13 compares the simulation and experimental results of inductance during load at different frequencies, [Kim 2010], [Mee 2008].

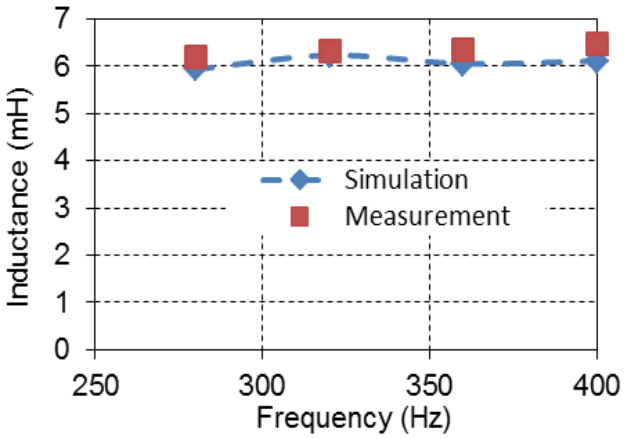

Figure 10.13. Phase inductance vs. frequency of the PM machine A.

10.3.7. Measurement of the Efficiency of the PM Machine A

Figures 10.14 and 10.15 depict experimental losses and the efficiency of PM machine A during three-phase resistive load, with a phase load resistance of 28.9 Ω.

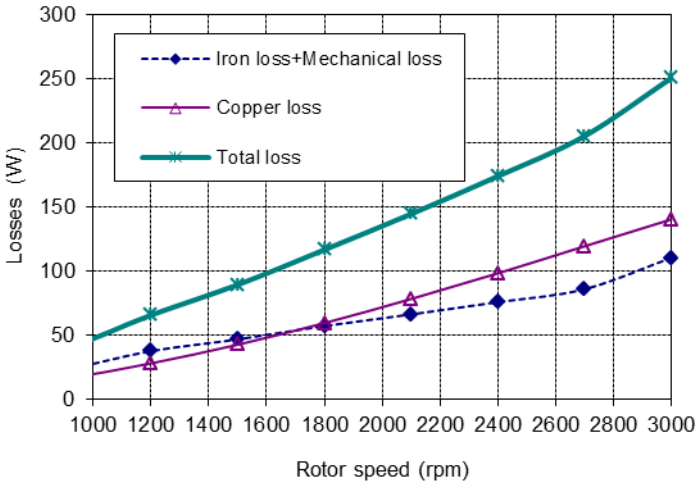

Figure 10.14. Experimental losses of the PM Machine A.

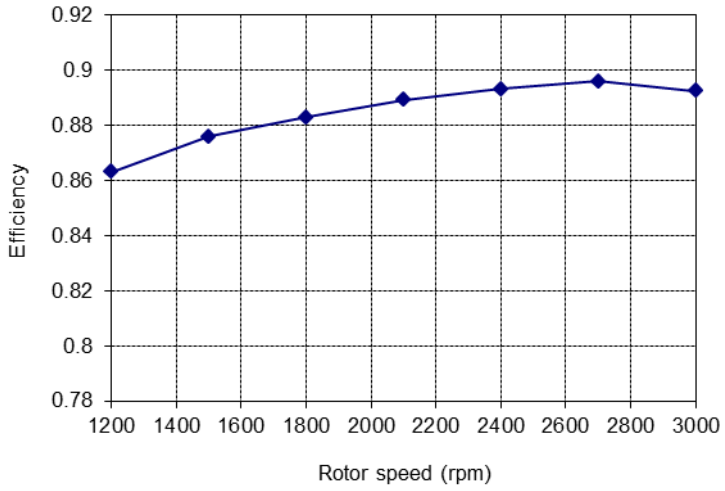

Figure 10.15. Measured efficency of PM Machine A including mechanical loss.

10.4. Experimental Validation of the Slotting Effect on EMF and Total Iron Loss

In Chapter 5, the slotting effect on internal voltage was investigated. In this section, the model of internal voltage computation is validated for fully open slot and semi open slot PM machines. The no-load electrical losses of the two PM machines are experimentally compared. Components of the PM machine with semi-open slot are shown in Figure 10.16. Two PM machines with concentrated windings as shown in Figure 10.17, a semi-open slot machine (Machine C) and a fully open slot machine (Machine D) are manufactured. Note that the slot opening of the semi-open slot PM machine is optimally designed (as presented in Chapter 7) for minimizing eddy current loss in magnets, while maximizing internal voltage. As discussed in Chapter 5, the internal voltage of a turn of the fully open slot PM machine D is smaller than that of the semi-open slot Machine C. In addition, in order to keep the voltage of the two machines as similar as possible, the designed turn number per tooth of Machine D is twice higher than that of Machine C, i.e., the turn number per tooth increases by 11%. The main parameters of the two PM machines such as the combination of slot and pole, rotor and stator diameters, etc are identical.

Figures 10.18 and 10.19 present the FEM simulation of surface flux density of Machine C and Machine D respectively. The internal voltage comparison (Figure 10.20 and 10.21) of the simulation and experimental results for both semi-open slot Machine C and fully open slot Machine D shows very good agreement. It is confirmed that the nonlinear transient 2D-FEM model including rotor motion is very suitable for the analysis and design of PM machines for the

application considered in this thesis. Details of experiments of machines C and D can be found in [Nad 2010].

It was stated in Chapter 7 that the fully open slot causes very high rotor eddy current loss leading to high total iron loss of rotor and stator, while the rotor eddy current loss can be minimized by optimizing the slot opening. Therefore, the total iron loss of the rotor and stator of a semi-open slot PM machine is much smaller than that of fully open slot PM machine. To validate the statement, simulation and experimental results of total iron losses of the semi-open slot PM Machine C and fully open slot PM Machine D during no-load are compared as shown in Figure 10.22. As can be seen the total iron loss of the rotor and stator of Machine D is significantly higher than that of Machine C. This agrees with analysis results in Chapter 7.

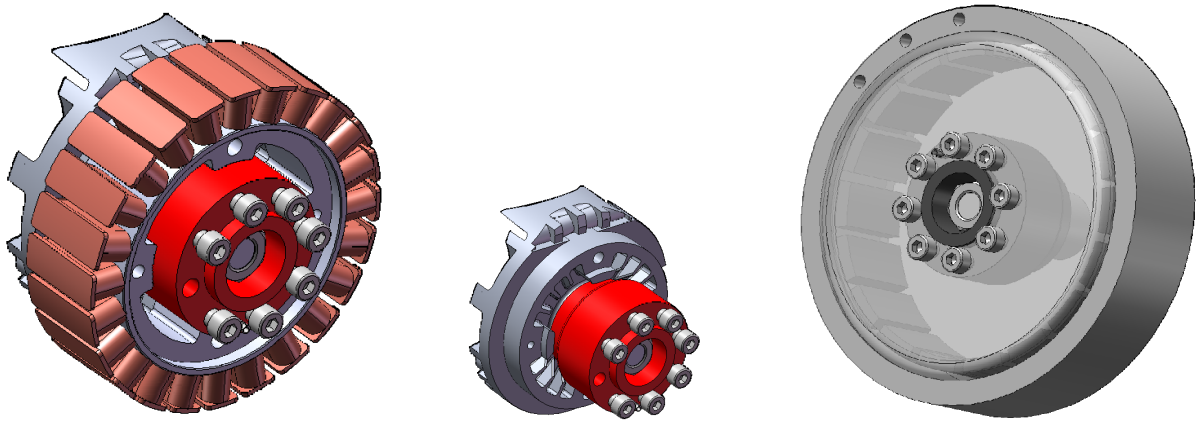

Figure 10.16. Components of the PM machine with semi-open slot (Mastervolt).[2]

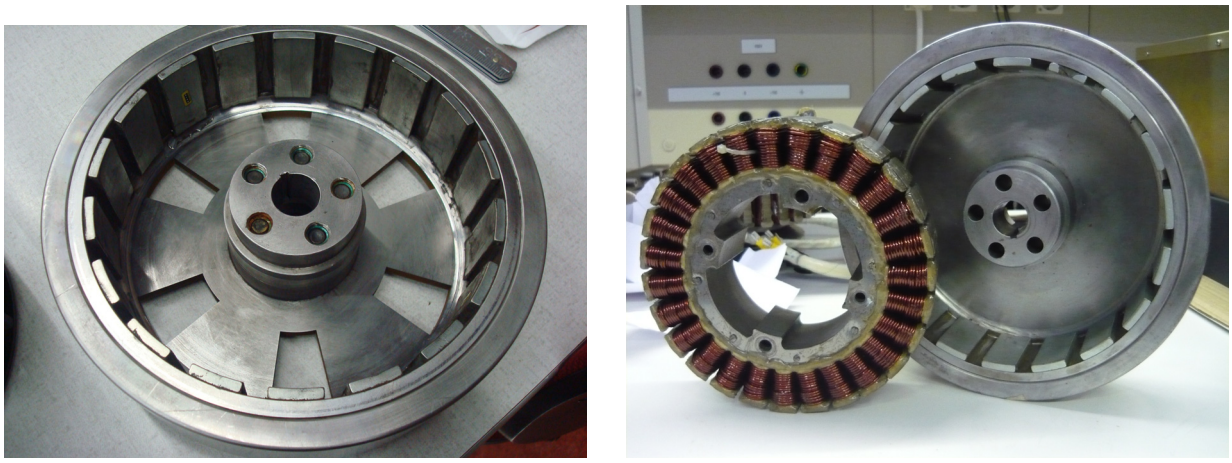

a) Rotors and stators of 9kW PM machines C and D with 18 poles.

[2] The machine is the product of the project called the "Mastervolt project".

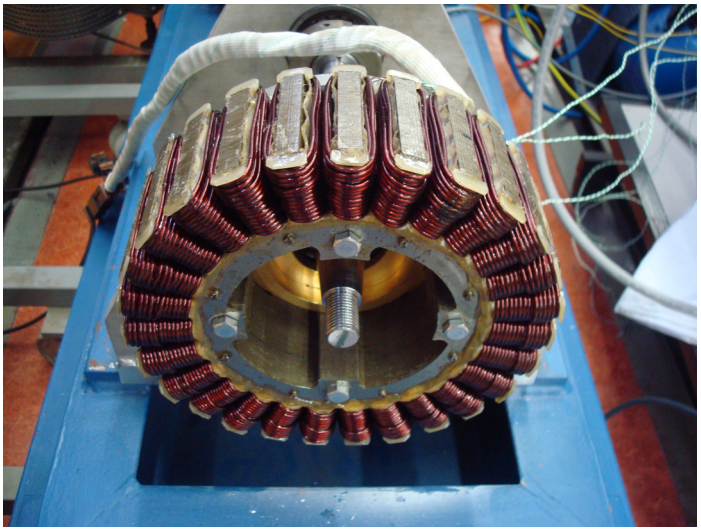

b) Stator with fully open slot.

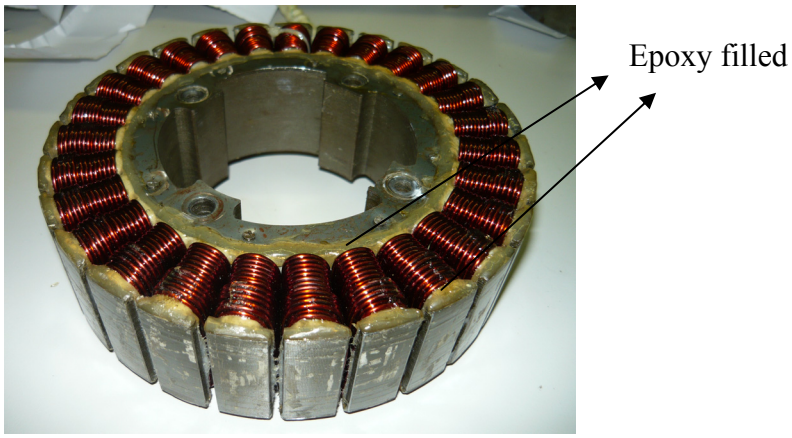

c) Stator with semi-open slot, slot opening of 4 mm

Figure 10.17. Rotor and stators of 9 kW exterior rotor PM machines, i.e., Machine C and D with concentrated windings and a slot/pole combination of 3/2.

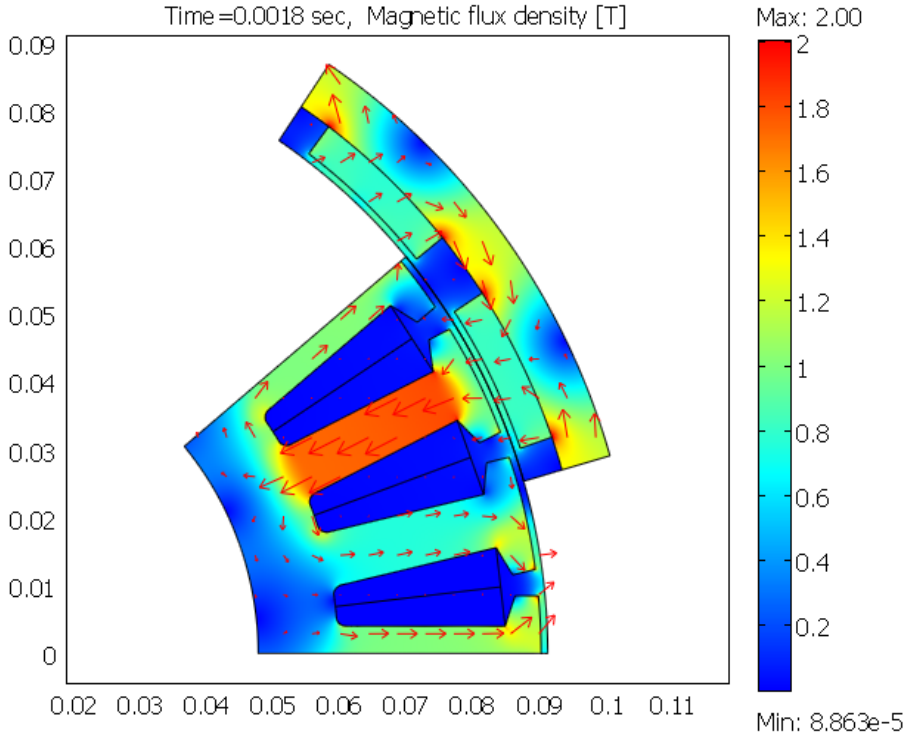

Figure 10.18. FEM simulation of the semi-open slot Machine C

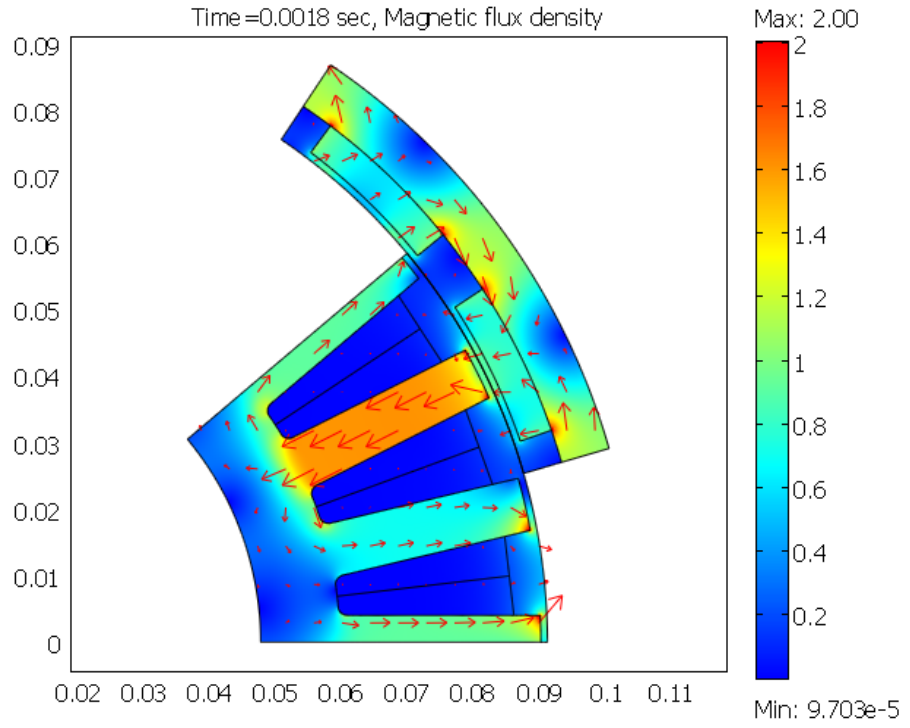

Figure 10.19. FEM simulation of the fully open slot Machine D.

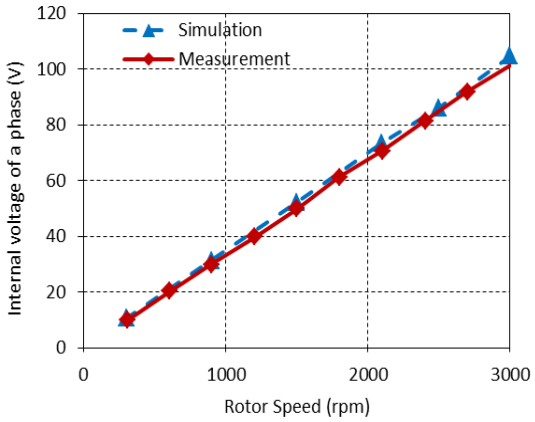

Figure 10. 20. Internal voltage vs. rotor speed, comparison of simulation and experimental results, Machine C with semi-open slot.

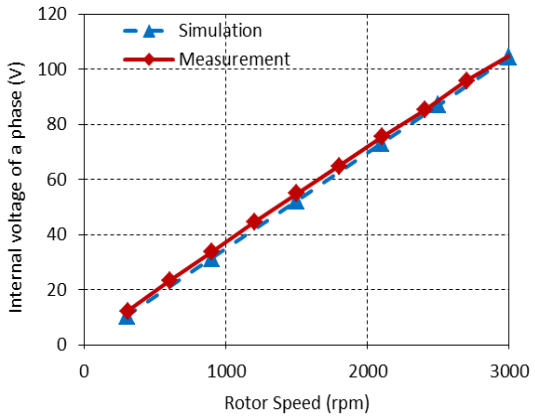

Figure 10.21. Internal voltage vs. rotor speed, comparison of simulation and experimental results, Machine D with fully open slot.

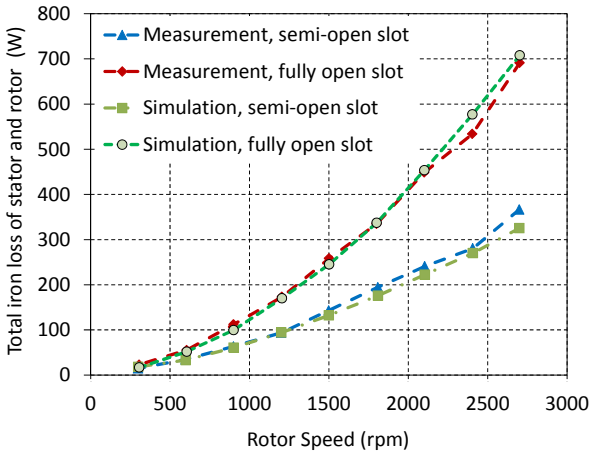

Figure 10.22. Comparison of experimental total iron losses of the rotor and stator of the semi-open slot and fully-open slot PM machines during noload.

10.5. Conclusions

The non-linear transient FEM model including rotor motion coupled to the electric circuit of load, as described in Chapter 4, is validated. The resistance of windings was taken into account in the FEM simulation to ensure the accuracy of the model.

A comparison of the FEM simulation and the experimental results with the flux linkage and internal voltage of Machine B shows good agreement in terms of amplitude and waveform.

Calculated results of electromotive force, voltage on load, electric current, electromagnetic torque, total iron loss of the rotor and stator, short circuit current, and reactance using the FEM model showed good agreement with measured results (using Machine A) with an error margin smaller than 3%. It is shown that the end effects of a PM machine with concentrated windings having a large number of teeth and poles can be neglected, even when the machine's diameter is larger than its length. Therefore, the 2D-FEM simulation can be used effectively for this application.

The FEM model during three-phase short circuit is experimentally validated. This model is used to evaluate magnet demagnetization during three-phase short circuit. Analysis results during three-phase short circuit of Machine A show that short-circuit current can be limited strongly by armature reaction in the d-axis direction, leading to small voltage drops on windings, even though the winding resistance is much smaller than the reactance.

To validate statements regarding the influence of the slotting effect on internal voltage and total iron loss of the rotor and stator in Chapter 5 and Chapter 7, two additional PM machines are manufactured: one has a fully open slot and the other a semi-open slot. A comparison of the simulation and experimental results of internal voltage show very good agreement. The comparison of experimental total iron loss in the rotor and stator of the two PM machines confirmed the statement made in Chapter 7 that a fully open slot causes high rotor eddy current loss. As a result, the total iron loss of the rotor and stator of a fully open slot PM machine is much higher than that of a semi-open slot PM machine with open slot designed optimally.

CHAPTER 11

CONCLUSIONS AND RECOMMENDATIONS

11.1. Introduction

In this thesis the modeling, analysis, and design of exterior rotor PM machines with concentrated windings are dealt with, as well as results of experiments. Special attention is paid to the slotting effect.

As described in Chapter 1, the main objectives of the thesis are to find the most suitable configuration of the PM machine in a flywheel in the small-scale ship application and to develop models for design of the PM machines with better compromise between calculation time and calculation accuracy.

In Chapter 2, an overview and comparison of PM machine types are given. In Chapter 3 to 7, the electromagnetic models and analyses are investigated. In Chapter 8, the circuit thermal model is developed for the design of the PM machine taking in to account temperature constraints. In Chapter 9, the automated nonlinear transient FEM including rotor motion is used to compare machine configurations. The developed models are verified by experimental measurements as shown in Chapter 10.

In this chapter, the noteworthy points of this thesis are summarized and reviewed, conclusions are drawn, and recommendations for further research are made.

11.2. Reviews and Conclusions

Subsection 11.2.1 to Subsection 11.2.7 will give a summary of what has been achieved in this thesis, while in Subsection 11.2.8 conclusions of the scientific contribution of this thesis are given.

11.2.1. Selection of Configuration of PM Machine

- **Criteria for selection of the PM machine in a flywheel of the small-scale ship application**

Each application has individual characteristics so that the different applications have different criteria leading to different choices of PM machine configuration. The criteria used to select generator for the small-scale ship application are ease of mounting on a diesel engine, the possibility of integration in a flywheel, cost effectiveness, high efficiency, and high torque density.

- **Choice of configuration of PM machine (Chapter 2)**

To select the right structure of the PM machine for the application, a comparison of PM machines with different configurations such as radial, axial, switched, and transverse flux PM machines; interior and exterior PM machines; and distributed and concentrated PM machines was done. The advantages and disadvantages of each PM machine were discussed. As a result, the exterior rotor surface-mounted permanent magnet machine with double-layer concentrated windings is selected for this application.

- **Impact of concentrated winding layout on rotor eddy current loss (Chapter 3)**

To select a concentrated winding layout for a PM machine, the MMF-harmonic components are, apart from the winding factor, also an important criterion for the choice, because they influence rotor eddy current loss. By comparing the MMF-harmonics of different concentrated winding layouts, a rough comparison of rotor eddy current loss during load with different concentrated winding layouts was made. This provides quick insight into the influence of the winding layout on rotor eddy current loss and helps to select a feasible winding layout for the application.

- **Comparison of PM machines with different combination of slot and pole number (Chapter 9)**

Five typical PM machines numberred from 1 to 5, namely 24-slot/16-pole, 27-slot/18-pole, 24-slot/20-pole, 27-slot/24-pole and 24-slot/28-pole PM machines, corresponding to slot and pole combination of 3/2, 3/2, 6/5, 9/8 and 6/7, were selected for further comparison by using transient FEM computation. Results are summarized as follows. If using criterion of maximum torque density then the PM machine 5 is the best selection. If the criterion is maximum efficiency, the PM machine 2 is the best option. However, if using a multi-criteria that compromises between maximum torque density and maximum efficiency, the PM machine 3 is the best option.

11.2.2. Design Process and Electromagnetic Models for Design of PM Machines

- **Design Process and Electromagnetic Models of the PM machine: analytical model, static FEM model, automated transient FEM model including rotor motion, and hybrid model**

There are number of electromagnetic models developed in this study such as the analytical model, the static FEM model, the transient FEM model, and the hybrid model for analysis and design optimization. The analytical model developed in Chapter 3 can be used to find feasible dimension sets of the PM machine. This provides quick insight into influence of design parameters on performances of the PM machine. Meanwhile, the automated transient FEM model developed in Chapter 4 can be used for analysis and refining the design result. For design optimization, analytical model is less accurate because it neglects some effects such as magnetic saturation, fringing, and slotting effect. The nonlinear transient 2D-FEM model including rotor motion is accurate for design optimization, but time-consuming as the number of design variables is large. Therefore, a design process including the hybrid model described in Chapter 5 was developed for design optimization in an attempt to compromise between calculation time and calculation accuracy.

The hybrid model, which combines the analytical model and the static FEM model with single rotor position, is more accurate than the analytical model and faster than the transient FEM model including rotor motion. The hybrid model automatically updates the correction factors for slotting effect, fringing effect, magnetic saturation at each iteration number of the design optimization process. These factors are calculated by a static FEM program with single rotor position.

- **Magnetic saturation (Chapter 4)**

The magnetic saturation models and solvers are investigated. These ensure that the FEM program is convergent and runs faster during high magnetic saturation.

- **Demagnetization model (Chapter 4)**

Demagnetization model has been developed to evaluate the demagnetization of magnets. This is to ensure that the designed PM machine is safe during the worst operation mode.

11.2.3. Slotting Effect on Electromagnetic Field and Internal Voltage

- **The influences of slot opening on the distribution of flux density in the air gap and magnet (Chapter 5)**

The influences of slot opening on the distribution of flux density in the gap and magnet are investigated. The edge effects of magnet and slot opening are also discussed.

- **The slotting effect on internal voltage and torque in the range of small slot opening (Chapter 5 and Chapter 6)**

The characteristic performances of flux linkage and internal voltage with respect to slot opening were investigated. It is shown that conventional literature on the slotting effect using Carter factor has a limitation in the range of small slot opening. According to the traditional approach, while the slot opening decreases, the Carter factor decreases. Therefore, voltage as well as mean electromagnetic torque increases. However, it was found in the study that when the slot opening decreases, the leakage flux through the tooth tips increases and the flux linkage decreases (Figure 5.11), leading to a decrease in voltage as well as mean torque (as shown in Figure 5.12 and Figure 6.15). Thus, the study has provided insight into the influence of slotting on flux linkage and internal voltage (discussed in Chapter 5) as well as on mean electromagnetic torque (discussed in Chapter 6) at small slot opening, which has not been mentioned in literature before.

11.2.4. Optimal Electromagnetic Torque Performance

The influence of slot opening and magnet width on cogging torque, torque ripple and mean torque is investigated. The four-step process for evaluating the peak-peak cogging torque is proposed in Section 6.4, Chapter 6. The relation of mean electromagnetic torque to slot opening is evaluated as shown in Figure 6.15. This can be used to choose slot openings for maximizing mean electromagnetic torque. The analyses therefore offer insight into the relation of design parameters to torque performances. It is shown that optimization of slot opening and magnet width is the efficient way to optimize electromagnetic torque performance, without causing any more difficulties for manufacturers and without increasing cost like other methods.

11.2.5. Losses in PM Machines

- **The slotting effect on rotor eddy current loss**

In Chapter 7, the influence of slot opening on the eddy current loss in magnets, rotor back iron and stator iron loss was investigated. The characteristic performance of magnet eddy current loss with respect to slot opening is plotted. The FEM simulation results showed that magnet eddy current density increases when the slot opening increases. However, the frequency of the eddy current at a point in a magnet is not dependent on slot opening. Eddy current density in magnets reaches peak values at positions opposite slot opening. The proposed approach and analysis results can be used to select the slot opening for minimum rotor eddy current losses and maximum internal voltage.

- **Reducing eddy current loss by using magnet segmentation**

The use of segmented magnets to reduce the eddy current loss is investigated. The result shows that that magnet segmentation method is an efficient way to reduce magnet eddy current loss in the PM machines in the application considered in this study.

- **Stator iron loss model**

A stator iron loss model is developed. The coefficients of hysteresis loss, eddy current loss and excess loss are calculated by combining the curve-fitting method with manufacturer's data and the results of experiment.

11.2.6. The Thermal Model for the Design of PM machines

The proposed thermal mode of the PM machine with concentrated windings having special parts, for instance, bolts, spokes, and cooling plate with a special geometry placed both in the stator hollow and at the end side of the machine, is made based on the lumped-parameter method and empirical correlation coefficients of thermal convection found in literature. A thermal model program for combining of the electromagnetic transient FEM model and the circuit thermal model is created. This achieves a fast and accurate temperature computation for design optimization taking into account temperature constraints. Solutions for improving heat transfer from the PM machine to environment are proposed. The temperature comparison between simulation and experimental results in the steady-state temperature shows good agreement.

11.2.7. Experimental Validation of Transient FEM Model

A non-linear FEM model including rotor motion combined with the circuit model developed in Chapter 4, is validated. Resistance of windings is taken into account in FEM simulation to ensure model accuracy.

Calculated results of electromotive force, voltage, electric current, electromagnetic torque, total iron loss of rotor and stator, short circuit current and reactance using the transient FEM model show good agreement with measured results with an error margin smaller than 3%. It is shown that the end effects of a PM machine with concentrated windings, having a large number of teeth and poles can be neglected, even when its diameter is larger than its length. Therefore, 2D-FEM simulation is effectively used for the application in this study.

To validate the influence of slotting effect on internal voltage and total iron loss of rotor and stator, two additional PM machines are manufactured: one has fully open slots and the other has semi-open slots. A comparison between simulation and experimental results of internal voltage shows very good agreement. Comparison of experimental total iron loss of rotor and stator of the two PM machines confirms the statement in Chapter 7 that the fully open slot PM machine has high rotor eddy current loss. As a result, the total iron loss of the rotor and stator of the fully open slot PM machine is much higher than that of the semi-open slot PM machine with the slot opening designed optimally.

11.2.8. Conclusions regarding the Scientific Contributions of this Study

The main scientific contributions of this thesis are summarized as follows.

- In this thesis, insight into the influence of slotting effect on performances of PM machines with small slot opening is supplied.

  In the study the limitation of the current literature regarding the slotting effect at small slot opening is given. The relations of flux linkage, internal voltage, mean electromagnetic torque, and rotor eddy current loss with respect to slot opening presented in this thesis have never been mentioned in literature. Therefore, this study gives a new view of the influence of the slotting effect on flux linkage, internal voltage, and mean electromagnetic torque at small slot opening.

- Carter factor expressions found in literature are evaluated:

  In the thesis, a method for separating the slotting effect and the fringing effect in the FEM computation is proposed in Section 5.5, Chapter 5. This leads to the Carter factor expressions found in literature being evaluated by comparing to the FEM calculation to find the most suitable expression for the design of PM machines.

- A design process (Figure 5.19) based on the hybrid model and the automated nonlinear transient FEM including rotor motion considering the temperature constraint is developed:

  In the study, a method is proposed for calculating the total correction factor of slotting, fringing, and magnetic saturation effects. The proposed method is designed to overcome the limitations of the traditional analytical design model at the small slot opening. To apply the method regarding correction factors on the design of PM machines, a hybrid model is proposed in Chapter 5. The hybrid model is combination of the analytical model and the static FEM model with single rotor position. The hybrid model updates correction factors such as slotting effect, fringing effect, and magnetic saturation factors at each iteration of the design process. The hybrid model is therefore an improvement on the analytical model in the term of accuracy, but still retains the advantage of the analytical model namely fast calculation in comparison with the transient FEM model. A proposed design process including the hybrid and the automated dynamic FEM model coupled with the thermal model is an efficient tool for design optimization of the PM machine in the small-scale ship application.

- A method is proposed for comparing PM machines to find the most suitable configuration of the PM machine in a flywheel in small-scale ship application:

Numerous comparisons of electric machine configurations are done in Chapter 2 in order to select an exterior rotor PM machine with double-layer concentrated windings. After the configuration is chosen, performances of Ferrite and Neodymium PM machines; and surface-mounted and inset PM machines are compared in Chapter 9. To select a winding layout for minimizing rotor eddy current loss, the MMF harmonics of PM machines are used in Chapter 3 to roughly evaluate the effect of winding layout on rotor eddy current loss. In Chapter 6, a four-step process to estimate the peak-peak cogging torque is proposed. The process can be used to select the combination of slot and pole for minimizing the peak-peak cogging torque. For further comparisons, the five typical PM machines with different combinations of slot and pole are compared in Chapter 8. The series of comparisons offers insight into the merits and drawbacks of the configuration of electric machines. As a result, the comparison to find the most suitable configuration of electric machine for the specific application is a contribution to scientific knowledge.

11.3. Recommendations

- The proposed hybrid model for design optimization of PM machines is better than the analytical model because it improves the calculation of slotting, fringing, and magnetic saturation effects. More correction factors for computing iron loss might result in a more accurate model for design optimization, but this will be more time consuming. Therefore, finding a solution for a better compromise between time and computation accuracy for design optimization is recommended.
- The thermal model in this thesis was designed for the purpose of designing PM machines considering temperature constraint. It was developed based on a combination of the lumped-parameter method and empirical correlation coefficients of thermal convection. This method is reliable and there is good agreement with the measurements. However, only the mean temperature of key components of the PM machine is estimated. To improve computation accuracy and obtain detailed temperature distribution in PM machines, some CFD computation coupled to FEM computation should be investigated.
- To validate simulation about the distribution of eddy current, some experiments using nondestructive testing (NDT) technology are recommended for further study.

BIBLIOGRAPHY

[Alb 2008] L. Alberti and N. Bianchi, "A Coupled Thermal-Electromagnetic Analysis for A Rapid and Accurate Prediction of IM Performance", IEEE Trans. Ind. Electron., vol. 55, p.3575 , 2008.

[Alo 2010] J. Alonso-Martínez, J.E. Carrasco, S. Arnaltes, "Table-Based Direct Power Control: A Critical Review for Microgrid Applications", Power Electronics, IEEE Transactions on, On page(s): 2949 - 2961, Volume: 25 Issue: 12, Dec. 2010.

[Ama 2005] Y. Amara, J. Wang and D. Howe, "Analytical Prediction of Eddy-Current Loss in Modular Tubular Permanent-Magnet Machines", IEEE Trans. Energy Conversion, vol. 20, no. 4, pp. 761–769, Dec 2005.

[Ani 2007] S.O. Ani, "Report on experiment of a Ferrite PM machine", EPP group, TU Delft, 2007 (Internal report).

[Arj 2005] M.A.L. Arjona, R. Escarela-Perez, E. Melgoza-Vázquez and C. Hernández F., Convergence Improvement in Two-Dimensional Finite Element Nonlinear Magnetic Problems: A Fuzzy Logic Approach; Finite Elements in Analysis and Design, Volume 41, Issue 6, pp.583 – 598, March, 2005.

[Ash 2011] M. Ashabani, Y.A.-R.I. Mohamed, "Multiobjective Shape Optimization of Segmented Pole Permanent-Magnet Synchronous Machines With Improved Torque Characteristics," Magnetics, IEEE Transactions on , vol.47, no.4, pp.795-804, April 2011.

[Ayd 2004] M. Aydin, S. Huang, T.A. Lipo; "Axial Flux Permanent Magnet Disc Machines: A Review"; Research report, University of Wisconsin-Madison, USA, 2004.

[Ayd 2008] M. Aydin, "Magnet Skew in Cogging Torque Minimization of Axial Gap Permanent Magnet Motors", Proceedings of the 2008 International conference on electric machines, (ICEM 2008).

[Bar 2012] M. Barcaro, N. Bianchi, F. Magnussen, "Permanent-Magnet Optimization in Permanent-Magnet-Assisted Synchronous Reluctance Motor for a Wide Constant-Power Speed Range," Industrial Electronics, IEEE Transactions on , vol.59, no.6, pp.2495-2502, June 2012.

[Bej 1993] A. Bejan, "Heat Transfer", John Wiley & Sons, New York, 1993.

[Bi 1996] C. Bi, Z. J. Liu, and T. S. Low, "Analysis of unbalanced-magnetic-pulls in hard disk drive spindle motors using a hybrid method," IEEE Trans. Magn., vol. 32, no. 5, pp. 4308–4310, Sep. 1996.

[Bia 2002] N. Bianchi and S. Bolognani, "Design Techniques for Reducing the Cogging Torque in Surface-Mounted PM Motors," IEEE Trans. IA, vol. 38, no. 5, pp. 1259–1265, Sep/Oct. 2002.

[Bia 2005] N. Bianchi, "Electrical Machine Analysis using Finite Elements", Taylor&Francis, 2005.

[Bia 2006] N. Bianchi, S. Bolognani, M.D. Pre, G. Grezzani, "Design considerations for fractional-slot winding configurations of synchronous machines," Industry Applications, IEEE Transactions on , vol.42, no.4, pp.997-1006, July-Aug. 2006.

[Bog 2003] A. Boglietti, A. Cavagnino, M. Lazzari, and M. Pastorelli, "A Simplified Thermal Model for Variable-Speed Self-Cooled Industrial Induction Motor";. IEEE Trans. IA., vol. 39, no. 4, July/August 2003.

[Bog 2009] A. Boglietti, A. Cavagnino, D. Staton, M. Shanel, M. Mueller, C. Mejuto, "Evolution and Modern Approaches for Thermal Analysis of Electrical Machines," Industrial Electronics, IEEE Transactions on , vol.56, no.3, pp.871-882, March 2009.

[Bol 2005] I. Boldea; "The Electric Generators Handbook"; Taylor&Francis, 2005.

[Bor 2011] A. Borisavljevic, "Limits, Modelling and Design of High-Speed Permanent Magnet Machines", PhD Thesis, Delft University of Technology, Netherlands, 2011.

[Bou 2010] K. Boughrara, R. Ibtiouen, D. Žarko, O. Touhami, A. Rezzoug, "Magnetic Field Analysis of External Rotor Permanent-Magnet Synchronous Motors Using Conformal Mapping," Magnetics, IEEE Transactions on , vol.46, no.9, pp.3684-3693, Sept. 2010.

[Buc 2008] D. Bucherl, R. Nuscheler, W. Meyer, H.-G. Herzog, "Comparison of electrical machine types in hybrid drive trains: Induction machine vs. permanent magnet synchronous machine," Electrical Machines, 2008. ICEM 2008. 18th International Conference on , vol., no., pp.1-6, 6-9 Sept. 2008.

[Cah 2005] Cahier technique no. 158, "Calculation of short-circuit currents," *The Schneider Electric*, 2005.

[Cal 2010] W.P. Calixto, et al, "A New Methodology to Calculate Carter Factor using Genetic Algorithms"; International Journal of Numerical Modeling: Electronic Networks, Devices and Fields, 2010.

[Car 1900] F.W Carter, "Note on air-gap and interpolar induction," Electrical Engineers, Journal of the Institution of , vol.29, no.146, pp.925-933, July 1900.

[Car 1926] F.W. Carter, "The magnetic field of the dynamo-electric machine," Electrical Engineers, Journal of the Institution of , vol.64, no.359, pp.1115-1138, November 1926.

[Car 2008] F. Caricchi, F. Maradei, G. De Donato and F. Giulii Capponi, "Single Phase Permanent-Magnet Generator with Low Armature Reaction for Induction Heating Gen Sets", Proceedings of the 2008 International Conference on Electrical Machines (ICEM 2008).

[Car 2010] F. Caricchi, F. Maradei, G. De Donato, F.G. Capponi, "Axial-Flux Permanent-Magnet Generator for Induction Heating Gensets," Industrial Electronics, IEEE Transactions on , vol.57, no.1, pp.128-137, Jan. 2010.

[Cen 1997] Y. A. Cengel, "Introduction to Thermodynamics and Heat Transfer"; McGraw-Hill, 1997.

[Cha 2008] K.T. Chau , C.C. Chan and C. Liu "Overview of Permanent-Magnet Brushless Drives for Electric and Hybrid Electric Vehicles", IEEE Trans. Ind. Electron., vol. 55, no. 6, pp.2246 - 2257 , 2008.

[Cha 2011] H. R. Cha, et al, "Design of Outer Rotor IPM Type PMSM for 3 Wheel Electric Vehicle", ICEMS 2011, Beijing, China, 2011.

[Che 2005] Y. Chen, P. Pillay, "Axial-Flux PM Wind Generator with A Soft Magnetic Composite Core," Industry Applications Conference, 2005. Fourtieth IAS Annual Meeting. Conference Record of the 2005, vol.1, no., pp. 231- 237 Vol. 1, 2-6 Oct. 2005.

[Che 2010] N. Chen , S. L. Ho and W. N. Fu, "Optimization of Permanent Magnet Surface Shapes Electric Motors for Minimization of Cogging Torque using FEM", IEEE Trans. Magn., vol. 46, no. 6, pp.2478 - 2481 , 2010.

[Che 2011a] J.T. Chen, Z.Q. Zhu, S. Iwasaki, R.P. Deodhar, "Influence of Slot Opening on Optimal Stator and Rotor Pole Combination and Electromagnetic Performance of Switched-Flux PM Brushless AC Machines," Industry Applications, IEEE Transactions on , vol.47, no.4, pp.1681-1691, July-Aug. 2011.

[Che 2011b] M. Cheng, W. Hua, J. Zhang, W. Zhao, "Overview of Stator-Permanent Magnet Brushless Machines," Industrial Electronics, IEEE Transactions on , no.99, pp.1, 0.

[Chi 1996] P.R.N. Childs, C.A. Long ; "A Review of Forced Convective Heat Transfer in Stationary and Rotating Annuli"; Journal of Mechanical Engineering Science; pp. 123-134. Vol.210, 1996.

[Chi 2011] A. Chiba, et al, "Rare-Earth-Free AC Motors – An Alternative Approach Advances", IEEE-IEMDC 2011, Canada, May, 2011.

[Cho 2009] J.H. Choi and Y. S. Baek , "Theoretical Analysis and its Applications of A PM Synchronous Motor with Minimized Cogging Force", IEEE Trans. Magn., vol. 45, no. 10, pp. 4692 - 4695 , 2009.

[Chu 2003] M. Chunting, G.R. Slemon, R. Bonert, "Modeling of iron losses of permanent-magnet synchronous motors," Industry Applications, IEEE Transactions on , vol.39, no.3, pp. 734- 742, May-June 2003.

[Cob 1955] E.C. Cobb, O.A. Saunders; "Heat Transfer from Rotating Disk"; Proceedings of the Royal Society of London. Series A, Mathematical and Physical Sciences, 1955.

[Com 2010] Comsol Multiphysics, FEM software, 2010.

[Cro 2002] J. Cros, P. Viarouge, "Synthesis of High Performance PM motors with Concentrated Windings ," Energy Conversion, IEEE Transactions on , vol.17, no.2, pp.248-253, Jun 2002.

[Dah 2005] Dahaman Ishak, Z. Q. Zhu and David Howe, "Eddy-current Loss in the Rotor Magnets of Permanent-Magnet Brushless machines Having a Fractional Number of Slots Per Pole", IEEE Trans. Magn., vol. 41, no. 9, pp. 2462–2469, Sept 2005.

[Daj 2010] G. Dajaku, D. Gerling, "Stator Slotting Effect on the Magnetic Field Distribution of Salient Pole Synchronous Permanent-Magnet Machines," Magnetics, IEEE Transactions on , vol.46, no.9, pp.3676-3683, Sept. 2010.

[Dan 2005] Dan M. Ionel, et al, "Assessment of Torque Components in Brushless Permanent Magnet Machines through Numerial Analysis of the Electromagnetic Field " IEEE Industry application, vol. 41, no. 5, pp. 1149 – 1158, 2005.

[Den 1999] F. Deng, "An improved iron loss estimation for permanent magnet brushless machines," Energy Conversion, IEEE Transactions on, vol.14, no.4, pp.1391-1395, Dec 1999.

[Deo 2010] Deok-je Bang, " Design of Transverse Flux Permanent Magnet Machines for Large Direct-Drive Wind Turbines," Phd Thesis, Delft University of Technology, Oct 2010.

[Dor 2008] D.G. Dorrell, "Combined Thermal and Electromagnetic Analysis of Permanent-Magnet and Induction Machines to Aid Calculation", IEEE Trans. Ind. Electron., vol. 55, p.3566 , 2008.

[Dor 2010] D.G. Dorrell, M. Popescu, L. Evans, D.A. Staton, A.M. Knight, "Comparison of Permanent Magnet Drive Motor with a Cage Induction Motor Design for a Hybrid Electric Vehicle," Power Electronics Conference (IPEC), 2010 International , vol., no., pp.1807-1813, 21-24 June 2010.

[Dor 2011] D.G. Dorrell, M. Hsieh, M. Popescu, , L. Evans, D.A. Staton, V. Grout, "A Review of the Design Issues and Techniques for Radial-Flux Brushless Surface and Internal Rare-Earth Permanent-Magnet Motors," Industrial Electronics, IEEE Transactions on , vol.58, no.9, pp.3741-3757, Sept. 2011.

[Dos 2007] L. Dosiek and P. Pillay, "Cogging Torque Reduction in Permanent Magnet Machines", IEEE Industry application, vol. 43, no. 6, pp. 1656 – 1571, 2007.

[Dro 1956] D. Dropkin, A. Carmi, "Natural Convection Heat Transfer from a Horizontal Cylinder Rotating in Air", Trans. ASME (1956) 741–749.

[Dub 2004] M. Dubois, "Optimized permanent magnet generator topologies for direct drive wind turbines", Ph.D. dissertation, Delft University of Technology, Delft, The Netherlands, 2004.

[Ete 1955] G.A. Etemad, "Free Convection Heat Transfer from A Rotating Cylinder to Ambient Air, with Interferometric Study of Flow", Trans. ASME, 1955.

[Fan 2010] J. Fan; C. Zhang; Z. Wang; Y. Dong; C.E. Nino, A.R. Tariq, E.G. Strangas, "Thermal Analysis of Permanent Magnet Motor for the Electric Vehicle Application Considering Driving Duty Cycle," Magnetics, IEEE Transactions on , vol.46, no.6, pp.2493-2496, June 2010.

[Fei 2010] W. Fei, P. Luk, "A New Technique of Cogging Torque Suppression in Direct-Drive Permanent-Magnet Brushless Machines," Industry Applications, IEEE Transactions on , vol.46, no.4, pp.1332-1340, July-Aug. 2010.

[Fis 2011] Website of Fischer Panda company about generator system: http://fischerpanda.com/marinegen.

[Fit 2002] A.E. Fitzgerald, Charles Kingsley Jr., "Electric Machinery", Chapter 5, McGraw-Hill, 2002.

[For 2010] E. Fornasiero, et al , "Considerations on Selecting Fractional—Slot Windings," Energy Conversion Congress and Exposition (ECCE), 2010 IEEE , vol., no., pp.1376-1383, 12-16 Sept. 2010.

[FY 2006] FY 2006 Progress Report, U.S. Department of Energy, Advanced Power Electronics and Technology Area. Available from: http://www1.eere.energy.gov/vehiclesandfuels/pdfs/apeta_06/3_electric_machinery.pdf

[Ger 2000] H. De Gersem, R. Mertens, D. Lahaye, S. Vandewalle, K. Hameyer, "Solution strategies for transient, field-circuit coupled systems ," Magnetics, IEEE Transactions on , vol.36, no.4, pp.1531-1534, Jul 2000.

[Ger 2004] H. De Gersem, K. Hameyer, Th. Weiland, "Field–circuit coupled models in electromagnetic simulation", Journal of Computational and Applied Mathematics, Volume 168, Issues 1-2, 1 July 2004, Pages 125-133.

[Gue 2008] J.A. Güemes, A.M. Iraolagoitia, M.P. Donsión and J.I. Del Hoyo, "Analysis of Torque in Permanent Magnet Synchronous Motors with Fractional Slot Windings", Proceedings of the 2008 International Conference on Electric Machines, (ICEM 2008).

[Gut 2009] J.M. Gutierrez-Alcaraz, N. Al-Fartusi, H. Polinder, J.A. Ferreira, "Rapid modelling and design of Variable Speed Permanent Magnet Generators for maritime applications," Power Electronics and Applications, 2009. EPE '09. 13th European Conference on , vol., no., pp.1-10, 8-10 Sept. 2009.

[Gut 2010] J.M. Gutierrez-Alcaraz, S.W.H. de Haan, , J.A. Ferreira, "Seawater based cold plate for power electronics," Energy Conversion Congress and Exposition (ECCE), 2010 IEEE , vol., no., pp.2985-2992, 12-16 Sept. 2010.

[Haf 2008] M. Hafner, M. Schoning, K. Hameyer, "Automated Sizing of Permanent Magnet Synchronous Machines with Respect to Electromagnetic and Thermal Aspects," Electrical Machines, 2008. ICEM 2008. 18th International Conference on , vol., no., pp.1-6, 6-9 Sept. 2008.

[Haf 2010] M. Hafner, M. Schöning, K. Hameyer, "Automated sizing of permanent magnet synchronous machines with respect to electromagnetic and thermal aspects", COMPEL: The International Journal for Computation and Mathematics in Electrical and Electronic Engineering, Vol. 29 Iss: 5, pp.1205 – 1217, 2010.

[Han 1994] D.C. Hanselman, "Brushless Permanent Magnet Motor Design"; McGraw-Hill, New York, 1994.

[Hen 1994] J.R. Hendershot, T.Miller, "Design of Brushless Permanent-Magnet Motors", Magna Physics Publishing, Oxford, 1994.

[Hol 1997] P. Holman, "Heat Transfer", McGraw-Hill, 1997.

[Hol 2003] R. Holm; "Modeling and Optimization of a Permanent Magnet Machine in a Flywheel", Phd Thesis, TU Delft, 2003.

[Hol 2003] S.R. Holm, "Modelling and optimization of a permanent-magnet machine in a flywheel", Ph.D. dissertation, Delft University of Technology, Delft, The Netherlands, 2003.

[Hol 2007] S.R. Holm, H. Polinder, and J. A. Ferreira, "Analytical Modeling of a Permanent-Magnet Synchronous Machine in a Flywheel," IEEE Trans. Magn., vol. 43, no. 5, pp. 1955–1967, May. 2007.

[How 2011] D.A. Howey, A.S. Holmes, K.R. Pullen, "Measurement and CFD Prediction of Heat Transfer in Air-Cooled Disc-Type Electrical Machines," Industry Applications, IEEE Transactions on , vol.47, no.4, pp.1716-1723, July-Aug. 2011.

[How 2012] D. A. Howey, P. R. N. Childs, A. S. Holmes, "Air-Gap Convection in Rotating Electrical Machines," Industrial Electronics, IEEE Transactions on , vol.59, no.3, pp.1367-1375, March 2012.

[Hua 2011] Y. Huang; J. Dong; L. Jin; J. Zhu; Y. Guo, "Eddy-Current Loss Prediction in the Rotor Magnets of a Permanent Magnet Synchronous Generator With Modular Winding Feeding a Rectifier Load", Magnetics, IEEE Transactions on , vol.47, no.10, pp.4203-4206, Oct. 2011.

[Hun 2011] Hung Vu Xuan; S. O. Ani, D. Lahaye, H. Polinder, J.A. Ferreira, "Validation of non-linear dynamic FEM model for design of PM machines with concentrated windings in ship application," Power Electronics and Applications (EPE 2011), Proceedings of the 2011-14th European Conference on , vol., no., pp.1-9, Aug. 30 2011-Sept.1 2011. Birmingham, UK.

[Hwa 2006] C.C. Hwang, M.H. Wu, S.P. Cheng, "Influence of pole and slot combinations on cogging torque in fractional slot PM motors", Journal of Magnetism and Magnetic Materials, Volume 304, Issue 1, September 2006, Pages e430-e432.

[Ilh 2010] E. Ilhan, B.L.J. Gysen, J.J.H. Paulides, E.A. Lomonova, "Analytical Hybrid Model for Flux Switching Permanent Magnet Machines," Magnetics, IEEE Transactions on , vol.46, no.6, pp.1762-1765, June 2010.

[Inc 2002] F.P. Incropera, D.P. Dewitt, "Introduction to Heat Transfer", John Wiley & Sons, New York, 2002.

[Ish 2004] D. Ishak, Z.Q. Zhu, D. Howe, "High Torque Density Permanent Magnet Brushless Machines with Similar Slot and Pole Numbers," Journal of Magnetism and Magnetic Materials., pp. 272–276, 2004.

[Ish 2006] D. Ishak, Z.Q. Zhu, D. Howe "Comparison of PM Brushless Motors, Having Either all Teeth or Alternate Teeth Wound," Energy Conversion, IEEE Transactions on , vol.21, no.1, pp. 95- 103, March 2006.

[Isl 2009] R. Islam, I. Husain, A. Fardoun, K. McLaughlin, "Permanent-Magnet Synchronous Motor Magnet Designs With Skewing for Torque Ripple and Cogging Torque Reduction", IEEE Industry application, vol. 45, issue. 1, pp. 152 – 160, 2009.

[Iso 1986] S. Isobe and M. Takemoto; “Carter Coefficient of Iron Core with Magnetic Wedge for Rotating Machinery”; Electrical Engineering in Japan, Vol. 106, No. 6, 1986, Vol. 106-B, No. 10, pp. 844-850, October 1986.

[Iva 1988] A. Ivanov-Smolensky, “Electrical Machines”, vol.1, 2, 3, English Translation, Mir Publisher, 1988.

[Jab 2004] M.A. Jabbar, et al, “Modeling and Numerical Simulation of a Brushless Permanent-Magnet DC Motor in Dynamic Conditions by Time-Stepping Technique”, IEEE Trans. IA., vol. 40, no. 3, pp. 763–770, May/June. 2004.

[Jac 1996] A.G. Jack, B.C. Mecrow, J.A. Haylock, "A comparative study of permanent magnet and switched reluctance motors for high-performance fault-tolerant applications," Industry Applications, IEEE Transactions on , vol.32, no.4, pp.889-895, Jul/Aug 1996.

[Jac 1999] A.G. Jack, B.C. Mecrow, C. Weiner, "Switched reluctance and permanent magnet motors suitable for vehicle drives-a comparison," Electric Machines and Drives, 1999. International Conference IEMD '99 , vol., no., pp.505-507, May 1999.

[Jah 2011] T.M. Jahns, “The Expanding Role of PM Machines in Direct-Drive Applications”, ICEMS 2011, Beijing, China, 2011.

[Jak 1999] R. Jakoby, S. Kim, S. Wittig, “Correlations of The Convection Heat Transfer in Annular Channels with Rotating Inner Cylinder”, Transaction of ASME Journal of Engineering for Gas Turbines and Power, vol.121, 670–677, 1999.

[Jia 2011] L. Jian; G. Xu, C.C. Mi, K.T. Chau, C.C. Chan, "Analytical Method for Magnetic Field Calculation in a Low-Speed Permanent-Magnet Harmonic Machine," Energy Conversion, IEEE Transactions on , vol.26, no.3, pp.862-870, Sept. 2011.

[Kaw 2006] Y. Kawase, T. Yamaguchi and K. Hashimoto, “Effects of Coil Current Phase on Eddy Current Loss of Permanent Magnets in IPM Motors”, The international Journal for Computation and Mathematics in Electrical and Electronic Engineering, vol.25, No.3, pp.748-752, 2006.

[Kay 1956] W.M. Kays, I.S. Bjorklund, “Heat Transfer from A Rotating Cylinder With and Without Cross Flow”, Trans. ASME, paper No.56-a-71, 1956.

[Kim 2006] Ki-Chan Kim, Seung-Bin Lim, Dae-Hyun Koo, Ju Lee; , "The Shape Design of Permanent Magnet for Permanent Magnet Synchronous Motor Considering Partial Demagnetization," Magnetics, IEEE Transactions on , vol.42, no.10, pp.3485-3487, Oct. 2006.

[Kim 2009] Ki-Chan Kim, Kwangsoo Kim, Hee Jun Kim, Ju Lee, "Demagnetization Analysis of Permanent Magnets according to Rotor Types of Interior Permanent Magnet Synchronous Motor," IEEE Transactions on Magnetics, vol.45, issue.6, pp. 2799-2802, June 2009.

[Kim 2010] Ki-Chan Kim, “A study on the performance simulation of interior permanent magnet synchronous motor for electric vehicle considering nonlinear parameters”, International Journal of Applied Electromagnetics and Mechanics, IOS Press, Vol. 33, No. 1-2, pp. 343-350, 2010.

[Kre 2000] F. Kreith, “The CRC Handbook of Thermal Engineering”, CRC Press, 2000.

[Kro 2012] J. Krotsch, B. Piepenbreier, "Radial Forces in External Rotor Permanent Magnet Synchronous Motors With Non-Overlapping Windings," Industrial Electronics, IEEE Transactions on , vol.59, no.5, pp.2267-2276, May 2012.

[Kue 1976] T. H. Kuehn and R. J. Goldstein; “An Experimental and Theoretical Study of Natural Convection in The Annulus between Horizontal Cylinder”; J . Fluid Mech., vol. 74, part 4, pp. 695-719, 1976.

[Kyu 2010] Kyungil Woo and Daesuk Joo; “Fault Analysis of 3-Phase Cage Induction Motor Based on Winding Function Theory”, book: Computer Field Models of Electromagnetic Devices, Volume 34, 2010; IOS Press, 2010.

[Lah 2000] D. Lahaye, H. De Gersem, S. Vandewalle, K. Hameyer, "Algebraic multigrid for complex symmetric systems," Magnetics, IEEE Transactions on , vol.36, no.4, pp.1535-1538, Jul 2000.

[Lah 2001] D. Lahaye, “Algebraic Multigrid for Two-Dimentional Time-Harmonic Magnetic Field Computations”, PhD thesis, Katholieke Universiteit Leuven, December 2001.

[Lah 2002] D. Lahaye, S. Vandewalle, K. Hameyer, "An algebraic multilevel preconditioner for field-circuit coupled problems," Magnetics, IEEE Transactions on , vol.38, no.2, pp.413-416, Mar 2002.

[Lee 1991] K. Lee, M. J. DeBortoli, M. J. Lee, and S. J. Salon, “Coupling finite elements and analytical solution in the airgap of electric machines,” IEEE Trans. Magn., vol. 27, no. 5, pp. 3955–3957, Sep. 1991.

[Lib 2004] F. Libert and J. Soulard, “Investigation on Pole-Slot Combination for Permanent Magnet Machines with Concentrated Windings.” Proceedings, ICEM, 2004.

[Lip 1996] T. A. Lipo, “Introduction to AC Machine Design”, Wisconsin Power Electronics Research Center, Univ. Wisconsin, Madison, 1996.

[Lip 2011] T. A. Lipo, “Open Winding Variable Speed Electrical Machines – Recent Developments”, ICEMS 2011, Beijing, China, 2011.

[Liu 2008] Z.J. Liu, J.T. Li, "Accurate Prediction of Magnetic Field and Magnetic Forces in Permanent Magnet Motors Using an Analytical Solution," Energy Conversion, IEEE Transactions on , vol.23, no.3, pp.717-726, Sept. 2008.

[Lub 2010] T. Lubin, S. Mezani, A. Rezzoug, "Exact Analytical Method for Magnetic Field Computation in the Air Gap of Cylindrical Electrical Machines Considering Slotting Effects," Magnetics, IEEE Transactions on , vol.46, no.4, pp.1092-1099, April 2010.

[Lui 1993] Z.J. Liu, D. Howe, P. H. Mellor, and M. K. Jenkins, “Thermal Analysis of Permanent Magnet Machines,” in Proc. 6th Int. Conf. Elect. Mach. Drives, 1993, pp. 359–364.

[Mac 1995] Winding Function for Electric Machine Analysis, 1995. Available from: http://www.scribd.com/doc/35671102/Winding-Function-for-Electrical-Machine-Analysis

[Mad 2003] C. Mademlis, "Compensation of magnetic saturation in maximum torque to current vector controlled synchronous reluctance motor drives," Energy Conversion, IEEE Transactions on , vol.18, no.3, pp. 379- 385, Sept. 2003.

[Mag 2003] F. Magnussen, and C. Sadarangani, "Winding Factors and Joule Losses of Permanent Magnet Machines with Concentrated Windings," International Electric Machines and Drives Conference (IEMDC), Madison, USA, 1-4 June 2003, pp.333-339.

[Mag 2007] F. Magnussen and H. Lendenmann, "Parasitic Effects in PM Machines with Concentrated Windings," IEEE Trans. on Industry Applications, vol.43, no.5, pp.1223-1232, 2007.

[Mag 2012] Integrated Magnetics, Available at: http://www.intemag.com/magnet_materials.html. Last accesed 0 March 2012.

[Mal 2001] M. Malinowski, M.P. Kazmierkowski, S. Hansen, F. Blaabjerg, G.D. Marques, "Virtual-flux-based direct power control of three-phase PWM rectifiers," Industry Applications, IEEE Transactions on , vol.37, no.4, pp.1019-1027, Jul/Aug 2001.

[Mal 2003] M. Malinowski, M.P. Kazmierkowski, A.M. Trzynadlowski, "A comparative study of control techniques for PWM rectifiers in AC adjustable speed drives," Power Electronics, IEEE Transactions on , vol.18, no.6, pp. 1390- 1396, Nov. 2003.

[Man 2011] G. Manuel, et al “Laminated Circumferential Transverse Flux Machines – Lamination Concept and Applicability to Electrical Vehicles.”, IEMDC 2011, Canada, May, 2011.

[Mar 2005] W. Martienssen, H. Warlimont, Springer Handbook of Condensed Matter and Materials Data, Springer, 2005.

[Mas 2004] B.A. Maslov et al; “Rotary permanent magnet electric motor with varying air gap between interfacing between stator and rotor elements”, USA patent number: 6727630; 27 April 2004.

[Mce 2011] Magnetic Component Engineering (MCE), available at: http://www.mceproducts.com/knowledge-base/article/article.aspx.

[Mee 2008] K.J. Meessen, P. Thelin, J. Soulard, E.A. Lomonova, "Inductance Calculations of Permanent-Magnet Synchronous Machines Including Flux Change and Self- and Cross-Saturations," Magnetics, IEEE Transactions on , vol.44, no.10, pp.2324-2331, Oct. 2008

[Mei 2008] F. Meier, “Permanent Magnet Synchronous Machine with Non-overlapping Concentrated Windings for Low-Speed Direct-Drive Application”; PhD thesis, Royal Institute of Technology, Sweden, 2008.

[Mei 2008a] F. Meier, J. Soulard, "Analysis of Flux Measurements on a PMSM with Non-Overlapping Concentrated Windings," Industry Applications Society Annual Meeting, 2008. IAS '08. IEEE , vol., no., pp.1-8, 5-9 Oct. 2008.

[Mei 2008b] F. Meier and J. Soulard, "dq theory applied to a permanent magnet synchronous machine with concentrated windings," Power Electronics, Machines and Drives, 2008. PEMD 2008. 4th IET Conference on , vol., no., pp.194-198, 2-4 April 2008.

[Mel 1991] P.H. Mellor, D. Robertsm, D.R. Turner, "Lumped Parameter Thermal Model for Electrical Machines of TEFC Design"; IEE proceedings-B, Vol138, No.5, sep 1991.

[Mil 1989] T.J.E. Miller, "Brushless Permanent-Magnet and Reluctance Motor Drives", Oxford Science Publications, 1989.

[Mil 1999] A. F. Mills, "Heat Transfer", Prentice-Hall, 1999.

[Moh 1995] A.K. Mohanty, A.A. Tawfek, B.V.S.S.S. Prasad, "Heat Transfer from A Rotating Cylinder in Cross Flow", Previews of Heat and Mass Transfer, vol. 21, 54–61, 1995.

[Moh 2004] S.I. Mohammad, et al, "Issue in Reducing the Cogging Torque of Mass – Produced Permanent Magnet Brushless DC Motor", IEEE Industry application, vol. 40, no. 3, pp. 813 – 820, 2004.

[Moh 2009] B. Mohammad, K. Shaarbafi, J. Faiz, M.R. Feyzi, "Slot Fringing Effect on the Magnetic Characteristics of Electrical Machines"; Journal of Electrical Engineering, vol. 60, no. 1, 2009, 18–23.

[Mor 2007a] J. Morren and S.W.H. de Haan, "Short-Circuit Current of Wind Turbines With Doubly Fed Induction Generator," Energy Conversion, IEEE Transactions on , vol.22, no.1, pp.174-180, March 2007.

[Mor 2007b] S. Morimoto, "Trend of Permanent Magnet Synchronous Machines"; IEEJ Trans 2007; 2: 101–108.

[Nad 2010] A.F. Nada, "Permanent Magnet Synchronous Generator to Use on Board of Yachts", Master thethis, EPP group, TU Delft, 2010.

[Nas 1964] S.A. Nasar, "Electromagnetic Theory of Electrical Machines", Proc.IEE, Vol.111, No.6, June 1964, pp.1123-1131.

[Ner 2008] J. Nerg, M. Rilla, J. Pyrhonen, "Thermal Analysis of Radial-Flux Electrical Machines With a High Power Density," Industrial Electronics, IEEE Transactions on , vol.55, no.10, pp.3543-3554, Oct. 2008.

[Ngu 2008] Nguyen Phung Quang, J.Andreas Dittrich, "Vector Control of Three-Phase AC Machines", Springer, 2008.

[Nia 2005] P. Niazi, " Permanent Magnet Assisted Synchronous Reluctance Motor Design and Performance", Phd thesis, Texas A&M University, 2005.

[Nog 1998] T. Noguchi, H. Tomiki, S. Kondo, I. Takahashi, "Direct power control of PWM converter without power-source voltage sensors," Industry Applications, IEEE Transactions on , vol.34, no.3, pp.473-479, May/Jun 1998.

[Nog 2006] T. Noguchi, A. Sato, D. Takeuchi, "Minimization of DC Reactor and Operation Characteristics of Direct-Power-Controlled Current-Source PWM Rectifier", IEEE Industrial Electronics, IECON 2006 - 32nd Annual Conference on, On page(s): 2787 - 2792, Volume: Issue: , 6-10 Nov. 2006.

[Nua 1998] N.A. Al-Nuaim, H. Toliyat, "A novel method for modeling dynamic air-gap eccentricity in synchronous machines based on modified winding function theory," Energy Conversion, IEEE Transactions on , vol.13, no.2, pp.156-162, Jun 1998.

[Oua 2006] S. Ouali, D. Saury, S. Harmand, O. Phillipart, D. Laloy; "Convective Heat Transfer Inside A Rotating Cylinder With An Axial Air Flows"; International Journal of Thermal Sciences, vol.45, 1166–1178, 2006.

[Owe 2011] R. Owen, et al, "Review of Variable-flux Permanent Magnet machines", ICEMS 2011, Beijing, China, 2011.

[Oze 2000] B. Ozerdem, "Measurement of Heat Transfer Coefficient for A Horizontal Cylinder Rotating in Quiescent Air", International Communication on Heat & Mass Transfer 27 (3), 389–395, 2000.

[Oze 2000] B. Ozerdem; "Measurement of Convective Heat Transfer Coefficeint for A Horizontal Cylinder Rotating in Quiescent"; Heat and Mass Transfer, Vol. 27, No. 3, pp. 389--395, 2000.

[Par 2005] A. Parviainen, "Design of Axial-Flux Permanent-Magnet Low-Speed Machines and Performance Comparison between Radial-Flux and Axial-Flux Machines", Phd Thesis, Lappeen University of Technology, Finland, 2005.

[Par 2005] A. Parviainen, “Design of Axial-Flux Permanent-Magnet Low-Speed Machines and Performance Comparison Between Radial-Flux and Axial-Flux Machines”, PhD thesis, Lappeenrantaenis University of Technology, Filand, 2005.

[Pol 1998] H. Polinder, “On the Losses in A High-Speed Permanent Magnet Generator with Rectifier with Special Attention to the Effect of a Damper Cylinder”; PhD thesis, TU Delft, 1998.

[Pol 1999] H. Polinder and M. J. Hoeijmakers, “Eddy-Current Losses in the Segmented Surface-Mounted Magnets of a PM Machine”, IEE Proc.Electr. Power Appl., vol.146, No.3, May 1999.

[Pol 2003] H. Polinder, J.G. Slootweg, M. Hoeijmakers, J.C. Compter, "Modeling of a linear PM Machine including magnetic saturation and end effects: maximum force-to-current ratio," Industry Applications, IEEE Transactions on , vol.39, no.6, pp. 1681- 1688, Nov.-Dec. 2003.

[Pol 2005] H. Polinder, et al "Design, modelling and test results of the AWS PM linear generator", European Transactions on Electrical Power, Vol.15, Iss.3, pp.245, 2005.

[Pol 2006] H. Polinder, F.F.A. van der Pijlde, G.-J. Vilder, P.J. Tavner, "Comparison of Direct-drive and Geared Generator Concepts for Wind Turbines," Energy Conversion, IEEE Transactions on , vol.21, no.3, pp.725-733, Sept. 2006.

[Pol 2007] H. Polinder, M.J. Hoeijmakers, M. Scuotto, "Eddy-Current Losses in the Solid Back-Iron of PM Machines for different Concentrated Fractional Pitch Windings," Electric Machines & Drives Conference. IEMDC '07. IEEE International , vol.1, no., pp.652-657, 3-5 May 2007.

[Pos 2005] M. Popescu, D.M. Ionel, T.J.E. Miller, S.J. Dellinger, M.I. McGilp, "Improved Finite Element Computations of Torque in Brushless Permanent Magnet Motors," Electric Power Applications, IEE Proceedings - , vol.152, no.2, pp. 271- 276, 4 March 2005.

[Pra 1991] B.V.S.S.S. Prasad, A.A. Tawfek, A.K. Mohanty, “Heat Transfer from A Circular Cylinder Rotating about An Orthogonal Axis in Quiescent Air”, Experiments in Fluids, vol.10, 267–272, 1991.

[Pro 2012] Protean, Electric Protean Ford Truck, http://www.proteanelectric.com/, last accessed the website on 7th March 2012.

[Pur 2006] J. Puranen, “Induction Motor versus PM Motor in Motion Control Applications”, PhD Thesis, Finland, 2006.

[Pyr 2008] J. Pyrhonen, et al, “Design of Rotating Electrical Machines”, John Wiley& Sons, Ltd, 2008.

[Qis 1985] G. Qishan and G. HongZhan, “Effective Slotting in Permanent Magnet Electric Machines”; Electric Machines and Power Systems, 1985.

[Ras 2001] M.H. Rashid, “Power Electronics Handbook”, Elsevier, 2001.

[Ref 2004] A.M. EL-Refaie, N.C. Harris, T.M. Jahns, K.M. Rahman, "Thermal Analysis of Multibarrier Interior PM Synchronous Machine using Lumped Parameter Model," Energy Conversion, IEEE Transactions on , vol.19, no.2, pp. 303- 309, June 2004.

[Ref 2005] A.M. EL-Refaie and T.M. Jahns, "Optimal flux weakening in surface PM machines using fractional-slot concentrated windings," Industry Applications, IEEE Transactions on , vol.41, no.3, pp. 790-800, May-June 2005.

[Ref 2006] A.M. El-Refaie, T.M. Jahns, and D. W. Novotny, “Analysis of Surface Permanent Magnet Machines with Fractional-Slot Concentrated Windings,”IEEE Trans. EC., vol.21, no.1, pp.34–43, Mar. 2006.

[Ref 2008a] A.M. EL-Refaie and T. M. Jahns, "Comparison of Synchronous PM Machine Types for Wide Constant-Power Speed Range Operation", COMPEL: The International Journal for Computation and Mathematics in Electrical and Electronic Engineering, Vol. 27 Iss: 5, pp.967 – 984, 2008.

[Ref 2008b] A.M. El-Refaie, Z.Q. Zhu, T.M. Jahns, D. Howe, "Winding Inductances of Fractional Slot Surface-Mounted Permanent Magnet Brushless Machines," Industry Applications Society Annual Meeting, 2008. IAS '08. IEEE , vol., no., pp.1-8, 5-9 Oct. 2008.

[Ref 2010] A.M. EL-Refaie, "Fractional-Slot Concentrated-Windings Synchronous Permanent Magnet Machines: Opportunities and Challenges," Industrial Electronics, IEEE Transactions on , vol.57, no.1, pp.107-121, Jan. 2010.

[Ref 2011] A.M. EL-Refaie, "Motors/generators for traction /propulsion applications: A review," Electric Machines & Drives Conference (IEMDC), 2011 IEEE International , vol., no., pp.490-497, 15-18 May 2011.

[Rol 2002] L.G.B. Rolim, et al, "Flywheel generator with switched reluctance machine", *Proceedings of the XV International Conference on Electrical Machines*, 2002.

[Rol 2003] B.B. Rolf and A.V. Ioan, "On the Single-Sided Transverse Flux Machine Design", Electric Power Components and Systems, 31:2, 109-128, 2003.

[Ros 2007] W. Roshen, "Iron loss model for permanent-magnet synchronous motors", IEEE Trans. Magn., vol. 43, no. 8, pp. 3428–3434, Aug 2007.

[Rou 2007] H. Rouhani, et al, "Lumped Thermal Model for Switched Reluctance Motor Applied to Mechanical Design Optimization"; Mathematical and Computer Modelling, vol.45, 625–638, 2007.

[Ruo 2010] S. Ruoho, "Modeling Demagnetization of Sintered NdFeB Magnet Material in Time-Discretized Finite Element Analysis", Phd Thesis, Aalto University, Finland, 2011.

[Saa 1998] J. Saari; "Thermal Analysis of High Speed Induction Motor Machines", PhD Thesis, Finland, 1998.

[Sah 2001] F. Sahin, "Design and Development of A High-Speed Axial-Flux Permanent-Magnet Machine", Eindhoven University of Technology, 2001.

[Sal 2004] P. Salminen, M. Niemela, J. Pyhonen, J. Mantere, "Performance Analysis of Fractional Slot Wound PM-Motors for Low Speed Applications," Industry Applications Conference, 2004. 39th IAS Annual Meeting. Conference Record of the 2004 IEEE , vol.2, no., pp. 1032- 1037 vol.2, 3-7 Oct. 2004.

[Sat 2011] A. Sato, T. Noguchi, "Voltage-Source PWM Rectifier–Inverter Based on Direct Power Control and Its Operation Characteristics", Power Electronics, IEEE Transactions on, On page(s): 1559 - 1567, Volume: 26 Issue: 5, May 2011.

[Sha 2010] M.R. Shah and A.M. El-Refaie, "End Effects in Multiphase Fractional Slot Concentrated-Winding Surface Permanent Magnet Synchronous Machines," Energy Conversion, IEEE Transactions on , vol.25, no.4, pp.1001-1009, Dec. 2010.

[She 2006] Sheng Chung Tzeng, "Heat Transfer in A Small Gap between Co-Axial Rotating Cylinders"; International Communications in Heat and Mass Transfer, vol.33, 737–743, 2006.

[Sin 2003] B. Singh, B.N. Singh, A. Chandra, K. Al-Haddad, A. Pandey, D.P. Kothari, "A Review of Single-Phase Improved Power Quality AC-DC Converters," Industrial Electronics, IEEE Transactions on , vol.50, no.5, pp. 962- 981, Oct. 2003.

[Sin 2004] B. Singh, B.N. Singh, A. Chandra, K. Al-Haddad, A. Pandey, D.P. Kothari, "A Review of Three-Phase Improved Power Quality AC-DC Converters," Industrial Electronics, IEEE Transactions on , vol.51, no.3, pp. 641- 660, June 2004.

[Sle 1990] G.R. Slemon, X. Liu, "Core losses in permanent magnet motors," Magnetics, IEEE Transactions on , vol.26, no.5, pp.1653-1655, Sep 1990.

[Sle 1992] G. R. Slemon and X. Liu, "Modeling and Design Optimization Of Permanent Magnet Motors", Electric Machines & Power Systems, Vol. 20, Iss. 2, 1992.

[Sle 1994] G.R. Slemon, "On the Design of High-Performance Surface-Mounted PM Motors," Industry Applications, IEEE Transactions on , vol.30, no.1, pp.134-140, Jan/Feb 1994.

[Sta 2001] D. Staton, et al, "Recent Advancement in the Thermal Design of Electric Motors"; SMMA, Fall Technical Conference "Emerging Technologies for Electric Motion Industry", Durham, North Carolina, USA, 3-5 Oct, 2001.

[Sta 2008] D.A. Staton, Cavagnino, A.; , "Convection Heat Transfer and Flow Calculations Suitable for Electric Machines Thermal Models," Industrial Electronics, IEEE Transactions on , vol.55, no.10, pp.3509-3516, Oct. 2008.

[Tot 2004] H. Tota, et al, "Rotor Eddy-Current Loss in Permanent Magnet Brushless Machines", IEEE Trans. On Magnetics, Vol. 40, No. 4, July 2004.

[Vio 2007] I.A. Viorel,.; K. Hamemeyer, L. Strete,"On the Carter's Factor Calculation for Slotted Electric Machine"; Advances in Electrical and Computer Engineering, Vol.7, No.2, 2007.

[Wan 2008] X. Wang and et al, "Simulation of Three-Phase Voltage Source PWM Rectifier Based on Direct Current Control," Image and Signal Processing, 2008. CISP '08. Congress on , vol.5, no., pp.194-198, 27-30 May 2008.

[Wan 2010a] D. Wang , X. Wang , Y. Yang and R. Zhang "Optimization of Magnetic Pole Shifting to Reduce Cogging Torque in Solid-Rotor Permanent Magnet Synchronous Motors", IEEE Trans. Magn., vol. 46, no. 5, pp.1228 - 1234 , 2010.

[Wan 2010b] J. Wang, K. Atallah, R. Chin, W.M. Arshad, H. Lendenmann, "Rotor Eddy-Current Loss in Permanent-Magnet Brushless AC Machines," Magnetics, IEEE Transactions on , vol.46, no.7, pp.2701-2707, July 2010.

[War 1977] P. A. Ward and P. J. Lawrenson, "Magnetic Permeance of Doubly-salient Air gaps", Proc. IEE, vol. 124, no. 6, pp.542-544, 1977.

[Wlo 2006] Z. Wlodarski, "Analytical Description of Magnetization Curves," Physica B., vol.373, pp.323–327, 2006.

[Wro 2008] R. Wrobel and P. H. Mellor, "Design Considerations of a Direct Drive Brushless Machine with Concentrated Windings," IEEE Trans. EC., vol. 23, no. 1, pp. 1–8, March. 2008.

[Wu 2011a] L.J. Wu, Z.Q. Zhu, D. Staton, M. Popescu, D. Hawkins, "Subdomain Model for Predicting Armature Reaction Field of Surface-Mounted Permanent-Magnet Machines Accounting for Tooth-Tips," Magnetics, IEEE Transactions on , vol.47, no.4, pp.812-822, April 2011.

[Wu 2011b] L.J. Wu, Z.Q. Zhu, D. Staton, M. Popescu, D. Hawkins, "An Improved Subdomain Model for Predicting Magnetic Field of Surface-Mounted Permanent Magnet Machines Accounting for Tooth-Tips," Magnetics, IEEE Transactions on , vol.47, no.6, pp.1693-1704, June 2011.

[Xin 2003] W. Xing-hua, W. Shu-hong, L.I. Qun-feng L.I. Qing-fu, "Analytical Calculation of No-Load Air-Gap Magnetic Field of Surface Permanent Magnet Motor", Electrical Machines and Systems, the 6th ICEMS 2003.

[Yam 2009] K. Yamazaki and Y. Fukushima, "Effect of Eddy-Current Loss Reduction by Magnet Segmentation in Synchronous Motors with Concentrated Windings," Electrical Machines and Systems, 2009. ICEMS 2009. International Conference on, vol., no., pp.1-6, 15-18 Nov. 2009.

[Yam 2010] K. Yamazaki, et al, "Reduction of Magnet Eddy-Current Loss in Interior Permanent-Magnet Motors With Concentrated Windings," IEEE Trans. IA., vol. 46, no. 6, pp. 2434–2441, Nov/Dec. 2010.

[Yam 2011] K. Yamazaki, et al, "Design of Interior Permanent Magnet Motor Considering Cross Magnetization caused by Magnetic Saturation", ICEMS 2011, Beijing, China, 2011.

[Yan 1988] H.Q. Yang, K.T. Yang, "Rotational Effects on Natural Convection in a Horizontal Cylinder"; AIChE Journal, 1988.

[Yan 2006] Y. Yang, X. Wang, R. Zhang, T. Ding, and R. Tang, "The Optimization of Pole Arc Coefficient to Reduce Cogging Torque in Surface-Mounted Permanent Magnet Motors," IEEE Trans. Magn., vol. 42, no. 4, pp. 1135–1138, Apr. 2006.

[Yan 2009] J. Yan; et al, "Magnetic Field Analysis of a Novel Flux Switching Transverse Flux Permanent Magnet Wind Generator with 3-D FEM," Power Electronics and Drive Systems, 2009. PEDS 2009. International Conference on , vol., no., pp.332-335, 2-5 Nov. 2009.

[Yan 2010] S. Yan, X. Wang, Y. Li, "Power Control of Three-Phase PWM Rectifier for Microturbine", Advanced Computer Control (ICACC), 2010 2nd International Conference on, On page(s): 219 - 223, Volume: 1 Issue: , 27-29 March 2010.

[Yi 2010] Yi Wang; S.W.H. de Haan, J.A. Ferreira, "High Power Density Design of High-Current DC-DC Converter With High Transient Power," Energy Conversion Congress and Exposition (ECCE), 2010 IEEE , vol., no., pp.3001-3008, 12-16 Sept. 2010.

[Yos 2000] K. Yoshida, Y. Hita and K. Kesamaru, "Eddy-Current Loss Analysis in PM of Surface-Mounted-PM SM for Electric Vehicles", IEEE Trans. On Magnetics, vol. 36,No. 4, July 2000.

[Zar 2006] D. Zarko , D. Ban and T. A. Lipo "Analytical calculation of magnetic field distribution in the slotted air gap of a surface permanent-magnet motor using complex relative air-gap permeance", IEEE Trans. Magn., vol. 42, p.1828 , 2006.

[Zhu 1993a] Z.Q. Zhu, D. Howe, E. Bolte, B. Ackermann, "Instantaneous magnetic field distribution in brushless permanent magnet DC motors. I. Open-circuit field," Magnetics, IEEE Transactions on , vol.29, no.1, pp.124-135, Jan 1993.

[Zhu 1993b] Z.Q. Zhu, et al, "Instantaneous Magnetic Field Distribution in Brushless Permanent Magnet DC Motors, part III: Effect of Stator Slotting," IEEE Trans. Magn., vol. 29, no. 1, pp. 143–151, Jan.1993.

[Zhu 1997] Z.Q. Zhu, D. Howe, "Winding inductances of brushless machines with surface-mounted magnets," Electric Machines and Drives Conference Record, 1997. IEEE International , vol., no., pp.WB2/2.1-WB2/2.3, 18-21 May 1997.

[Zhu 2000] Z.Q. Zhu and D. Howe, "Influence of Design Parameters on Cogging Torque in Permanent Magnet Machines", IEEE Trans. Energy Conversion, vol. 15, no. 4, pp. 407-412, 2000.

[Zhu 2002] Z.Q. Zhu, D. Howe and C.C. Chan, "Improved analytical model for predicting the magnetic field distribution in brushless permanent-magnet machines", IEEE Trans. Magn., vol. 38, p.229 , 2002.

[Zhu 2004] Z.Q. Zhu, K. Ng, N. Schofield and D. Howe, "Improved Analytical Modelling of Rotor Eddy Current Loss in Brushless Machines Equipped with Surface-Mounted Permanent Magnets", IEE Proc.-EPA., vol. 151, no. 6, pp. 641-650, 2004.

[Zhu 2009a] Z.Q. Zhu, Z.P. Xia, L.J. Wu and G.W. Jewell, "Influence of Slot and Pole Number Combination on Radial Force and Vibration Modes in Fractional Slot PM Brushless Machines Having Single-and Double-Layer Windings," IEEE Energy Conversion Congress and Exposition, ECCE2009, 20-24 Sept. 2009, San Jose, California, USA.

[Zhu 2009b] Z.Q. Zhu, "Fractional Slot Permanent Magnet Brushless Machines and Drives for Electric and Hybrid Propulsion Systems", Ecological Vehicles and Renewable Energies (EVER 09), 26-29 March 2009, Monaco.

[Zhu 2009c] Z.Q. Zhu, Z.P. Xia, L.J. Wu, G.W. Jewell, "Analytical Modelling and Finite Element Computation of Radial Vibration Force in Fractional-Slot Permanent Magnet Brushless Machines," Electric Machines and Drives Conference, 2009. IEMDC '09. IEEE International , vol., no., pp.144-151, 3-6 May 2009.

[Zhu 2009d] Z.Q. Zhu, "A simple method for measuring cogging torque in permanent magnet machines," Power & Energy Society General Meeting, 2009. PES '09. IEEE , vol., no., pp.1-4, 26-30 July 2009.

[Zhu 2010] Z.Q. Zhu, L.J. Wu, Z.P. Xia, "An Accurate Subdomain Model for Magnetic Field Computation in Slotted Surface-Mounted Permanent-Magnet Machines," Magnetics, IEEE Transactions on , vol.46, no.4, pp.1100-1115, April 2010.

[Zhu 2011a] Z.Q. Zhu, "Recent Advances on Permanent Magnet Machines Including IPM Technology", IEEE-IEMDC 2011, Canada, May, 2011.

[Zhu 2011b] Z.Q. Zhu, "Switched Flux Permanent Magnet Machines: Innovation Continues", ICEMS 2011, Beijing, China, 2011.

[Zhu 2011c] Z.Q. Zhu, X. Liu, "Individual and Global Optimization of Switched Flux Permanent Magnet Motors", ICEMS 2011, Beijing, China, 2011.

[Ziv 2006] V. Zivotic-Kukolj, W.L. Soong and N. Ertugrul, " Iron Loss Reduction in an Interior PM Automotive Alternator", IEEE Trans. IA., vol. 42, no. 6, pp. 1478–1486, Nov/Dec. 2006.

Modeling of Exterior Rotor Permanent Magnet Machines with Concentrated Windings

PhD thesis

By **Vũ Xuân Hùng**

Background and Objectives

The incentive for the work in this thesis originates from a research project concerning the design of a generator system in a vessel application. The modeling, analysis, and design of the exterior rotor permanent magnet (PM) machines with concentrated windings in a flywheel are dealt with. The developed models are verified with measurements. Such a generator system can be used in hybrid cars, hybrid trains, and mobile ground power stations.

The first objective of this thesis is to find the most suitable configuration of the PM machine in a flywheel. The criteria to select generator for the application are ease of mounting on a diesel engine, the possibility of integration in a flywheel, high torque density, high efficiency and low cost. Another objective in this thesis is to develop a new model for the design of PM machines. It would be better to compromise between calculation time and calculation accuracy in comparison with the existing models in literature. The influence of design parameters on the performance of the PM machine, with special attention to slotting effect is also addressed in this study.

Finding the Most Suitable Configuration of a PM Machine

The exterior rotor surface-mounted permanent magnet machine with double-layer concentrated windings is selected for this application. This PM machine is well integrated in a flywheel, has high torque density and high efficiency, and is cost-effective.

Electromagnetic and Thermal Models for Design of the PM Machine

A number of electromagnetic models are developed in this study such as the analytical model, the static FEM model, the dynamic FEM model, and the hybrid model for the analysis and design optimization of the PM machine. The analytical model is used to find the feasible

dimension sets of the PM machine. It provides quick insight into changes of design parameters. Meanwhile, the automated nonlinear transient FEM model including rotor motion can be used for analysis, refining design results or direct-design optimization with the number of design variables limited. For design optimization, the analytical model is less accurate because it neglects some effects such as magnetic saturation, fringing effect, and slotting effect or because these are hard to model. The nonlinear transient 2D-FEM model including rotor motion is accurate, but very time-consuming when there are a great number of design variables. Therefore, a new hybrid model is developed for design optimization in an attempt to compromise between calculation time and calculation accuracy.

A demagnetization model is also developed to evaluate the demagnetization of magnets. This is to ensure that the designed PM machine will be safe during the worst operation.

A circuit thermal model coupled with the electromagnetic transient FEM model of the PM machine is developed for design optimization of PM machines.

Slotting Effect

The influence of slotting and other design parameters on flux linkage, internal voltage, cogging torque, mean electromagnetic torque, rotor eddy current loss, and stator iron loss is investigated. It is shown that conventional literature of the slotting effect using Carter factor has a limitation in the range of small slot opening. For traditional approach, when slot opening is decreasing, Carter factor decreases. Therefore, the voltage as well as mean electromagnetic torque increases. However, in the range of small slot opening, when slot opening is decreasing, the leakage flux through tooth tips is in fact increasing and flux linkage is decreasing, leading to a decrease in the voltage as well as mean torque. This study has provided a new view about the influence of slot opening on flux linkage, internal voltage, and mean electromagnetic at small slot opening, which has not been covered in literature before this study.

The influence of slotting and other design parameters on flux linkage, internal voltage, cogging torque, mean electromagnetic torque, rotor eddy current loss, and stator iron loss is investigated. It is shown that conventional literature about the slotting effect using the Carter factor shows limitations in the range of small slot opening. According to the traditional approach, when the slot opening decreases, the Carter factor decreases. Therefore, the voltage as well as the mean electromagnetic torque increases. However, it was found in this study that in the range of small slot opening, when the slot opening decreases, the leakage flux through tooth tips in fact increases and flux linkage is decreases, leading to a decrease in the voltage as well as the mean torque. This study has thus provided a new insight into the influence of slot opening

on flux linkage, internal voltage and mean electromagnetic at small slot opening, which was not covered in literature before this study was undertaken.

Experimental Validation of Models

A non-linear FEM model including rotor motion and coupled to the circuit model is validated. Calculated results of electromotive force, voltage, electric current, electromagnetic torque, total iron loss of rotor and stator, three-phase short circuit current, and reactance using the FEM model showed good agreement with experimental results with an error margin smaller than 3%. It is shown that the end effects of a PM machine with concentrated windings having a large number of teeth and poles can be neglected, even when its diameter is larger than its length. Therefore, the 2D-FEM simulation is sufficient for the application considered in this study. The FEM model during the three-phase short circuit is also experimentally validated. This model is used to evaluate magnet demagnetization during short circuit.

To validate the influence of the slotting effect on internal voltage and total iron loss of rotor and stator, two additional PM machines are designed and manufactured: one is fully open slot machine and the other is semi-open slot machine. Comparison of simulation and experimental results of internal voltage shows good agreement. Comparison of the total iron loss of the stator and rotor of the two PM machines confirms that the total iron loss of the rotor and stator of a fully open slot PM machine is much higher than that of a semi-open slot PM machine. This is due to high rotor eddy current loss of the fully open slot machine.

In Conclusion

The analyses, comparisons, and experiments in this thesis offer insight into the merits and drawbacks of the configuration of PM machines. This helps in the selection of the right configuration of PM machine for the specific application. A four-step process to select a combination of slot and pole for minimizing peak-peak cogging torque is proposed. The influence of design parameters on the performance of the PM machine is presented. The results of the study give an insight into the influence of the slotting effect on flux linkage, internal voltage, mean electromagnetic torque, rotor eddy current loss, and stator iron loss at small slot opening. A method for separating the slotting effect and the fringing effect in FEM computation is proposed in order to evaluate the Carter factor expressions in literature. A method for calculating the total correction factor of slotting, fringing, and magnetic saturation effects is proposed to overcome the limitations of the traditional analytical design model at small slot opening. The developed hybrid model as well as the automated dynamic FEM model including rotor motion becomes an indispensable tool for the design optimization of the PM machines in small-scale ship application.

Modellering van buitenrotor permanent magneet machines met geconcentreerde wikkelingen

Proefschrift
Door **Vũ Xuân Hùng**

Achtergrond en doelstellingen

Het onderzoek leidend tot dit proefschrift is onderdeel van een onderzoeksproject gericht op het ontwerp van een generatorsysteem voor een scheepvaarttoepassing. Onderzocht zijn de modellering, analyse, ontwerp van en experimenten met permanente-magneetmachines met buitenrotor en geconcentreerde wikkelingen, gemonteerd in een vliegwiel. Zo een generatorsysteem kan gebruikt worden in hybride auto's, hybride treinen, aggregaten, enz.

De eerste doelstelling van dit proefschrift is het vinden van de geschiktste configuratie voor de PM-machine gemonteerd in een vliegwiel. Selectiecriteria voor de generator in deze toepassing zijn een eenvoudige montage op een dieselmotor, de mogelijkheid tot integratie in het vliegwiel, een hoge koppeldichtheid, een hoog rendement en lage kosten. De tweede doelstelling van dit proefschrift is de ontwikkeling van een nieuw model voor het ontwerp van PM-machines. Dit model moet een beter compromis bieden tussen rekentijd en nauwkeurigheid dan bestaande modellen uit de literatuur. De invloed van ontwerpparameters op de prestaties van de PM-machine wordt beschouwd, met speciale aandacht voor vertandings-effecten (*slotting*).

Vind de geschiktste configuratie voor de PM-machine

De PM-machine met buitenrotor, opgelegde magneten en dubbellaags geconcentreerde wikkeling is geselecteerd voor deze toepassing. Dit machine-type is goed te integreren in een vliegwiel, heeft een hoge koppeldichtheid en rendement en is goedkoop te produceren.

[3] Translated to Dutch by Martin van der Geest.

Elektromagnetische en thermische modellen voor het ontwerp van de PM-machine

Een aantal elektromagnetische modellen is ontwikkeld in deze studie, zoals een analytisch model, een statisch en dynamisch eindig-elementenmodel (FE) en een hybride model voor de analyse en optimalisatie van de PM-machine. Met het analytische model kunnen geschikte dimensies van de PM-machine worden bepaald. Het geeft ook snel inzicht op de invloeden van de ontwerpparameters op de prestaties. Tegelijkertijd kunnen automatische niet-lineaire transiënte FE-modellen met rotorbeweging gebruikt worden voor verdere verfijning van een ontwerp of een directe optimalisatie met een beperkt aantal ontwerpparameters. Een analytisch model is minder geschikt voor optimalisatie omdat bepaalde zaken, zoals magnetische verzadiging, uitbloezen van het veld (*fringing*) en vertanding (*slotting*), niet, of slechts versimpeld beschouwd kunnen worden. Een niet-lineaire transiënte 2D FEM-simulatie heeft deze beperkingen niet, maar is zeer tijdrovend bij een groot aantal ontwerpparameters. Voor de optimalisering van een machine-ontwerp is daarom een nieuw hybride model ontwikkeld dat een beter compromis biedt tussen rekentijd en nauwkeurigheid.

Daarnaast is ook een demagnetisatie-model ontwikkeld om de mate van demagnetisatie te bepalen, zodat verzekerd kan worden dat de machine niet demagnetiseert onder elke mogelijke belasting. Verder is er ook een thermisch model ontwikkeld, gekoppeld aan de elektromagnetische FEM-simulaties, zodat temperatuursbeperkingen mee genomen kunnen worden in de optimalisaties.

Vertandingseffect

De invloed van vertanding en andere ontwerpparameters op de gekoppelde flux, interne spanning, kleefkoppel, gemiddelde elektromagnetische koppel, rotorwervelstroomverliezen en de stator-ijzerverliezen is onderzocht. Het wordt aangetoond dat de conventionele literatuur over vertanding, gebaseerd op de Carter-factor, een beperking heeft bij kleine groef-openingen. Bij de traditionele benadering neemt de Carter-factor af bij een kleiner wordende groefopening, waardoor de spanning en het gemiddelde elektromagnetische koppel toenemen. In werkelijkheid nemen bij kleiner wordende groefopeningen de lekflux toe en de gekoppelde flux af, wat leidt tot een daling in de spanning en het gemiddelde koppel. Dit onderzoek geeft een nieuw inzicht in het effect van de groefopening op de gekoppelde flux, interne spanning, kleefkoppel en gemiddeld elektromagnetische koppel bij kleine groefopeningen, wat vooralsnog niet beschreven is in de literatuur.

Experimentele validatie

Een niet-lineair FE-model waarbij de rotorbeweging gekoppeld is aan het elektrische circuit model is gevalideerd met metingen. De spanning, elektrische stroom, elektromagnetisch koppel,

totaal ijzerverlies, drie-fase-kortsluitstroom en reactantie, berekend met het FE-model, toonden een goede overeenkomst met experimentele resultaten met een foutmarge kleiner dan 3%. Het blijkt dat het eind-effecten in een PM-machine met geconcentreerde wikkelingen en een groot aantal tanden en polen kunnen worden verwaarloosd, zelfs wanneer de diameter groter is dan de lengte. 2D-FE-simulaties volstaan daarom in deze toepassing. Het FE model voor een drie-fase kortsluiting is ook experimenteel gevalideerd. Dit model wordt gebruikt om de mate van demagnetisatie van de magneten te bepalen tijdens een kortsluiting.

Om bovendien de invloed van de vertanding op de interne spanning en totale ijzerverliezen te bepalen zijn twee extra PM-machines ontworpen en gebouwd: één met open groeven en één met halfopen groeven. De gesimuleerde en gemeten EMK tonen een goede overeenkomst. Een vergelijking van de experimenteel bepaalde elektrische nullastverliezen van beide machines bevestigt dat open groeven tot hogere rotorwerverstroomverliezen leiden. Als gevolg zijn de totale elektrische nullastverliezen van PM-machines met open groeven veel hoger dan met halfopen groeven.

Ter conclusie

De reeks analyses, vergelijkingen en experimenten in dit proefschrift geeft inzicht in de voor- en nadelen van verschillende types PM-machines. Dit helpt bij het selecteren van het geschikte type voor de specifieke toepassing. Een vier-stappenplan voor het kiezen van een tand-pool combinatie met minimale piek-piek kleefkoppel wordt voorgesteld. De invloed van ontwerpparameters op de prestaties van de PM machine wordt gepresenteerd. Het onderzoek geeft inzicht in de invloed van vertanding op de gekoppelde flux, interne spanning, gemiddeld elektromagnetische koppel, rotorwervelstroomverliezen en de stator-ijzerverliezen bij kleine groefopeningen. Methodes voor het scheiden van vertandings-en uitbloezingseffecten in FE-berekeningen en het berekenen van correctiefactoren voor deze effecten alsook verzadigingseffecten worden voorgesteld. Het ontwikkelde hybride model en het geautomatiseerde dynamische FE-model met rotorbeweging zijn een onmisbaar instrument geworden voor de optimalisatie van PM-machines in kleinschalige scheepvaarttoepassingen.

LIST OF PUBLICATIONS

1. Hung Vu Xuan, D. Lahaye, H. Polinder, J.A. Ferreira, "Influence of stator slotting on the performance of permanent magnet machines with concentrated windings," *IEEE Transactions on Magnetics,* vol.48, issue.99, doi: 10.1109/TMAG.2012.2212025.
2. Hung Vu Xuan, D. Lahaye, H. Polinder, J.A. Ferreira, "Modeling, measurement and comparison of fractional slot permanent magnet machines with concentrated windings in small-scale ship application," *Considering for publication*.
3. Hung Vu Xuan, H. Polinder, D. Lahaye, J.A. Ferreira, "Modeling for the design of fractional slot permanent magnet machines with concentrated windings protected from demagnetization during three-phase short-circuit," *The 2012 IEEE Energy Conversion Congress and Exposition (ECCE)*, Raleigh, North Carolina, USA, September 16-20.
4. Hung Vu Xuan, D. Lahaye, H. Polinder, J.A. Ferreira, "Thermal model for an exterior rotor permanent magnet machine with concentrated windings in a flywheel," *International conference SPEEDAM,* Italy, 2012.
5. Hung Vu Xuan, D. Lahaye, H. Polinder, J.A. Ferreira, "An efficient method for analysis and design of PM machines in flywheels," *IEEE JOINT IAS/PELS/PES BENELUX CHAPTER*, the sixth *IEEE YRS*, Delft, The Netherlands, 16-17 April, 2012.
6. Hung Vu Xuan, S.O. Ani, D. Lahaye, H. Polinder, J.A. Ferreira, "Validation of non-linear dynamic FEM model for design of PM machines with concentrated windings in ship application," *Power Electronics and Applications (EPE 2011), Proceedings of the 2011-14th European Conference on* , vol., no., pp.1-9, Aug. 30 2011-Sept.1 2011. Birmingham, UK. E-ISBN: 978-90-75815-15-3. Print ISBN: 978-1-61284-167-0.
7. Hung Vu Xuan, D. Lahaye, S.O. Ani, H. Polinder, J.A. Ferreira, "Electrical generators for maritime application," *Electrical Machines and Systems (ICEMS), 2011 International Conference on*, vol., no., pp.1-6, 20-23 Aug. 2011, Beijing, China. doi: 10.1109/ICEMS.2011.6073526.
8. Hung Vu Xuan, D. Lahaye, H. Polinder, J.A. Ferreira, "Influence of slot/pole number combination on performances of permanent magnet machines with concentrated windings for ship application," *Electrical Machines and Systems (ICEMS), 2011 International Conference on*, vol., no., pp.1-6, 20-23 Aug. 2011, Beijing, China. doi: 10.1109/ICEMS.2011.6073667.
9. Hung Vu Xuan, D. Lahaye, S.O. Ani, H. Polinder, J.A. Ferreira, "Effect of design parameters on electromagnetic torque of PM machines with concentrated windings using

nonlinear dynamic FEM," *Electric Machines & Drives Conference (IEMDC), 2011 IEEE International*, vol., no., pp.383-388, 15-18 May 2011, Canada. doi: 10.1109/IEMDC.2011.5994625.

10. Hung Vu Xuan, D. Lahaye, H. Polinder, J.A. Ferreira, "Improved model for design of permanent magnet machines with concentrated windings," *Electric Machines & Drives Conference (IEMDC), 2011 IEEE International* , vol., no., pp.948-954, 15-18 May 2011, Canada. doi: 10.1109/IEMDC.2011.5994943.
11. Hung Vu Xuan, D. Lahaye, M.J. Hoeijmakers, H. Polinder, J.A. Ferreira, "Studying rotor eddy current loss of PM machines using nonlinear FEM including rotor motion," *Electrical Machines (ICEM), 2010 XIX International Conference on*, vol., no., pp.1-7, 6-8 Sept. 2010. Rome, Itali. doi: 10.1109/ICEM MACH.2010.5608045.
12. Hung Vu Xuan, D. Lahaye, M.J. Hoeijmakers, H. Polinder, J.A. Ferreira, "Modeling magnetic saturation for the design of exterior rotor permanent magnet machines," *Power Electronics Conference (IPEC), 2010 International*, vol., no., pp.1299-1305, 21-24 June 2010, Sapporo, Japan. doi: 10.1109/IPEC.2010.5543387.

BIOGRAPHY

Vũ Xuân Hùng was born in Hagiang, Vietnam. He received the Bachelor's degree and Master's degree (both first-class) in electrical engineering, from the Hanoi University of Science and Technology, Vietnam, in 2000 and 2003, respectively.

He was a lecturer at the Hanoi University of Communication and Transport, Vietnam. He took part in several projects concerning the manufacture and factory acceptance testing of distribution and power transformers, electric machine drives, and the design of integrated control systems based on programmable logic controllers and micro-controllers.

He started working towards a PhD degree in 2008, at the Electrical Power Processing group, Department of Electrical Sustainable Energy, Faculty of Mathematics, Science Computer and Electrical Engineering, Delft University of Technology, The Netherlands.

His current research interests include finite element analysis, thermal analysis, design optimization of permanent magnet machines, and electric drives.